Meshless numerical method for modeling of heterogeneous materials

Jalušić, Boris

University of Zagreb

FACULTY OF MECHANICAL ENGINEERING
AND NAVAL ARCHITECTURE

Boris Jalušić

MESHLESS NUMERICAL METHOD FOR MODELING OF HETEROGENEOUS MATERIALS

DOCTORAL THESIS

Zagreb, 2016

University of Zagreb

FACULTY OF MECHANICAL ENGINEERING
AND NAVAL ARCHITECTURE

Boris Jalušić

MESHLESS NUMERICAL METHOD FOR MODELING OF HETEROGENEOUS MATERIALS

DOCTORAL THESIS

Supervisor:
Prof. dr. sc. Jurica Sorić

Zagreb, 2016

Sveučilište u Zagrebu

FAKULTET STROJARSTVA I BRODOGRADNJE

Boris Jalušić

BEZMREŽNA NUMERIČKA METODA ZA MODELIRANJE HETEROGENIH MATERIJALA

DOKTORSKI RAD

Mentor:
Prof. dr. sc. Jurica Sorić

Zagreb, 2016

BIBLIOGRAPHY DATA

UDC:	519.6 : 519.63 : 531.3 : 539.3
Keywords:	heterogeneous material, MLPG concept, collocation method, mixed approach, gradient elasticity, operator-split procedures
Scientific area:	Technical sciences
Scientific field:	Mechanical engineering
Institution:	Faculty of Mechanical Engineering and Naval Architecture (FAMENA), University of Zagreb
Supervisor:	Dr. sc. Jurica Sorić, Professor
Number of pages:	161
Number of pages (in total):	200
Number of figures:	100
Number of tables:	4
Number of references:	204
Date of oral examination:	5. October 2016.
Committee members:	Dr. sc. Tomislav Jarak, Assistant Professor, University of Zagreb, Croatia Dr. sc. Jurica Sorić, Professor, University of Zagreb, Croatia Dr. sc. Božidar Šarler, Professor, University in Nova Gorica, Slovenia
Archive:	Faculty of Mechanical Engineering and Naval Architecture (FAMENA), University of Zagreb

Acknowledgments

Foremost, I wish to express my gratitude to my Thesis supervisor, Prof. dr. sc. Jurica Sorić for introducing me to the novel numerical field of meshless methods. In addition, I would also like to extend my thanks for his support and suggestions throughout the entire research period in which the work enveloped in this Thesis was made.

Secondly, my sincere appreciation goes out to Assist. prof. dr. sc. Tomislav Jarak for his enormous effort in the form of constructive talks, guidance and discussions that helped me resolve many of the theoretical, mathematical and numerical implementation issues.

Furthermore, I would like to thank committee member Prof. dr. sc. Božidar Šarler for finding the time to read and review the Thesis and for providing valuable suggestions and comments.

I would like to extend gratitude to all of my friends at the Faculty of Mechanical Engineering and Naval Architecture especially to my colleagues from the Institute of Applied Mechanics. Within the Institute big thank you is expressed to my former roommates at the University, Assist. prof. dr. sc. Marko Jokić and postdoc. researcher dr. sc. Jasna Leder Horina for their friendship and support. Also a special thanks for creating an enjoyable every day working environment goes to my dear coworkers comprised in the Laboratory of Numerical Mechanics, Prof. dr. sc. Zdenko Tonković, Prof. dr. sc. Igor Karšaj and Assist. prof. dr. sc. Ivica Skozrit, along with the postdoc. researcher dr. sc. Tomislav Lesičar and research assistants Lana Virag, Filip Putar, Ivan Trapić, Nino Horvat and Joško Frančeski. I also wish to express my appreciation to my former coworkers dr. sc. Josip Hoster and dr. sc. Eduard Marenić for their valuable discussions.

In closing, I wish to express my deepest gratitude to my family, my parents Katarina and Josip, my sister Ivana and her husband Tomislav. Thanks you for all your patience and support through the years.

Finally, my enormous thanks goes to my fiancée Mateja who brightens my every day life in every imaginable way. Thank you for believing in me, understanding and your unconditional support.

Boris Jalušić

Zagreb, September 2016.

Special acknowledgment

I wish to express my deepest gratitude to the Croatian Science Foundation who financed the research conducted in this Thesis through the project Multiscale Numerical Modeling of Material Deformation Responses from Macro- to Nanolevel (2516).

Boris Jalušić

Zagreb, September 2016.

Contents

List of Figures

List of Tables

List of Symbols

Abbreviations

RPICM Radial Point Interpolation Collocation Method 55

RPIM Radial Point Interpolation Method 4

S-PIM Smoothed Point Interpolation Method 9

TPS Thin Plate Spline RBF 49

Greek symbols

$\boldsymbol{\alpha}$ diagonal matrix of penalty parameters 33

α_{c} Gaussian (exponential) RBF shape parameter 49

α_{q} first Multi-Quadrics RBF shape parameter 49

α_{s} arbitrary scalar value for determining the size of the MLS support domain . 43

δ_{ij} Kronecker delta symbol 18

$\mathrm{d}\Gamma$ differential of the global outer boundary 19

$\mathrm{d}\Omega$ differential of the global problem domain 19

∂_x first-order partial derivative with respect to Cartesian coordinate x 18

∂_y first-order partial derivative with respect to Cartesian coordinate y 18

ε regularization parameter of the weight function of the MLS approximation . 47

$\boldsymbol{\varepsilon}$ strain vector within domain Ω 18

$\boldsymbol{\varepsilon}^{\mathrm{c}-}$ classical strain vector within domain Ω^- 111

$\boldsymbol{\varepsilon}^{\mathrm{c}+}$ classical strain vector within domain Ω^+ 111

$\boldsymbol{\varepsilon}^{-}$ strain vector within domain Ω^- 60

$\boldsymbol{\varepsilon}^{+}$ strain vector within domain Ω^+ 60

$\varepsilon_{ij}^{\mathrm{c}}$ classical strain tensor within domain Ω 27

$\varepsilon_{ij}^{\mathrm{c}-}$ classical strain tensor within domain Ω^- 107

$\varepsilon_{ij}^{\mathrm{c}+}$ classical strain tensor within domain Ω^+ 107

$(\hat{\varepsilon}_{ij}^{\mathrm{c}+})_J$ nodal values of classical strains for node J within Ω^+ 109

$\varepsilon_{ij}^{\mathrm{dev}}$ strain deviator tensor 133

$\varepsilon_{\mathrm{eq}}$ equivalent strain 133

$\hat{\boldsymbol{\varepsilon}}_{\mathrm{G}}^{\mathrm{g}-}$ vector of nodal values of derivatives of strains $\varepsilon^{\mathrm{g}-}$ within domain Ω^- . . . 120

$\hat{\boldsymbol{\varepsilon}}_{\mathrm{G}}^{\mathrm{g}+}$ vector of nodal values of derivatives of strains $\varepsilon^{\mathrm{g}+}$ within domain Ω^+ . . . 120

$\varepsilon_{ij}^{\mathrm{g}}$ gradient strain tensor within domain Ω 27

$(\hat{\varepsilon}_{ij}^{\mathrm{g}+})_J$ nodal values of gradient strains for node J within Ω^+ 110

$(\hat{\varepsilon}_{\mathrm{G}ij}^{\mathrm{g}+})_J$ nodal values of derivatives of strains $\varepsilon^{\mathrm{g}+}$ for node J within Ω^+ 110

$\phi_{J,i}$ first-order derivatives of the shape function with respect to coordinate x_i . . 45

μ_{ij} higher-order stress tensor within domain Ω 23

$\psi_{ijk}^{\mathrm{g}-}$ third-order tensor of first derivatives of strains on $\Gamma_{\mathrm{t}}^{\mathrm{g}-}$ 107

$\psi_{ijk}^{\mathrm{g}+}$ third-order tensor of first derivatives of strains on $\Gamma_{\mathrm{t}}^{\mathrm{g}+}$ 107

ρ material density within domain Ω 20

$\boldsymbol{\sigma}$ stress vector within the domain Ω 18

σ_{ij} Cauchy stress tensor within domain Ω 18

σ_j^{anal} analytical values of stresses 66

σ_{ij}^{c-} Cauchy stress tensor within domain $\Omega^{\mathrm{c}-}$ 106

σ_{ij}^{c+} Cauchy stress tensor within domain $\Omega^{\mathrm{c}+}$ 106

σ_j^{FEM} numerical values of stresses obtained by using FEM 66

σ_j^{MM} numerical values of stresses obtained by using MM 66

σ_{ij}^{-} Cauchy stress tensor within domain Ω^{-} 56

σ_{ij}^{+} Cauchy stress tensor within domain Ω^{+} 56

$(\hat{\sigma}_{ij}^{+})_J$ nodal values of stress components associated with node J within Ω^{+} 59

$\widetilde{\sigma}_{ij}$ Aifantis stress tensor within domain Ω 23

σ_{ij}^{c} classical stress tensor within domain Ω 28

σ_{ij}^{g} gradient stress tensor within domain Ω 28

τ_{ijk} higher-order stress tensor within the domain Ω 24

Latin symbols

$\mathbf{a}$ vector of unknown coefficients in the RPIM associated with RBFs 49

$\mathbf{a}(\mathbf{x})$ vector of unknown coefficients of the MLS approximation at $\mathbf{x}$ 40

$\mathbf{A}(\mathbf{x})$ moment matrix of the MLS approximation at the point of interest $\mathbf{x}$ 40

$\mathbf{b}$ vector of unknown coefficients in the RPIM associated with polynomials . . 49

b_i body force vector within domain Ω 20

b_i^{-} body force vector within domain Ω^{-} 56

b_i^{+} body force vector within domain Ω^{+} 56

$\mathbf{B}_J(\mathbf{x})$ J-th column of the matrix $\mathbf{B}(\mathbf{x})$ in the MLS approximation 46

$\mathbf{B}_{MJ}^{-}$ matrix of first-order derivatives of shape functions for the nodes within Ω^{-} . 61

$\mathbf{B}_{IJ}^{+}$ matrix of first-order derivatives of shape functions for the nodes within Ω^{+} . 61

$\mathbf{B}(\mathbf{x})$ matrix $\mathbf{B}$ of the MLS approximation at the point of interest $\mathbf{x}$ 41

Other symbols

Abstract

In recent decades, an increasing interest in using meshless methods has existed due to their beneficial properties in comparison to more commonly used numerical methods such as the Finite Element Method (FEM). In this class of numerical approaches, the discretization of geometry and the approximation of unknown field variables have been done by using only points that are not connected into elements. Hence, there is no need for a time-consuming mesh creation process and the problems associated with the distorsion of elements are avoided. Despite these attractive properties of meshless methods, high numerical costs and low accuracy associated with the calculation of high-order derivatives of approximation functions, which are particularly needed for solving problems involving the gradient elasticity, still represent a severe setback. The use of meshless methods based on the mixed approach can alleviate the aforementioned drawbacks since they require a lower continuity degree of the approximation functions. The research conducted in the frame of this Thesis is related to the improvement of numerical modeling of heterogeneous materials using newly developed meshless collocation methods based on the mixed approach. The heterogeneous materials are defined by partitioning the total material domain into subdomains with different linear-elastic isotropic properties. These subdomains define the homogeneous constituents. The discretization and approximation of unknown field variables is done for each homogeneous material independently, therein the interface of the homogeneous materials is discretized with overlapping nodes. The solution for the entire heterogeneous structure is obtained by enforcing appropriate boundary conditions at the nodes representing the interface boundary depending on the utilized formulation. The methods are applied to the linear elastic and the strain gradient formulation of the boundary value problem. For the approximation, the Moving Least Squares method with the imposed interpolation condition and Radial Point Interpolation method with polynomial reproduction are utilized. The numerical efficiency of the presented methods is demonstrated by suitable numerical examples. The obtained results are compared with a standard fully displacement meshless approach, as well as with available analytical and numerical solutions. Excellent agreement of the solutions is obtained and improved modeling of material discontinuity is achieved. Furthermore, the use of the mixed approach reduces the required degree of continuity of the approximation function, which increases accuracy and stability in comparison to the same class of meshless methods based only on the approximation of the displacements used up to now.

Key words

heterogeneous material

MLPG concept

collocation method

mixed approach

gradient elasticity

operator-split procedures

Ključne riječi

heterogeni materijal

MLPG koncept

kolokacijska metoda

mješoviti pristup

gradijentna elastičnost

stupnjevani postupci rješavanja

Prošireni sažetak

Uvod

Većina današnjih inženjerskih materijala koji se primjenjuju u praksi imaju heterogenu strukturu. Često ih se klasificira kao višefazne ili kompozitne materijale. S inženjerskog stajališta, heterogeni materijali su poželjni jer mogu biti izrađeni tako da se iskoriste najbolja svojstva svakog pojedinog konstituenta. U inženjerskim konstrukcijama često se koriste mnogi heterogeni materijali kao što su stijena, beton, drvo i drugi slični materijali. Međutim, zbog svojih dobrih materijalnih svojstava, najvažniji i najviše upotrebljavani su zasigurno vlaknima ojačani kompoziti i legure metala. Značajan utjecaj na ponašanje materijala na makrorazini imaju veličina, oblik, prostorni raspored, volumni udio i svojstva pojedinih konstituenata koji čine mikrostrukturu. Posljednjih godina posebna pozornost usmjerena je na istraživanja odnosa između makroskopskih svojstava materijala i njihove mikrostrukture, pri čemu veliku primjenu imaju numeričke metode.

Poznato je da klasična mehanika kontinuuma ne može uzeti u obzir strukturne efekte u materijalu na mikrorazini te stoga ne može dovoljno točno opisati procese deformiranja heterogenih materijala. Iz tog razloga razvijene su tzv. višerazinske (engl. *multi-scale*) numeričke metode koje omogućuju procjenu ponašanja materijala na makrorazini iz poznatih svojstava konstituenata i mikrostrukture. Pritom se rješenja dobivena analizom na mikrorazini odgovarajućim numeričkim postupcima prenose se na makrorazinu [1–3]. Za rješavanje problema rubnih vrijednosti na mikrorazini najčešće se kao reprezentativni model mikrostrukture koriste jedinična ćelija (engl. *unit cell*) [4] ili statistički reprezentativni uzorak materijala, reprezentativni volumenski element (RVE) [2]. Metoda jediničnih ćelija pogodna je za opisivanje materijala s pravilnom mikrostrukturom kod kojih se može pretpostaviti pravilan raspored heterogenosti te se uvelike primjenjuje za analizu kompozitnih materijala [5, 6]. S obzirom da su istraživanja pokazala da prostorna nejednolikost mikrostrukture ima značajan utjecaj na svojstva materijala, u novije vrijeme problem rubnih vrijednosti na mikrorazini rješava se diskretizacijom reprezentativnog volumenskog elementa (RVE) uz primjenu postupka homogenizacije [7, 8]. Matematički model računalne homogenizacije temelji se na analizi problema rubnih vrijednosti RVEa na mikrorazini te izračunavanju tenzora naprezanja i konstitutivne matrice uprosječivanjem po njegovu volumenu.

Za rješavanje problema rubnih vrijednosti primjenom višerazinskih algoritama pri razmatranju heterogenih materijala u današnje vrijeme najčešće se primjenjuje metoda konačnih elemenata (MKE) [1, 7]. Za heterogeni materijal sastavljen od više homogenih dijelova sa svojim pripadnim svojstvima, stvaranje mreže konačnih elemenata u blizini granice spoja područja s različitim materijalnim svojstvima nije jednostavno kao što se to može vidjeti na primjeru kompozitnog materijala [9, 10]. Radi što točnijeg opisivanja polja derivacija u blizini spoja područja s različitim materijalnim karakteristikama, potrebno je primijeniti konačne elemente manje veličine. Pri umrežavanju često dolazi do distorzije elemenata, što može narušiti točnost rješenja. U nekim slučajevima velikih gradijenata pomaka u blizini spoja potrebno je primijeniti i tehnike adaptivnog umrežavanja, što može dovesti do naglog povećanja broja nepoznanica sustava jednadžbi, a samim time i povećati vrijeme računanja. U opisanim slučajevima metoda konačnih elemenata nije najbolji izbor numeričke metode. Stoga su u sklopu ove disertacije razvijeni novi bezmrežni postupci koji mogu biti primijenjeni i implementirani u višerazinske numeričke algoritme za analizu heterogenih materijala u nekim od budućih istraživanja.

Uz poznatu klasičnu linearno-elastičnu teoriju za analizu deformiranja materijala, danas se također primjenjuje i tzv. gradijentna (engl. *strain gradient*) teorija [11, 12]. Za razliku od klasičnih teorija gdje gustoća energije elastičnog deformiranja ovisi samo o simetričnom tenzoru deformacije, kod gradijentnih teorija funkcija je još i gradijenta deformacije. Gradijentne teorije uvedene su kako bi se točno opisale fizikalne pojave koje se ne mogu dovoljno točno opisati primjenom klasičnih materijalnih teorija. Neke od njih uključuju pojavu lokalizacije deformacija ili naprezanja na spoju dvaju različitih materijala, odnosno pojavu popuštanja materijala pri modeliranju oštećenja [13]. U današnje vrijeme postoji veliki broj gradijentnih teorija s različitim brojem parametara koji se uzimaju u obzir u svrhu što točnijeg opisivanja ponašanja mikrostrukture heterogenog materijala. Radi jednostavnosti implementacije spomenutih teorija u numeričke metode poželjno je da se koriste one s što je moguće manjim brojem parametara. Stoga su u današnje vrijeme najkorištenije Eringenova [14] i Aifantisova [15] teorija s samo jednim mikrostrukturalnim parametrom. Analiza deformiranja izotropnih materijala primjenom Aifantisove gradijentne teorije matematički je problem opisan eliptičkom diferencijalnom jednadžbom četvrtog reda. Stoga rješavanje ovog problema nije jednostavno i analitička rješenja se mogu izvesti samo za najjednostavnije primjere. Rješavanje ovog problema primjenom metode konačnih elemenata uvjetuje osiguranje C^1 kontinuiteta aproksimacijske funkcije. Stupnjevi slobode u tom slučaju sastoje se od čvornih pomaka i gradijenata čvornih pomaka što rezultira kompliciranim i neučinkovitim formulacijama te velikim brojem čvornih nepoznanica po konačnom elementu [16, 17]. Osim formulacija temeljenih na metodi pomaka, razvijeni su konačni elementi temeljeni na mješovitoj

formulaciji koji zahtijevaju zadovoljavanje kompliciranih uvjeta za osiguranje stabilnosti metode te također posjeduju velik broj nepoznanica [18]. Stoga je očito da trenutno ne postoji dovoljno učinkovita formulacija metode konačnih elemenata kojom bi se rješavali problemi opisani gradijentnom teorijom.

Kao alternativa MKE u novije vrijeme sve veću primjenu imaju bezmrežne metode zbog svojih komparativnih prednosti [19, 20]. Primjenom bezmrežnih metoda moguće je ukloniti numerički zahtjevan proces generiranja mreže konačnih elemenata, a u skladu s tim i probleme s distorzijom mreže i adaptivnim umrežavanjem [21, 22]. Još jedna od prednosti bezmrežnih numeričkih metoda u odnosu na MKE jest jednostavno definiranje aproksimacijskih funkcija visokog stupnja kontinuiteta [23]. Nedostatak bezmrežnih metoda jest dosta složeniji postupak izračunavanja funkcija oblika i njezinih derivacija te u općem slučaju manje učinkovita numerička integracija slabih oblika jednadžbi modela [24]. Potonji nedostatak može se izbjeći primjenom kolokacijske metode [25]. Također, primjena bezmrežnih metoda za rješavanje problema gradijentnom teorijom uvelike smanjuje veličinu konačnog sustava jednadžbi te za isti broj čvorova mogu rezultirati točnijim rješenjima u usporedbi s metodom konačnih elemenata [26]. Točnost i učinkovitost trenutno korištenih metoda za analizu heterogenih materijala može se stoga povećati primjenom i razvojem novih bezmrežnih postupaka. Postoji velik broj različitih bezmrežnih metoda koje su se počele razvijati u zadnja dva desetljeća, međutim u ovoj disertaciji značaj je stavljen na metode temeljene na bezmrežnom lokalnom Petrov-Galerkinovom konceptu (engl. *Meshless local Petrov-Galerkin (MLPG) concept*) [27]. Primjenom MLPG koncepta izvode se bezmrežne metode kod kojih nema potrebe za stvaranjem pozadinske mreže za integraciju jednadžbi ravnoteže u slabom obliku [28]. Novo izvedene bezmrežne metode sa svojim navedenim prednostima povećat će točnost i numeričku učinkovitost proračuna u odnosu na MKE. S obzirom na način stvaranja diskretiziranih sustava jednadžbi, bezmrežne metode mogu se podijeliti u dvije osnovne skupine. Prva se temelji na integraciji slabog oblika diferencijalnih jednadžbi ravnoteže [29, 30], dok je druga temeljena na jakom obliku diferencijalnih jednadžbi ravnoteže (kolokacijske metode) [31, 32]. Slabi oblik temelji se na integralnom zapisu jednadžbi ravnoteže primjenom metode težinskog reziduala po nekom unaprijed određenom području. Primjenom slabog oblika svi integrali u formulaciji rješavaju se približno tj. integral umnoška reziduala dobivenog uvrštavanjem aproksimacije nepoznatih veličina polja i kinematički prihvatljive težinske funkcije po nekom području mora biti jednak nuli. U kolokacijskim metodama jednadžbe ravnoteže zapisuju se i zadovoljavaju u čvorovima diskretizacije numeričkog modela. Za jednak broj čvorova diskretizacije kolokacijske metode brže su od metoda u kojima se koriste slabi oblici jednadbi jer nema numeričkog integriranja. U usporedbi s metodama temeljenim na integraciji slabog oblika jednadbi, kolokacijske

metode su netočnije i nestabilnije ukoliko se u modelu javljaju prirodni (Neumannovi) rubni uvjeti [33]. Postoji više različitih pristupa za zadovoljavanje prirodnih rubnih uvjeta od kojih se najčešće koriste direktno zadovoljavanje te zadovoljavanje primjenom kaznene metode [34]. Prilikom rješavanja fizikalnih problema primjenom bezmrežnih metoda javlja se potreba za izračunavanjem derivacija funkcija oblika višeg reda što smanjuje numeričku točnost samih metoda. Spomenuti problem može se ublažiti primjenom mješovitog pristupa kod kojeg se uz veličine polja aproksimiraju i veličine polja višeg reda te smanjuje potrebni stupanj kontinuiteta aproksimacijskih funkcija i potreba za izračunavanjem derivacija višeg reda čime se povećava točnost i stabilnost [35, 36]. Stoga, primjenom mješovitog pristupa, aproksimacijske funkcije moraju imati samo C^1 kontinuitet u slučaju rješavanja problema linearno-elastičnom teorijom. Definiranje bezmrežnih aproksimacijskih funkcija visokog stupnja kontinuiteta na razini modela je povoljno svojstvo pri rješavanju problema kao što su analiza savijanja tankih ploča [37] i ljusaka [38] ili modeliranje materijala primjenom gradijentnih teorija [39]. Međutim, visok stupanj kontinuiteta bezmrežnih funkcija uzrokuje poteškoće u rješavanju problema s diskontinuitetom derivacija nepoznatih veličina polja. Tako se pri modeliranju heterogenih materijala na granicama dijelova modela s različitim homogenim svojstvima javljaju diskontinuiteti u polju derivacija. Modeliranje takvih materijala pomoću bezmrežnih metoda stoga zahtijeva primjenu posebnih numeričkih postupaka koji osiguravaju globalni kontinuitet aproksimacijske funkcije nepoznate veličine polja (npr. pomaci ili temperatura), ali i nagli skok u njenim derivacijama na samom spoju [40, 41]. Većina postojećih spomenutih postupaka za modeliranje diskontinuiteta prikazana je i opisana u sklopu pregleda predmetnog područja. Analizom gore izloženih prednosti i nedostatka može se zaključiti da bezmrežne metode mogu biti prihvatljiva alternativa MKE za rješavanje problema deformiranja heterogenih materijala. U sklopu ovog istraživanja odabrana je bezmrežna mješovita kolokacijska metoda čije su glavne prednosti jednostavnost i brzina, a koja uz primjenu mješovitog pristupa rezultira povećanjem točnosti dobivenih rezultata. Pregledom dosadašnjih istraživanja uočeno je da mješovita kolokacijska metoda do sada nije primijenjena za rješavanje problema rubnih vrijednosti heterogenih materijala.

Trenutno stanje predmetnog područja

Naglim razvojem računalnih resursa zadnjih godina, bezmrežne metode počele su se primjenjivati za rješavanje sve složenijih problema. Jedan od tih problema jest i rješavanje problema rubnih vrijednosti prilikom modeliranja deformiranja heterogenih materijala. Pri modeliranju heterogenih materijala, najčešći problem koji se javlja kod bezmrežnih metoda jest kako opisati diskontinuitet u polju derivacija na spoju dvaju područja s

različitim materijalnim karakteristikama. Zbog visokog stupnja kontinuiteta aproksimacijskih funkcija potrebno je primijeniti posebne procedure za opisivanje diskontinuiteta u polju deformacija, odnosno derivacija aproksimacijske funkcije za pomake duž granice spoja. Istodobno, polje pomaka treba biti kontinuirano po cijelom području. U ovom odjeljku će se prikazati do sada najčešće korišteni postupci za modeliranje diskontinuiranih derivacija veličina polja u bezmrežnim metodama, zajedno s kritičkim osvrtom na njihovu numeričku učinkovitost. Također, ukratko će se prikazati i do sada postojeće i korištene bezmrežne metode za modeliranje materijala primjenom teorija višeg reda. Prije toga potrebno je spomenuti da su do sada sve dostupne bezmrežne metode za modeliranje heterogenih materijala temeljene na aproksimaciji samo primarnih veličina polja (pomak ili temperatura) u kojima je potrebno izračunavati derivacije funkcija višeg reda, što povećava računalne troškove i smanjuje točnost i stabilnost same numeričke metode.

Modeliranje diskontinuiteta primjenom bezmrežnih metoda

Postupke za modeliranje diskontinuiteta je moguće podijeliti u četiri skupine s obzirom na način zadovoljavanja geometrijskih (Dirichletovih) rubnih uvjeta na granici spoja dvaju homogenih područja: metodu Lagrangeovih multiplikatora, metodu skočnih funkcija, metodu modificiranja baznih funkcija i metodu direktnog zadovoljavanja geometrijskih (Dirichletovih) i prirodnih (Neumannovih) rubnih uvjeta. Prirodni rubni uvjeti na spoju dvaju područja pritom mogu biti zadovoljeni korištenjem slabog oblika jednadžbi ravnoteže, promjenom aproksimacijske bezmrežne funkcije ili direktno u čvorovima na granici spoja, ovisno o odabranoj metodi korištenoj za zadovoljavanje geometrijskih rubnih uvjeta.

Metoda Lagrangeovih multiplikatora

Metoda Lagrangeovih multiplikatora koristi se uglavnom u bezmrežnim formulacijama temeljenim na slabom obliku jednadžbi ravnoteže [42, 43]. Dirichletovi rubni uvjeti tj. kontinuitet pomaka zadovoljen je u integralnom obliku po granici spoja dvaju homogenih područja. Neummanovi rubni uvjeti na granici spoja zadovoljeni su korištenjem slabog oblika jednadžbi. Metoda vuče korijene iz proširenih varijacijskih principa [44] izvedenih za potrebe rješavanja metodom konačnih elemenata [45]. Prvi put je primijenjena za modeliranje diskontinuiteta materijala EFG metodom (engl. *Element Free Galerkin*) [46] i to za probleme jednodimenzijskog štapa izrađenog od dvaju različitih materijala te za problem kružne uključine u beskonačnoj ploči [42]. Kasnije je primijenjena i za rješavanje problema toplinskog provođenja u kružnom disku izrađenom od dva različita homogena materijala [43] pomoću MLPG5 metode [47]. Heterogeno tijelo se u oba slučaja promatra kao unija odvojenih homogenih područja i po svakom od njih diskretizacija se provodi

zasebno, uključujući i aproksimaciju nepoznatih veličina polja. Za spajanje spomenutih područja koriste se integralni uvjeti kontinuiteta. U integralnom uvjetu pojavljuje se nepoznanica u vidu Lagrangeovog multiplikatora koji se fizikalno može interpretirati kao površinska sila potrebna za nametanje kontinuiteta pomaka [42]. Prednosti metode korištenja Lagrangeovih multiplikatora su da za isti broj čvorova rezultira manjom greškom u usporedbi s metodom skočnih funkcija i daje veliku točnost rezultata za pomake u čvorovima [43]. Međutim, metoda također posjeduje relativno velik broj nedostataka: u nekim slučajevima potrebni su posebni rješavači za globalni sustav diskretiziranih jednadžbi [48], povećava se broj čvornih nepoznanica [48], javljaju se oscilacije u derivacijama polja pomaka oko spoja [42, 49], zbog korištenja slabog oblika jednadbi potrebna je integracija po granici spoja što uzrokuje povećanje vremena računanja [50] i konačno, točnost je manja nego kod metode konačnih elemenata [50].

Metoda skočnih funkcija

Metoda skočnih funkcija (engl. *jump functions*) temelji se na proširenju aproksimacijske funkcije prikladnom skočnom funkcijom definiranom lokalno u području oko granice spoja homogenih područja različitih materijalnih karakteristika. Aproksimacijska funkcija veličine polja opisuje se preko cijelog heterogenog područja i sastoji se od dva dijela, regularnog i singularnog. U regularnom dijelu aproksimacije koristi se standardna bezmrežna aproksimacijska funkcija, dok se za singularni dio kao proširenje odabire skočna funkcija. Skočnu funkciju potrebno je konstruirati unaprijed i to tako da su aproksimacija i njena prva derivacija kontinuirane svugdje osim na granici spoja, gdje prva derivacija mora biti diskontinuirana. Ovakvo proširenje aproksimacijske funkcije naziva se ekstrinzičnim proširenjem te rezultira novim nepoznanicama na globalnoj razini modela kao što je npr. amplituda skočne funkcije. Metoda je prvi put razvijena, testirana i primijenjena s EFG metodom. Standardna bezmrežna aproksimacijska funkcija pomičnih najmanjih kvadrata (engl. *Moving Least Squares - MLS*) [51] proširena je s dvije razliite skočne funkcije (engl. *spline i ramp*) [52]. Metoda skočnih funkcija primijenjena je također za rješavanje problema provođenja topline [43] u kombinaciji s MLPG1 metodom [47]. Provedena je detaljna matematička analiza metode iz [52] i izvedena je metoda kod koje se standardna bezmrežna aproksimacijska funkcija MLS proširuje klinastom skočnom funkcijom (engl. *wedge function*) [53]. Tako dobivena proširena aproksimacijska funkcija primijenjena je u kombinaciji s kolokacijskom metodom (engl. *Point collocation method - PCM*) [54] za rješavanje problema eliptičkih diferencijalnih jednadžbi. Primjena metode skočnih funkcija na modele s malim brojem čvorova na granici spoja rezultira manjom greškom u usporedbi s metodom Lagrangeovih multiplikatora, ali trend se mijenja povećanjem broja čvorova [43]. Međutim, u nekim slučajevima mogu se dobiti vrlo točni rezultati na spoju

i u neposrednoj blizini spoja [52]. Nedostaci metode zabilježeni i navedeni u literaturi su sljedeći: s povećanjem broja čvorova norme grešaka ostaju nepromijenjene [43], za metodu je potrebna interpolacija u krivocrtnim koordinatama što postaje vrlo složeno kod trodimenzijskih problema [50], skočnu funkciju je potrebno definirati unaprijed i njen oblik utječe na točnost dobivenih rezultata [49], potrebni su dodatni stupnjevi slobode za određivanje amplitude skočne funkcije [49].

Metoda modificiranja baznih funkcija

U metodi modificiranja baznih funkcija standardne baze bezmrežnih aproksimacija mijenjaju se dodatnim članovima tako da se na granici spoja homogenih materijala različitih svojstava dobije njihov diskontinuitet derivacija. Heterogeni materijal diskretizira se kao jedno područje te se u skladu s tim aproksimacijska funkcija veličine polja također definira preko cijelog heterogenog tijela. Prirodni rubni uvjeti na granici spoja direktno su zadovoljeni korištenjem modificirane bezmrežne aproksimacije. Bezmrežne aproksimacijske funkcije mijenjaju se direktno promjenom baze što ne rezultira novim nepoznanicama na globalnoj razini (intrinzično proširenje). Promjena bazne funkcije može se izvršiti na dva načina. Prvi način prikazan je u [49], gdje je za jednodimenzijski problem umjesto standardne linearne MLS aproksimacijske funkcije definirana bilinearna MLS aproksimacijska funkcija koja ima diskontinuiranu derivaciju na granici spoja. Nepoznati koeficijenti određeni su minimiziranjem težinskog funkcionala, slično kao i kod standardne MLS aproksimacije. Bezmrežna aproksimacija s modificiranom bazom primijenjena je u EFG metodi za probleme jednodimenzijskog štapa izrađenog iz dva različita materijala, problem heterogenog rotirajućeg diska, problem savijanja grede sastavljene od dva različita materijala i problem kružne uključine u beskonačnoj ploči [49]. Drugi način prikazan je u [55] gdje je aproksimacijska funkcija podijeljena na dva dijela, regularni i singularni. Kao i kod metode skočnih funkcija u regularnom dijelu aproksimacije koristi se neka od standardnih bezmrežnih aproksimacijskih funkcija, dok se za singularni dio kao intrinzično proširenje odabire funkcija koja ne unosi dodatne nepoznanice u krajnju bezmrežnu aproksimacijsku funkciju. Tako modificirana aproksimacijska funkcija mora osigurati kontinuitet veličine polja i diskontinuitet u derivaciji veličine polja na spoju dvaju homogenih područja. U [55] je za singularni dio aproksimacijske funkcije odabrana slična klinasta funkcija (engl. *wedge function*) kao i u [53]. Takva modificirana aproksimacijska funkcija [55] iskorištena je u kombinaciji s kolokacijskom metodom (engl. *Point collocation method - PCM*) za rješavanje problema jednodimenzijskog heterogenog štapa i Poissonovog problema sa skokom derivacija. Prednosti ove metode su sljedeće: daje vrlo točne rezultate, nema potrebe za definiranjem dodatnih parametara funkcija te uvođenja dodatnih stupnjeva slobode i aproksimacija se provodi jednostavno preko cijelog modela

[49, 55]. Značajan nedostatak je kompliciranа aproksimacija za dvodimenzijske i trodimenzijske probleme [49].

Metoda direktnog zadovoljavanja rubnih uvjeta

U metodi direktnog zadovoljavanja rubnih uvjeta na granici spoja dvaju homogenih tijela različitih materijalnih karakteristika u svakom od čvorova na granici eksplicitno se postavljaju geometrijski i prirodni rubni uvjeti, odnosno postavlja se kontinuitet pomaka ili temperature i recipročnosti vektora naprezanja ili kontinuitet toplinskog toka. Heterogeno tijelo promatra se kao unija odvojenih homogenih područja, slično kao u metodi Lagrangeovih multiplikatora. Na granici spoja diskretizacija se vrši pomoću dvostrukih čvorova, odnosno pozicije čvorova koji pripadaju različitim homogenim područjima se međusobno poklapaju. Zbog svoje jednostavnosti metoda je široko primjenjiva i do sada je poslužila za rješavanje problema elastičnog deformiranja heterogenih materijala [48, 50, 56], mikromehaničke analize kompozitnih materijala [19, 20, 57] te problema provođenja topline [58]. Korištena je u rješavanju problema bezmrežnim metodama temeljenim na integraciji slabog oblika jednadžbi ravnoteže [19, 20, 48, 57, 58], na jakom obliku jednadžbi ravnoteže (kolokacijske metode) [56] kao i na njihovoj kombinaciji [50]. Metoda posjeduje neke od najvažnijih prednosti: jednostavna je za implementaciju, numerički je učinkovita i točna [19, 20, 48, 50, 56, 57], zadovoljavanje rubnih uvjeta kontinuiteta na granici spoja može se izvesti bez numeričke integracije (u jakom obliku) [56]. Jedini nedostatak metode je potreba za istovremenim eksplicitnim nametanjem Dirichletovih i Neummanovih rubnih uvjeta [56].

Iz prikazanih prednosti i nedostataka pojedinih metoda za modeliranje diskontinuiranih derivacija veličina polja može se uočiti da najmanji broj nedostataka imaju metoda modificiranja baznih funkcija i metoda direktnog zadovoljavanja geometrijskih i prirodnih rubnih uvjeta. Metoda modificiranja baznih funkcija ima jedno jako nepovoljno svojstvo, a to je kompliciranа i računski skupa aproksimacija pri rješavanju dvodimenzijskih i trodimenzijskih problema. S druge strane, metoda direktnog zadovoljavanja Dirichletovih i Neummanovih rubnih uvjeta na granici spoja jednostavna je, učinkovita i točna metoda te ne unosi dodatne nepoznanice u sustav na globalnoj razini kao što je to slučaj kod metode Lagrangeovih multiplikatora ili metode skočnih funkcija. Dosad je uspješno primijenjena za rješavanje širokog spektra fizikalnih problema, te je stoga korištena u sklopu novih bezmrežnih metoda sadržanih u ovoj disertaciji.

Modeliranje materijala primjenom bezmrežnih metoda temeljenih na teorijama višeg reda

Osim poznate klasične linearno-elastične teorije za analizu deformiranja materijala primjenom bezmrženih metoda u današnje vrijeme primjenjuje se i tzv. gradijentna (engl. *strain gradient*) teorija. Gradijentne teorije uvedene su kako bi se točno opisale fizikalne pojave koje ovise o mikrostrukturi materijala i mogu se samo približno opisati primjenom klasičnih materijalnih teorija kao npr. problemi deformiranja konstrukcije kada odziv same konstrukcije ovisi o veličini razmatranog uzorka [59] te problem opisivanja polja naprezanja oko propagirajuće pukotine [13]. Deformiranje dvodimenzijskih izotropnih materijala primjenom gradijentnih teorija može se opisati eliptičkom diferencijalnom jednadžbom četvrtog reda te se stoga prilikom rješavanja javlja potreba za izračunavanjem derivacija funkcija oblika visokog reda. U području problema elastičnog deformiranja konstrukcija razvila se posebna skupina deformacijskih gradijentnih teorija sa samo jednim unutarnjim duljinskim parametrom (engl. *internal length parameter*) [15] koje se najčešće koriste u kombinaciji s bezmrežnim metodama radi svoje izravne i jednostavne implementacije. Gradijentne bezmrežne metode su do sada primijenjene na probleme modeliranja utjecaja veličine razmatranog uzorka na deformiranje konstrukcije [26, 39, 60, 61], modeliranje oštećenja u nehomogenim materijalima [62], analizu utjecaja razine modeliranja materijala na deformiranje mikro slojeva [63] i izvijanje ugljičnih nano cijevi [64]. Iako su dobiveni točni rezultati, visoki troškovi izračunavanja derivacija veličina polja visokog reda općenito predstavljaju velik problem u postojećim numeričkim kodovima. Stoga postoji potreba za razvojem novih bezmrežnih strategija za rješavanjem problema gradijentnom teorijom.

Cilj i hipoteze istraživanja

Cilj istraživanja je razvoj bezmrežnih kolokacijskih metoda temeljenih na mješovitom principu za numeričku analizu procesa deformiranja heterogenih materijala. Primjenom bezmrežne metode umjesto do sada najčešće korištene metode konačnih elemenata, unaprijedit će se način rješavanja problema rubnih vrijednosti heterogenog materijala.

- Prvi cilj istraživanja jest izvesti bezmrežnu mješovitu kolokacijsku metodu za rješavanje jednodimenzijskog i dvodimenzijskog problema rubnih vrijednosti heterogenih materijala sastavljenih iz više različitih homogenih područja primjenom klasične linearno-elastične teorije. Jednadžbe ravnoteže diskretizirat će se u kolokacijskim čvorovima, neće biti potrebe za numeričkom integracijom, te će se do konačnog sustava jednadžbi stići puno brže i računski učinkovitije u odnosu na postojeće bezmrežne formulacije.

- Drugi cilj istraživanja odnosi se na proširenje izvedene bezmrežne mješovite kolokacijske metode za rješavanje problema rubnih vrijednosti heterogenih materijala na rješavanje problema primjenom gradijentne teorije. Pomoću spomenute bezmrežne metode smanjit će se broj nepoznanica u diskretizacijskim čvorovima, što je značajna prednost u odnosu na metodu konačnih elemenata. Na taj način postići će se točniji i numerički učinkovitiji algoritmi u odnosu na postojeće formulacije u literaturi.

Hipoteze istraživanja su:

1. Primjenom mješovite bezmrežne metode postići će se veća točnost i numerička učinkovitost pri numeričkom modeliranju procesa deformiranja heterogenih materijala u odnosu na postojeće numeričke postupke temeljene na metodi konačnih elemenata.

2. Bezmrežna metoda omogućit će učinkovitije postizanje potrebnog kontinuiteta interpolacijske funkcije pri primjeni gradijentne deformacijske teorije, što bi moglo povećati točnost modeliranja diskontinuiteta u heterogenim materijalima.

Zaključak i doprinos rada

Sve do sada dostupne bezmrežne metode za modeliranje heterogenih materijala temeljene su na metodi pomaka (osnovni pristup) u kojima je potrebno izračunavati druge derivacije bezmrežnih funkcija što povećava računalne troškove. U novo izvedenim bezmrežnim mješovitim kolokacijskim metodama za modeliranje deformiranja heterogenih materijala primjenom linearno elastične teorije sve komponente pomaka i naprezanja aproksimirane su istim funkcijama koje moraju imati samo C^1 kontinuitet. Sukladno tome u izvedenoj mješovitoj kolokacijskoj metodi temeljenoj na Aifantisovoj gradijentnoj teoriji aproksimirane su komponente gradijenata pomaka ili deformacija, odnosno komponente čvornih pomaka ili deformacija koje također moraju posjedovati samo C^1 kontinuitet. Odnosno, za sklapanje čvornih matrica krutosti kod obje formulacije problema potrebno je izračunavati samo prve derivacije funkcija oblika. U oba slučaja dobiva se sustav rješivih jednadžbi u kojima su nepoznanice samo čvorni pomaci, odnosno čvorne deformacije ovisno o formulaciji. Primjenom adekvatnih kinematičkih relacija i prikladne konstitutivne jednadžbe mogu se izračunati sve ostale potrebne veliine. Numerička učinkovitost i točnost modeliranja heterogenih materijala ovdje je stoga povećana smanjenjem potrebnog reda derivacija aproksimacijskih funkcija. Rješenja dobivena primjenom izvedenih metoda točnija su u odnosu na postojeće formulacije što se i očituje analizom grešaka u numeričkim primjerima.

Očekivani znanstveni doprinos istraživanja:

1. Razvoj nove mješovite bezmrežne kolokacijske metode za modeliranje deformiranja heterogenih materijala temeljene na linearno elastičnoj formulaciji problema rubnih vrijednosti.

2. Izvod nove bezmrežne formulacije temeljene na gradijentnoj deformacijskoj teoriji koja će omogućiti točnije i učinkovitije modeliranje deformiranja materijala od do sada raspoloživih bezmrežnih numeričkih algoritama temeljenih na teorijama višeg reda.

1 Introduction

1.1. Background and motivation

Most engineering materials that are utilized in practice have a heterogeneous structure. From the engineering standpoint, heterogeneous materials are desirable because they can be designed to take advantage of the best properties of each individual constituent [65]. Size, shape, spatial distribution and properties of each constituent that make up the microstructure have a significant impact on the behaviour of the material at the macro level [66]. Accordingly, the development of new more durable materials is a challenge and it is usually done empirically. In so doing, a large number of specimens with different microstructure has to be fabricated and rigorously tested until a desired material behavior is achieved, which increases costs. Consequently, accurate numerical models are preferable in order to reduce the time and financial costs of the experimental methods. For this reason, in recent time, the boundary value problem at the micro level is solved using numerical methods, where the Finite Element Method (FEM) [67] is mostly applied. In the numerical modeling of the heterogeneous materials composed of more homogeneous parts with different material properties, creating of a mesh of finite elements near their interface can be time-consuming and numerically demanding. Therefore, especially for spatial discretization, there is a need for techniques that use adaptive remeshing. This technique of using ever smaller elements increases the computing time by introducing new nodal unknowns, as well as the risk of element distortion, which may corrupt the accuracy of the solution.

Thus, as an alternative to FEM, meshless methods are applied because of their comparative advantages [68]. These methods have the potential to overcome time-consuming mesh generation and element distortion problems associated with the widely used FEM. In that way, computational models are discretized using only a set of nodes that are not connected into elements [69]. In addition, the derivation of approximation functions with a high degree of continuity can be accomplished in a relatively simple manner [70], which

is extremely beneficial when gradient theories are utilized. Despite the recent wide use of meshless methods in the scientific community, high computational costs associated with the calculation of meshless approximation functions still represent a severe setback [69]. Hence, an improvement in this field is more than necessary and accordingly, even better meshless methods have to be developed. The accuracy and numerical efficiency of currently used methods for the analysis of heterogeneous materials can therefore be improved by the application and development of new meshless methods. In the presented research, the Meshless Local Petrov-Galerkin (MLPG) [28] concept in combination with the collocation methods based on the mixed approach [71] is utilized for the first time to solve the deformation problem of heterogeneous materials. The developed mixed collocation methods are applied for the classical linear elastic and gradient elasticity boundary value problem.

1.2. Overview of meshless methods

It is well known that any occurrence, either of physical, geological, mechanical, electrical or biological nature, can often be described using algebraic, differential or integral equations. Getting the correct solution for the problems described by these equations is an ideal scenario. Unfortunately, exact solutions are possible only for a limited number of practical problems because most of the real problems in the nature are very complex. Therefore, the use and development of numerical methods to obtain approximate solutions are inevitable. The conventional numerical methods utilize the predefined connection between discretization nodes, hence relying on the use of predetermined meshes. The FEM [72] and the Finite Volume Method (FVM) [73] are perhaps the best known examples of these today already thoroughly developed methods. In contrast, in the last decades a new class of numerical methods has been developed in which the approximation of partial differential equations is performed only by using sets of scattered nodes, without the need for burdensome creation of meshes. Therefore, in this section numerical methods called meshless methods are described along with their properties and chronological development.

1.2.1. Description and properties of meshless methods

Throughout the last four decades, a large number of meshless methods has been researched and, in doing so, attributed various different names. Despite the different names it is interesting to note that in fact there are many similarities regarding all of these methods. Before the overview of todays meshless methods is given, a description of their most important properties is presented. The mentioned properties are at the same time also

compared with the properties of numerical methods that use meshes for the discretization of the geometry.

- **No mesh needed**
  - ◇ In meshless methods the connectivity of nodes is determined during the numerical calculation.
  - ◇ Conformity of discretization meshes does not have to be fulfilled. Big problem with methods that rely on meshes, for example when modeling the propagation of cracks or shear layer effects [74].
  - ◇ Simple h-adaptivity by just adding nodes in a numerical model and calculating of new connectivity between the nodes. The p-adaptivity is also performed in a more simple manner compared to methods based on meshes.
  - ◇ No adaptive meshing during calculation. When modeling problems with large deformations or moving discontinuities with mesh-based methods, there is a frequent need for remeshing, which can lead to significant problems in obtaining accurate solutions [75].
- **Construction of shape functions with arbitrary degree of continuity**
  - ◇ Meshless methods easily meet the required necessary continuity conditions of shape functions for most engineering problems. In comparison, in the methods that rely on the use of meshes, ensuring the needed continuity of the approximation functions can sometimes pose a problem [16].
  - ◇ Additional post-processing is not necessary to determine the required smooth contours of fields, for example strains and stresses.
  - ◇ There are also special cases where high continuity meshless functions can be a drawback. For example, when there is the discontinuity in the strain or stress fields at the material interfaces or when modeling crack initiation and propagation. These situations can be overcome by using various numerical procedures [50, 76].
- **Convergence**
  - ◇ For the same order of consistency, numerical tests indicate that the convergence of meshless methods can be significantly faster than methods that rely on the use of meshes [77].

- **Computational efficiency**
  - ◇ In practice, for certain reasonable accuracy, meshless methods require considerably more time than the methods that use meshes.
  - ◇ The construction of meshless shape functions is quite complex in comparison to FEM where functions have polynomial form.
  - ◇ The number of integration points required for the exact calculation of the integrals in the weak form methods is significantly higher because the shape functions are not of polynomial character.
  - ◇ In collocation methods, there is no need for numerical integration, but they have certain problems related to the accuracy and stability [27].
  - ◇ In meshless methods, at each integration point, certain numerical procedures for the calculation of a shape function and its derivatives are often needed, such as: creating lists of neighboring nodes, solving of small systems of equations and matrix multiplication operations.
  - ◇ The bandwidth of the final system of equations in meshless methods is generally higher when compared to the mesh-based methods [75].
- **Essential and natural boundary conditions**
  - ◇ Some meshless shape functions do not possess Kronecker delta property, in contrast to the methods that use mesh-based discretization. Therefore, the fulfillment of essential and natural boundary conditions requires special attention [34], because it can affect the convergence of numerical methods [78].

As can be seen from the above properties, meshless methods have certain advantages, but there are also some disadvantages. Therefore, great caution and a good critical review of obtained numerical solutions are necessary regardless of the method applied. Nowadays, there is a large number of meshless methods as a result of new improvements and formulations added and developed over the years. Some of the most known meshless methods are given in the approximate chronological order of development and comprised in Table 1.1. A classification and overview of most meshless methods can be also found in [74, 75, 79, 80].

In the scope of this Thesis, in order to solve the problem of deformation of heterogeneous materials, using both classical and gradient linear elasticity, the Meshless Local Petrov-Galerkin procedure [27] with the Moving Least Squares (MLS) [28] with interpolation properties (IMLS) [106] and the Radial Point Interpolation Method (RPIM) [107] functions are utilized. The derived methods with the corresponding meshless interpolation functions are shown in more detail in the chapters that follow.

Table 1.1: Chronological overview of meshless methods

No.	Name of meshless method	Abbreviation
1.	Finite Difference Method [81]	FDM
2.	Method of Fundamental Solutions [82]	MFS
3.	Smooth Particle Hydrodynamics [83]	SPH
4.	Diffuse Element Method [84]	DEM
5.	Element Free Galerkin [85]	EFG
6.	Reproducing Kernel Particle Method [86]	RKPM
7.	Finite Point Method [87]	FPM
8.	HP-Cloud method [88]	HPC
9.	Partition of Unity Method [89]	PUM
10.	Natural Element Method [90]	NEM
11.	Meshfree Polynomial Point Interpolation Method [91]	PPIM
12.	Local Boundary Integral Equation [92]	LBIE
13.	Generalized Finite Element Method [93]	GFEM
14.	Meshless Local Petrov-Galerkin method [94]	MLPG
15.	Least-Squares Meshfree Method [95]	LSMM
16.	Meshless Finite Element method [96]	MFEM
17.	Meshfree Local Radial Point Interpolation Method [97]	LRPIM
18.	Reproducing Kernel Element Method [98]	RKEM
19.	Radial Basis Function Collocation Method [99]	RBFCM
20.	Radial Basis Collocation Method [100]	RBCM
21.	Discrete Least-Squares Meshless Method [101]	DLSMM
22.	Smoothed Point Interpolation Method [102]	S-PIM
23.	Viscous Vortex Domains method [103]	VVD
24.	Optimal Transportation Method [104]	OTM
25.	Radial Basis Integral Equation method [105]	RBIE

1.2.2. Classification of meshless methods

Meshless methods can be divided into three basic groups according to the manner of obtaining and solving discretized system of equations. This section will therefore briefly describe the approach, limitations, applications, advantages and disadvantages of particular groups of methods.

- **Strong form methods**

  The methods are based on the strong form of differential equations of equilibrium and are usually referred to as collocation methods [71, 108]. In the collocation methods, the equilibrium equations are written and imposed at the discretization nodes of the numerical model. There is no numerical integration, so there is also no need to create background cells for integration. Hence, the strong form methods are truly meshless methods. Therefore, they possess several attractive advantages. For example, a simple algorithm for assembling a solvable system of equations, speed and computational efficiency. Also, they are efficient in a sense that they result in accurate solutions if only essential boundary conditions need to me enforced in the numerical model. As some of the representatives of the methods based on the strong form, the Finite Difference Method [81], the Radial Basis Function Collocation Method [99] and the Radial Basis Collocation Method [100] can be mentioned. However, this type of meshless method can be often unstable and inaccurate, especially if natural boundary conditions are present in the numerical model. Unlike integration that has a smoothing character, taking derivatives increases the error of approximation. This input of errors is partly responsible for the instability of solutions that occurs when solving the partial differential equations with the strong form methods. In the collocation methods, there are several different approaches for enforcing the natural boundary conditions of which direct collocation [71] and the penalty method [34] are most commonly used. The procedure suitable for one type of problem does not necessarily have to be the best option for a similar or different type of problem. Therefore, there is still a need for the development of a stable collocation method. The mentioned problems can be alleviated to a certain extent by using a mixed approach. This approach reduces the demand on the continuity degree of approximation function and the need for the higher derivative calculations, which increases accuracy and stability [71, 76].

- **Weak form methods**

  In weak form methods, the partial differential equations with the accompanied natural boundary conditions are reshaped to the integral form using different numerical approaches. Weak forms are then used to obtain the system of algebraic equations through numerical integration procedure using predetermined background cells that can be defined globally over the entire problem domain or locally over the part of the computational domain [28, 35]. There are several properties associated with using the weak forms that should be noted. The operation of integration smudges the error within the integrated area and this increases the accuracy of solutions.

Integrating acts as some kind of regularization to stabilize the numerical solution. A request on the continuity of a test function is also reduced by applying the divergence theorem, resulting in the decreasement of the needed order of derivatives in the integral equations. The natural boundary conditions are satisfied in the weak sense, because they appear in the the weak form equations. Therefore, the system of equations and the natural boundary conditions are a part of the same integral equation. These properties give the weak form methods certain advantages such good stability and excellent accuracy for a wide range of problems. There is no need for additional equations and the numerical methods for the imposition of the natural boundary conditions. Such meshless method is applicable to many problems, and a set of parameters used to solve one problem can be used for a wide range of other problems. The mentioned robustness is shown in a large number of solved practical engineering problems. Today, there are many variations of the weak form methods. Hence, the meshless methods based on the global weak form of equations are called simply meshless global weak form methods while those based on local weak form of equations are referred to as meshless local weak form methods. The meshless global weak form methods are based on the integration of the global Galerkin weighted residual equations and the use of meshless approximations functions. These methods are meshless only in terms of the approximation of desired fields components. Background cells are required over the entire computational domain for the purpose of integration. As some of the representatives of the global weak form methods the Element Free Galerkin (EFG) [85] and the Reproducing Kernel Particle Method (RKPM) [86] can be mentioned. The meshless local weak form methods are based on the integration of the local weak forms of Galerkin equations and meshless approximation of field unknowns over local domains. Herein, local integration areas are often very simple, circular or rectangular in shape, and are automatically constructed during the calculation process. Some of the representatives of these methods are the HP-Cloud method [88] and the Meshless Local Petrov-Galerkin (MLPG) method [94]. Numerical integration makes this group of global and local weak form methods computationally more expensive when compared to the collocation methods. Although the development of meshless local weak form methods is an important step in the reaching the ideal meshless method, numerical integration is still a severe obstacle. This is especially the case for the nodes positioned at or near the outer boundary of the computational domain when the boundary is complex shaped. Local integration is also computationally expensive for some practical engineering problems. It is therefore desirable to reduce the need for integration in the numerical methods.

- **Weak-strong form methods**

  Weak-strong form methods have been designed to utilize the advantages of both weak and strong methods, and avoid their disadvantages [109, 110]. They have been created for the purpose of removing the need for background integration cells as much as possible, and at the same time to provide stable and accurate solutions even in problems in which the derivative boundary conditions are present. The main idea of this type of methods is to create a system of discretized equations where weak and strong methods are used selectively, depending on the position of the discretization nodes. The weak form methods are used only for nodes in which or near which the natural boundary conditions are prescribed. The strong form methods are utilized in all remaining nodes of the computational model. The advantage of this approach is that the natural boundary conditions can be enforced simply and precisely using only the weak form for arbitrary arrangements of nodes. Furthermore, the methods use only a small number of background cells for integration to speed up the calculations. Also, the methods are regarded as stable, accurate and computationally efficient.

Each meshless method has certain advantages and disadvantages. After a detailed analysis of these advantages and disadvantages, a suitable method for solving each particular problem can be chosen. In order to asses the quality of a meshless method the convergence speed and the accuracy of the solution are most important. Here, it should be stated that this Thesis deals only with the development of collocation methods of the mixed type that are fast and applicable for solving of the boundary value problem of heterogeneous materials. Hence, these type of methods will be presented and described in detail in the upcoming chapters.

1.3. Meshless modeling of heterogeneous materials

The definition of the meshless approximation functions with a high degree of continuity at the level of the numerical model is a convenient feature when solving problems such as bending of thin plates [111] or shells [112]. However, a high degree of continuity of the meshless functions causes difficulties when solving the problems with the discontinuity of unknown field variables. Also, the modeling of such problems with meshless methods requires the application of special numerical approaches to ensure the continuity of the global approximation functions of unknown field, and a sudden jump in its derivatives at the material interface [50]. Furthermore, using classical linear elasticity formulation only sharp jump in derivative fields at the material interfaces can be captured [56]. Therefore, for more accurate description of the derivative fields and the behaviour of the entire heterogeneous structure at the micro scale, strain gradient elasticity formulation can be

applied [113]. Lately, strain gradient material formulations are often used for the modeling of size effects in homogeneous materials [39] or the removal of discontinuities in heterogeneous materials [13]. They are still very much utilized when solving the problem using FEM, but with the continuous increase in the computational power, more meshless methods based on higher-order theories should arise. In the following subsections, the existing methods for the modeling of material discontinuity and meshless methods based on gradient elasticity are presented and discussed.

1.3.1. Modeling of material discontinuity

Besides well-known finite element procedures, through past decades a large number of various meshless methods has been considered for the modeling of heterogeneous structures. Some of these methods include the Element Free Galerkin method (EFG) [85], the Reproducing Kernel Particle Method (RKPM) [86], the Meshless Local Petrov-Galerkin method (MLPG) [28], the Point Collocation Method (PCM) [91], the Radial Basis Collocation Method (RBCM) [100], the Discontinuous Galerkin Meshfree Method (DGMM) [114] and the Smoothed Point Interpolation Method (S-PIM) [115], with appropriate enhancements in order to accurately capture the derivative fields in heterogeneous problems. One of the first methods developed for the modeling of material discontinuity is based on the introduction of the interface continuity condition in the classical variational form using Lagrange multipliers [42] in the EFG method. In general, this type of Lagrange multiplier method yields a non-positive definite matrix and increases the global number of unknowns. The work in [42] was later expanded using the approach based on the augmented Lagrangian formulation [44]. Therein, neither the Lagrangian multipliers nor the penalty method needed to be utilized. Accordingly, no additional unknowns had to be determined and the discretized system of equations remained well-conditioned. Another strategy considered for the modeling of the material interface is the enrichment of conventional meshless approximation schemes with special jump or wedge functions [52]. This enrichment can be done in two different manners. The first one is intrinsical [49, 55], where the basis of the approximation function is modified without introducing any additional unknowns whilst at the same time ensuring the accurate description of the derivative field near the interface. The second one is extrinsical [53, 116], where the approximation function is simply expanded with a term governed by the jump (wedge) functions, which is only activated for the nodes near the material interface. This methods demonstrate better accuracy that using classical variational form with Lagrange multipliers [49]. However, additional degrees of freedom are sometimes required in order to determine the amplitude of the jump function [52]. Approximations can be constructed where no additional degrees of freedom are needed [116], but the jump (wedge) functions still need to be determined

in advance and the choice of their shape also affects the accuracy of the methods considered. Similar enrichment methods in combination with the Reproducing Kernel methods can be also found in [40, 117]. A more detailed comparison of the discontinuity methods using the Lagrange multipliers and jump functions are presented in [43] for the modeling of axisymmetric transient heat conduction in bimetallic disks, where two different MLPG (MLPG1 and MLPG5) [47] methods are employed. Another procedure for the modeling of derivative discontinuity that follows straightforward from using the DGMM is the imposition of field variable continuity and the interface traction fluxes across the interface boundary in a weak form [41]. Very recently, an interesting approach has been introduced [118], which combines the meshless and isogeometric approximations in order to exploit the robustness and flexibility of meshless methods in local discretization refinements and the geometrical exactness of the isogeometric approach in the frame of a single formulation. In [119], the isogeometric approach is used to accurately describe the geometry of the material interface, as well as to describe the jump in the strain field. Thereby, the fact that the C^0 continuity of the B-spline approximation at the interface boundary can be easily achieved by simply repeating the B-spline knots positioned at the interface is exploited. In the regions away from the interface, a quasi-convex meshless scheme is applied for the approximation purposes, and the isogeometric and meshless regions are blended by defining coupled isogeometric-meshless functions. It has been found out that such approach yields better accuracy than a comparable classical meshless formulation, while retaining the exact geometry description of the isogeometric approach. Probably the most broadly prevailed methods for modeling the material discontinuity are the direct methods. These methods can be also divided into two sub-groups. The first one deals only with the direct imposition of essential boundary condition at the interface [48, 120], while the second one uses the direct imposition of essential and natural boundary conditions using the double node discretization of the material interface [50, 56]. From the available literature [56], it can be observed that the better accuracy of the solution can be achieved by enforcing both the appropriate displacement and the traction conditions at the interface. Concerning the class of MLPG methods which is used in this Thesis, for modeling of the derivative jump on the interface, the combination of MLPG2 and MLPG5 approaches [27] can be utilized as in [50]. Therein, the MLPG2 method is used at the nodes on the boundaries, while the MLPG5 computational strategy is applied for the nodes within the domain, so the domain integration is eliminated and the best features of both methods are exploited. Nevertheless, for each method different basis functions are considered, so the method lacks the consistency condition of the applied formulation [41, 49]. Other applications of the direct imposition method include such problems as the steady state heat conduction in heterogeneous materials [58] and the micromechanical

modeling of unidirectional fiber reinforced composites [20, 57].

1.3.2. Meshless gradient elasticity modeling

Along with the well-known classical linear elastic material theory for the analysis of the deformation of materials, nowdays also the so-called gradient theory [11, 12] is utilized. In contrast to the classical theory, where the density of the elastic deformation energy depends only on the symmetric strain tensor, in the gradient theory it is also a function of strain gradient. Gradient theories have been introduced in order to describe more accurately the physical phenomena that can not be precisely described by the application of a widely known laws of continuum mechanics. Such problems include: problems of plastic deformation of structures with a very complex response [59], the problem of describing the stress fields around propagating cracks [13] and the description of the appearance of a discontinuity in the strain field at the interface of areas with different material properties [13]. Nowdays, there is a variety of gradient theories with a different number of parameters for the purpose of accurately describing the microstructure. In order to simplify the implementation of the mentioned theories in numerical methods, it is preferred to use those with the smallest possible number of parameters. For this reason, today most used gradient theories are those with only one microstructural parameters such as the Eringen [14] or the Aifantis [15] theory. The Aifantis theory is utilized and implemented in the newly developed meshless methods presented in this Thesis. The analysis of deformation of isotropic materials using the Aifantis gradient theory is the mathematical problem described by the elliptical differential equation of the fourth-order. Therefore, solving this problem is not a trivial task and analytical solutions can be derived only for the simplest examples. During the solution process, there is a need for the calculation of high-order derivatives of the shape functions. Solving this problem using FEM requires C^1 continuity of the approximation functions. In this case, the degrees of freedom consist of nodal displacements and nodal displacement derivatives, resulting in complicated and ineffective formulations with a large number of nodal unknown per finite element [16]. In addition to the formulation based on the displacement method, finite elements based on a mixed approaches have been developed, which require complicated satisfaction of the well known LBB conditions to ensure the stability of the method and also possess a large number of unknown variables [18]. Therefore, it is obvious that currently there is no efficient formulation of the finite element method for solving the problems with the gradient material theory. In the elasticity, a special group of strain gradient theories with only one internal length scale parameter [15] is developed. These theories are most commonly used in the combination with meshless methods because of their direct and simple implementation. So far, the gradient meshless methods have been applied to solve

several demanding engineering problems. Some of these problems include: the modeling of deformation in which the size of the considered numerical model directly influences the response of the structure [60, 61, 63], damage modeling in the non-homogeneous material [62] and buckling of carbon nano-tubes [64]. Although accurate results have been obtained, in general the large computational costs of calculating the high-order derivatives are a major drawback in the existing numerical codes. Hence, there is a need to develop new meshless strategies for solving the problems using the deformation gradient theory.

1.4. Hypotheses, scope and objectives of the thesis

This section is dedicated to presenting the research hypotheses and the conducted research covered in the Thesis. Firstly, the hypotheses of the newly developed meshless methods for heterogeneous materials are mentioned. Secondly, the research conducted in two phases is thoroughly described.

1.4.1. Hypothesis and goals of the thesis research

The objective of the presented research is the development of the mixed meshless collocation methods for the numerical analysis of deformation of heterogeneous materials. The solution of the boundary value problems using classical linear elastic and strain gradient theory has been investigated.

The hypotheses of the research are:

1. The application of the mixed meshless method will ensure greater accuracy and numerical efficiency in the modeling of deformation process of the heterogeneous materials in comparison to the existing numerical methods based on finite element method.

2. The mixed meshless method will enable more efficient implementation of deformation gradient theories in the numerical meshless methods, which could increase the accuracy and the reliability of numerical modeling of realistic materials deformation at both the micro and the macro level.

1.4.2. Description of the research conducted

As mentioned earlier, the research in the scope of the Thesis is divided into two phases. In the first phase, the research is concerned with the solving of the standard boundary value problem of heterogeneous materials. The mixed meshless collocation formulation

for the numerical modeling of one-dimensional (1D) and two-dimensional (2D) boundary value problems of heterogeneous materials is developed and compared to the existing formulations based only on the approximation of unknown displacement components [56]. Each homogeneous area is discretized by a set of nodes in which the equilibrium equations are employed in accordance to the collocation method [55]. The strong form of the equilibrium equations in a meshless formulation can be considered as a special case of the MLPG method, where the Dirac delta function [47] is chosen as the test function. It is assumed that the homogeneous areas have linear elastic properties and the theory of small strains is applied. The equilibrium equations are discretized using the stress components and the system of equations is closed by employing the relations between displacements and stress components [121]. Because the equilibrium equations are written only at the discretization nodes, numerical integration is avoided and therefore the calculation of the system matrix is very easy and quick. The displacement field solution for the entire domain of heterogeneous material is obtained by connecting the subdomains with different material properties by directly enforcing the essential and natural boundary conditions at the collocation nodes on the interface of these regions [50], i.e. at the nodes on the interface the displacement continuity and traction reciprocity conditions are imposed. The independent variables are approximated by using the same meshless approximation functions in such a way that each homogeneous area within the heterogeneous material is considered separately. All the displacement and stress components are approximated using the interpolation functions which must have at least C^1 continuity, i.e. the function and the first derivatives of the function must be continuous [71]. For the approximation, meshless approximations utilizing the Interpolating Moving Least Squares (IMLS) method [122] and the Radial Point Interpolation Method with polynomial reproduction (RPIM) [123] are used. The displacement conditions on the external boundaries are imposed directly at the collocation nodes as in FEM due to the interpolatory properties of the meshless shape functions.

In the second phase, the derived mixed collocation meshless formulation based on the classical linear elastic theory is extended to solve the problem of deformation by applying the gradient theory [13]. Herein, the model of the deformation strain gradient elasticity according to Aifantis [15], based on the Mindlin theory [12], is implemented. Since solving the deformation problem of isotropic heterogeneous materials using Aifantis gradient theory can be replaced by solving the elliptic differential equation of fourth-order, there exists a need for calculating the relatively high-order derivatives of the approximation function, which creates inaccuracy in the considered numerical method. This problem can be overcome by splitting the problem into two related problems described by the differential equations of second-order [124]. This can be only done when linear gradi-

ent elasticity according to Aifantis is utilized [13]. In addition to the displacement and strain components, the derivatives of displacement and strain components are also approximated with the same interpolation functions. Therefore, the equilibrium equations are discretized using displacement or strain components and derivatives of displacement or strain components, and then the solvable system of equations is obtained by using the appropriate kinematic relations which link displacements or strains to derivatives components of both fields. The application of these numerical methods results in the solvable system of equations with only nodal displacements or strains as unknowns, dependent on which operator split procedure is utilized. At the nodes on outer boundaries the classical and gradient boundary conditions are enforced directly.

When using meshless collocation methods, some problems with convergence of the solution can be observed if there are natural boundary conditions [71] present in the model, so their impact on the accuracy and instability of the obtained solutions is investigated in both phases. Since the problems with large strain gradients are analysed, the influence of the discretization on the achieved accuracy of the numerical methods is investigated. Herein, the impact of non-uniform and random nodal discretizations of the computational domain on the accuracy is considered. The appropriate values of the meshless parameters that affect the numerical solutions are determined by using parametric analyses. All the developed numerical procedures are programmed in FORTRAN. New algorithms are tested by appropriate numerical examples. Results are compared with the available analytical and numerical solutions to determine the efficiency and accuracy of the new proposed algorithms.

1.4.3. Expected scientific contribution

In this dissertation, the Meshless Local Petrov-Galerkin (MLPG) procedure based on the mixed approach [71] is considered as an efficient remedy for the deficiencies arising in FEM or primal meshless methods for the modeling of heterogeneous materials. Previously, this method has been successfully applied for solving certain demanding engineering problems, such as bending of plates [121] and shells [125], topology optimization [126] and the modeling of steady-state heat transfer [127]. Herein, it is considered for the modeling of material discontinuity in heterogeneous structures for the first time. The collocation method (MLPG2) is applied which may be considered as a special case of the MLPG approach [27], where the Dirac delta function is employed as a test function in a local weak form obtained by using the weighted residual approach at each discretization node in the model. Since the collocation method is utilized, no cumbersome numerical integration over the computational domain or the boundaries is necessary. This ensures that the discretized system of governing equations is obtained in a fast and straightforward man-

ner. The mixed approach is considered, where each homogeneous region is discretized by using independent interpolations of both displacements and stress components. The interpolatory property of the meshless shape functions allows simple and direct impositions of the boundary conditions at the discretization nodes, as well as the imposition of the appropriate conditions at the material interface. No additional treatment or parameter determination at the material interface is needed. A final closed system of discretized governing equations with the displacements (strains) as unknown variables is obtained through the kinematic and constitutive relations.

The expected scientific contribution of the Thesis is:

1. The development of a new mixed meshless collocation method for the modeling of deformation of heterogeneous materials based on the linear elastic formulation of boundary value problem.

2. The Development of a new meshless formulation based on the Aifantis strain gradient theory, which will enable more accurate and efficient material modeling in comparison to the available numerical algorithms.

1.4.4. Outline of the thesis

The Thesis is organized in seven chapters. In Chapter 2 overview of basic continuum mechanics relations regarding classical linear elasticity and strain gradient linear elasticity is given. Therein, kinematics, constitutive relations, equilibrium equations, essential and natural boundary conditions are discussed for both material formulations. Global and local weighted residual approaches are presented in Chapter 3. Herein, the utilized MLPG procedure is also shown. The construction and derivation of meshless approximation schemes used in this dissertation, IMLS and RPIM, are presented and explained in Chapter 4. Furthermore, Chapter 5 describes the derivation of the proposed mixed collocation method for the classical linear elasticity. In addition, the discretization of the displacement and stress field variables using meshless functions and an overview of the discretized governing equations for the considered two dimensional heterogeneous material problem are shown. Several numerical examples showing the accuracy, computational efficiency and robustness of the proposed mixed collocation method are also presented. Chapter 6 is dedicated to the modeling of the material deformation using gradient elasticity. Two mixed meshless collocation methods based on different operator split procedures are investigated along with the discretization of the equilibrium equations and appropriate boundary conditions. Several one dimensional and two dimensional numerical examples of homogeneous and heterogeneous structures are utilized in order to describe material

deformation using newly developed methods. Herein, the accuracy of the methods, the ability to describe the size effect behaviour in a homogeneous material and the removal of discontinuities in a heterogeneous material is tested. The final concluding remarks and future investigations are given in Chapter 7.

2 Overview of continuum mechanics relations

2.1. Classical linear elasticity

In this section, the basic relations of continuum mechanics for linear elasticity necessary to derive the meshless formulations contained in this dissertation are presented. Since the heterogeneous materials are comprised of different homogeneous areas, the geometry and deformation modeling of these are firstly discussed. It should be noted that only problems of two-dimensional linear-elastic deformation analysis of materials with the assumption of small displacements and small strains are analyzed. In addition, appropriate boundary conditions are highlighted. Also, the equilibrium equations for two-dimensional continuum are shown. All of the indices used in this chapter can only adopt values 1 or 2, if not specified otherwise.

2.1.1. Geometry and kinematics

In this research only two-dimensional problems of simple geometry are analyzed. The geometry of the problems is described using discretization nodes of the models. The discretization nodes in the meshless methods are in the general case chosen arbitrarily, but in most examples discussed here, a uniform distribution of nodes is utilized in order to avoid problems with the stability of collocation methods. Each point in the two-dimensional deformable continuum has two displacement components u_1 and u_2, in the direction of Cartesian coordinate axes x_1 and x_2. In technical practice, it is common to denote displacement components by u and v, and the coordinate axes by x and y.

The displacement vector at any 2-D continuum point is

$$\mathbf{u}^{\mathrm{T}} = [\, u \quad v \,]. \tag{2.1}$$

Under the assumption of small strains according to [128], the strain tensor can be written and calculated as

$$\varepsilon_{ij} = \frac{1}{2}(u_{i,j} + u_{j,i}). \tag{2.2}$$

In the case of two-dimensional isotropic problems the strain tensor is reduced to only three different independent components, which are often written in a vector form in order to facilitate numerical implementation in codes and to reduce needed computational time, as

$$\boldsymbol{\varepsilon}^{\mathrm{T}} = [\, \varepsilon_x \quad \varepsilon_y \quad 2\varepsilon_{xy} \,]. \tag{2.3}$$

The equation (2.2) can also be written in the matrix form

$$\boldsymbol{\varepsilon} = \mathbf{D}_{\mathrm{K}}\mathbf{u}, \tag{2.4}$$

where $\mathbf{D}_{\mathrm{K}}$ represents the 2-D kinematic differential operator matrix in the form

$$\mathbf{D}_{\mathrm{K}} = \begin{bmatrix} \partial_x & 0 \\ 0 & \partial_y \\ \partial_y & \partial_x \end{bmatrix}. \tag{2.5}$$

In the relation (2.5), the operators ∂_x i ∂_y denote the first-order partial derivatives with respect to Cartesian coordinates x i y.

2.1.2. Constitutive relations

Constitutive equations for a two-dimensional classical linear elasticity case, which provide a link between the strain tensor and the stress tensor, can be written using the generalized Hooke's law [128]

$$\sigma_{ij} = C_{ijkl}\varepsilon_{kl}, \tag{2.6}$$

where the σ_{ij} represents the Cauchy stress tensor, while C_{ijkl} is the material tensor. As in the case of a strain tensor ε_{ij}, for two-dimensional isotropic material, there are also only three different independent components of the stress tensor. These are usually displayed in the field of computational mechanics in the form of a stress vector

$$\boldsymbol{\sigma}^{\mathrm{T}} = [\, \sigma_x \quad \sigma_y \quad \sigma_{xy} \,]. \tag{2.7}$$

In the Cartesian coordinate system components of the material tensor can be written as

$$C_{ijkl} = \lambda\delta_{ij}\delta_{kl} + \mu(\delta_{ik}\delta_{jl} + \delta_{il}\delta_{jk}), \tag{2.8}$$

where λ i μ denote the two Lame's elastic constants

$$\lambda = \frac{E\nu}{(1+\nu)(1-2\nu)}, \tag{2.9}$$

$$\mu = \frac{E}{2(1+\nu)}. \tag{2.10}$$

In the relations (2.9) and (2.10), E represents the Young's modulus, while ν describes the Poisson's ratio. The constitutive equation (2.6) is also easily transformed to the matrix form which states

$$\boldsymbol{\sigma} = \mathbf{D}\boldsymbol{\varepsilon}, \tag{2.11}$$

where $\mathbf{D}$ denotes the linear elasticity material matrix or simply the elasticity matrix. For the purpose of numerical modeling of two-dimensional linear-elastic isotropic materials, two well-known approaches are usually utilized, referred to as plane stress and plain strain state. Accordingly, two different elasticity matrices are used. Therefore, to describe the plane stress state

$$\mathbf{D} = \frac{E}{1-\nu^2}\begin{bmatrix} 1 & \nu & 0 \\ \nu & 1 & 0 \\ 0 & 0 & \dfrac{1-\nu}{2} \end{bmatrix}, \tag{2.12}$$

is applied, while for the plane strain case elasticity matrix is equal to

$$\mathbf{D} = \frac{E}{(1+\nu)(1-2\nu)}\begin{bmatrix} 1-\nu & \nu & 0 \\ \nu & 1-\nu & 0 \\ 0 & 0 & \dfrac{1-2\nu}{2} \end{bmatrix}. \tag{2.13}$$

2.1.3. Equilibrium equations and boundary conditions

Consider the two-dimensional continuum which occupies domain Ω bounded by the global outer boundary Γ, shown in Figure 2.1 in time t. On the continuum surface, the traction forces $\mathbf{t}$ defined per unit edge boundary $\mathrm{d}\Gamma$ and volume forces $\mathbf{b}$ defined per unit surface area $\mathrm{d}\Omega$ are applied.

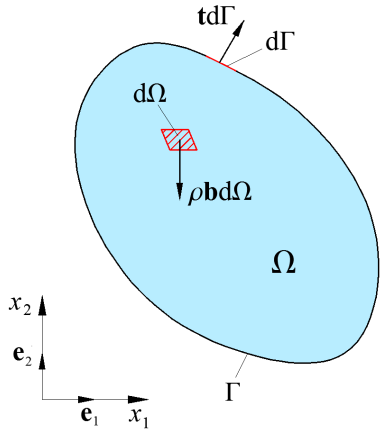

Figure 2.1: Equilibrium equations - Balance of momentum

By writing the balance of linear momentum for the above continuum with respect to the Cartesian coordinate system (x_1, x_2) according to [129], for every moment of time t

$$\sigma_{ij,j} + b_i = \rho \frac{\mathrm{D}v_i}{\mathrm{D}t}, \tag{2.14}$$

is obtained. Herein, b_i represents the body force vector, ρ denotes the material density and v_i the velocity vector. Equations (2.14) are also called the equations of motion. Since only static problems are considered here, the acceleration in this case is equal to zero for each point within Ω and the equations of motion transform to the equilibrium equations.

$$\sigma_{ij,,j} + b_i = 0. \tag{2.15}$$

The essential and natural boundary conditions associated with the classical linear elasticity on the outer boundary Γ, are the prescribed displacements or the prescribed traction forces. For the meshless functions with the Kronecker delta property, such as IMLS and RPIM used here, the imposition of the essential boundary conditions is as simple as in FEM and is done in a direct manner. The enforcement of the natural boundary depends on the choice of the utilized meshless method [33, 126]. The traction forces $\mathbf{t}$ on the outer boundary Γ are calculated as

$$t_i = n_j \sigma_{ij}, \tag{2.16}$$

where n_j is the unit normal vector on the outer boundary. The traction vector (2.16) can be written in the matrix form using (2.7) as

$$\mathbf{t} = \mathbf{N}\boldsymbol{\sigma}, \tag{2.17}$$

where $\mathbf{N}$ is the matrix of the unit normal vector components on the outer boundary Γ

$$\mathbf{N} = \begin{bmatrix} n_1 & 0 & n_2 \\ 0 & n_2 & n_1 \end{bmatrix}. \tag{2.18}$$

2.2. Strain gradient linear elasticity

Gradient elasticity theories used in this work provide extensions of the classical continuum theories, with additional higher-order spatial derivatives of strains, in order capture the influence of the microstructure on the macroscopic deformation response of the material. The focus is on the gradient theories where the higher-order terms are the Laplacian of the corresponding lower-terms. These theories are often utilized for such problems as the removal of discontinuities in heterogeneous materials, as well as the size dependent mechanical response of structures. In this section, a brief overview of historical

development of these theories is shown, along with the their differences and numerical implementation issues. The utilized Aifantis theory which has only one additional parameter is more thoroughly discussed. Due to its versatility and simple implementation in numerical procedures, it was the best choice for the presented research. Furthermore, the utilized staggered solution procedures for the gradient elasticity are presented. The use of these procedures decreases the continuity requirements of the meshless trial functions. Hence, the calculation of the high-order derivatives in the developed numerical methods is also avoided.

2.2.1. On the historical development of strain gradient theories

The utilization of the gradient theories for the modeling of material deformation is not a novel concept, it has been around since the 19^{th} century. The first efforts in this field were done by Cauchy and include the idea to enrich the continuum equations of elasticity with additional higher-order derivatives in order to approximate the behaviour of discrete lattice models. These formulations had more of an explorative character and lacked mathematical completeness. They were later extended and completed by Voigt to include the description of kinematics, balance laws and constitutive relations for lattice models of crystals [130]. However, the solutions for the formulated boundary value problems were complicated and obtainable only for a limited number of cases using additional assumptions [131]. Later on, in the early 20^{th} century Voight's research was expanded by the Cosserat brothers. They suggested the formulation of 3-D continuum equations with three displacement components and three micro-rotations. Furthermore, they included the couple-stresses in the equations of motion which they conjugated with the aformentioned micro-rotations [132]. Cauchy, Voigt and the Cosserat brothers are today considered as pioneers in the field of gradient elasticity. After the work of the Cosserat brothers in took scientists several decades in order to revive the research in this field. Hence, in 1960s a large number of papers was published regarding this topic. Two groups of independent researches, Soviet and Western school, concerned with improving gradient theories could be distinguished. The work of the Soviet scientists can be found in papers from Aero and Kuvshinskii [133], Pal'mov [134] and Kunin [135], while the most known papers from the Western scientists include ones from Toupin [136], Mindlin [137] and Kröner [138] to mention a few. At the time, most of the research was focused on expanding the existing Cosserat continuum theories [132] and the couple-stress theory [11, 136], but from this also full gradient theories have arisen [12, 137, 138]. These full gradient theories consider including the mathematically complete set of higher-order gradients in the formulation which results, in elaborate and complicated theories which are not applicable for use in computer codes due to a large number of material parame-

ters. Hence, the need for a more simple theories with fewer higher-order terms and smaller number of additional constitutive constant that need to undergo experimental testing was inherent. In the 1980s Eringen and Aifantis developed two such theories that utilize only one additional constitutive parameter. Eringen derived his theory using his earlier work on integral non-local theories [14]. On the other hand, Aifantis formulated his gradient elasticity theory for finite [139] and infinitesimal deformations [15] inspired by his earlier research in plasticity [140]. In these simpler theories, only higher-order terms that are necessary to more accurately describe the analyzed material behaviour are included in the formulation. In recent years, because of the rapid increase in the computational speed and power, gradient elasticity is becoming more and more interesting for numerical implementation. Herein, mostly FEM formulations prevail but there are also some papers on meshless formulations. The implementation of gradient elasticity with FEM is not such a trivial task due to the more complex formulation resulting from the use of element-based interpolation. Nevertheless, researchers have successfully applied FEM formulations not only using the simpler newer gradient theories [141, 142], but also the more complicated theories from the 1960s as can be observed in [143, 144]. Some authors also used meshless methods for the implementation of gradient elasticity since the required C^1 continuity of the approximation is easily obtained, unlike in FEM. These formulation can be found in [26, 39, 63]

2.2.2. Aifantis form of strain gradient theory

Many different formats of gradient elasticity theory exist, Cosserat-type theories, couple stress theories or Laplacian based theories, as already mentioned. Herein, the main goal is to present the utilized linear elasticity Aifantis theory under assumption of small strains. It should be stated that the Aifantis theory is formally a special case of the Mindlin theory of elasticity with microstructure [145]. However, the Mindlin's full gradient theory [12] is not appropriate for implementation in numerical codes. In his theory, Mindlin distinguished between the kinematic quantities at two different scales, micro and macro, and also suggested that the kinetic and deformation energy density also be written using quantities at both scales. This lead to a very complex formulation with 6 different constitutive tensors of various orders containing 903 different independent coefficients for a general material representation. If only isotropic material is considered the number of elastic coefficients drops to 18 (2 Lame's and 16 additional constants) but this is still a large number of parameters which have to be experimentally determined. Later, Mindlin also developed simpler version of his theory in which the deformation energy density is only expressed in terms of macroscopic displacements which lowers the needed number of additional parameters to only 3. These independent parameters were named length

scales since they have the dimension of length, and can be linked to the microstructure of the material. Aifantis further simplified Mindlin's theory by taking two length scale equal to each other thus arriving to the probably most well-known formulation with only one material (microstructural) parameter [15].

2.2.2.1. Constitutive relation based on Aifantis form

In the field of statics, the gradient elasticity is mostly applied for removing the singularities at crack tips and smoothing the discontinuities at material interfaces. These kind of research can be found in a wide variety of publications [146–148]. The Aifantis gradient elasticity falls into the category of Laplacian based theories since Laplace operators are used for the description of the non-local redistribution effects. Furthermore, in this Thesis the special form II of the Mindlin theory is utilized, where the microscopic deformation gradient is assumed to be the first gradient of the macroscopic strain [13]. For this simplest form of gradient elasticity [149], the constitutive relation is taken as

$$\widetilde{\sigma}_{ij} = \sigma_{ij} - \mu_{ij}, \tag{2.19}$$

where $\widetilde{\sigma}_{ij}$ represents the Aifantis stress tensor which is defined as a difference between the classical Cauchy stress tensor σ_{ij} and the higher-order stress tensor μ_{ij}. In the relation (2.19) the mentioned stress tensors are defined as

$$\sigma_{ij} = C_{ijkl}\varepsilon_{kl}, \tag{2.20}$$

$$\mu_{ij} = C_{ijkl}l^2\varepsilon_{kl,mm}. \tag{2.21}$$

In the equations (2.20) and (2.21) the C_{ijkl} and ε_{kl} are the material tensor defined by (2.8) and the strain tensor equal to the ones in classical linear elasticity, while l denotes the Aifantis microstructural material parameter. Kinematic relations connecting the strain tensor and the displacement components for the gradient problem remain the same as in the classical elasticity and are defined by relation (2.2). By inserting the relations for stress tensors (2.20) and (2.21) into the equation (2.19), a slightly different form of the Aifantis constitutive relation can be obtained

$$\widetilde{\sigma}_{ij} = C_{ijkl}(\varepsilon_{kl} - l^2\varepsilon_{kl,mm}). \tag{2.22}$$

Herein, the introduced parameter l represents the underlying microstructure and can be related to microstructural properties. For example, for a regular lattice of discrete particles it can be linked to the distance between particles comprising the lattice, for a heterogeneous material consisting of various randomly distributed constituents in a material matrix it can be connected to the utilized size of the RVE used in homogenization

procedures [150]. Furthermore, it should be stated that the negative sign in front of the higher-order term in equation (2.22) is chosen because of the issues related to stability and the uniqueness of the problem solution [145, 151]. Through the years also a positive sign has been considered. The obtained numerical solutions have been compared to the behaviour of the methods where the negative sign has been utilized [151, 152].

2.2.2.2. Equilibrium equations and boundary conditions based on Aifantis form

The equilibrium equations of gradient elasticity for the two-dimensional continuum depicted in Figure 2.1 are derived in a similar manner as explained for the classical linear elasticity and can be simply written as

$$\widetilde{\sigma}_{ij,j} + b_i = 0. \tag{2.23}$$

As evident, the above relation represents the fourth-order differential equations. If the differential equations are solved in a direct manner, C^1 continuity of the approximation function is needed [13]. This should not be a problem if the discretization and approximation is done using a meshless method [26], but leads to relatively complex element formulations [153] if FEM is utilized. Since the equilibrium equations are of higher-order, the associated essential and natural boundary conditions are not as simple as is the classical linear elasticity. In recent years, the variational consistency of these boundary conditions was thoroughly investigated [154, 155]. Herein, the essential boundary conditions are the displacements u_i and their normal derivatives η_i, while the natural boundary conditions are the classical traction t_i and the higher-order tractions m_i [143]. The essential boundary conditions are related to the kinematic variables (displacements and their derivatives) and can be defined as

$$u_i = \bar{u}_i, \tag{2.24}$$

$$\frac{\partial u_i}{\partial x_j} n_j = \bar{\eta}_i, \tag{2.25}$$

while the natural boundary conditions are linked to the stress variables and are equal to

$$n_j(\sigma_{ij} + n_h \tau_{ijh}(\delta_{lm} - n_l n_m)\frac{\partial n_l}{\partial x_m}) - (\delta_{jm} - n_j n_m)\frac{\partial (n_h \tau_{ijh})}{\partial x_m} = \bar{t}_i, \tag{2.26}$$

$$n_j n_h \tau_{ijh} = \bar{m}_i. \tag{2.27}$$

Herein, in the natural boundary conditions (2.26) and (2.27), τ_{ijh} represents the higher-order stress tensor

$$\tau_{ijh} = l^2 C_{ijkl} \varepsilon_{kl,h}, \tag{2.28}$$

while δ_{ij} denotes the Kronecker delta tensor. From the analysis of boundary condition (2.27) and (2.28), it can be seen that the higher-order tractions are related to the strain

derivatives or the second-order derivatives of displacements. Furthermore, it is easily observed that the calculation of high-order derivatives of the meshless functions is needed for the discretization of the standard tractions (2.26) and the higher-order tractions (2.27). This can be a burdensome task because most of the meshless functions do not have polynomial character. Furthermore, it is also computationally not efficient since the time needed for the calculation increases rapidly with each order of derivatives. Because of these drawbacks, only in the case of linear gradient elasticity, there is certain remedy in using the staggered solution procedures [124] in which the fourth-order equilibrium equations (2.23) are solved as an uncoupled sequence of two second-order equations. Hence, the use of these procedures changes the field equations. They are no longer the same as those of the original fourth-order equations. Furthermore, the corresponding boundary conditions are also transformed into a less complex form. More on this, as well as the reason why the staggered solution strategy based on the Aifantis theory is chosen for the analysis, can be found in the following subsection.

2.2.2.3. Staggered solution procedures (operator-split methods)

Different solution procedures have been developed [156] depending on the point at which the fourth-order equilibrium equations (2.23) are split into two second-order differential equations. In this subsection two different solution strategies (u-RA and ε-RA) with the accompanying boundary conditions are presented. Firstly, by introducing the relations (2.19) - (2.21) into equation (2.23), the third-order differential equations in terms of strains is obtained

$$C_{ijkl}(\varepsilon_{kl} - l^2\varepsilon_{kl,mm})_{,j} + b_i = 0. \tag{2.29}$$

Secondly, if the kinematic relations (2.2) are also applied to the above equation, fourth-order differential equations in terms of displacements is written

$$\frac{1}{2}C_{ijkl}[u_{k,jl} + u_{l,jk} - l^2(u_{k,jl} + u_{l,jk})_{,mm}] + b_i = 0. \tag{2.30}$$

The above equation for gradient linear elasticity can be rewritten by rearranging the order of derivatives and according to [124]

$$\frac{1}{2}C_{ijkl}[(u_k - l^2u_{k,mm})_{,jl} + (u_l - l^2u_{l,mm})_{,jk}] + b_i = 0. \tag{2.31}$$

As stated before, the above equations are not suitable for the numerical solving of a problem because of the need for high-order derivative calculation, not only in the equilibrium equations (2.29) and (2.31), but also for imposing natural boundary conditions (2.26) and (2.27). Therefore, the application of staggered solution procedures in order to lower the needed order of derivatives can be beneficial.

- ***u*-RA staggered procedure**

  The differential equation (2.31) describing gradient elasticity can be transformed into two problems in such a way that the terms expressed in the parentheses are declared a new classical displacement field u_k^{c}. This exchange is possible since the resulting differential equation of the second-order describes the behavior of a linear elastic homogeneous material when classical linear elasticity is utilized. Hence, the first equation of the u-RA procedure is equal to

  $$\frac{1}{2}C_{ijkl}(u_{k,jl}^{\mathrm{c}} + u_{l,jk}^{\mathrm{c}}) + b_i = 0. \tag{2.32}$$

  Accordingly, the second equation that links the classical displacement field u_i^{c} and the gradient displacement field u_i^{g} can be derived from the substitution. This equation is a second-order non-homogeneous Helmholtz equation

  $$u_i^{\mathrm{g}} - l^2 u_{i,mm}^{\mathrm{g}} = u_i^{\mathrm{c}}. \tag{2.33}$$

  Boundary value problems defined by equations (2.32) and (2.33) are now solved using a staggered scheme, or one after the other, where the solution of the first problem is used as an input on the right hand side of the second differential equation (2.33). As a result, both the classical displacement components u_k^{c} as well as the gradient displacement components u_i^{g} are obtained. Here, relation (2.32) actually represents the equation of the classical problem of elasticity analogous to (2.15), where the Cauchy stress is written through constitutive and kinematic relations. It can be seen that the complexity of the solution of the gradient elasticity problem (2.32) - (2.33) is reduced when compared to the original fourth-order equation (2.31) once the classical solution from the first equation is obtained. In the literature, this has been extensively analyzed by employing the analytical solution strategies [152, 157]. In this staggered procedure based on displacements, as discussed in [156], the boundary conditions of the classical problem

  $$u_i^{\mathrm{c}} = \bar{u}_i^{\mathrm{c}}, \tag{2.34}$$

  $$t_i^{\mathrm{c}} = \sigma_{ij}^{\mathrm{c}} n_j^{\mathrm{c}} = \bar{t}_i^{\mathrm{c}}, \tag{2.35}$$

  and boundary conditions of the gradient problem

  $$u_i^{\mathrm{g}} = \bar{u}_i^{\mathrm{g}}, \tag{2.36}$$

  $$R_i^{\mathrm{g}} = \frac{\partial^2 u_i^{\mathrm{g}}}{\partial n^{\mathrm{g}2}} = \bar{R}_i^{\mathrm{g}}, \tag{2.37}$$

  on the outer boundary Γ can be distinguished. As seen, the second-order of normal derivatives in terms of gradient displacements are needed for the imposition of the

natural boundary conditions when solving the second equation using direct analytical methods [124] or meshless collocation methods [158]. However, within the framework of weak form methods, for instance FEM, after the use of the divergence theorem in the gradient equation the first-order of displacement derivatives should suffice [141].

- **ε-RA staggered procedure**

  This approach is based on using the operator-split procedure at the strain level. So the first equation is simply obtained by introducing the new classical strain field $\varepsilon^{\mathrm{c}}_{kl}$ into equation (2.29) and is equal to

$$C_{ijkl}\varepsilon^{\mathrm{c}}_{kl,j} + b_i = 0. \tag{2.38}$$

  Now, by utilizing the kinematic relations (2.2) in the equation (2.38), the relation equal to (2.32) is obtained. This means that the first equation of the staggered procedures is the same for both cases, and so are the corresponding boundary conditions. By performing a simple derivation of the Helmholtz equation (2.33), the equation in terms of corresponding strain fields [159] is observed

$$\varepsilon^{\mathrm{g}}_{ij} - l^2\varepsilon^{\mathrm{g}}_{ij,mm} = \varepsilon^{\mathrm{c}}_{ij}. \tag{2.39}$$

  The above equation relates the non-local (gradient) strain tensor $\varepsilon^{\mathrm{g}}_{ij}$ to the local (classical) strain tensor $\varepsilon^{\mathrm{c}}_{ij}$. Both strain tensors can be written in terms of corresponding displacements using kinematic relation (2.2). This staggered approach consists of solving the classical elasticity problem defined by (2.32), then computing the local strain tensor $\varepsilon^{\mathrm{c}}_{ij}$ and using it as a source term for solving the Helmholtz gradient equation now written in terms of strains (2.39). It should be noted that the solution of the second equation in this procedure is the gradient strain field $\varepsilon^{\mathrm{g}}_{ij}$, not the gradient displacement field u^{g}_i as in u-RA approach. As the second equation of the staggered solution procedure changes, so do the corresponding gradient boundary conditions. While the boundary conditions corresponding to the classical equation remain the same and are equal to (2.34) and (2.35) the boundary conditions of the gradient problem are changed and can be written as

$$\varepsilon^{\mathrm{g}}_{ij} = \bar{\varepsilon}^{\mathrm{g}}_{ij}, \tag{2.40}$$

$$R^{\mathrm{g}}_{ij} = \frac{\partial\varepsilon^{\mathrm{g}}_{ij}}{\partial n^{\mathrm{g}}} = \bar{R}^{\mathrm{g}}_{ij}. \tag{2.41}$$

  Herein, $\varepsilon^{\mathrm{g}}_{ij}$ denotes the gradient strain tensor defined according to (2.2) on the outer boundary Γ.

It is obvious from the presented relations that the field equations solved in the staggered procedures are different from those represented by the original fourth-order Aifantis gradient elasticity. Hence, the boundary conditions are also not the same. All of the presented solution procedures along with the boundary conditions are comprised and shown in Table 2.1 [156].

Table 2.1: Boundary conditions in Aifantis gradient elasticity

Solution method / Boundary condition	**Original equation** (4^{th} order)	***u*-RA** (2^{nd} order)	***ε*-RA** (2^{nd} order)
Essential	u_i	u_i^{c}	u_i^{c}
Natural	t_i	t_i^{c}	t_i^{c}
Higher-order essential	$\dfrac{\partial u_i}{\partial n}$	u_i^{g}	$\varepsilon_{ij}^{\text{g}}$
Higher-order natural	m_i	$\dfrac{\partial^2 u_i^{\text{g}}}{\partial n^2}$	$\dfrac{\partial \varepsilon_{ij}^{\text{g}}}{\partial n}$

The second equation of the staggered approach can also be expressed in terms of stresses. For instance, if both sides of equation (2.39) are multiplied by the material tensor C_{ijkl} the relation reads

$$C_{ijkl}(\varepsilon_{ij}^{\text{g}} - l^2 \varepsilon_{ij,mm}^{\text{g}}) = C_{ijkl}\varepsilon_{ij}^{\text{c}}, \tag{2.42}$$

or in terms of stresses

$$\sigma_{ij}^{\text{g}} - l^2 \sigma_{ij,mm}^{\text{g}} = \sigma_{ij}^{\text{c}}. \tag{2.43}$$

The same relationship linking the local (classical) σ_{ij}^{c} and the non-local (gradient) σ_{ij}^{g} stress fields is observed when Eringen's integral strain gradient theory is utilized [14]. This leads to the conclusion that these two gradient elasticity theories are quite similar, so here the main difference between these approaches should be noted. In the Aifantis theory, when employing the operator-split procedures in the first equation, the equilibrium is expressed in terms of the divergence of the classical (local) stress field [156]

$$\sigma_{ij,j}^{\text{c}} + b_i = 0, \tag{2.44}$$

while in the Eringen's theory this is done by applying the divergence of the gradient (non-local) stress field [13]

$$\sigma_{ij,j}^{\text{g}} + b_i = 0. \tag{2.45}$$

Hence, a clear distinction between the two theories can be observed. Furthermore, the difference in the equilibrium equations (2.44) and (2.45) results in different solution procedures that need to be applied. If the Aifantis theory is utilized, the local stress field

σ^{c}_{ij} is obtained directly from the derivative of the local displacements u^{c}_i, for instance by solving (2.32). The computed classical displacements can then be used as an input for the Helmholtz equation (2.33), and the gradient fields in the process of computation are obtained in a staggered manner using an *uncoupled* set of equations. In comparison, it can be seen from (2.43) that the relation between the non-local stress field σ^{g}_{ij} and the displacements u^{c}_i is a differential equation. Consequently, the equations (2.43) and (2.45) remain *coupled* and should be solved at the same time. Hence, the staggered solution strategy cannot be used if the Eringen theory is utilized.

3 Weighted residual methods and MLPG concept

3.1. Weighted residual approach for partial differential equations

Since the newly proposed meshless methods are based on the use of the weighted residual approach, these mathematical techniques will be briefly discussed and presented in this section. The weighted residual methods utilize the weak form of differential equations in order to determine the approximated solution of a chosen problem. Furthermore, they can differ depending on the size of the area that they are applied upon. Therein, two different approaches can be distinguished, the global and the local weighted residual approach. The discussion start with the weighted residual methods based on the global approach. Later, it is transferred to the application of the local approach. In addition, the main differences between the two approaches are discussed.

3.1.1. Global weighted residual approach

In the process of numerical solution of one-dimensional partial differential equation (PDE), the goal is to find a solution function f that satisfies the general equation $\mathfrak{D}f = g$, where $\mathfrak{D}$ is the differential operator dependent of the problem being solved, while g denotes to the right hand side of the equation. One of the most popular methods for solving the PDEs are the methods based on the weighted residual. As some of the representatives of these methods the Finite Volume Method (FVM), the Finite Element Method (FEM) and the Meshless Methods (MM) can be mentioned. In these methods the approximation of the required field variable f is in general defined by using functions Φ_i, usually called the shape functions, and the unknown nodal values f_i as

$$f^{(h)}(\mathbf{x}) = \sum_i \Phi_i \hat{f}_i = \mathbf{\Phi}^{\mathrm{T}} \hat{\mathbf{f}}. \tag{3.1}$$

By substituting the approximated function $f^{(h)}(\mathbf{x})$ into the initial PDE we obtain

$$\mathfrak{D}f^{(h)}(\mathbf{x}) - g = R_e, \tag{3.2}$$

where R_e is the residual error that appears as a consequence of the utilization of the approximated solution function. Furthermore, the methods are based on the integration of the obtained residual error multiplied by arbitrary kinematically admissible test (weight) function W. By applying the appropriate test (weight) function and by integrating over the global domain Ω depicted in Figure 2.1, the following relation is written

$$\int_{\Omega} W R_e \mathrm{d}\Omega = \int_{\Omega} W(\mathfrak{D}f^{(h)}(\mathbf{x}) - g)\mathrm{d}\Omega = 0 \tag{3.3}$$

The integral expressions of the weak form of PDEs are usually evaluated numerically. This is necessary to obtain the solutions. In doing so, firstly the initial boundary conditions have to be satisfied. Thereafter, the essential and natural boundary conditions of the problem have to be taken into account during the solution process. The resulting algebraic system of equations can be written in the classical form $\mathbf{L}\hat{\mathbf{f}} = \mathbf{s}$ and the unknown nodal solutions $\hat{\mathbf{f}}$ can be determined. It should be noted that in the derivation process of the integral equations of the weak form the Gauss-Ostrogradsky (divergence) theorem is often utilized. This is done in order to reduce the need for calculation of high-order derivatives within the integrands and to incorporate the natural (Neumann) boundary conditions directly in the integral equation of the weak form.

The procedure of the global weighted residual method is presented here for the case of linear differential equations. For the 2-D continuum according to equations (2.15) and (2.16), two general forms of symbolic system of PDE can be written

$$\mathfrak{M}(\mathbf{u}) = \mathbf{0}, \qquad \text{within } \Omega, \tag{3.4}$$

$$\mathfrak{N}(\mathbf{u}) = \mathbf{0}, \qquad \text{on } \Gamma. \tag{3.5}$$

The equation (3.4) refers to the F system equations of the static problem defined within the domain Ω, where $\mathbf{u}$ is the vector of unknown solutions of displacements, while relation (3.5) refers to the G system equations comprised of essential and natural boundary conditions on the outer boundary Γ. The differential equations $\mathfrak{M}(\mathbf{u})$ and $\mathfrak{N}(\mathbf{u})$ can be also written in their strong forms as follows

$$\mathfrak{D}_{\Omega}(\mathbf{u}) - \mathbf{b} = \mathbf{0}, \qquad \text{within } \Omega, \tag{3.6}$$

$$\mathfrak{D}_{\Gamma}(\mathbf{u}) - \mathbf{t} = \mathbf{0}, \qquad \text{on } \Gamma, \tag{3.7}$$

where $\mathfrak{D}_{\Omega}$ and $\mathfrak{D}_{\Gamma}$ are the differential operators, while $\mathbf{b}$ and $\mathbf{t}$ are known vectors of body forces within Ω and traction forces on outer boundary Γ. From the analysis of (3.6) and

(3.7), it can be determined that if k is the highest order of derivatives within the operator $\mathfrak{D}_\Omega$, the highest order of derivatives within $\mathfrak{D}_\Gamma$ can only be k-1. For the purpose of solving the equation systems the approximation of the solution $\tilde{\mathbf{u}}^h(\mathbf{x})$ in accordance with (3.1) is defined, based on one of the meshless schemes. The approximate displacement solution function is defined as a linear combination of independent base functions

$$\tilde{\mathbf{u}}^h = [\, \tilde{u}_1 \quad \tilde{u}_2 \quad \cdots \quad \tilde{u}_i \quad \cdots \quad \tilde{u}_n \,]^{\mathrm{T}}. \tag{3.8}$$

By substituting the approximated function (3.8) into the systems of differential equations (3.4) and (3.5) the residual errors are observed

$$\mathbf{R}_\Omega = \mathfrak{M}(\tilde{\mathbf{u}}^h) = \mathfrak{D}_\Omega(\tilde{\mathbf{u}}^h) - \mathbf{b}, \qquad \text{within } \Omega, \tag{3.9}$$

$$\mathbf{R}_\Gamma = \mathfrak{N}(\tilde{\mathbf{u}}^h) = \mathfrak{D}_\Gamma(\tilde{\mathbf{u}}^h) - \mathbf{t}, \qquad \text{on } \Gamma. \tag{3.10}$$

In an arbitrary case, it is very difficult to assume the exact shape and type of the solution function in advance. Therefore, the presented residual errors are generally not equal to zero. For this reason, the weight residual method (3.3) is applied and it is expected that the approximated solution fulfills the integral condition within the predefined domain Ω

$$\int_\Omega \mathbf{w}^{\mathrm{T}} \mathbf{R}_\Omega \mathrm{d}\Omega = 0, \tag{3.11}$$

where $\mathbf{w}$ is the vector of arbitrary test (weight) functions defined as

$$\mathbf{w}^{\mathrm{T}} = [\, w_1 \quad w_2 \quad \cdots \quad w_i \quad \cdots \quad w_n \,]. \tag{3.12}$$

For a detailed description of constraints that a function has to meet in order to be considered admissible for the weight function the reader is referred to [160]. The total number of test functions is equal to the total number of equations (3.4). Hence, for an arbitrary selection of the admissible test function in $\mathbf{w}$ it can be shown that the relation (3.11) is equal to strong forms of the equations (3.6) and (3.7) if the essential boundary conditions (displacements) are fulfilled in advance (*a priori*) [160]. The solutions of the system of equations (3.11) can be determined only if it is possible to calculate the integral expressions appearing in the accompanying weak form. For this reason, there are certain limitations also on the choice of the approximation function. Accordingly, the demands made on the approximation (trial) function $\tilde{\mathbf{u}}^h$ are that the derivatives up to the order k-1 must be continuous [72], if k is the largest order of derivatives which appear in the kinematic operator $\mathfrak{D}_\Omega$. Such functions are generally referred to as C^{k-1} continuous functions, which means that all the derivatives of the order j, where j is in the interval $0 \leq j \leq k-1$, exist and are continuous within the domain Ω. On the test (weight) function on the other hand there are no special demands, it's selection is arbitrary and

can also be a C^{-1} function. Therefore, by choosing a variety of test functions different meshless methods can be derived. In the general case, as a approximation function, any function that satisfies the aforementioned condition of continuity can be used. However, the accuracy of the solutions can be greatly impaired by a bad choice of approximation function. The same can be stated also for the choice of the test function, which can be completely arbitrary in character. Therefore, nowdays there are already established and often employed acceptable sets of test functions [160]. Depending on the choice of the test (weight) function, different forms of classical methods of weighted residual can be derived [21].

The satisfaction and imposition of boundary conditions play an important role in every numerical method. For this reason treatment of boundary conditions within the framework of weighted residual methods is discussed. In order to increase the accuracy of the weighted residual method, often before the direct integration of the weak form of equations (3.11), the Gaussian integral theorem is applied that reduces the demand on the continuity of the approximation functions $\tilde{\mathbf{u}}^h$. After applying the Gauss theorem, natural (force) boundary conditions contained implicitly within the integral terms can be observed [47, 72]. In this way, the natural boundary conditions are satisfied directly in a weak form of equations or *a posteriori*. All other boundary conditions which are not included in the weak form (displacement boundary conditions) are called essential boundary conditions and their imposition is necessary for the validity of the method. The essential boundary conditions can be imposed *a priori*, by selecting such approximation functions which presatisfy the conditions, or *a posteriori* in the system of discretized equations using additional numerical procedures. When solving complex problems, it is difficult to define the approximation function of solutions $\tilde{\mathbf{u}}^h$ that satisfies the essential boundary conditions in advance. Therefore, for this purpose the constrained weighted residual method is often utilized in the literature [22]. In this method one of the most common approaches used to impose the essential boundary conditions is the penalty method [23, 161]. The weak form of the equations in this case is written as

$$\int_{\Omega} \mathbf{w}^{\mathrm{T}} \mathbf{R}_{\Omega} \mathrm{d}\Omega + \int_{\Gamma_{\mathrm{u}}} \breve{\mathbf{w}}^{\mathrm{T}} \boldsymbol{\alpha} (\tilde{\mathbf{u}}^h, \bar{\mathbf{u}}) \mathrm{d}\Gamma = 0, \tag{3.13}$$

where Γ_{u} is a part of the outer boundary Γ on which the essential boundary conditions are prescribed. In equation (3.13), $\boldsymbol{\alpha}$ denotes a diagonal matrix of penalty parameters, while the $\breve{\mathbf{w}}$ represents the vector of arbitrary test functions associated with the essential boundary conditions. As a rule, for simplicity the functions in $\breve{\mathbf{w}}$ are chosen to be the same as in the vector (3.12). However, this is not always the case. Penalty parameters in the matrix $\boldsymbol{\alpha}$ are arbitrary positive scalar values that must be large enough to ensure the fulfillment of basic boundary conditions. On the other hand, caution is needed when choosing the

values for the penalty parameters, because excessive values can cause problems with the stability of numerical method. The penalty approach is a very simple method that does not increase the number of global unknowns of the final algebraic system. Hence, it is often implemented into numerical codes. As an alternative to the penalty methods, the method of Lagrange multipliers [22] is often utilized. Therein, additional unknowns to be determined are Lagrange multipliers for each boundary condition set in the problem. The method of Lagrange multipliers is often used in the EFG method [46] which is based on the global Galerkin weighted residual method.

3.1.2. Local weighted residual approach

Instead of writing the global equation (3.11) over the entire global domain, there exist a different approach, where the weighted residual method is applied only over small local domains $\Omega_{\mathrm{s}}^{\mathrm{w}}$ which cover the global problem domain Ω, as shown in Figure 3.1.

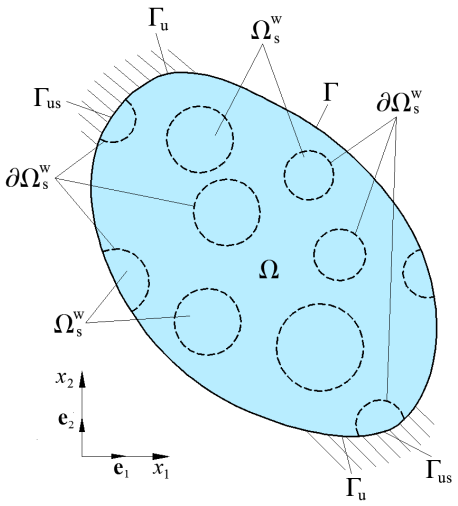

Figure 3.1: Global domain Ω with the outer boundary Γ and local regions $\Omega_{\mathrm{s}}^{\mathrm{w}}$

That approach is in the literature referred to as the local weighed residual method and is applied for the derivation of truly meshless methods [21]. These meshless methods do not use any background mesh of integration cells for evaluating the integrals of the weak form of equations. To solve the problem described by the (3.6) analogous method is applied but this time over small local domains $\Omega_{\mathrm{s}}^{\mathrm{w}}$. Hence, the integral weak form of the problem is then

$$\int_{\Omega_{\mathrm{s}}^{\mathrm{w}}} \mathbf{w}^{\mathrm{T}}\mathbf{R}_{\Omega}\mathrm{d}\Omega + \int_{\Gamma_{\mathrm{us}}} \breve{\mathbf{w}}^{\mathrm{T}}\boldsymbol{\alpha}(\tilde{\mathbf{u}}^{h}, \bar{\mathbf{u}})\mathrm{d}\Gamma = 0, \tag{3.14}$$

where Γ_{us} is the part of the outer boundary of the local domain $\Omega_{\mathrm{s}}^{\mathrm{w}}$ which coincides with Γ_{u}. Or in other words, it denotes the part of the outer boundary $\partial\Omega^{\mathrm{w}}$ on which the essential boundary conditions are prescribed, as presented in Figure 3.1. Local small

domains Ω_s^w are found within the global domain Ω and theoretically the local approach (3.14) should be equivalent to the global residual approach (3.13) as long as they cover the entire computational area.

3.2. Meshless Local Petrov Galerkin concept

The Meshless Local Petrov Galerkin (MLPG) concept is based on the presented local weighted residual method [47]. Since the application of local regions to integrate the weak form of equations alleviates the need of the use of background mesh, all meshless methods based on the local Petrov-Galerkin approach belong to the group of truly meshless methods [22]. In order to develop the solvable algebraic system of equations, the global domain Ω bounded by the outer boundary Γ is firstly discretized using a set of nodes $S = \{\mathbf{x}_I, I = 1, 2, ..., Z : \mathbf{x}_I \subseteq \Omega \cup \Gamma\}$, where Z represents the total number of discretization nodes. Secondly, a local subdomain Ω_s^w is defined around each node I with the position $\mathbf{x}_I$, as previously presented in Figure 3.1. In the next step, the weak form of the governing equations is employed over every local subdomain Ω_s^w using the local Petrov-Galerkin weighted residual approach. The choice of the size and the shape of local subdomains is arbitrary and they can also overlap. As already mentioned, as long as they cover the entire domain Ω, the equilibrium equations (3.4) and boundary condition (3.5) are satisfied in their weak forms. However, it has also been deducted that a high-quality solution can be obtained even if the subdomains do not cover the entire global region [35]. By using the MLPG concept, numerous meshless methods depending on the choice of the test (weight), approximation functions and appropriate integration procedures [29], can be derived. Thus, the main characteristic of the Petrov-Galerkin procedure is the free choice of the test and approximation (trial) functions. Furthermore, the test and approximation functions typically do not have to be the same and can be defined in different spaces, which is not the case in classical Galerkin method.

In the methods derived by utilizing the MLPG concept, also different types of local subdomains appear which need to be distinguished. Here, they will be only briefly mentioned for the purpose of completeness and understanding of the terminology in the later discussion at the end of the section. There are five different regions that arise when applying the general MLPG procedure. There is the aformentioned local subdomain for a node, which is denoted as Ω_s^w. This region is the domain over which the numerical integration of the local weak form is carried out in order to obtain the solvable algebraic system of equations. Secondly, there is also the test (weight) function support domain for the node, usually referred to as Ω_t. Within this region, the value of the chosen test function for the discretization node is different from zero. The third region is the trial (approximation)

function domain for the node orΩ_{s}. Similarly to the previous region, here the chosen trial (approximation) function associated with the discretization node $\mathbf{x}_I$ has non-zero values. Another region that is present in all the methods derived using the MLPG concept is the domain of definition of the point of interest $\mathbf{x}$ which can be denoted as Ω_{def}. This region includes all of the nodes within S that influence the approximation at the point of interest x. The last area that can be noted is the domain of influence of the node or Ω_{inf}. This region cover all the nodes whose shape functions have non-zero values over the local subdomain $\Omega_{\mathrm{s}}^{\mathrm{w}}$ of the node. In theory, the shapes of the regions Ω_{s}, Ω_{t} and Ω_{tr} can be chosen arbitrarily. However, the choice of more complex shapes often results in numerical implementation issues. Hence, in most engineering applications, only simple shapes of these domains are used, i.e. circular or rectangular, with the nodes positioned at their center. For a more extensive explanation on each of the regions the reader is referred to [27, 35]. In addition, based on the choice of the test function, meshless MLPG methods can be divided into six categories [27]:

- MLPG1
  The test function is equal to the weight function of the MLS or RKPM approximations. The test function is bell-shaped and its value is zero at the outer boundary of the local subdomains $\partial\Omega_{\mathrm{s}}^{\mathrm{w}}$ in case $\Omega_{\mathrm{s}}^{\mathrm{w}}$ does not intersect the global boundary of the considered problem Γ.

- MLPG2
  As a test functions, the Dirac delta function is chosen, which yields the collocation method [56]. At each discretization node, strong form of differential equations is solved, so there is absolutely no need for numerical integration.

- MLPG3
  For the test function, the error (residual) function obtained by the discrete least squares method is utilized.

- MLPG4
  The test function is the modified fundamental solution of the differential equation. The derived method is identical to the LBIE method [162].

- MLPG5
  The Heaviside function is applied as the test function in every local subdomain $\Omega_{\mathrm{s}}^{\mathrm{w}}$. As a result, the evaluation of the integrals over the regions $\Omega_{\mathrm{s}}^{\mathrm{w}}$ is no longer needed, only the integration over the local subdomain boundary $\partial\Omega_{\mathrm{s}}^{\mathrm{w}}$ are carried out. Therefore, this type of method is very attractive for reducing the computational time of the problem.

- MLPG6

  The test function is equal to the approximation (trial) function. The resulting method is similar to the EFG method [46] or DEM [163], with the important difference that the approximation is carried out over local approximation (trial) function domains Ω_{s}, rather than over the entire domain by a background mesh.

For the derivation of the meshless methods based on the mixed approach comprised in the framework of this Thesis, only the MLPG2 (collocation) methods have been utilized. Hence, for the test function the Dirac delta function is chosen, which has the value zero everywhere except at the discretization node. The delta function can be also described as a hypothetical function whose graph is an infinitely high, infinitely thin spike at the origin, with total area equal to one. With the utilization of this type of test function the weight function support domain Ω_{t} for the node $\mathbf{x}_I$ does not exist. The weak form over a local subdomain $\Omega_{\mathrm{s}}^{\mathrm{w}}$ is simply transferred to the strong form of equations at a collocation node. This means that the discretized system of equations is solved without any need for numerical integration. Therefore, the size of the local subdomain $\Omega_{\mathrm{s}}^{\mathrm{w}}$ is equal to zero. Furthermore, only the trial support domain Ω_{s} is utilized for the purpose of construction the meshless approximation functions.

4 Meshless approximation schemes

In meshless methods (MM), a very important and vital part of the entire numerical method are the approximation functions. For the approximation in MM, functions that can describe the data on an grid of arbitrarily positioned points are utilized [164]. In doing so, no additional predefined meshes are used. Thus, when comparing to the FEM, the approximation is not carried out over some predefined regions (elements). In FEM, to approximate the field values within the element, only the nodes that belong to that element are used, which limits the use of arbitrary degree of approximation. In MM, for constructing the approximation at some point of interest, a finite number of nodes in the immediate vicinity of that point is utilized. But in MM, these point are not connected. As an exception to this rule, there are also MM that use Voronoi cells [165] or Delaunay triangulation [166] for the approximation of field variables. Approximation of unknown field values in these cases is constructed using the nodes that are positioned at the vertices of adjacent cells or triangles.

Given that the numerical procedure of creating the meshless approximation functions is more complex when compared to the calculation of the polynomial functions in FEM, the process requires a longer computational time. The reason for that lies in the analytical form of meshless functions, which is far more complex and in general have non-polynomial rational character. Therefore, in order to reduce the calculation time, it is beneficial that the number of points affecting the approximation at the point of interest $\mathbf{x}$ is as low as possible. Of course, this number cannot be to low since the requirement of minimal number of nodes influencing the approximation needs to be fulfilled. This depends directly on the order of the approximation applied for solving of the considered problem. Thus, it can be stated that the order of the approximation function in MM is arbitrary, provided that a sufficient number of discretization nodes in utilized within the domains in which the approximation is being constructed. Another convenient feature of the meshless functions is the locality of the approximations. As a result, a sparse system matrix which can be solved quickly by utilizing appropriate numerical solvers is obtained. In comparison to

FEM, domains used for the approximation and integration of a weak form of governing equations do not necessarily have to be same. Sometimes this can lead to large problems when numerically evaluating the integrals in the weak form. The most of the meshless functions do not possess the Kronecker delta property at the nodes which is always the case when FEM is used. In these cases, the imposition of essential boundary conditions is not so simple as in FEM and requires additional numerical procedures. In the last decades, the researchers have developed and applied a large number of meshless approximation methods in order to solve the most demanding engineering problems. Some of these methods include: the Moving Least Squares (MLS) method [28], the Interpolating Moving Least Squares (IMLS) method [106] and the Radial Point Interpolation Method (RPIM) [23]. Herein, only the methods utilized in the research comprised in this Thesis are mentioned. These methods, along with their characteristics, are described and presented in this chapter. A more detailed summary on all of the approximation functions that are often used in meshless methods can be found in [23, 164, 167, 168].

4.1. Moving Least Squares (MLS) approximation

The Moving Least Squares approximation can be considered as a variation of a more known method of the Discrete Least Squares, which is often used for accurate description of curves and surfaces using only a set of arbitrary scattered points [169]. Hence, in this section the construction of the utilized MLS approximation and its derivatives is presented and explained. The main characteristics of the approximation are also noted. At the end of the section, the imposition of the interpolatory properties on the MLS approximation is discussed.

4.1.1. Construction of MLS approximation

Construction of the MLS function is based on the assumption that the approximation of an arbitrary function $f(\mathbf{x})$, which is here denoted as $f^{(h)}(\mathbf{x})$, is influenced the most by the points in the vicinity of the point for which the approximation is written. In the literature, this point is usually referred to as the point of interest $\mathbf{x}$. In such a manner, the locality of the approximation is introduced since the points that are far enough from $\mathbf{x}$ do not influence the approximation. According to [170], the approximant $f^{(h)}(\mathbf{x})$ approximates the function $f(\mathbf{x})$ using an arbitrarily distributed set of points $\mathbf{x}_I = 1, 2, \ldots, N$ positioned within the domain Ω. Hence, in the MLS procedure, to obtain the value of the approximated function at point $\mathbf{x}$, the vector of basis functions $\mathbf{p}(\mathbf{x})$ is

multiplied by the vector of unknown coefficients $\mathbf{a}(\mathbf{x})$,

$$f^{(h)}(\mathbf{x}) = \mathbf{p}^{\mathrm{T}}(\mathbf{x})\mathbf{a}(\mathbf{x}). \tag{4.1}$$

In the equation (4.1), the vector of basis function of the MLS approximation is equal to

$$\mathbf{p}(\mathbf{x})^{\mathrm{T}} = [\, p_1(\mathbf{x}) \quad p_2(\mathbf{x}) \quad \cdots \quad p_k(\mathbf{x}) \quad \cdots \quad p_m(\mathbf{x}) \,], \tag{4.2}$$

where m represents the total number of monomials in the basis vector. As a general rule, for the vector of basis function, complete polynomials are used in order to preserve the consistency of the MLS approximations. For this purpose, various polynomials [171] or other functions are considered if they are suitable for solving of the problem [172]. The number of terms in the complete polynomial of the order s which are used in the vector od basis functions are usually determined using Pascal's triangle [72]. This number can also be calculated by using the expression $m = (s+1)(s+2)/2$. In the numerical examples presented in this dissertation, complete polynomial from first- up to third-order are utilized. The vector of unknown coefficients $\mathbf{a}(\mathbf{x})$ in equation (4.1) is defined as

$$\mathbf{a}(\mathbf{x})^{\mathrm{T}} = [\, a_1(\mathbf{x}) \quad a_2(\mathbf{x}) \quad \cdots \quad a_k(\mathbf{x}) \quad \cdots \quad a_m(\mathbf{x}) \,]. \tag{4.3}$$

As obvious, it is a function of $\mathbf{x}$ and should be evaluated for every point of interest. The values of the unknown coefficients are influenced only by a small finite number of points near the point of interest $\mathbf{x}$. According to the common meshless procedure, around each point of interest $\mathbf{x}$, a local domain of definition of the MLS approximation for that point is formed. Here, it is denoted simply as $\Omega_{\mathrm{s}}^{\mathrm{MLS}}$. The vector of coefficients $\mathbf{a}(\mathbf{x})$ is obtained by minimizing the weighted discrete L_2-norm

$$J(\mathbf{a}(\mathbf{x})) = \sum_{J=1}^{n} W_J(\mathbf{x})(\mathbf{p}(\mathbf{x}_J)\mathbf{a}(\mathbf{x})) - \hat{f}_J)^2, \tag{4.4}$$

where $W_J(\mathbf{x})$ is a MLS weight function at $\mathbf{x}$, and $\hat{f}_J$ is the value of the function associated with the node J. The total number of nodes within the domain $\Omega_{\mathrm{s}}^{\mathrm{MLS}}$ is denoted as n. Hence, within $\Omega_{\mathrm{s}}^{\mathrm{MLS}}$ there is a set of nodes $\mathbf{x}_J$, $J = 1, 2, \ldots, n$, whose weight function values are bigger then zero at the point of interest $\mathbf{x}$. The domain of definition of the MLS approximation for the point of interest $\mathbf{x}$ can be seen in Figure 4.1. By minimizing the functional in (4.4), following system of equations is obtained

$$\mathbf{A}(\mathbf{x})\mathbf{a}(\mathbf{x}) = \mathbf{B}(\mathbf{x})\hat{\mathbf{f}}, \tag{4.5}$$

where $\mathbf{A}(\mathbf{x})$ is the moment matrix of the MLS approximation defined as

$$\mathbf{A}(\mathbf{x}) = \sum_{J=1}^{n} W_J(\mathbf{x})\mathbf{p}(\mathbf{x}_J)\mathbf{p}^{\mathrm{T}}(\mathbf{x}_J), \tag{4.6}$$

while the matrix $\mathbf{B}(\mathbf{x})$ is equal to

$$\mathbf{B}(\mathbf{x}) = [\, W_1(\mathbf{x})\mathbf{p}(\mathbf{x}_1) \quad W_2(\mathbf{x})\mathbf{p}(\mathbf{x}_2) \quad \cdots \quad W_J(\mathbf{x})\mathbf{p}(\mathbf{x}_J) \quad \cdots \quad W_n(\mathbf{x})\mathbf{p}(\mathbf{x}_n)\,]. \tag{4.7}$$

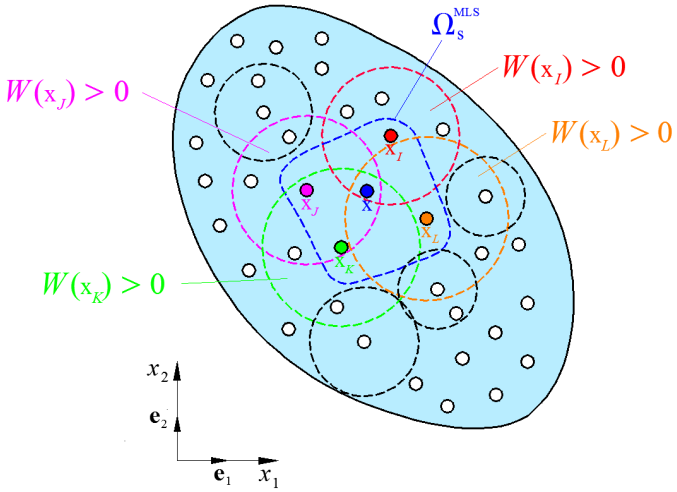

Figure 4.1: The domain of definition for the MLS approximation function at the point $\mathbf{x}$

Vector $\hat{\mathbf{f}}$ is comprised of the fictitious nodal values

$$\hat{\mathbf{f}}^{\mathrm{T}} = [\, \hat{f}_1 \quad \hat{f}_2 \quad \cdots \quad \hat{f}_J \quad \cdots \quad \hat{f}_n)\,]. \tag{4.8}$$

The unknown coefficients are determined by solving the system of equations (4.5) according to

$$\mathbf{a}(\mathbf{x}) = \mathbf{A}^{-1}(\mathbf{x})\mathbf{B}(\mathbf{x})\hat{\mathbf{f}}. \tag{4.9}$$

By inserting the unknown coefficients (4.9) into the MLS approximation function (4.1) we obtain

$$f^{(h)}(\mathbf{x}) = \mathbf{p}^{\mathrm{T}}(\mathbf{x})\mathbf{A}^{-1}(\mathbf{x})\mathbf{B}(\mathbf{x})\hat{\mathbf{f}}. \tag{4.10}$$

The equation (4.10) is often written in the following form

$$f^{(h)}(\mathbf{x}) = \sum_{J=1}^{n} \phi_J(\mathbf{x})\hat{f}_J, \tag{4.11}$$

where $\phi_J(\mathbf{x})$ is the shape function associated to the node $\mathbf{x}_J$ defined as

$$\phi_J(\mathbf{x}) = \sum_{k=1}^{m} p_k(\mathbf{x})[\mathbf{A}^{-1}(\mathbf{x})\mathbf{B}(\mathbf{x})]_{kJ}. \tag{4.12}$$

It should be stressed out that in the general case the MLS approximation function does not interpolate the nodal values at $\mathbf{x}_J$, or in other words $f^{(h)}(\mathbf{x}_J) = \hat{f}_J$ does not stand. For that reason, the nodal values $\hat{f}_J$ are called fictitious values. The non-interpolating property

of the MLS approximation function is presented in Figure 4.2 for an one-dimensional approximation problem.

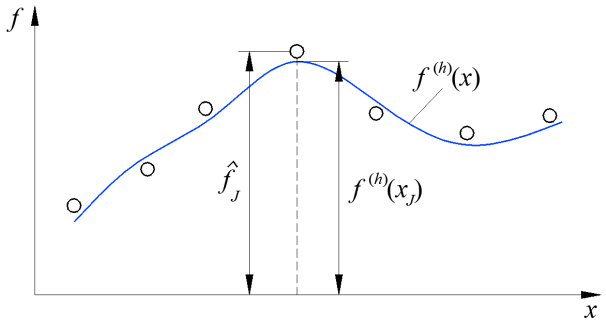

Figure 4.2: Non-interpolating property of the MLS approximation function

By analyzing the equation (4.10), it is obvious that the necessary condition to obtain a good approximation is the existence of the inverse of the moment matrix $\mathbf{A}^{-1}$. It is therefore essential to ensure that the momentum matrix is non-singular and well conditioned. The inverse of the moment matrix is usually determined by utilizing standard numerical procedures like the LU factorization with pivoting, the QR factorization or the Singular Value Decomposition (SVD) [173]. With a more detailed analysis, it can be shown that the inverse of the moment matrix exists only if the number of nodes n within the area of approximation Ω_x is greater or equal than the number of monomials m within the vector of basis functions $\mathbf{p}(\mathbf{x})$. Also, it is preferred that the arrangement of the nodes within the approximation domain is not uniform. In other words, nodes should not be arranged in such a way that some of their coordinates are equal. These type of distributions can sometimes cause the non-invertible moment matrix. A detailed theoretical analysis of the MLS approximation functions can be found in [174].

The choice of the weight function (4.4) also has a significant impact on final properties of the MLS approximation function. According to [47], the chosen weight function has to fulfill certain necessary conditions:

- Positivity

  The weight function has to have a value greater than zero over its support domain, i.e. $W_J(\mathbf{x}) > 0$. This type of weight function guarantees the existence of the minimum of the discrete L_2 error norm defined by (4.4).

- Compactness

  The weight function has the value zero, $W_J(\mathbf{x}) = 0$, outside the support domain. The compact support ensures the locality of the function since only the nodes within the support domain influence the approximation at the point of interest $\mathbf{x}$. For these nodes, $W_J(\mathbf{x}) \neq 0$ can be written.

- Monotonic decrease

  Such weight function should be chosen that it has the largest value at the point of interest $\mathbf{x}$, which then monotonically decreases away from $\mathbf{x}$. This guarantees that the nodes within the support domain closer to $\mathbf{x}$ have a larger impact on the approximation.

Any arbitrary functions that satisfies the presented conditions can be used as a weight function in the MLS approximation. As a desirable feature of the weight function for the MLS approximations, Kronecker delta property can be mentioned. In the case that the chosen weight function $W_J(\mathbf{x})$ has a delta property, that will be also true for the constructed MLS approximation function [106]. Thus, the Kronecker delta property facilitates the fulfillment of essential boundary conditions, which can be enforced in a simple manner identical to the procedures in in FEM. However, in the case that the chosen weight function does not possess the delta property, the essential boundary conditions need to be enforced by utilizing additional numerical procedures. In doing so, the complexity and the computational time of the method is increased. Furthermore, the choice of the weight function $W_J(\mathbf{x})$ also directly influences the order of continuity of the approximation function $f^{(h)}(\mathbf{x})$. The most utilized weight functions are those of Gaussian or polynomial character. More details on these functions can be found in [23, 175]. One of the most common selection for the weight function is a polynomial (spline) function of the fourth-order with a circular support domain which is defined as

$$W_J(\mathbf{x}) = w_{\mathrm{s}J}(\mathbf{x}) = \begin{cases} 1 - 6\big(\frac{d_J}{r_{\mathrm{s}J}}\big)^2 + 8\big(\frac{d_J}{r_{\mathrm{s}J}}\big)^3 - 3\big(\frac{d_J}{r_{\mathrm{s}J}}\big)^4 & 0 \leq d_J \leq r_{\mathrm{s}J} \\ 0 & d_J > r_{\mathrm{s}J} \end{cases} . \tag{4.13}$$

In the relation (4.13) $d_J = |\mathbf{x} - \mathbf{x}_J|$ denotes the distance between the node $\mathbf{x}_J$ influencing the approximation to the point of interest $\mathbf{x}$, while $r_{\mathrm{s}J}$ represents the size of the MLS weight function $W_J(\mathbf{x})$ support domain. It should be noted that the weight function defined in (4.13) is also one of the most commonly used in the MLPG meshless methods [47]. The size of the support domain is often determined by multiplying the characteristic average distance between the nodes h_{s} with any chosen scalar value α_{s} such that the support domain covers a sufficient number of nodes within the approximation domain Ω_{x}. The accuracy and stability of the MLS approximation is directly influenced by the choice of the parameter α_{s}. Therefore, for the purpose of optimizing the computational procedure parametric analyses of the accuracy of the solution depending on the size of the $r_{\mathrm{s}J}$ are often carried out.

4.1.2. Characteristics of MLS approximation

All of the approximation functions based on the MLS scheme possess similar properties, which are mentioned and noted in this subsection. These properties include:

- High order of continuity
  A order of continuity of the MLS approximation is directly affected by the continuity of the functions used within the base vector $\mathbf{p}(\mathbf{x})$ and the choice of the weight function $W_J(\mathbf{x})$. In most cases, the continuity of functions in $\mathbf{p}(\mathbf{x})$ is higher than the continuity of $W_J(\mathbf{x})$, so the MLS approximation function inherits the continuity order from the weight function [22].

- Reproducibility
  The MLS approximation functions possesses the property of reproducibility, which means that they can replicate the functions contained within the vector of basis functions $\mathbf{p}(\mathbf{x})$ [75].

- Consistency
  The consistency is defined as the ability of the approximation function to reproduce the complete polynomial function of a certain order [21]. Since the MLS function has the property of reproducibility, it can be observed that it is also consistent if a complete polynomial is used in $\mathbf{p}(\mathbf{x})$. The order of consistency is equal to the order of the complete polynomial comprised in the vector of basis functions $\mathbf{p}(\mathbf{x})$.

- Partition of unity
  The partition of unity is a very common property of the meshless approximation functions. It refers to the characteristic that the sum of all shape function values function within the approximation domain is equal to one. This property allows the description of rigid body motions in computational mechanics [23].

- Complex shape function form
  For the construction of the meshless shape functions, the computation of the matrix $\mathbf{A}^{-1}$ is required. Hence, the needed computational time is much larger in comparison to the construction of the polynomial shape functions in FEM [47]. The MLS shape functions are rational polynomial functions. This often leads to a more demanding numerical integration procedures in meshless methods based on the weak form of equations.

- Robustness
  The MLS scheme achieves the reasonable accuracy of the approximation using randomly scattered data points if the parameters that influence the quality of the

approximation are chosen correctly. This parameters include the size of the approximation domain and the shape parameters associated with the chosen weight function. For this reason, the parametric analyses of the accuracy of the solution depending on the mentioned parameters are often initially performed. Also, different methods for defining the optimal size of the approximation domain are available in the literature [168, 176].

4.1.3. Derivative calculations of MLS approximation

The derivatives of the MLS approximation function needed for the numerical solving of the problems can be calculated in two different manners. The first one is the classical approach, which is based on the direct differentiation of the approximation function $f^{(h)}$, while the second one is proposed by Belytschko and Fleming [172] and is based on the introduction of the auxiliary vector $\boldsymbol{\gamma}(\mathbf{x})$ and solving of the system of equations. The application of both manners produces exactly the same derivatives of the approximation functions, but the second one is computationally faster and more efficient. Thus, in the numerical methods presented in this Thesis, the latter manner of derivative calculation is utilized. In this subsection, the most important relations for the calculation of derivatives for both manners are presented.

The direct differentiation of the relation (4.11) leads to

$$f_{,i}^{(h)}(\mathbf{x}) = \sum_{J=1}^{n} \phi_{J,i}(\mathbf{x}) \hat{f}_J, \tag{4.14}$$

where $\phi_{J,i}$ represents the first-order partial derivative of the shape function for the J_{th} node influencing the approximation at $\mathbf{x}$, which is equal to

$$\phi_{J,i} = \sum_{k=1}^{m} [p_{k,i}(\mathbf{A}^{-1}\mathbf{B})_{kJ} + p_k(\mathbf{A}_{,i}^{-1}\mathbf{B} + \mathbf{A}^{-1}\mathbf{B}_{,i})_{kJ}]. \tag{4.15}$$

In the relation (4.15), the first-order partial derivatives of the inverse moment matrix $\mathbf{A}^{-1}$ appear which are calculated as

$$\mathbf{A}_{,i}^{-1} = -\mathbf{A}^{-1}\mathbf{A}_{,i}\mathbf{A}^{-1} \tag{4.16}$$

The second-order partial derivatives of the MLS approximation function $\phi_{J,ij}$ are calculated by differentiation of (4.14) and can be written

$$\begin{aligned} \phi_{J,ij} = \sum_{k=1}^{m} [& p_{k,ij}(\mathbf{A}^{-1}\mathbf{B})_{kJ} + p_{k,i}(\mathbf{A}_{,j}^{-1}\mathbf{B} + \mathbf{A}^{-1}\mathbf{B}_{,j})_{kJ} + \\ & p_{k,j}(\mathbf{A}_{,i}^{-1}\mathbf{B} + \mathbf{A}^{-1}\mathbf{B}_{,i})_{kJ} + p_k(\mathbf{A}_{,ij}^{-1}\mathbf{B} + \mathbf{A}_{,i}^{-1}\mathbf{B}_{,j} + \\ & \mathbf{A}_{,j}^{-1}\mathbf{B}_{,i} + \mathbf{A}^{-1}\mathbf{B}_{,ij})_{kJ}], \end{aligned} \tag{4.17}$$

where the second-order derivatives of the inverse moment matrix are equal to

$$\begin{aligned}\mathbf{A}^{-1}_{,ij} = \mathbf{A}^{-1}\mathbf{A}_{,j}\mathbf{A}^{-1}\mathbf{A}_{,i}\mathbf{A}^{-1} - \mathbf{A}^{-1}\mathbf{A}_{,ij}\mathbf{A}^{-1} + \\ \mathbf{A}^{-1}\mathbf{A}_{,i}\mathbf{A}^{-1}\mathbf{A}_{,j}\mathbf{A}^{-1}.\end{aligned} \tag{4.18}$$

The more efficient way of calculating the derivatives is based on the rewriting of the equation (4.12) in the form

$$\phi_J(\mathbf{x}) = \mathbf{p}(\mathbf{x})\mathbf{A}^{-1}(\mathbf{x})\mathbf{B}_J(\mathbf{x}) = \boldsymbol{\gamma}(\mathbf{x})\mathbf{B}_J(\mathbf{x}), \tag{4.19}$$

where $\mathbf{B}_J(\mathbf{x})$ denotes the J^{th} column of the matrix $\mathbf{B}(\mathbf{x})$ which is associated with the J^{th} node within the approximation domain Ω_{x}. In the relation (4.19), $\boldsymbol{\gamma}(\mathbf{x})$ represents the auxiliary vector which is obtained from solving of the system of algebraic equations

$$\mathbf{A}(\mathbf{x})\boldsymbol{\gamma}(\mathbf{x}) = \mathbf{p}(\mathbf{x}). \tag{4.20}$$

Since the vector $\boldsymbol{\gamma}(\mathbf{x})$ can be determined from the above system of equation by simple LU-decomposition, this approach is computationally more efficient. Hence, there is no need for the calculation of the inverse moment matrix. The derivatives of the shape function are determined by further differentiation of the relation (4.19) which leads to

$$\phi_{J,i}(\mathbf{x}) = \boldsymbol{\gamma}_{,i}(\mathbf{x})\mathbf{B}_J(\mathbf{x}) + \boldsymbol{\gamma}(\mathbf{x})\mathbf{B}_{J,i}(\mathbf{x}), \tag{4.21}$$

$$\begin{aligned}\phi_{J,ij}(\mathbf{x}) = \boldsymbol{\gamma}_{,ij}(\mathbf{x})\mathbf{B}_J(\mathbf{x}) + \boldsymbol{\gamma}_{,i}(\mathbf{x})\mathbf{B}_{J,j}(\mathbf{x}) + \\ \boldsymbol{\gamma}_{,j}(\mathbf{x})\mathbf{B}_{J,i}(\mathbf{x}) + \boldsymbol{\gamma}(\mathbf{x})\mathbf{B}_{J,ij}(\mathbf{x}).\end{aligned} \tag{4.22}$$

As obvious, the derivatives of the auxiliary vector $\boldsymbol{\gamma}(\mathbf{x})$ also appear in the equations (4.21) and (4.22). They are calculated after $\boldsymbol{\gamma}(\mathbf{x})$ is determined as the solution of the system of equations given by (4.20) using following relations

$$\mathbf{A}(\mathbf{x})\boldsymbol{\gamma}_{,i}(\mathbf{x}) = \mathbf{p}_{,i}(\mathbf{x}) - \mathbf{A}_{,i}(\mathbf{x})\boldsymbol{\gamma}(\mathbf{x}), \tag{4.23}$$

$$\begin{aligned}\mathbf{A}(\mathbf{x})\boldsymbol{\gamma}_{,ij}(\mathbf{x}) = \mathbf{p}_{,ij}(\mathbf{x}) - \mathbf{A}_{,ij}(\mathbf{x})\boldsymbol{\gamma}(\mathbf{x}) - \\ \mathbf{A}_{,i}(\mathbf{x})\boldsymbol{\gamma}_{,j}(\mathbf{x}) - \mathbf{A}_{,j}(\mathbf{x})\boldsymbol{\gamma}_{,i}(\mathbf{x})\end{aligned} \tag{4.24}$$

Now, the values of the shape functions $\phi_J(\mathbf{x})$ and its derivatives $\phi_{J,i}(\mathbf{x})$ and $\phi_{J,ij}(\mathbf{x})$ are determined by substituting the solutions of the system of equations given by (4.20), (4.23) and (4.24) into equations (4.19), (4.21) and (4.22)

4.1.4. Interpolatory MLS approximation with regularized weight function

The MLS approximation function constructed using the weight function according to (4.13) does not possess the Kronecker delta property. In other words, they do not

interpolate the nodal values [177], which makes the imposition of the essential boundary conditions more difficult. This leads to the use of additional numerical procedures for enforcing of the necessary boundary conditions.

However, there are different approaches with which the interpolation property of the MLS approximation can be achieved. The first of them is referred to as the kinematic transformation procedure [47], wherein the values of the approximated functions at the nodes have a predefined value. In this approach a system of equations for all the nodes in the numerical model is obtained. This system needs to be solved in order to determine the fictitious nodal values as a function of the interpolated nodal values. However, this often results in the approximation function with bad properties. It can be proven that the condition number of the coefficient matrix of the approximation system of equations gets worse as the number of degrees of freedom in the numerical model increases [178]. Another simple and efficient approach that results in the interpolation properties of approximation functions at the nodes is the application of the regularized weight functions according to [106] in the form

$$W_{\mathrm{R}J}(\mathbf{x}) = \frac{\tilde{w}_{\mathrm{R}J}(\mathbf{x})}{\sum\limits_{I=1}^{n} \tilde{w}_{\mathrm{R}I}(\mathbf{x})}, \tag{4.25}$$

where $\tilde{w}_{\mathrm{R}J}(\mathbf{x})$ is equal to

$$\tilde{w}_{\mathrm{R}J}(\mathbf{x}) = \frac{\left(\left(\frac{d_J}{r_{\mathrm{s}J}}\right)^q + \varepsilon\right)^{-2} - (1+\varepsilon)^{-2}}{\varepsilon^{-2} - (1+\varepsilon)^{-2}}. \tag{4.26}$$

In the equation (4.25), n denotes the number of nodes within the approximation domain Ω_{x}, q represents the arbitrary parameter of the regularized weight function, while ε is the regularization parameter of the considered function. In (4.25), the values of parameters q and ε influence the layout of the weight function and need to be chosen so as to ensure the Kronecker delta condition of the MLS shape function with high accuracy [122]. In this dissertation, for the calculation of the numerical examples values of parameters $q = 4$ and $\varepsilon = 10^{-5}$ are used. In the literature, the weighting function $\tilde{w}_{\mathrm{R}J}(\mathbf{x})$ is often substituted with $W_{\mathrm{R}J}(\mathbf{x})$ to reduce the calculation time. By using any of these weight functions, the same MLS shape functions are obtained. Furthermore, the first- and second-order derivatives of the weight function (4.25) are not equal zero at the boundary of the support domain and have only C^0 continuity. Given that in the numerical solution process high-order of derivatives are often needed, the sufficient continuity of the approximation function is achieved my multiplying the regularized weight function (4.25) with some standard function that possesses a higher-order of continuity [122]. Herein, this is achieved

by multiplying the fourth-order spline function (4.13) and the regularized function (4.26)

$$W_J(\mathbf{x}) = \begin{cases} w_{\mathrm{S}J}(\mathbf{x})\tilde{w}_{\mathrm{R}J}(\mathbf{x}) & 0 \leq d_J \leq r_{\mathrm{s}J} \\ 0 & d_J > r_{\mathrm{s}J} \end{cases} . \tag{4.27}$$

By utilizing the weight function according to (4.27), the constructed MLS function possesses the interpolation properties at the nodes, which ensures easier imposition of the essential boundary conditions using numerical procedures analogous to FEM.

4.2. Radial point interpolation method (RPIM)

As the name implies, in the Radial Point Interpolation Method (RPIM) the approximation is constructed by letting the function pass through the function values at all of the nodes positioned within the defined domain of approximation [22]. Herein, it is considered as an alternative approximation to MLS. Furthermore, meshless methods that employ the Radial Basis Functions (RBF) have some clear advantages in comparison to other meshless methods due to numerically simpler construction of interpolatory approximation functions [179]. Traditional RBFs that use global domain approximation yield fully-populated matrices [180], which is a big limitation to their wider engineering application. Therefore, in this dissertation, efficient RPIM [107] is utilized for the approximation, which uses RBFs in a locally supported domains, so that the obtained system of equations is sparse, which decreases required computational effort. Within the RPIM, the polynomials are added into the basis in order to ensure the consistency of the shape functions. As stated in [22], adding polynomial terms can also attribute to the accuracy of the numerical solution. Hence, in this section the construction of the used RPIM function with polynomial reproduction is explained. Since the approximation is highly dependent on the choice of RBF, an overview of the most common functions is given. A more detailed description for the utilized Gaussian RBF is also presented. Furthermore, the main properties and features associated with this type of approximation are mentioned. At the end of the section, the calculation of derivatives of the RPIM functions is discussed.

4.2.1. Radial Basis Functions

The Radial Basis Functions (RBF) are the most important part of the considered approximation since they ensure the non-singularity of the moment approximation matrix [181]. To the present day, within the mathematical community a large number of different forms of RBFs have been utilized. Newer forms [182] are often derived from the classical (conventional) ones [22]. The classical forms have been widely tested and applied to

problems of surface fitting [183, 184] and for the construction of approximate solutions for PDEs [185, 186]. As some of the most popular RBFs used for the approximation of the field variables, the Gaussian function (EXP) [187], the Multi-quadrics (MQ) function [188] and the Thin Plate Spline function (TPS) [189] can be mentioned. These RBFs with the dimensionless shape parameters [190] are given in the Table 4.1. A more detailed classification and characteristics of the most commonly used RBFs can be found in [191].

Table 4.1: RBFs with dimensionless shape parameters

Radial Basis Functions	**Mathematical definition**	**Shape parameters**
Gaussian	$R_J(\mathbf{x}) = \exp\big[-\alpha_c\big(\frac{r_J}{d_c}\big)^2\big]$	α_c
Multi-quadrics	$R_J(\mathbf{x}) = \big(r_J^2 + (\alpha_c d_c)^2\big)^{q_q}$	α_q , q_q
Thin plate spline	$R_J(\mathbf{x}) = r_J^\eta$	η

Depending on the RBF chosen for the approximation, several shape parameters of the function need to be chosen in advance. In general, these parameters are often obtained by numerical examinations. Fine tuning of the shape parameters can result in more accurate and better performance of the meshless method. In this dissertation, the 2-D Gaussian RBF

$$R_J(x,y) = \exp\big[-\alpha_c\big(\frac{r_J}{d_c}\big)^2\big]. \tag{4.28}$$

is considered for numerical computations. In the equation (4.28), d_c is an average nodal spacing calculated using all nodes within the local domain of approximation, while r_J denotes the radial distance of the node to the other nodes that influence the approximation. The function uses only one shape parameter α_c that needs to be determined. The detailed investigations of this parameter are done using appropriate numerical examples in the next chapter.

4.2.2. Construction of RPIM function

By using n nodes within the approximation domain RPIM with the included polynomial basis functions approximates a field variable in the form

$$f^{(h)}(\mathbf{x}) = \sum_{J=1}^{n} R_J(\mathbf{x})a_J + \sum_{H=1}^{m} p_H(\mathbf{x})b_H = \mathbf{R}^{\mathrm{T}}(\mathbf{x})\mathbf{a} + \mathbf{p}^{\mathrm{T}}(\mathbf{x})\mathbf{b}, \tag{4.29}$$

where $R_J(\mathbf{x})$ is the chosen RBF, n is the total number of nodes that influence the approximation at $\mathbf{x}$, $p_H(\mathbf{x})$ are the monomials, m is the number of polynomial basis functions. The unknown coefficients, a_J and b_H, are determined by enforcing that the interpolation

passes through n nodes within the approximation domain. In doing so, often the minimal number of monomials in the basis is required, and more terms in the radial basis ($m < n$) are utilized in order to obtain better stability of the approximation. As obvious, here the unknown coefficients are not functions of the point of interest $\mathbf{x}$ as is the case in the MLS approximation. The interpolation equations for n nodes within the approximation domain can be presented in the matrix form as

$$\hat{\mathbf{f}} = \mathbf{R}_0\mathbf{a} + \mathbf{P}_\mathrm{m}\mathbf{b}, \tag{4.30}$$

where $\hat{\mathbf{f}}$ denotes the vector comprised of all the field nodal values within the approximation domain, while $\mathbf{R}_0$ and $\mathbf{P}_\mathrm{m}$ represent the moment matrices of the approximation corresponding to the radial basis and the polynomial functions, respectively. According to [192], an additional constraint condition of the polynomials should be satisfied. This constraint guarantees the uniqueness of the approximation [193] and is written as

$$\mathbf{P}_\mathrm{m}^\mathrm{T}\mathbf{a} = \mathbf{0}. \tag{4.31}$$

Equations (4.30) and (4.31) can be combined to obtain the system of equations

$$\begin{bmatrix} \mathbf{R}_0 & \mathbf{P}_\mathrm{m} \\ \mathbf{P}_\mathrm{m}^\mathrm{T} & \mathbf{0} \end{bmatrix} \begin{bmatrix} \mathbf{a} \\ \mathbf{b} \end{bmatrix} = \begin{bmatrix} \hat{\mathbf{f}} \\ \mathbf{0} \end{bmatrix}. \tag{4.32}$$

The coefficient matrix on the left hand side of the above system of equations is often referred to only as

$$\mathbf{G} = \begin{bmatrix} \mathbf{R}_0 & \mathbf{P}_\mathrm{m} \\ \mathbf{P}_\mathrm{m}^\mathrm{T} & \mathbf{0} \end{bmatrix}. \tag{4.33}$$

Herein, the moment matrices $\mathbf{P}_\mathrm{m}$ and $\mathbf{R}_0$ are equal to

$$\mathbf{P}_\mathrm{m} = \begin{bmatrix} P_1(\mathbf{x}_1) & P_2(\mathbf{x}_1) & \cdots & P_m(\mathbf{x}_1) \\ P_1(\mathbf{x}_2) & P_2(\mathbf{x}_2) & \cdots & P_m(\mathbf{x}_2) \\ \vdots & \vdots & \vdots & \vdots \\ P_1(\mathbf{x}_n) & P_2(\mathbf{x}_n) & \cdots & P_m(\mathbf{x}_n) \end{bmatrix}, \tag{4.34}$$

$$\mathbf{R}_0 = \begin{bmatrix} R_1(r_1) & R_2(r_1) & \cdots & R_n(r_1) \\ R_1(r_2) & R_2(r_2) & \cdots & R_n(r_2) \\ \vdots & \vdots & \vdots & \vdots \\ R_1(r_n) & R_2(r_n) & \cdots & R_n(r_n) \end{bmatrix}. \tag{4.35}$$

In this approximation the value of RBF at the point of interest is dependent on the radial distance from the other nodes within the approximation domain. Thus, this radial distance is usually computed as

$$r_k = \sqrt{(x_k - x_i)^2 + (y_k - y_i)^2}, \tag{4.36}$$

where x_i and y_i denote the coordinates of the point for which the approximation is being constructed, while x_k and y_k are the coordinates of the nodes influencing the approximation at $\mathbf{x}$. Because the $\mathbf{R}_0$ is symmetric, the matrix $\mathbf{G}$ will also be symmetric. Hence, if the inverse of matrix $\mathbf{G}$ exists, the unique solution for the interpolation coefficients can be obtained as simple as

$$\begin{bmatrix} \mathbf{a} \\ \mathbf{b} \end{bmatrix} = \mathbf{G}^{-1} \begin{bmatrix} \hat{\mathbf{f}} \\ \mathbf{0} \end{bmatrix}. \tag{4.37}$$

However, the calculation of the inverse of the matrix $\mathbf{G}$ in every approximation domain can be computationally burdensome. Hence, the equations for determination of the unknown coefficient vectors $\mathbf{a}$ and $\mathbf{b}$ can be rearranged into a slightly different but more efficient procedure. Since, the moment matrix $\mathbf{R}_0$ is a non-singular matrix, from the equation (4.30), the vector $\mathbf{a}$ can be expressed as

$$\mathbf{a} = \mathbf{R}_0^{-1}\hat{\mathbf{f}} - \mathbf{R}_0^{-1}\mathbf{P}_\mathrm{m}\mathbf{b}. \tag{4.38}$$

Now, if the equation (4.38) is substituted into the polynomial constraint equations (4.31) the expression for the vector $\mathbf{b}$ follows

$$\mathbf{b} = \mathbf{S}_\mathrm{b}\hat{\mathbf{f}}, \tag{4.39}$$

where $\mathbf{S}_\mathrm{b}$ represent the auxiliary matrix of the RPIM approximation associated with the vector $\mathbf{b}$, computed as

$$\mathbf{S}_\mathrm{b} = [\mathbf{P}_\mathrm{m}^\mathrm{T}\mathbf{R}_0^{-1}\mathbf{P}_\mathrm{m}]\mathbf{P}_\mathrm{m}^\mathrm{T}\mathbf{R}_0^{-1}. \tag{4.40}$$

It should be stresses that $\mathbf{P}_\mathrm{m}^\mathrm{T}\mathbf{R}_0^{-1}$ in the above relation has to be evaluated only once, which speeds up the numerical computation. Furthermore, if the unknown vector $\mathbf{b}$ (4.39) is now inserted back into relation (4.38), the unknown vector $\mathbf{a}$ is now computed as

$$\mathbf{a} = \mathbf{S}_\mathrm{a}\hat{\mathbf{f}}, \tag{4.41}$$

where

$$\mathbf{S}_\mathrm{a} = \mathbf{R}_0^{-1} - \mathbf{R}_0^{-1}\mathbf{P}_\mathrm{m}\mathbf{S}_\mathrm{b}. \tag{4.42}$$

From the analysis of the above expression, it can be observed that $\mathbf{R}_0^{-1}\mathbf{P}_\mathrm{m}$ is easily obtained from transposing $\mathbf{P}_\mathrm{m}^\mathrm{T}\mathbf{R}_0^{-1}$ which has been already computed in (4.39). This feature is also beneficial and further decreases the needed computational time of the approximation. Now, when the vectors $\mathbf{a}$ and $\mathbf{b}$ are known, the RPIM approximation function is written as follows

$$f^{(h)}(\mathbf{x}) = [\mathbf{R}^\mathrm{T}(\mathbf{x})\mathbf{S}_\mathrm{a} + \mathbf{p}^\mathrm{T}(\mathbf{x})\mathbf{S}_\mathrm{b}]\hat{\mathbf{f}}, \tag{4.43}$$

where the expression in the brackets denotes the vector of shape functions

$$\boldsymbol{\Phi}(\mathbf{x}) = \mathbf{R}^\mathrm{T}(\mathbf{x})\mathbf{S}_\mathrm{a} + \mathbf{p}^\mathrm{T}(\mathbf{x})\mathbf{S}_\mathrm{b}. \tag{4.44}$$

In the above equation, the terms in vector $\mathbf{\Phi}(\mathbf{x})$ denote the shape function values associated with nodes influencing the approximation equal to

$$\Phi_J(\mathbf{x}) = \sum_{J=1}^{n} R_J(\mathbf{x}) S_{\mathrm{a}J} + \sum_{H=1}^{m} p_H(\mathbf{x}) S_{\mathrm{b}H}. \tag{4.45}$$

It is easily observed that the auxiliary matrices $\mathbf{S}_\mathrm{a}$ and $\mathbf{S}_\mathrm{b}$ are constant matrices for the given locations of the n nodes within the approximation domain. Hence, as long the same nodes within the approximation domain are utilized these matrices do not change, which is of great significance in the derivative calculations. Finally, the constructed RPIM function defined by (4.43) passes through all of the nodal values at $\mathbf{x}_J$ within the approximation domain. In addition, it can be observed that at every node, the equation $f^{(h)}(\mathbf{x}_J) = \hat{f}_J$ can be written. Thus, the function possesses the interpolation properties at the nodes, as well as the Kronecker delta property. The interpolatory charachter of the RPIM function is depicted in Figure 4.3 using simple one-dimensional approximation example.

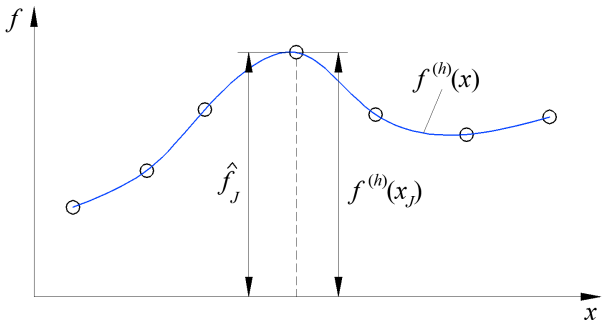

Figure 4.3: Interpolating property of the RPIM approximation function

4.2.3. Properties and features of RPIM function

The main characteristics of the RPIM approximation are presented in this subsection. Some of the properties and features of this type of approximation are:

- Delta function property

  All of the shape functions based on the PIM approximation schemes posses the Kronecker delta property which can be easily proven [22].

- Reproducibility

  The approximation augmented with polynomial terms can exactly reproduce the order of the polynomials comprised in the basis.

- Partition of unity

  RPIM shape functions have the partition of unity property if the linear polynomial terms are added in the basis. The feature is easily shown if the reproduction properties of the function are utilized [23].

- Compactness
  The shape functions are constructed using only a finite number of nodes within the local approximation domain. Thus, the functions are compactly supported.

- Continuity
  The RPIM function usually have higher-order continuity than most meshless approximations due to a high-order of the utilized RBFs.

- Compatibility
  It is possible that the compatibility of the functions in the entire global domain is not ensured if the RPIM approximation is constructed using the local approximation domain concept. Furthermore, the approximated field functions could be discontinuous when resolving problems where nodes frequently enter or leave the moving support domains.

4.2.4. Derivative calculations of RPIM functions

In this subsection main relations for computing the derivatives of the RPIM shape functions are presented. The derivatives of RPIM functions with polynomial reproduction are performed in a simple and straightforward manner due the auxiliary matrices $\mathbf{S}_\mathrm{a}$ and $\mathbf{S}_\mathrm{b}$ being constant. Thus, by the direct differentiation of the RPIM shape function (4.45), the first-order

$$\Phi_{J,i}(\mathbf{x}) = \sum_{J=1}^{n} R_{J,i}(\mathbf{x}) S_{\mathrm{a}J} + \sum_{H=1}^{m} p_{H,i}(\mathbf{x}) S_{\mathrm{b}H}, \tag{4.46}$$

and the second-order derivative

$$\Phi_{J,ij}(\mathbf{x}) = \sum_{J=1}^{n} R_{J,ij}(\mathbf{x}) S_{\mathrm{a}J} + \sum_{H=1}^{m} p_{H,ij}(\mathbf{x}) S_{\mathrm{b}H}, \tag{4.47}$$

of the shape functions are obtained. As obvious, the first-order derivatives of radial basis $R_{J,i}(\mathbf{x})$ and polynomial basis $p_{J,i}(\mathbf{x})$ functions are needed for computing the first-order derivative of the shape function (4.46). Herein, the derivatives of the polynomial terms are easy to obtain while the first-order derivatives of the utilized Gaussian RBF are computed as

$$R_{J,x}(x,y) = -\frac{2\alpha_\mathrm{c}}{d_\mathrm{c}^2} R_J(x,y)(x - x_J), \tag{4.48}$$

$$R_{J,y}(x,y) = -\frac{2\alpha_\mathrm{c}}{d_\mathrm{c}^2} R_J(x,y)(x - x_J). \tag{4.49}$$

Furthermore, to compute the second-order derivative of the shape function (4.47), the second-order derivatives of the radial $R_{J,ij}(\mathbf{x})$ and the polynomial part $p_{J,ij}(\mathbf{x})$ of the

approximation need to be utilized. For that purpose, the second-order derivatives of the Gaussian RBF are given by

$$R_{J,xx}(x,y) = \big[-2\big(\frac{\alpha_c}{d_c^2}\big) + 4\big(\frac{\alpha_c}{d_c^2}\big)^2 (x - x_J)\big] R_J(x,y), \tag{4.50}$$

$$R_{J,yy}(x,y) = \big[-2\big(\frac{\alpha_c}{d_c^2}\big) + 4\big(\frac{\alpha_c}{d_c^2}\big)^2 (y - y_J)\big] R_J(x,y), \tag{4.51}$$

$$R_{J,xy}(x,y) = 4\big(\frac{\alpha_c}{d_c^2}\big)^2 R_J(x,y)(x - x_J)(y - y_J). \tag{4.52}$$

5 Meshless modeling of heterogeneous materials using classical linear elasticity

For solving the boundary value problem of the heterogeneous materials using classical linear elasticity two different collocation methods are considered. The heterogeneous material is here composed of two different homogeneous isotropic materials with linear elastic properties. Both methods are based on the local MLPG concept. The methods applied can be denoted as the Meshless Local Petrov Galerkin collocation method (MLPG2) [194], which uses the IMLS function [195], and the Radial Point Interpolation Collocation Method (RPICM) [196] with RPIM [197] for the approximation of the unknown field variables. Furthermore, two different approaches, a fully-displacement (primal) [27] and a mixed [71], of each method have been utilized. Hence, this chapter is dedicated to meshless modeling of material discontinuity using collocation methods. Firstly, the governing equations and boundary conditions for the heterogeneous structure are presented. Secondly, the discretization of the heterogeneous structure is explained. Also, the discretized forms of equilibrium equations and the boundary conditions for the primal, and the mixed approach are derived. Since the collocation methods are utilized, the numerical integration is avoided so the system of discretized equations is obtained in a quick and straightforward manner. In the primal approach, for the unknown field variables, two components of displacements are considered, while in the mixed approach two components of displacements and three components of stresses are utilized. All field variables are approximated using same meshless functions, which are constructed independently for each homogeneous material. Since the applied approximations possess the interpolatory property at the nodes, the essential (displacement) boundary conditions are imposed using a simple procedure analogous to classical FEM. The natural (traction) boundary conditions are enforced at the discretization nodes using the direct collocation method. At the nodes representing the interface boundary between two homogeneous materials the displacement continuity and traction reciprocity are enforced in order to obtain the

unique solution for the entire heterogeneous structure. In both the primal and the mixed approach the final system of discretized equations has only nodal displacements as unknowns. At the end of the chapter, the numerical efficiency and accuracy of the applied collocation methods are closely examined in a several numerical examples.

5.1. Governing equations and boundary conditions

For the purpose of deriving the discretized system of governing equations for the material discontinuity problem, a 2-D heterogeneous structure which occupies the global computational domain Ω ($\Omega = \Omega^+ \cup \Omega^-$) bounded by the global outer boundary Γ ($\Gamma = \Gamma^+ \cup \Gamma^-$) is considered, as shown in Figure 5.1. The boundary Γ_s represents the interface between two homogeneous isotropic materials Ω^+ and Ω^- with different linear elastic material properties, while $\mathbf{n}^+$ and $\mathbf{n}^-$ denote unit outward normal vectors on outer boundaries, Γ^+ and Γ^-, and on the interface boundary Γ_s.

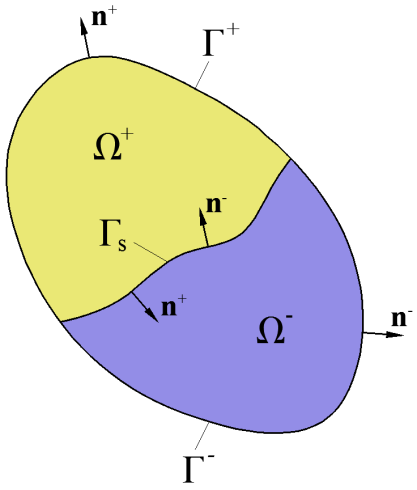

Figure 5.1: Heterogeneous structure consisting of two homogeneous materials

For the stationarity state of the two dimensional solid heterogeneous structure depicted in Figure 5.1, a strong form of elasto-static governing equations (2.15) can be written for each homogeneous material separately

$$\sigma^+_{ij,j} + b^+_i = 0, \quad \text{within } \Omega^+, \tag{5.1}$$

$$\sigma^-_{ij,j} + b^-_i = 0, \quad \text{within } \Omega^-. \tag{5.2}$$

In the equilibrium equations above, σ^+_{ij} and σ^-_{ij} are the Cauchy stress tensors, while b^+_i and b^-_i denote body forces for each homogeneous domain, Ω^+ and Ω^-, respectively.

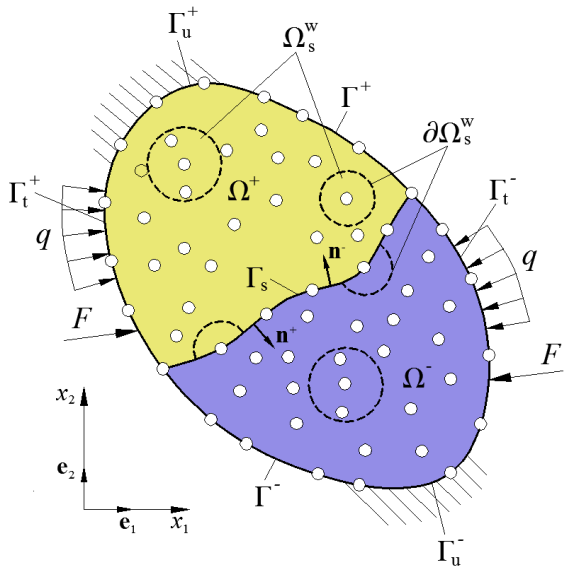

Figure 5.2: Boundary conditions of the discretized heterogeneous structure

On the outer boundaries Ω^+ and Ω^- of the heterogeneous structure, the following displacement and traction boundary conditions have to be satisfied

$$u_i^+ = \bar{u}_i^+, \quad \text{on } \Gamma_u^+, \tag{5.3}$$

$$u_i^- = \bar{u}_i^-, \quad \text{on } \Gamma_u^-, \tag{5.4}$$

$$t_i^+ = \sigma_{ij}^+ n_j^+ = \bar{t}_i^+, \quad \text{on } \Gamma_t^+, \tag{5.5}$$

$$t_i^- = \sigma_{ij}^- n_j^- = \bar{t}_i^-, \quad \text{on } \Gamma_t^-. \tag{5.6}$$

According to Figure 5.2, in the boundary equations (5.3) and (5.4), Γ_u^+ and Γ_u^- represent the parts of boundaries Γ^+ and Γ^- where the displacement conditions are prescribed, while in equations (5.5) and (5.6), Γ_t^+ and Γ_t^- denote the parts where the traction conditions are prescribed. The superposed bar indicates the prescribed values of the displacements and the tractions. In order to obtain the solution for the entire heterogeneous structure, interface conditions on the boundary Γ_s should also be applied. These conditions are needed to ensure the continuity of the displacement field along with the discontinuity (jump) in the displacement derivative field across the interface boundary Γ_s. In this dissertation, this is fulfilled in a simple manner by enforcing equations on Γ_s

$$u_i^+ - u_i^- = 0, \tag{5.7}$$

$$\sigma_{ij}^+ n_j^+ + \sigma_{ij}^- n_j^- = 0. \tag{5.8}$$

5.2. Discretization of the heterogeneous structure

The discretization of the global computational domain Ω is performed by two different sets of nodes $S^+ = \{\mathbf{x}_I, I = 1, 2, ..., N : \mathbf{x}_I \subseteq \Omega^+ \cup \Gamma^+ \cup \Gamma_s\}$ and $S^- = \{\mathbf{x}_M, M = 1, 2, ..., P : \mathbf{x}_M \subseteq \Omega^- \cup \Gamma^- \cup \Gamma_s\}$, where N and P indicate the total number of nodes within homogeneous materials Ω^+ and Ω^-, respectively. Furthermore, the discretization of the interface boundary Γ_s is achieved by using the overlapping nodes belonging to different homogeneous materials. According to the MLPG concept [28], a small domain of circular shape called a local subdomain, denoted as Ω_s^w, is defined around each discretization node $\mathbf{x} \in S^+ \cup S^-$. The local subdomain for the nodes positioned on the interface boundary Γ_s is truncated on either side of the interface, as seen in Figure 5.2. In that manner, the discretization nodes in the material Ω^+ can only be influenced by the nodes contained in that material. The same applies for the discretization nodes belonging to the material Ω^-. If the well-known weighted residual approach [27] is employed over each local subdomain Ω_s^w, a local weak form of equilibrium equations (5.1) and (5.2) may be expressed as

$$\int_{\Omega_s^w} w^+(\sigma_{ij,j}^+ + b_i^+)\mathrm{d}\Omega = 0, \quad I = 1, 2, ..., N, \quad \text{within } \Omega^+, \tag{5.9}$$

$$\int_{\Omega_s^w} w^-(\sigma_{ij,j}^- + b_i^-)\mathrm{d}\Omega = 0, \quad M = 1, 2, ..., P, \quad \text{within } \Omega^-. \tag{5.10}$$

In the obtained local weak forms, w^+ and w^- denote arbitrary chosen kinematically admissible test functions. In agreement with the collocation strategy [198], for each homogeneous material the Dirac delta functions

$$w^+ = \delta(\mathbf{x} - \mathbf{x}_I), \quad I = 1, 2, ..., N, \quad \text{within } \Omega^+, \tag{5.11}$$

$$w^- = \delta(\mathbf{x} - \mathbf{x}_M), \quad M = 1, 2, ..., P, \quad \text{within } \Omega^-, \tag{5.12}$$

are chosen as the test functions for each discretization node. By using these test functions, integral equations (5.9) and (5.10) are transferred to the strong form equilibrium equations at the discretization nodes

$$\sigma_{ij,j}^+(\mathbf{x}_I) + b_i^+(\mathbf{x}_I) = 0, \quad \text{within } \Omega^+, \tag{5.13}$$

$$\sigma_{ij,j}^-(\mathbf{x}_M) + b_i^-(\mathbf{x}_M) = 0, \quad \text{within } \Omega^-. \tag{5.14}$$

For the discretization of the boundary conditions relations (5.3) - (5.8), the analogous procedure as for the equilibrium equations can be applied. In the primal approach, only the displacement components are considered as the unknown field variables, while in the mixed approach, like the one proposed in [71], the displacement and stress components are chosen as the unknown field variables. All unknown field variables are approximated

separately within the homogeneous materials Ω^+ and Ω^-, on the outer boundaries and on the interface boundary, using the same approximation functions for all variables. Hence, for the homogeneous material Ω^+, and the boundaries Γ_{u}^+, Γ_{t}^+ and Γ_{s}^+, it can be written

$$u_i^{+(h)}(\mathbf{x}) = \sum_{J=1}^{N_{\Omega_\mathrm{s}}} \phi_J^+(\mathbf{x})(\hat{u}_i^+)_J, \tag{5.15}$$

$$\sigma_{ij}^{+(h)}(\mathbf{x}) = \sum_{J=1}^{N_{\Omega_\mathrm{s}}} \phi_J^+(\mathbf{x})(\hat{\sigma}_{ij}^+)_J, \tag{5.16}$$

where ϕ_J represents the nodal value of the two-dimensional shape function for node J, N_{Ω_s} stands for the number of nodes within the approximation domain, while $(\hat{u}_i^+)_J$ and $(\hat{\sigma}_{ij}^+)_J$ denote the nodal values of displacement and stress components. The approximation functions are derived over the trial function subdomain Ω_s. The displacement and stress components are analogously approximated over the material domain Ω^-. It is important to note that in this dissertation, the same nodes are used for both the displacement and the stress approximations.

5.3. Collocation method based on the primal approach

Firstly, the discretized equations of the fully-displacement (primal) meshless approach are presented. Herein, only the approximation of the displacement components is utilized. In the process of computing the discretized system of equations, different types of nodes are distinguished. At the nodes inside homogeneous constituents, e.g. nodes inside Ω^+ and Ω^-, the strong forms of the equilibrium equations are used, while on the outer boundaries, Γ^+ and Γ^-, and on the interface boundary Γ_s the corresponding boundary conditions are utilized. Thus, in this section the discretized equations for the primal meshless approach are derived and explained.

5.3.1. Discretized equilibrium equations of the primal approach

In the fully-displacement solution strategy, for the nodes positioned inside the domains Ω^+ and Ω^-, the stress components in strong form equilibrium equations (5.13) and (5.14) are firstly rewritten using constitutive equation (2.11), leading to

$$\mathbf{D}_\mathrm{K}^{+\mathrm{T}}\mathbf{D}^+\boldsymbol{\varepsilon}^+(\mathbf{x}_I) + \mathbf{b}^+(\mathbf{x}_I) = \mathbf{0}, \tag{5.17}$$

$$\mathbf{D}_\mathrm{K}^{-\mathrm{T}}\mathbf{D}^-\boldsymbol{\varepsilon}^-(\mathbf{x}_M) + \mathbf{b}^-(\mathbf{x}_M) = \mathbf{0}, \tag{5.18}$$

where $\mathbf{D}^+$ and $\mathbf{D}^-$ represent material tensors for each homogeneous material, while $\mathbf{D}_\mathrm{K}^+$ and $\mathbf{D}_\mathrm{K}^-$ denote 2-D kinematic differential operators consisting of the first-order derivatives

with respect to the Cartesian coordinates, defined as

$$\mathbf{D}_{\mathrm{K}}^{+} = \begin{bmatrix} \dfrac{\partial(\ )^{+}}{\partial x_1} & 0 \\ 0 & \dfrac{\partial(\ )^{+}}{\partial x_2} \\ \dfrac{\partial(\ )^{+}}{\partial x_2} & \dfrac{\partial(\ )^{+}}{\partial x_1} \end{bmatrix}, \tag{5.19}$$

$$\mathbf{D}_{\mathrm{K}}^{-} = \begin{bmatrix} \dfrac{\partial(\ )^{-}}{\partial x_1} & 0 \\ 0 & \dfrac{\partial(\ )^{-}}{\partial x_2} \\ \dfrac{\partial(\ )^{-}}{\partial x_2} & \dfrac{\partial(\ )^{-}}{\partial x_1} \end{bmatrix}. \tag{5.20}$$

Furthermore, in the equations (5.17) and (5.18), $\boldsymbol{\varepsilon}^{+}$ and $\boldsymbol{\varepsilon}^{-}$ are the strain vectors, while $\mathbf{b}^{+}$ and $\mathbf{b}^{-}$ are the vectors of body forces for the domains Ω^{+} and Ω^{-}, respectively. The kinematic relations (2.4) are also introduced into equations (5.17) and (5.18), so they are written as

$$\mathbf{D}_{\mathrm{K}}^{+\mathrm{T}}\mathbf{D}^{+}\mathbf{D}_{\mathrm{K}}^{+}\mathbf{u}^{+}(\mathbf{x}_I) + \mathbf{b}^{+}(\mathbf{x}_I) = \mathbf{0}, \tag{5.21}$$

$$\mathbf{D}_{\mathrm{K}}^{-\mathrm{T}}\mathbf{D}^{-}\mathbf{D}_{\mathrm{K}}^{-}\mathbf{u}^{-}(\mathbf{x}_M) + \mathbf{b}^{-}(\mathbf{x}_M) = \mathbf{0}, \tag{5.22}$$

where $\mathbf{u}^{+}$ and $\mathbf{u}^{-}$ denote the displacement vectors. If equations (5.21) and (5.22) are discretized by the displacement approximation (5.15), we obtain

$$\mathbf{D}_{\mathrm{K}}^{+\mathrm{T}}\mathbf{D}^{+}\sum_{J=1}^{N_{\Omega_{\mathrm{s}}}}\mathbf{B}_J^{+}(\mathbf{x}_I)\hat{\mathbf{u}}_J^{+} + \mathbf{b}^{+}(\mathbf{x}_I) = \mathbf{0}, \tag{5.23}$$

$$\mathbf{D}_{\mathrm{K}}^{-\mathrm{T}}\mathbf{D}^{-}\sum_{J=1}^{N_{\Omega_{\mathrm{s}}}}\mathbf{B}_J^{-}(\mathbf{x}_M)\hat{\mathbf{u}}_J^{-} + \mathbf{b}^{-}(\mathbf{x}_M) = \mathbf{0}. \tag{5.24}$$

Herein, $\mathbf{B}_J^{+}(\mathbf{x}_I) = \mathbf{B}_{IJ}^{+}$ and $\mathbf{B}_J^{-}(\mathbf{x}_M) = \mathbf{B}_{MJ}^{-}$ are the matrices composed of the first-order spatial derivatives of the shape function for the J^{th} node influencing the approximation at node I or node M, respectively. Thus, the matrices $\mathbf{B}_{IJ}^{+}$ and $\mathbf{B}_{MJ}^{-}$ are defined as

$$\mathbf{B}_{IJ}^{+} = \begin{bmatrix} \dfrac{\partial\phi_J^{+}}{\partial x_1}(\mathbf{x}_I) & 0 \\ 0 & \dfrac{\partial\phi_J^{+}}{\partial x_2}(\mathbf{x}_I) \\ \dfrac{\partial\phi_J^{+}}{\partial x_2}(\mathbf{x}_I) & \dfrac{\partial\phi_J^{+}}{\partial x_1}(\mathbf{x}_I) \end{bmatrix}, \tag{5.25}$$

$$\mathbf{B}_{MJ}^{-} = \begin{bmatrix} \dfrac{\partial \phi_J^-}{\partial x_1}(\mathbf{x}_M) & 0 \\ 0 & \dfrac{\partial \phi_J^-}{\partial x_2}(\mathbf{x}_M) \\ \dfrac{\partial \phi_J^-}{\partial x_2}(\mathbf{x}_M) & \dfrac{\partial \phi_J^-}{\partial x_1}(\mathbf{x}_M) \end{bmatrix}. \tag{5.26}$$

Relations (5.23) and (5.24) represent linear algebraic equations with nodal displacement as unknowns, which can be simply written in a classical way as

$$\mathbf{K}_{IJ}^{+}\hat{\mathbf{u}}_J^{+} = \mathbf{R}_I^{+}, \quad I = 1, 2, ..., N, \tag{5.27}$$

$$\mathbf{K}_{MJ}^{-}\hat{\mathbf{u}}_J^{-} = \mathbf{R}_M^{-}, \quad M = 1, 2, ..., P. \tag{5.28}$$

In the above equations, the nodal stiffness matrices $\mathbf{K}_{IJ}^{+}$ and $\mathbf{K}_{MJ}^{-}$ are expressed as

$$\mathbf{K}_{IJ}^{+} = \mathbf{D}_{\mathrm{K}}^{+\mathrm{T}}\mathbf{D}^{+}\sum_{J=1}^{N_{\Omega_\mathrm{s}}}\mathbf{B}_{IJ}^{+}, \tag{5.29}$$

$$\mathbf{K}_{MJ}^{-} = \mathbf{D}_{\mathrm{K}}^{-\mathrm{T}}\mathbf{D}^{-}\sum_{J=1}^{N_{\Omega_\mathrm{s}}}\mathbf{B}_{MJ}^{-}, \tag{5.30}$$

while the nodal force vectors $\mathbf{R}_I^{+}$ and $\mathbf{R}_M^{-}$ are

$$\mathbf{R}_I^{+} = -\mathbf{b}_I^{+}, \tag{5.31}$$

$$\mathbf{R}_M^{-} = -\mathbf{b}_M^{-}. \tag{5.32}$$

From equations (5.29) and (5.30) it can be easily seen that the second-order derivatives of shape functions need to be calculated in order to assemble nodal stiffness matrices.

5.3.2. Discretized boundary conditions of the primal approach

Since the utilized approximation functions possess the interpolatory property, the displacement boundary conditions (5.3) and (5.4) for the nodes on Γ_u^{+} and Γ_u^{-} are enforced straightforward by using a common procedure, analogous to the one in FEM. Therefore, the discretized displacement boundary conditions can be written simply as

$$\bar{\mathbf{u}}^{+}(\mathbf{x}_I) = \bar{\mathbf{u}}_I^{+} = \sum_{J=1}^{N_{\Omega_\mathrm{s}}}\phi_J^{+}(\mathbf{x}_I)\hat{\mathbf{u}}_J^{+}, \tag{5.33}$$

$$\bar{\mathbf{u}}^{-}(\mathbf{x}_M) = \bar{\mathbf{u}}_M^{-} = \sum_{J=1}^{N_{\Omega_\mathrm{s}}}\phi_J^{-}(\mathbf{x}_M)\hat{\mathbf{u}}_J^{-}. \tag{5.34}$$

Equations (5.33) and (5.34) are directly inserted in the rows of the global stiffness matrix corresponding to the node positioned on the global displacement boundary instead of

the corresponding equilibrium equations. For the nodes positioned on Γ_{t}^{+} and Γ_{t}^{-}, where traction boundary conditions are prescribed, the equations (5.5) and (5.6) are firstly rewritten using constitutive relations (2.11) obtaining

$$\bar{\mathbf{t}}^{+}(\mathbf{x}_I) = \mathbf{N}^{+}(\mathbf{x}_I)\mathbf{D}^{+}\boldsymbol{\varepsilon}^{+}, \tag{5.35}$$

$$\bar{\mathbf{t}}^{-}(\mathbf{x}_M) = \mathbf{N}^{-}(\mathbf{x}_M)\mathbf{D}^{-}\boldsymbol{\varepsilon}^{-}. \tag{5.36}$$

Next, in the traction boundary conditions the kinematic relations (2.4) are introduced and the displacement approximation (5.15) is then employed, leading to

$$\bar{\mathbf{t}}_I^{+} = \mathbf{N}_I^{+}\mathbf{D}^{+}\sum_{J=1}^{N_{\Omega_{\mathrm{s}}}}\mathbf{B}_{IJ}^{+}\hat{\mathbf{u}}_J^{+}, \tag{5.37}$$

$$\bar{\mathbf{t}}_M^{-} = \mathbf{N}_M^{-}\mathbf{D}^{-}\sum_{J=1}^{N_{\Omega_{\mathrm{s}}}}\mathbf{B}_{MJ}^{-}\hat{\mathbf{u}}_J^{-}, \tag{5.38}$$

where $\mathbf{N}_I^{+}$ and $\mathbf{N}_M^{-}$ denote matrices comprised of the unit normal vector components with respect to the Cartesian coordinate system, defined as

$$\mathbf{N}_I^{+} = \begin{bmatrix} n_1^{+}(\mathbf{x}_I) & 0 & n_2^{+}(\mathbf{x}_I) \\ 0 & n_2^{+}(\mathbf{x}_I) & n_1^{+}(\mathbf{x}_I) \end{bmatrix}, \tag{5.39}$$

$$\mathbf{N}_M^{-} = \begin{bmatrix} n_1^{-}(\mathbf{x}_M) & 0 & n_2^{-}(\mathbf{x}_M) \\ 0 & n_2^{-}(\mathbf{x}_M) & n_1^{-}(\mathbf{x}_M) \end{bmatrix}. \tag{5.40}$$

In a similar way, the interface boundary conditions (5.7) and (5.8), for the nodes on Γ_{s}, are discretized using only the displacement approximation (5.15), thus obtaining

$$\sum_{J=1}^{N_{\Omega_{\mathrm{s}}}}\phi_J^{+}(\mathbf{x}_I)\hat{\mathbf{u}}_J^{+} = \sum_{J=1}^{N_{\Omega_{\mathrm{s}}}}\phi_J^{-}(\mathbf{x}_M)\hat{\mathbf{u}}_J^{-}, \tag{5.41}$$

$$\mathbf{N}_I^{+}\mathbf{D}^{+}\sum_{J=1}^{N_{\Omega_{\mathrm{s}}}}\mathbf{B}_{IJ}^{+}\hat{\mathbf{u}}_J^{+} = -\mathbf{N}_M^{-}\mathbf{D}^{-}\sum_{J=1}^{N_{\Omega_{\mathrm{s}}}}\mathbf{B}_{MJ}^{-}\hat{\mathbf{u}}_J^{-}. \tag{5.42}$$

In the above equations, nodes I and M on the interface boundary Γ_{s} have the same coordinates since the overlapping node concept is utilized. Furthermore, in the equations (5.41) and (5.42) there is no summation over indices I and M.

5.4. Collocation method based on the mixed approach

As the second procedure for the discretization of the presented problem, a mixed meshless approach is utilized. Herein, the approximation of the stress components and

the displacement components are used. All of the referent boundaries and sets of nodes are exactly the same as in the previous section, where the equations for the primal approach have been analyzed. Furthermore, the same strong equilibrium equations are utilized for the nodes within the domains Ω^+ and Ω^-. On the outer boundaries, Γ^+ and Γ^-, and the interface boundary Γ_s, depending on the position of the discretization node, appropriate boundary conditions are imposed. In the following two subsections, the discretized equations for the mentioned mixed meshless approach are presented.

5.4.1. Discretized equilibrium equations of the mixed approach

According to the mixed meshless paradigm [199], the equilibrium collocation equations (5.13) and (5.14) are firstly discretized by the stress approximations defined by relation (5.16), leading to

$$\sum_{J=1}^{N_{\Omega_\mathrm{s}}} {\mathbf{B}_{IJ}^{+}}^{\mathrm{T}} \hat{\boldsymbol{\sigma}}_J^+ + \mathbf{b}^+(\mathbf{x}_I) = \mathbf{0}, \tag{5.43}$$

$$\sum_{J=1}^{N_{\Omega_\mathrm{s}}} {\mathbf{B}_{MJ}^{-}}^{\mathrm{T}} \hat{\boldsymbol{\sigma}}_J^- + \mathbf{b}^-(\mathbf{x}_M) = \mathbf{0}. \tag{5.44}$$

Herein $\mathbf{B}_{IJ}^+$ and $\mathbf{B}_{MJ}^-$ are the matrices composed of the first-order spatial derivatives of the shape function for the J^{th} node influencing the approximation at node I or node M, respectively. Thus, they are defined by relations (5.25) and (5.26). From equations (5.43) and (5.44), it is evident that the total number of equations at the global level is lower, $N_\mathrm{eq} = 2(N+P)$, than the total number of the stress unknowns $N_{\sigma\mathrm{un}} = 3(N+P)$. Hence, in order to obtain the closed and easily solvable system of equations, the compatibility is enforced at each node between the approximated stresses, $\sigma_{ij}^{+(h)}(\mathbf{x}_J) \approx \hat{\boldsymbol{\sigma}}_J^+, \mathbf{x}_J \in S^+$ and $\sigma_{ij}^{-(h)}(\mathbf{x}_J) \approx \hat{\boldsymbol{\sigma}}_J^-, \mathbf{x}_J \in S^-$, and the nodal values of displacements, $\hat{\mathbf{u}}_L^+; L = 1, 2, ..., N_{\Omega_\mathrm{s}}$, and $\hat{\mathbf{u}}_L^-; L = 1, 2, ..., N_{\Omega_\mathrm{s}}$, respectively. This is accomplished by consecutively using the constitutive relations of classical linear elasticity (2.11) for each of the considered homogeneous materials, and the kinematic equations for strains defined by (2.4). By inserting the kinematic equation (2.4) into the constitutive equations (2.11), the following relations for the heterogeneous structure are obtained

$$\boldsymbol{\sigma}^+ = \mathbf{D}^+ \mathbf{D}_\mathrm{K}^+ \mathbf{u}^+, \tag{5.45}$$

$$\boldsymbol{\sigma}^- = \mathbf{D}^- \mathbf{D}_\mathrm{K}^- \mathbf{u}^-. \tag{5.46}$$

Equations (5.45) and (5.46) are now written at every node and they are discretized by the displacement approximations defined by (5.15), leading to the expressions

$$\hat{\boldsymbol{\sigma}}_J^+ = \mathbf{D}^+ \sum_{L=1}^{N_{\Omega_\mathrm{s}}} \mathbf{D}_\mathrm{K}^+ \phi_L^+(\mathbf{x}_J) \hat{\mathbf{u}}_L^+ = \mathbf{D}^+ \sum_{L=1}^{N_{\Omega_\mathrm{s}}} \mathbf{B}_{JL}^+ \hat{\mathbf{u}}_L^+, \tag{5.47}$$

$$\hat{\boldsymbol{\sigma}}_J^- = \mathbf{D}^- \sum_{L=1}^{N_{\Omega_\mathrm{s}}} \mathbf{D}_\mathrm{K}^- \phi_L^-(\mathbf{x}_J)\hat{\mathbf{u}}_L^- = \mathbf{D}^- \sum_{L=1}^{N_{\Omega_\mathrm{s}}} \mathbf{B}_{JL}^- \hat{\mathbf{u}}_L^-. \tag{5.48}$$

By introducing (5.47) and (5.48) into the discretized equilibrium equations (5.43) and (5.44), a system of linear algebraic equations with only the nodal displacements as unknowns is obtained. Therefore, the final discretized system of equations can be written for each node as

$$\sum_{J=1}^{N_{\Omega_\mathrm{s}}} \mathbf{K}_{IJ}^+ \hat{\mathbf{u}}_J^+ = \mathbf{R}_I^+, \quad I = 1, 2, ..., N, \tag{5.49}$$

$$\sum_{J=1}^{N_{\Omega_\mathrm{s}}} \mathbf{K}_{MJ}^- \hat{\mathbf{u}}_J^- = \mathbf{R}_M^-, \quad M = 1, 2, ..., P, \tag{5.50}$$

where the nodal stiffness matrices $\mathbf{K}_{IJ}^+$ and $\mathbf{K}_{MJ}^-$ are equal to

$$\mathbf{K}_{IJ}^+ = \sum_{L=1}^{N_{\Omega_\mathrm{s}}} {\mathbf{B}_{LI}^+}^\mathrm{T} \mathbf{D}^+ \mathbf{B}_{JL}^+, \tag{5.51}$$

$$\mathbf{K}_{MJ}^- = \sum_{L=1}^{N_{\Omega_\mathrm{s}}} {\mathbf{B}_{LM}^-}^\mathrm{T} \mathbf{D}^- \mathbf{B}_{JL}^-, \tag{5.52}$$

while the nodal force vectors $\mathbf{R}_I^+$ and $\mathbf{R}_M^-$ are the same as in the primal approach and equal to (5.31) and (5.32). As can be observed from equations (5.49) and (5.50), by utilizing the mixed meshless approach only the first-order spatial derivatives of the shape functions need to be computed to assemble the nodal stiffness matrices $\mathbf{K}_{IJ}^+$ and $\mathbf{K}_{MJ}^-$. This statement can be considered as an advantage in comparison with the primal (fully displacement) formulation in which the second-order derivatives are necessary. Therefore, this valuable property decreases the continuity requirements on the trial function in the considered approach, which contributes the accuracy and numerical efficiency.

5.4.2. Discretized boundary conditions of the mixed approach

All approximation functions in this dissertation possess the interpolation property at the nodes. Consequently, the displacement boundary conditions in the mixed approach are enforced straightforward in the same manner as in the primal approach. Thus, the equations (5.33) and (5.34) are utilized to impose the essential boundary conditions on Γ_u^+ and Γ_u^-. For the nodes positioned on the boundaries Γ_t^+ and Γ_t^- the traction boundary conditions (5.5) and (5.6) are inserted into the global equation system instead of the equilibrium equations for corresponding node, similarly as in classical collocation approaches that employ the direct collocation approach. Thus, by applying the stress approximation (5.16) and by utilizing the compatibility between the approximated stresses and displacements defined by equations (5.45) and (5.46), the discretized traction boundary conditions

are computed as

$$\mathbf{t}_I^+ = \mathbf{N}_I^+ \mathbf{D}^+ \sum_{J=1}^{N_{\Omega_\mathrm{s}}} \mathbf{S}_{IJ}^+ \sum_{L=1}^{N_{\Omega_\mathrm{s}}} \mathbf{B}_{JL}^+ \hat{\mathbf{u}}_L^+, \tag{5.53}$$

$$\mathbf{t}_M^- = \mathbf{N}_M^- \mathbf{D}^- \sum_{J=1}^{N_{\Omega_\mathrm{s}}} \mathbf{S}_{MJ}^- \sum_{L=1}^{N_{\Omega_\mathrm{s}}} \mathbf{B}_{JL}^- \hat{\mathbf{u}}_L^-, \tag{5.54}$$

where $\mathbf{S}_{IJ}^+$ and $\mathbf{S}_{MJ}^-$ denote the diagonal matrices comprised of shape function values equal to

$$\mathbf{S}_{IJ}^+ = \begin{bmatrix} \phi_J^+(\mathbf{x}_I) & 0 & 0 \\ 0 & \phi_J^+(\mathbf{x}_I) & 0 \\ 0 & 0 & \phi_J^+(\mathbf{x}_I) \end{bmatrix}, \tag{5.55}$$

$$\mathbf{S}_{MJ}^- = \begin{bmatrix} \phi_J^-(\mathbf{x}_M) & 0 & 0 \\ 0 & \phi_J^-(\mathbf{x}_M) & 0 \\ 0 & 0 & \phi_J^-(\mathbf{x}_M) \end{bmatrix}. \tag{5.56}$$

Due to the interpolatory property of the approximations these matrices can for simplicity be omitted. Thus, the above expressions can be written in their final form as follows

$$\bar{\mathbf{t}}_I^+ = \mathbf{N}_I^+ \mathbf{D}^+ \sum_{L=1}^{N_{\Omega_\mathrm{s}}} \mathbf{B}_{IL}^+ \hat{\mathbf{u}}_L^+, \tag{5.57}$$

$$\mathbf{t}_M^- = \mathbf{N}_M^- \mathbf{D}^- \sum_{L=1}^{N_{\Omega_\mathrm{s}}} \mathbf{B}_{ML}^- \hat{\mathbf{u}}_L^-. \tag{5.58}$$

Furthermore, in the equations (5.57) and (5.58) there is no summation over indices I and M.

After discretization of the interface conditions (5.7) and (5.8) by employing the expressions (5.33), (5.34), (5.57) and (5.58) for the nodes positioned on the boundary Γ_s, the following discretized interface boundary conditions are obtained

$$\sum_{L=1}^{N_{\Omega_\mathrm{s}}} \phi_L^+(\mathbf{x}_I) \hat{\mathbf{u}}_L^+ = \sum_{L=1}^{N_{\Omega_\mathrm{s}}} \phi_L^-(\mathbf{x}_M) \hat{\mathbf{u}}_L^-, \tag{5.59}$$

$$\mathbf{N}_I^+ \mathbf{D}^+ \sum_{L=1}^{N_{\Omega_\mathrm{s}}} \mathbf{B}_{IL}^+ \hat{\mathbf{u}}_L^+ = -\mathbf{N}_M^- \mathbf{D}^- \sum_{L=1}^{N_{\Omega_\mathrm{s}}} \mathbf{B}_{ML}^- \hat{\mathbf{u}}_L^-. \tag{5.60}$$

These equations are inserted into the global stiffness matrix in the rows corresponding to the current node positioned on Γ_s. Yet again, in the above equations there is no summation over indices I and M.

5.5. Numerical examples - classical linear elasticity

In this section, the efficiency and robustness of the proposed mixed formulation for the classical linear elasticity is tested on five numerical examples involving heterogeneous structures: a bar under continuous axial load, a hollow cylinder subjected to essential boundary conditions, a hollow cylinder subjected to inner and outer pressure, a rectangular plate under uni-axial continuous linear load and a plate with circular inclusion loaded with unit horizontal traction. Furthermore, the accuracy of the presented mixed approach is compared to the solutions obtained by using the fully displacement (primal) formulation, where only the approximation of the unknown displacement components is utilized. The accuracy of both collocation methods is evaluated by using standard L_2 relative error norms of displacement and stress components. For the numerical examples such as the one-dimensional bar, the hollow cylinders and the plate with circular inclusion, where an analytical solution for the entire heterogeneous structure can be derived, the domain integration of L_2 norms is carried out numerically over a background mesh. Hence, the integral displacement and stress solution error norms are computed by the relations

$$||e_u|| = \int_{\Omega} \sqrt{\frac{||\mathbf{u}^{\mathrm{MM}} - \mathbf{u}^{\mathrm{anal}}||}{||\mathbf{u}^{\mathrm{anal}}||}} \mathrm{d}\Omega, \tag{5.61}$$

$$||e_\sigma|| = \int_{\Omega} \sqrt{\frac{||\boldsymbol{\sigma}^{\mathrm{MM}} - \boldsymbol{\sigma}^{\mathrm{anal}}||}{||\boldsymbol{\sigma}^{\mathrm{anal}}||}} \mathrm{d}\Omega. \tag{5.62}$$

In the case when an appropriate referent analytical solution are not available, in the example of the rectangular plate, discrete L_2 norms are used. They are then computed as

$$||e_u|| = \sum_{k=1}^{N_{\mathrm{cs}}} \sqrt{\frac{||\mathbf{u}^{\mathrm{MM}} - \mathbf{u}^{\mathrm{FEM}}||}{||\mathbf{u}^{\mathrm{FEM}}||}}, \tag{5.63}$$

$$||e_\sigma|| = \sum_{k=1}^{N_{\mathrm{cs}}} \sqrt{\frac{||\boldsymbol{\sigma}^{\mathrm{MM}} - \boldsymbol{\sigma}^{\mathrm{FEM}}||}{||\boldsymbol{\sigma}^{\mathrm{FEM}}||}}, \tag{5.64}$$

where N_{cs} stands for the total number of discretization nodes considered for error calculation.

5.5.1. Bar under continuous axial load

For the first numerical example heterogeneous bar is considered. The heterogeneous bar is composed of two different homogeneous materials with unit cross section area, length $L = 5$ and subjected to constant axial load $b_x = 5$. On both ends of the bar boundary conditions according to Figure 5.3 are prescribed, taken from the analytical solution.

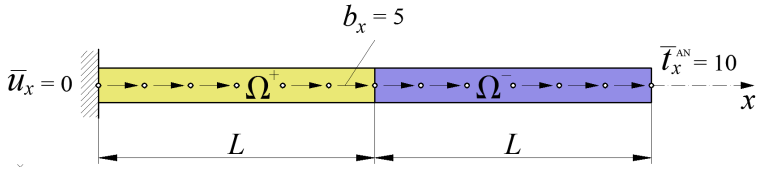

Figure 5.3: Discretized bar with boundary conditions

The material property of the left part of the bar is equal to $E^+ = 1000$, while the property of the right is $E^- = 10000$. In order to determine the appropriate size of a approximation domain, parametric studies for the presented problem are performed. The influence of the local approximation domain size (r_s/h_s) and the Gaussian shape function parameter α_c are investigated. Herein, the uniform grid of nodes is used for the discretization, with the average nodal distance h_s. Three different discretization employing 18, 30 and 42 nodes are used. Also, both primal (P) and mixed (M) discretization strategies are utilized. Firstly, in the Figure 5.4 the parametric study of accuracy employing (5.63) using first-order IMLS functions is presented.

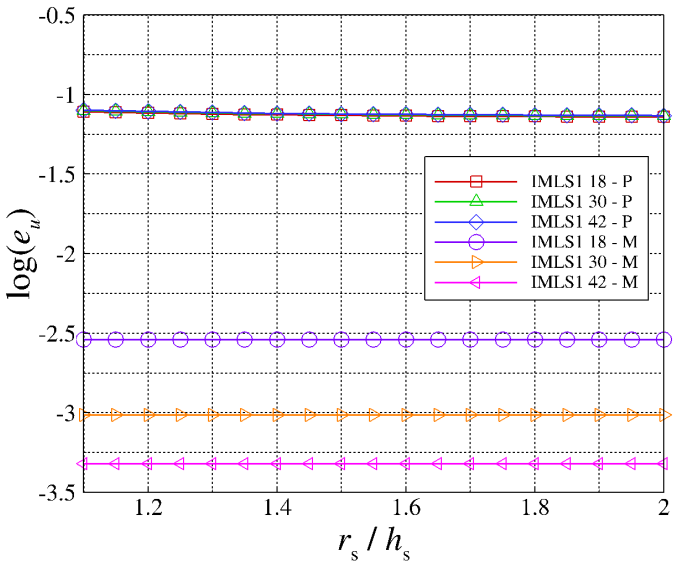

Figure 5.4: Bar - parametric study - IMLS1 functions

As obvious, from the above figure the size of the approximation domain does not influence the accuracy of the MLPG2 method. It can be also seen that by using the mixed approach, far more accurate solutions are obtained in comparison to the primal approach. Secondly, for the chosen size of the approximation domain $r_s = 1.25h_s$, parametric analysis of the influence of the shape parameter α_c in RPIM on the accuracy is performed.

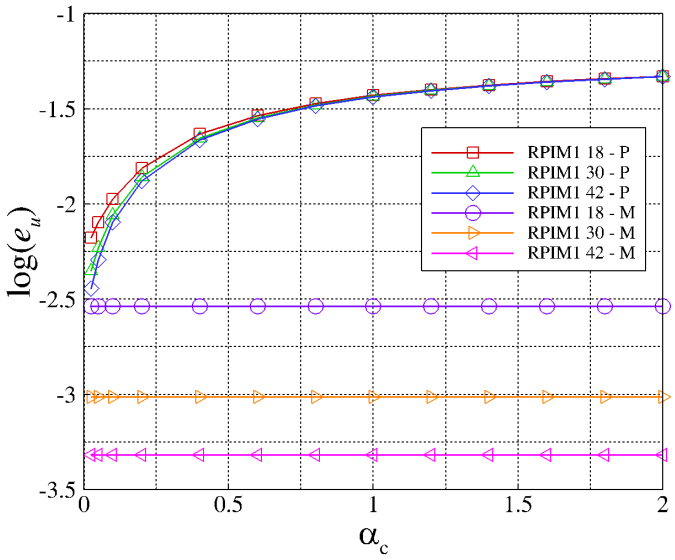

Figure 5.5: Bar - parametric study - RPIM1 functions

From Figure 5.5, it can be seen that the choice of the shape parameter α_c does not influence the accuracy of the solution when the mixed approach is utilized. This is not the case if the primal approach is employed. Hence, the mixed approach of the RPICM method seems to be robust. For further examination, the global accuracy of the methods, using the displacement convergence tests, is depicted in Figures 5.6 and 5.7. For the analysis first- and second-order approximation functions are used.

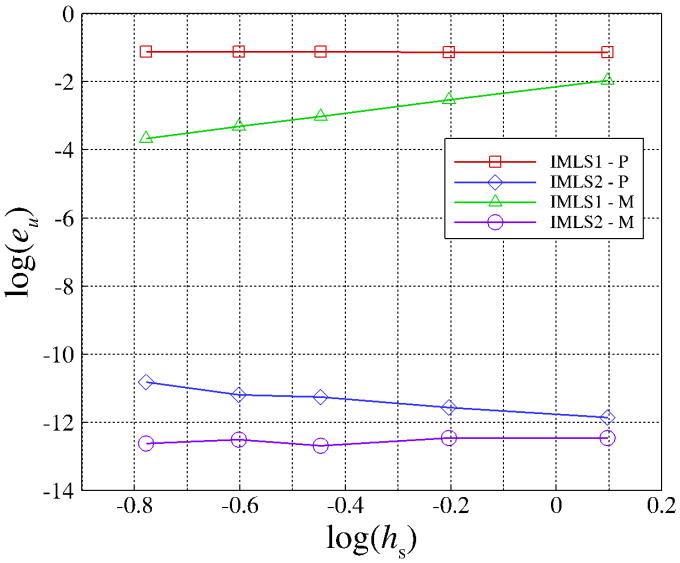

Figure 5.6: Bar - convergence study - IMLS functions

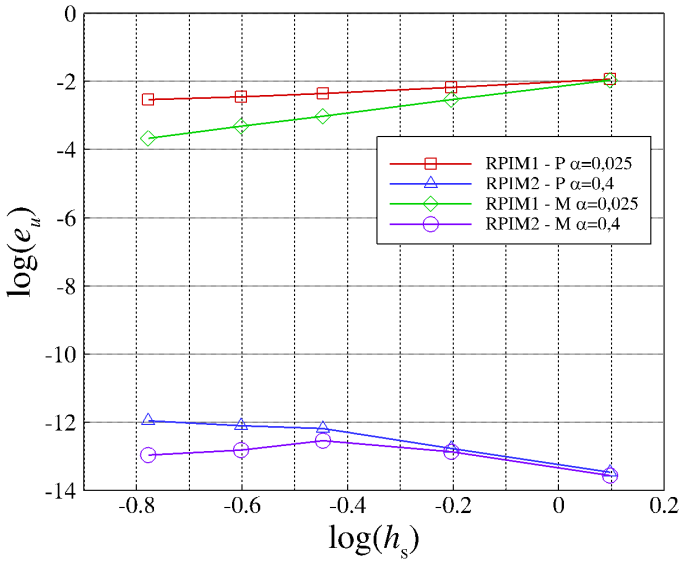

Figure 5.7: Bar - convergence study - RPIM functions

From the analysis, of the presented convergence studies it can be observed that the primal methods utilizing a low-order of approximation exhibit lower convergence. This can be to a certain extent alleviated by the choice of the appropriate Gaussian shape parameter in RPIM. But, this procedure is limited to a small number of cases where an analytical solution is known and can be used to fit the RPIM approximation parameter. In general, better convergence behaviour can be observed in both methods when the mixed approach is utilized. To further demonstrate this, the distributions of displacement and strain for the entire length of the bar are depicted in Figures 5.8 and 5.9. For the purpose of presenting the mentioned distributions, grid with 10 discretization nodes is utilized.

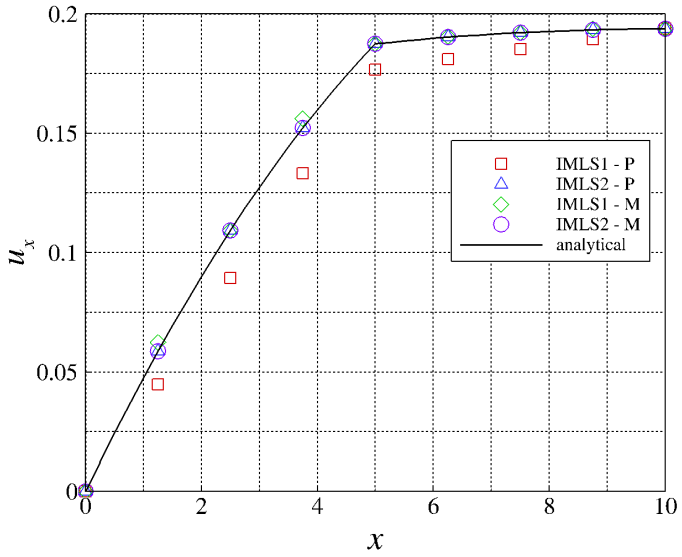

Figure 5.8: Bar - distribution of displacement u_x - IMLS functions

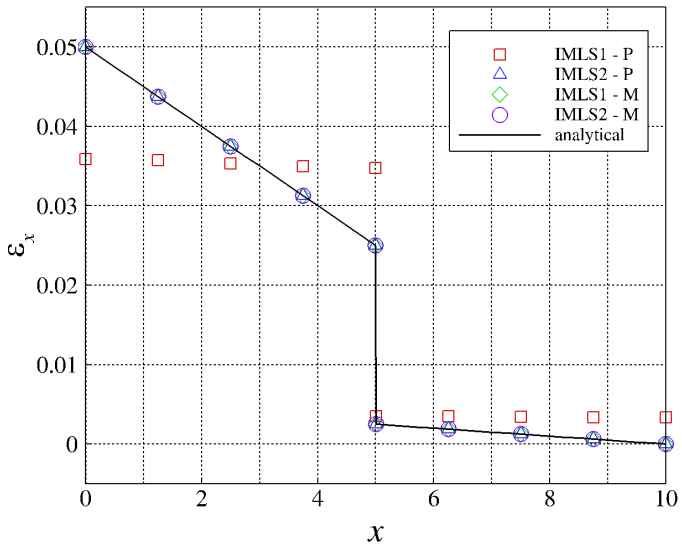

Figure 5.9: Bar - distribution of strain ε_x - IMLS functions

As evident, the mixed MLPG2 method can capture the analytical displacement and strain distributions successfully. Furthermore, the jump in the derivative field is accurately described by using the interface boundary conditions. From the above distributions, the primal approach utilizing the first-order approximation does not result in good solutions. In addition, it can be observed from (**??**) the MLPG2 with first-order IMLS does not converge for any number of discretization nodes..

5.5.2. Hollow cylinder under essential boundary conditions

As the second numerical example, a hollow heterogeneous cylinder consisting of two homogeneous subdomains, as shown in Figure 5.10, is considered. The geometry of the heterogeneous cylinder is defined by the inner radius $R_1 = 1$, the interface radius $R_2 = 2$ and the outer radius $R_3 = 4$.

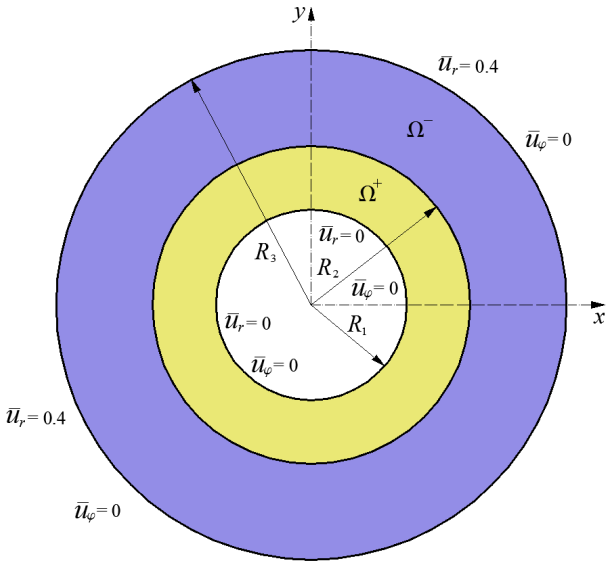

Figure 5.10: Geometry of the cylinder under essential boundary conditions (EssBCs)

Due to the symmetry, only a quarter model is used for obtaining the meshless solutions. For the analysis of deformation, only structured discretizations as in Figure 5.11 are used. The material properties of the inner part of cylinder are $E^+ = 1$, $\nu^+ = 0.25$, while the material properties of the outer part are $E^- = 10$, $\nu^- = 0.3$.

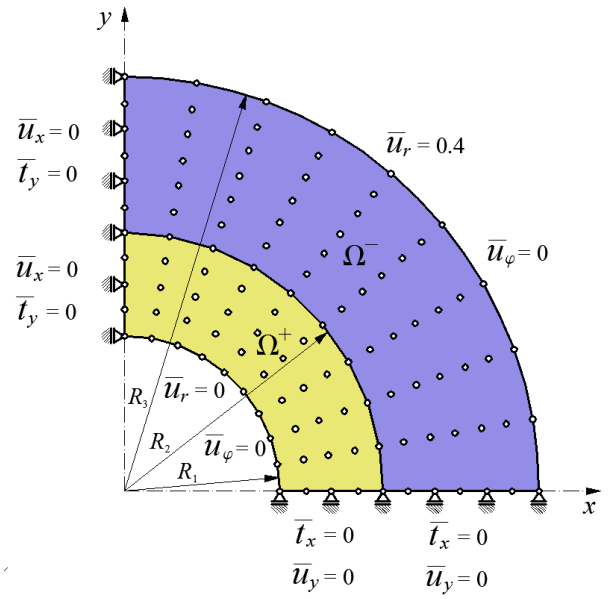

Figure 5.11: Discretized cylinder under essential boundary conditions (EssBCs)

In this example, structured equidistant discretizations in the parametric space defined by the coordinate Θ_1, Θ_2 are utilized, as shown in Figure 5.12.

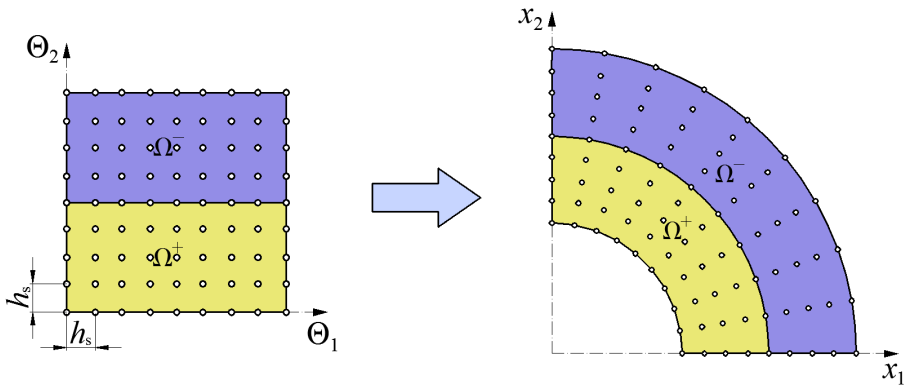

Figure 5.12: Discretization and calculation of the shape function derivatives

Thus, the calculation of the meshless shape functions and their derivatives is carried out using the parametric coordinates. All necessary nodal values are then mapped into the Cartesian coordinate x_1, x_2, as presented in Figure 5.12. Here, h_s denotes the nodal distance in the directions of coordinates Θ_1, Θ_2 as portrayed in Figure (5.12). When utilizing the primal approach for the problem solution, both first- and second-order derivatives of the shape functions need to be calculated with respect to the Cartesian coordinates in order to assemble the global stiffness matrix. For comparison, only the first-order derivatives need to be determined when the mixed approach is used which is considered as an advantage over the primal approach. The shape function derivatives with respect to the Cartesian coordinates are expressed as

$$\frac{\partial \phi}{\partial \mathbf{x}} = \mathbf{J}^{-1} \cdot \frac{\partial \phi}{\partial \boldsymbol{\Theta}}, \tag{5.65}$$

$$\frac{\partial^2 \phi}{\partial \mathbf{x}^2} = \mathbf{J}^{-\mathrm{T}} \cdot \frac{\partial^2 \phi}{\partial \boldsymbol{\Theta}^2} \cdot \mathbf{J}^{-1} + \frac{\partial \phi}{\partial \boldsymbol{\Theta}} \cdot \frac{\partial \mathbf{J}^{-1}}{\partial \mathbf{J}} : \frac{\partial^2 \mathbf{x}}{\partial \boldsymbol{\Theta}^2} \cdot \mathbf{J}^{-1}, \tag{5.66}$$

where $\mathbf{J}$ denotes the Jacobian matrix defined by

$$\mathbf{J} = \begin{bmatrix} \dfrac{\partial x_1}{\partial \Theta_1} & \dfrac{\partial x_2}{\partial \Theta_1} \\ \dfrac{\partial x_1}{\partial \Theta_2} & \dfrac{\partial x_2}{\partial \Theta_2} \end{bmatrix}. \tag{5.67}$$

More on the mapping procedures can be found in the literature [17, 200]. To show the performance of the presented approaches in a more clear way, the influence of the local approximation domain size ($r_\mathrm{s}/h_\mathrm{s}$) in the MLPG methods, and also the Gaussian radial basis shape parameter α_c in the RPIM on the accuracy of the solution is investigated. Here, the nodal distance of the uniform grid is again denoted as h_s, while the circular size of the approximation domain is r_s, respectively. Both primal (P) and mixed (M) approaches are utilized and the obtained numerical solutions are compared with the available analytical solution [41] employing the standard relative error of displacements in the L_2 norm (5.63).

For the analysis of deformation, the meshless interpolation schemes using the first- and second-order basis are applied and compared. Firstly, a detailed analysis of the meshless parameters has been done for both the IMLS and RPIM approximations. Hence, Figures 5.13 and 5.14 portray the effect of the size of the approximation domain on the accuracy of the solution when MLPG2 method is considered. For these IMLS parametric studies, discretization with 760 and 1300 nodes are utilized.

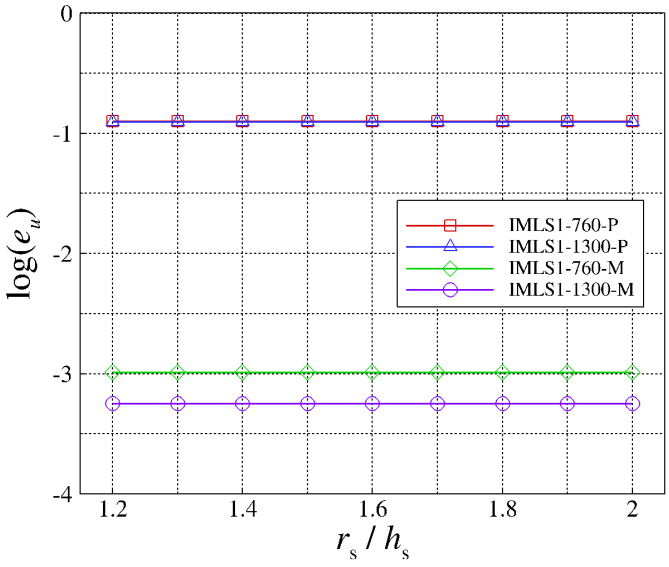

Figure 5.13: Cylinder under EssBCs - parametric study - IMLS1

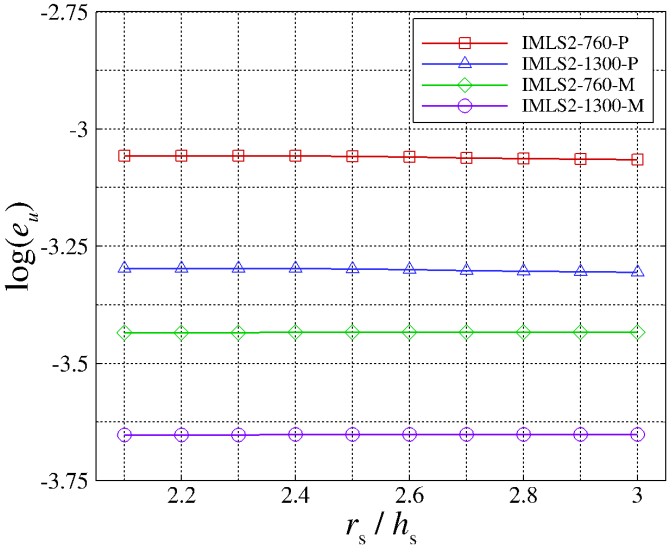

Figure 5.14: Cylinder under EssBCs - parametric study - IMLS2

Yet again, from the analysis of the portrayed studies it can be concluded that the accuracy of the MLPG2 method is not dependent on the size of the approximation domain for the considered uniform discretizations in parametric coordinates. Also, a clear advantage

in accuracy of the mixed approach can be seen for both order of approximations. Secondly, in the RPICM the parametric studies of two meshless parameters are conducted. These parameters include the size of the approximation domain, as in MLPG2, and the influence of the shape parameter α_c of the Gaussian RBF. Thus, Figures 5.15 - 5.18 show the influence of the mentioned parameters on the accuracy of the obtained numerical solutions. Herein, both the primal and the mixed approach are utilized. For the purpose of this RPIM parametric studies, the first- and second-order approximations (RPIM1 and RPIM2) are applied. For the discretization of the problem the grid of 364 nodes is used.

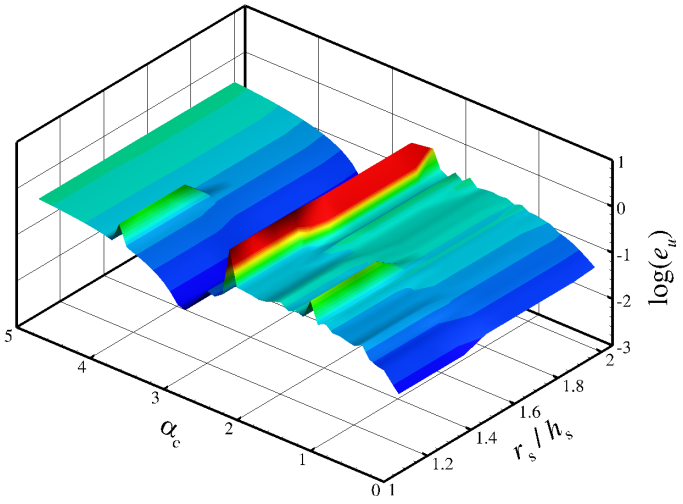

Figure 5.15: Cylinder under EssBCs - parametric study - primal - RPIM1 functions

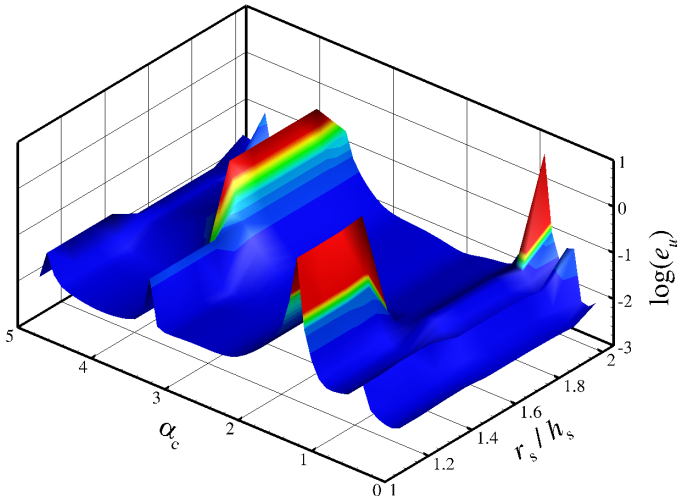

Figure 5.16: Cylinder under EssBCs - parametric study - mixed - RPIM1 functions

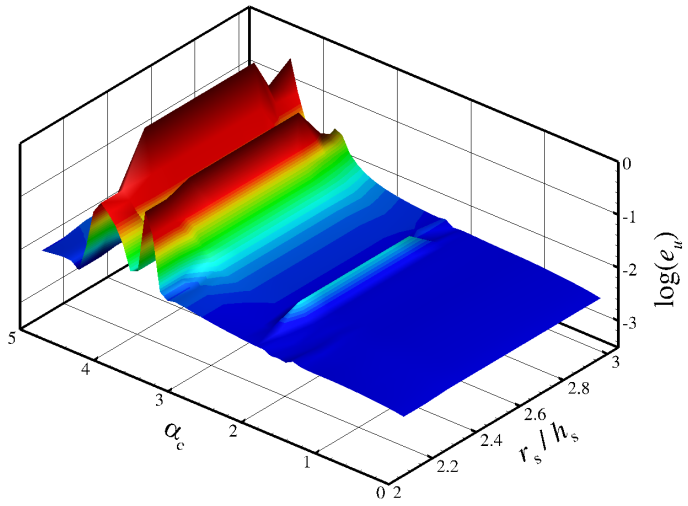

Figure 5.17: Cylinder under EssBCs - parametric study - primal - RPIM2 functions

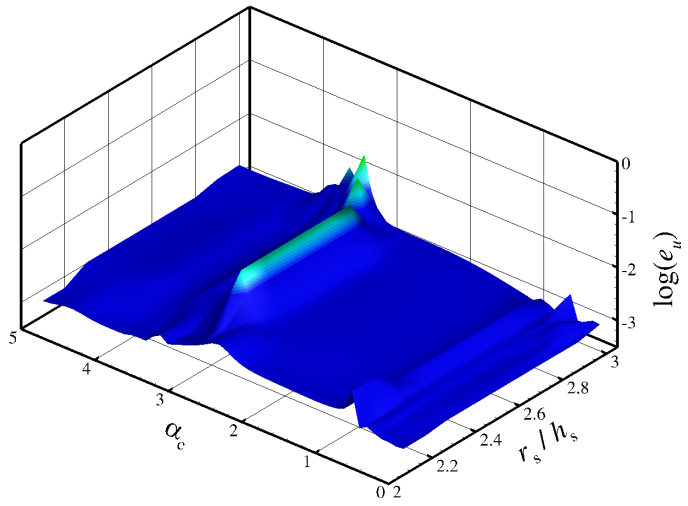

Figure 5.18: Cylinder under EssBCs - parametric study - mixed - RPIM2 functions

As evident from the above studies, the mixed approach is again superior to the primal formulation. A more accurate and numerically stable modeling of heterogeneous materials is achieved when the mixed RPICM formulation is utilized. For further verification of the presented approaches, the convergence studies of both methods employing the relative errors e_u and e_σ in the L_2 norm of displacements and stress components are shown in Figures 5.19 and 5.20. For the purpose of creating convergence tests, some meshless parameters from the parametric studies need to be chosen. This is done by employing the parameters that give the best accuracy of the methods. Hence, for the interpolation schemes with the first-order basis (IMLS1, RPIM1), the local approximation domain size $r_s/h_s = 1.6$ is utilized and for the schemes using the second-order basis (IMLS2, RPIM2) $r_s/h_s = 2.6$ is applied. In that way, the same local approximation domain sizes are utilized for both methods. For each of the approaches and for each order of the RPIM functions,

a different dimensionless radial basis shape parameter α_c is considered. Consequently, for the primal meshless formulation using the first-order basis (RPIM1-P) $\alpha_c = 3.2$ is chosen and for the mixed approach using the first-order basis (RPIM1-M) the shape parameter $\alpha_c = 2.0$ is considered. In addition, for the primal approach with the second-order meshless interpolation functions (RPIM2-P) $\alpha_c = 0.5$ is applied and for the mixed formulation with the second-order functions (RPIM2-M) $\alpha_c = 1.5$ is utilized.

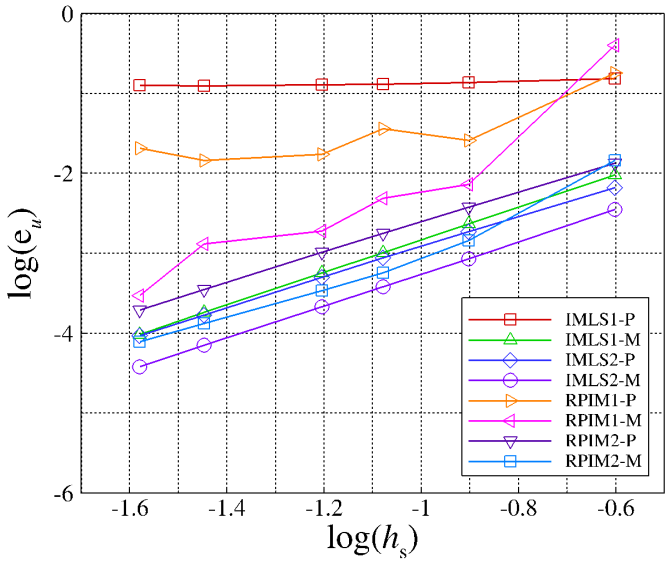

Figure 5.19: Cylinder under EssBCs - displacement e_u convergence test

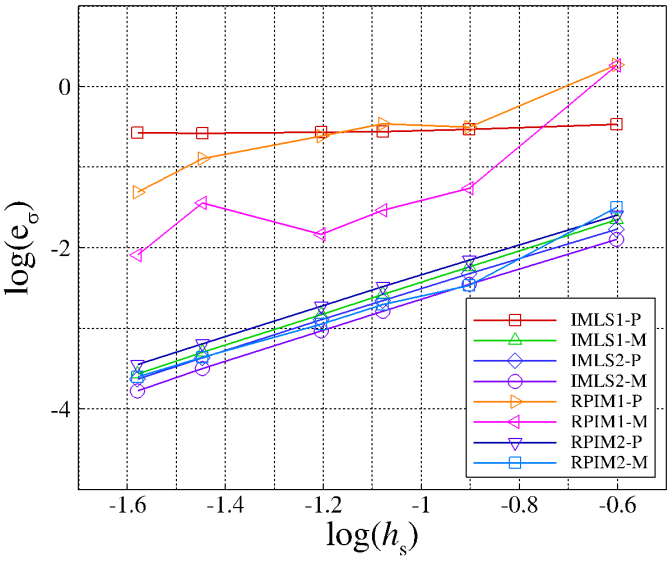

Figure 5.20: Cylinder under EssBCs - stress e_σ convergence test

From the analysis of the convergence rates, the mixed approach is superior to the primal formulation regardless of the utilized approximation function. Furthermore, the mixed approach converges to the analytical solutions irrespectively of the approximation

order. The superiority of the mixed approach is especially evident when the first-order of the approximations is utilized. As evident, the primal approach employing the first-order approximations (IMLS1-P, RPIM1-P) does not converge to the analytical solutions. It should be noted that this is the case regardless of the choice of the parameters of the meshless method, since they have been analyzed and best values have been chosen. In order to further present the accuracy of the methods, the distributions of the radial strain ε_r and the circular stress σ_ϕ along the line $y = 0$ are portrayed in Figures 5.21 and 5.22. Herein, the MLPG2 method and the numerical model with 112 nodes are considered.

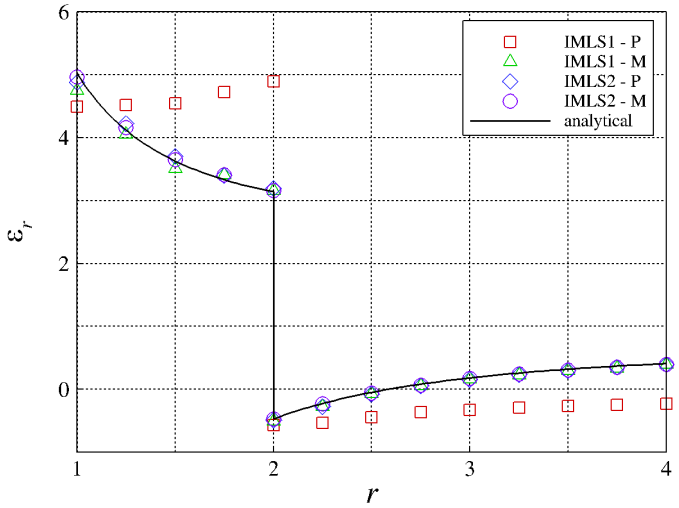

Figure 5.21: Cylinder under EssBCs - distribution of radial strain ε_r for $y = 0$

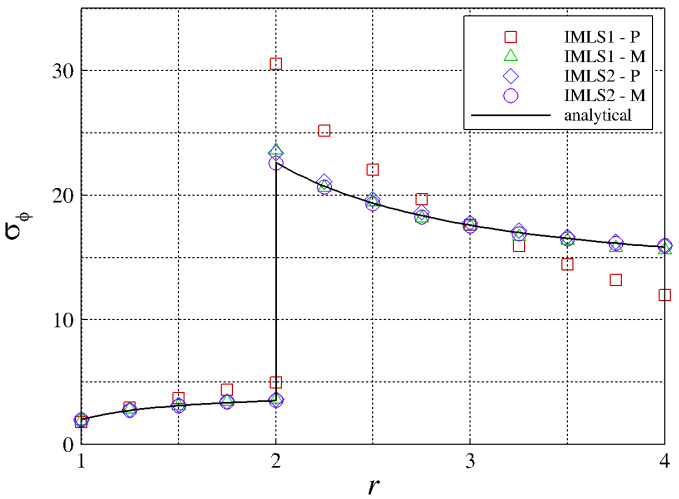

Figure 5.22: Cylinder under EssBCs - distribution of circular stress σ_ϕ for $y = 0$

From the analysis of the above distributions, yet again the advantage of the mixed approach can be seen. If the mixed approach is employed, it can be observed that the jumps in strain and stress field are accurately captured even if the first-order approxima-

tion is applied, which is not the case if the primal approach is utilized. As obvious, the primal approach in combination with a first-order approximation can yield large numerical errors and highly inaccurate distributions. The obtained numerical solutions should also be verified globally over the entire computational domain. Thus, the contour plots of the radial strain ε_r and the circular stress σ_ϕ obtained by the mixed MLPG2 method and the contour plots of the analytical solutions [41] are compared in Figures 5.23 - 5.26.

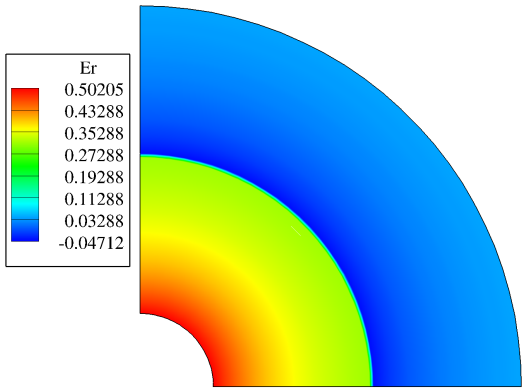

Figure 5.23: Cylinder under EssBCs - contour plot of ε_r - analytical solution

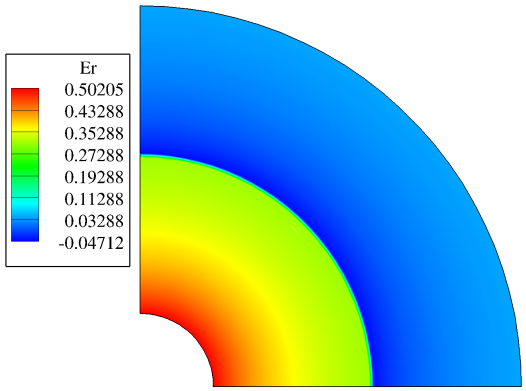

Figure 5.24: Cylinder under EssBCs - contour plot of ε_r - mixed MLPG2 - 760 nodes

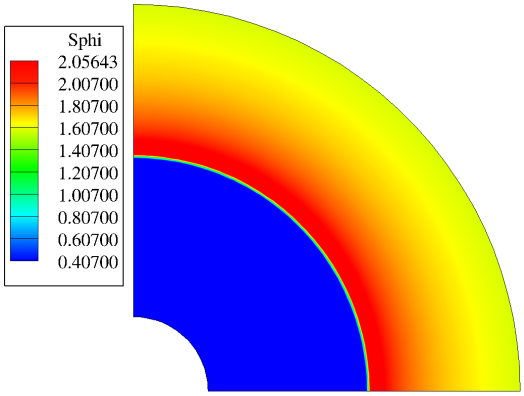

Figure 5.25: Cylinder under EssBCs - contour plot of σ_ϕ - analytical solution

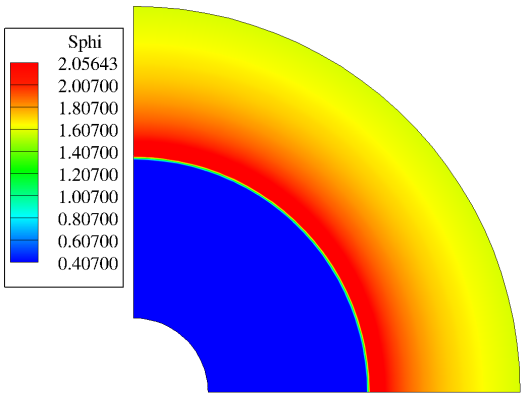

Figure 5.26: Cylinder under EssBCs - contour plot of σ_ϕ - mixed MLPG2 - 760 nodes

5.5.3. Hollow cylinder under natural boundary conditions

Another hollow heterogeneous cylinder consisting of two homogeneous subdomains, subjected to the inner ($p_1 = 0.5$) and outer ($p_2 = 1.5$) pressure is analyzed, as shown in Figure 5.27. The geometry of the cylinder is again defined by the inner radius $R_1 = 1$, interface radius $R_2 = 3$ and the outer radius $R_3 = 5$. The material properties of the subdomain Ω^+ are taken as $E^+ = 1$, $\nu^+ = 0.25$, while the properties of the subdomain Ω^- are $E^- = 10$ and $\nu^- = 0.3$.

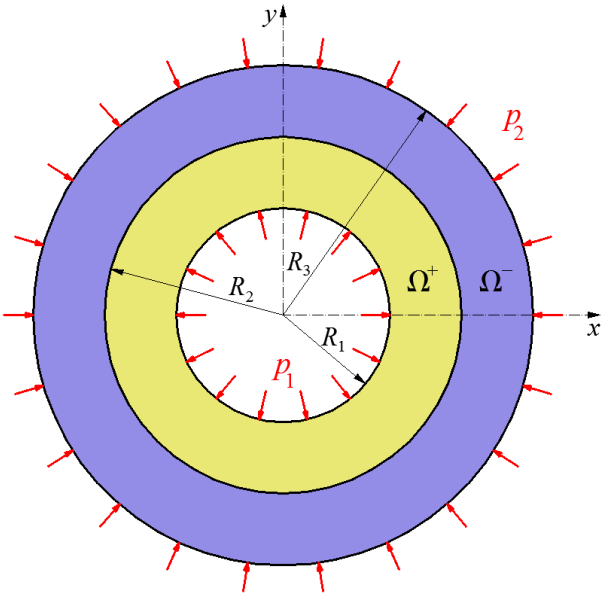

Figure 5.27: Geometry of the cylinder subjected to inner and outer pressure

Due to the geometrical, material and loading symmetry, only one quarter of the cylinder is considered. The numerical model with the loading and symmetry boundary conditions is depicted in Figure 5.28.

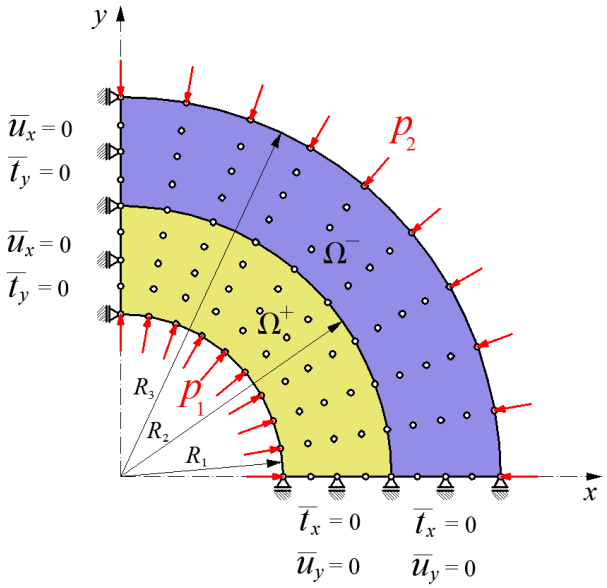

Figure 5.28: Discretized cylinder under natural boundary conditions (NatBCs)

The discretization of the cylinder is done using equidistant nodal arrangement using the procedure discussed in the previous example. The needed derivatives of the shape functions are firstly calculated with respect to the parametric coordinates and then their values are mapped to the global Cartesian coordinate system using equations (5.65) and (5.66). Since the global accuracy of the considered collocation methods depends on the choice of the meshless parameters, here again the parametric studies for both methods are conducted. The performance of the MLPG2 method has been analyzed as a function of the local approximation domain size (r_s/h_s), while the performance of RPICM has been investigated in a function of both the r_s/h_s and the value of the Gaussian RBF parameter α_c. Again, both of the presented approaches have been utilized for the modeling of deformation. The obtained meshless solutions have been evaluated and compared to the analytical solutions [201] using the standard L_2 norm defined by (5.63). The influence of the size of the approximation domain for the MLPG2 method on the accuracy of the solution is depicted in Figures 5.29 and 5.30. Herein, for the studies discretizations with 476 and 1000 grid points are utilized.

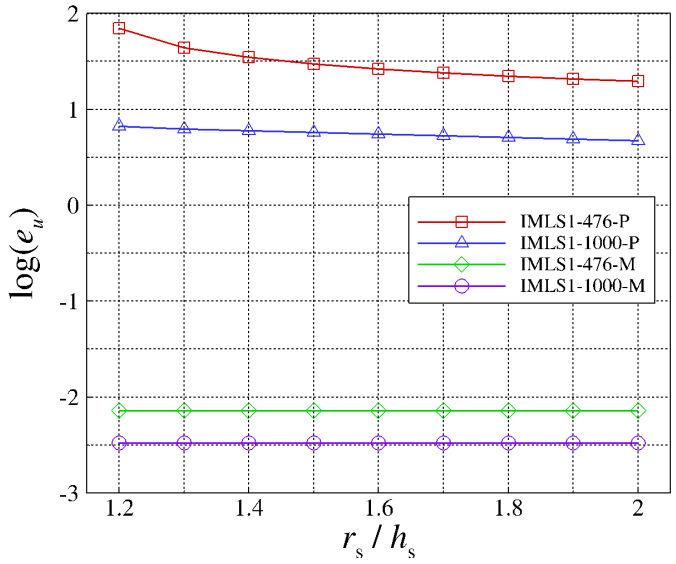

Figure 5.29: Cylinder under NatBCs - parametric study - IMLS1

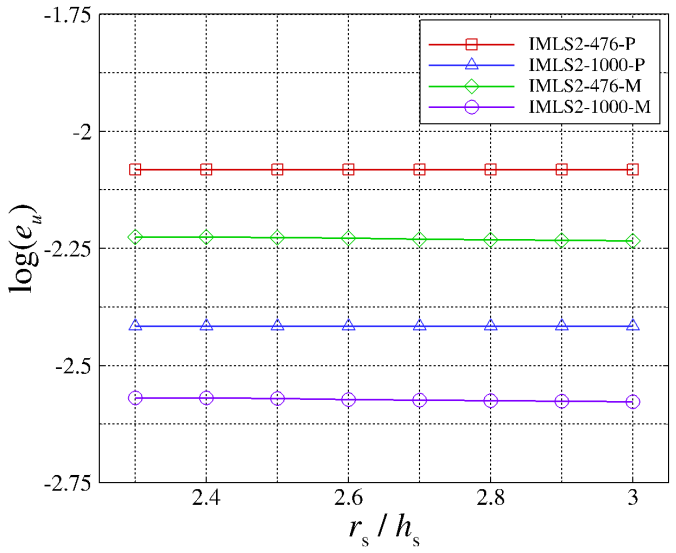

Figure 5.30: Cylinder under NatBCs - parametric study - IMLS2

In the Figure 5.29 slight influence of the size of the approximation domain on the accuracy is observed. However, this is only present for the first-order IMLS approximation, smaller approximation domains and smaller number of nodes used for discretization and computation. Furthermore, the use of the first-order IMLS approximation results in highly inaccurate solutions. This could be due to the natural boundary conditions being present in the model. As seen in Figure 5.30, the use of the second-order approximation diminishes the influence of the size of the approximation domain on the accuracy of the method. However, yet again clear distinction in accuracy can be observed depending on whether the primal or the mixed meshless approach is used. If the first-order of approximation is applied, the mixed approach is even more superior here for the case

where the derivative boundary conditions are present in the model. Parametric studies have been conducted also using RPICM with RPIM approximation whereby the Gaussian RBF is considered.

In the RPICM, the studies of two above mentioned parameters are conducted. Hence, Figures 5.31 - 5.34 present the influence of the meshless parameters on the accuracy of the RPICM for the first- and the second-order of RPIM approximation. Therein, the discretization of the problem with 476 nodes is considered.

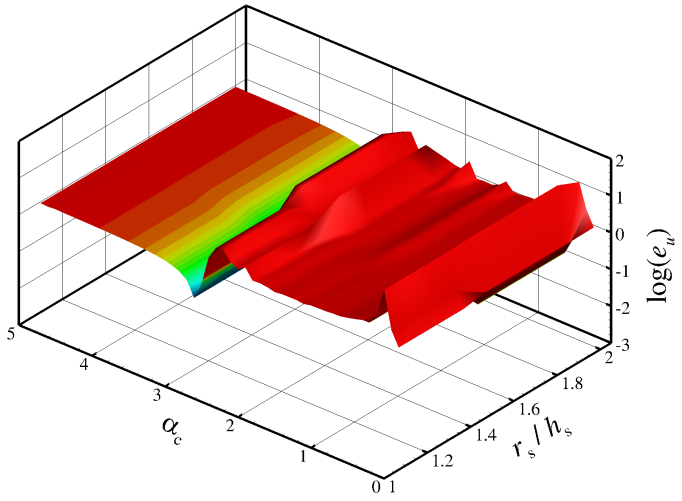

Figure 5.31: Cylinder under NatBCs - parametric study - primal - RPIM1 functions

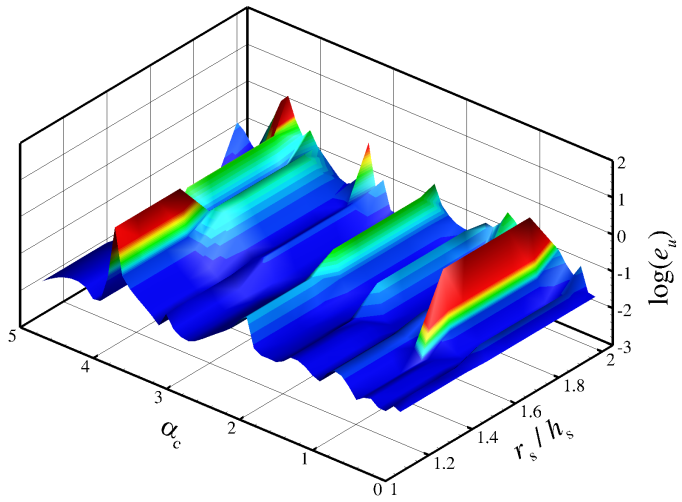

Figure 5.32: Cylinder under NatBCs - parametric study - mixed - RPIM1 functions

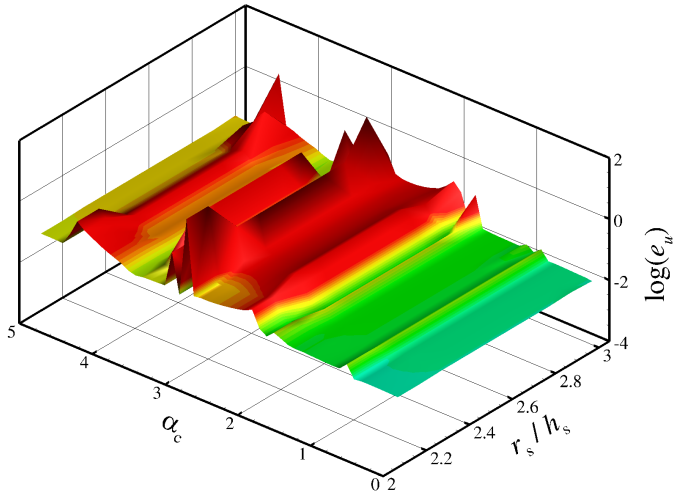

Figure 5.33: Cylinder under NatBCs - parametric study - primal - RPIM2 functions

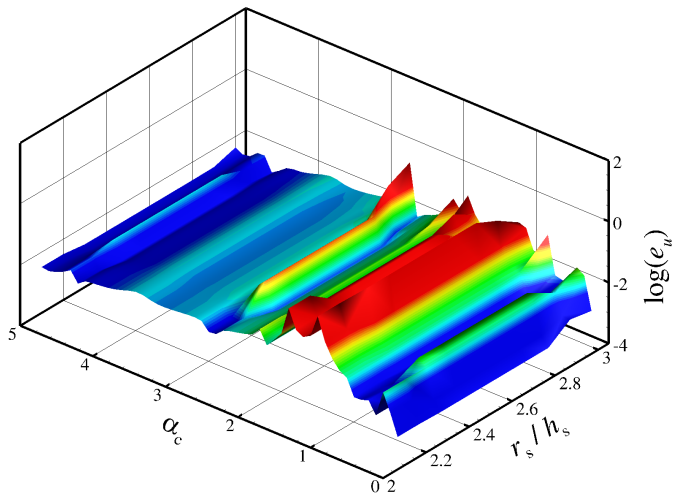

Figure 5.34: Cylinder under NatBCs - parametric study - mixed - RPIM2 functions

From the RPIM parametric studies it can be observed that the accuracy behaviour is more oscillatory if compared to the studies from the previous cylinder example. This is probably due to the introduction of natural boundary conditions in the numerical model. In addition, it can be observed that a wrong choice of the shape parameter in the primal approach can result in very inaccurate results, especially when the first-order approximation is considered. However, in the mixed method accurate solutions can be attained for a large number of combinations of meshless parameters even if the lowest-order is used. Thus, the mixed approach seems to be more insensitive to the choice of the RBF shape function parameter.

Here again, in order to present the convergence studies, the best parameters are chosen from the parametric studies. Thus, the convergence studies, portrayed in Figures 5.35 and 5.36, are computed using the relative errors e_u and e_σ in the L_2 norm of displacement and

stresses. For numerical convergence tests, the local approximation domain sizes used for the first- and the second-order approximations are equal to $r_s/h_s = 1.5$ and $r_s/h_s = 2.5$, respectively. As in the previous example, equal local approximation domain sizes are used for both approaches in order to compare the methods in a fair manner. For each approach and for each order of the RPIM function, an appropriate shape parameter α_c is used. Hence, for the primal approach with the first-order approximation (RPIM1-P) $\alpha_c = 3.0$ is utilized, while for the mixed approach of the same order (RPIM1-M) $\alpha_c = 3.4$ is considered. For the primal formulation using the second-order basis (RPIM2-P) $\alpha_c = 0.5$ is chosen and for the mixed formulation of the same order (RPIM2-M) $\alpha_c = 0.1$ is applied.

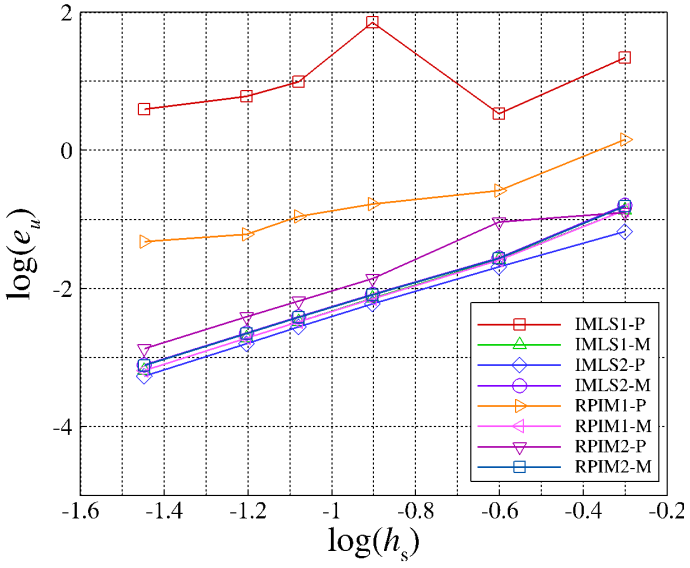

Figure 5.35: Cylinder under NatBCs - displacement e_u convergence test

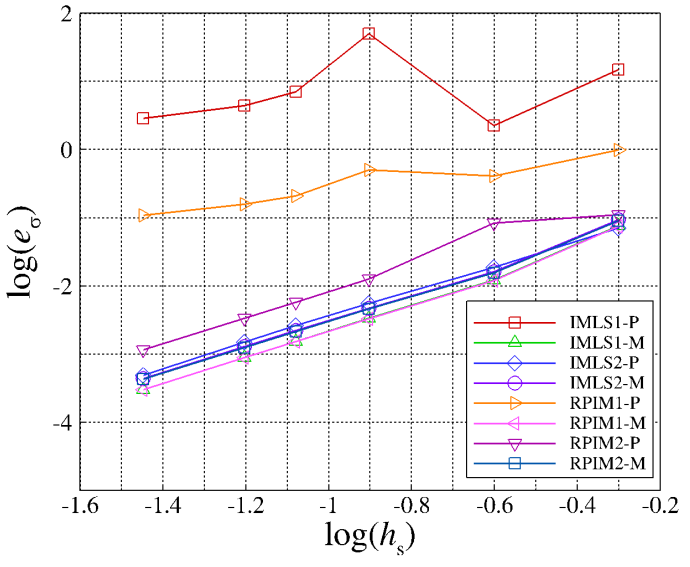

Figure 5.36: Cylinder under NatBCs - stress e_σ convergence test

If the IMLS approximation is analyzed, the mixed approach with the first-order approximation functions (IMLS1-M) achieves similar performance like the primal approach employing the second-order approximations (IMLS2-P). On the other hand, again no convergence is observed when the first-order approximations are employed in the primal approach (IMLS1-P). As obvious, with a proper choice of RBF shape parameter in the first-order of the RPIM approximation some accuracy can be gained, but the convergence rate remains very low. Furthermore, to present in detail the advantage of the mixed approach, the distributions of radial displacement u_r, radial strain ε_r, as well as the radial and circular stress σ_r and σ_ϕ, respectively, are shown in Figures 5.37 - 5.40. All computations have been performed by the numerical model with 144 grid points. The solutions obtained by the fully displacement formulation using the first-order interpolation function (IMLS1-P) are again excluded from some figures due to high numerical errors.

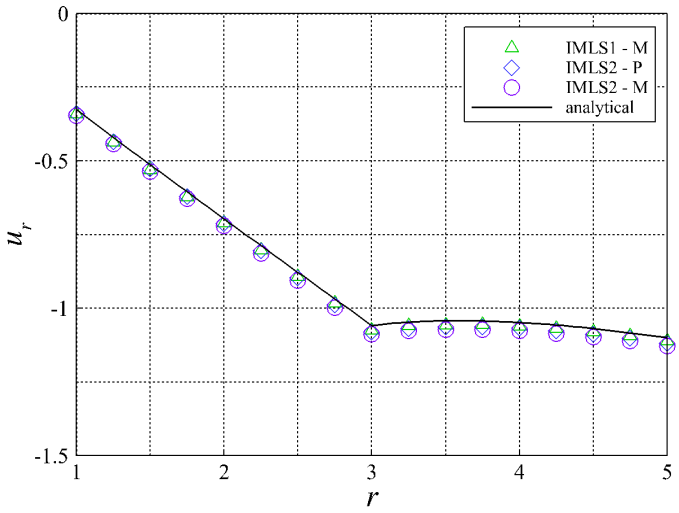

Figure 5.37: Cylinder under NatBCs - distribution of radial displacement u_r for $y = 0$

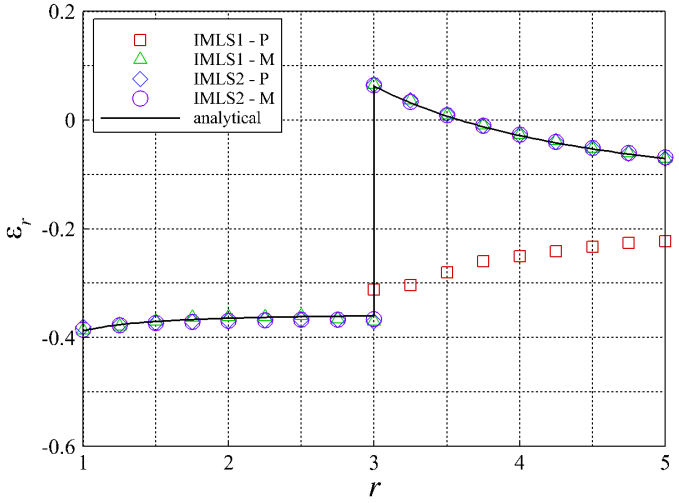

Figure 5.38: Cylinder under NatBCs - distribution of radial strain ε_r for $y = 0$

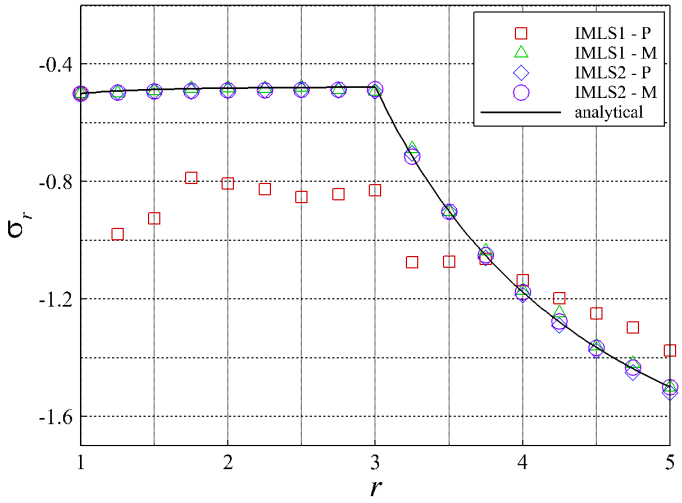

Figure 5.39: Cylinder under NatBCs - distribution of radial stress σ_r for $y = 0$

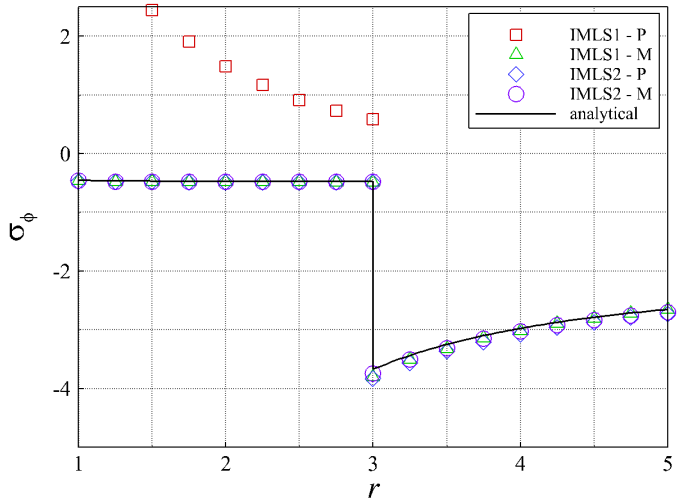

Figure 5.40: Cylinder under NatBCs - distribution of circular stress σ_ϕ for $y = 0$

The presented diagrams show that the proposed mixed approach captures the discontinuity within the heterogeneous structure with a high accuracy even in the case of IMLS1-M. In order to compare the numerical solutions obtained by the mixed collocation method to the analytical results, the contour plots of the distributions obtained using IMLS1-M for radial strain ε_r and circular stress σ_ϕ are shown in Figures 5.41 - 5.44. The accuracy of the proposed formulation is again displayed.

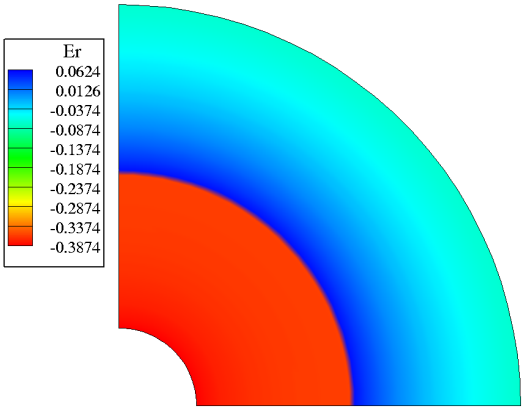

Figure 5.41: Cylinder under NatBCs - contour plot of ε_r - analytical solution

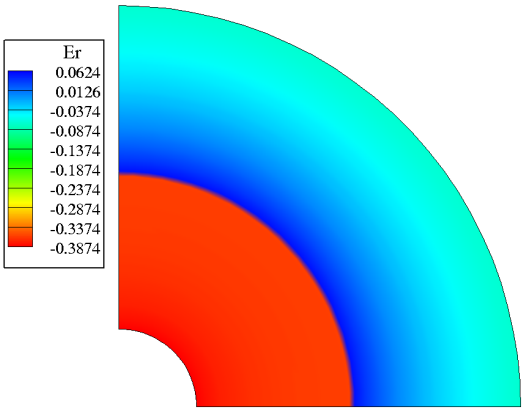

Figure 5.42: Cylinder under NatBCs - contour plot of ε_r - mixed MLPG2 - 1716 nodes

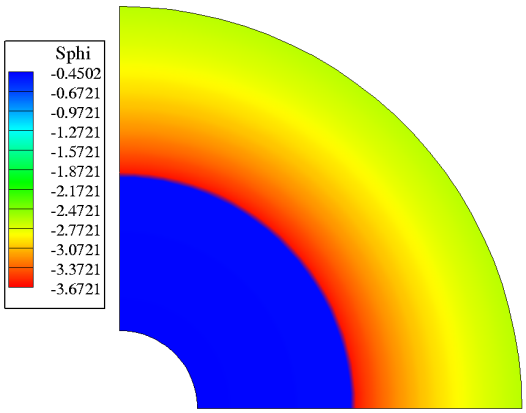

Figure 5.43: Cylinder under NatBCs - contour plot of σ_ϕ - analytical solution

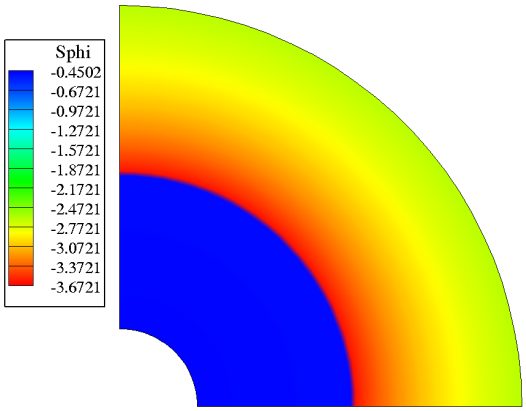

Figure 5.44: Cylinder under NatBCs - contour plot of σ_ϕ - mixed MLPG2 - 1716 nodes

5.5.4. Rectangular plate under linear traction load

A rectangular heterogeneous plate composed of two different materials Ω^+ and Ω^- separated by the vertical interface is chosen as the fourth numerical test, as depicted in Figure 5.45. The material properties of the left part of the plate are taken as $E^+ = 1000$ and $\nu^+ = 0.25$, while the material data of the right side are $E^- = 10000$ and $\nu^- = 0.3$. The geometry of each homogeneous subdomain is defined by the length $L = 3$ and the height $H = 3$. On the left edge of the plate the displacement components are suppressed, while the traction boundary conditions are imposed along other edges. As shown in Figure 5.45, a uni-axial linear continuous load defined as $\bar{t}_x^{\mathrm{RE}}$ is applied on the right edge. The plate is discretized by uniform nodal distributions, where the nodal distances in both x and y directions are denoted by h_{s}.

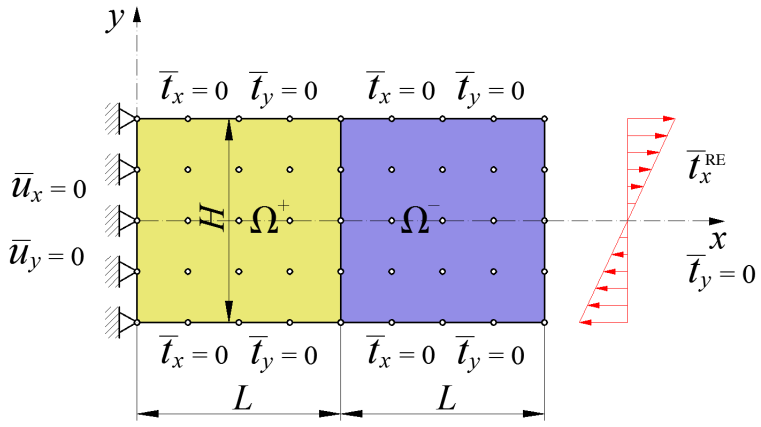

Figure 5.45: Discretized rectangular plate with boundary conditions

For the verification of the presented mixed approach (M), convergence studies are carried out and the results are compared to the solutions obtained by the fully displacement meshless formulation (P) [28]. The converged finite element solution obtained by 32768

CPS4 elements using software Abaqus [202] is taken as the reference solution. The error norms are computed by (5.63) and (5.64), whereby only the nodes along the line $y = -0.75$ are considered for the error calculation. The convergence studies of both approaches are portrayed in Figures 5.46 and 5.47.

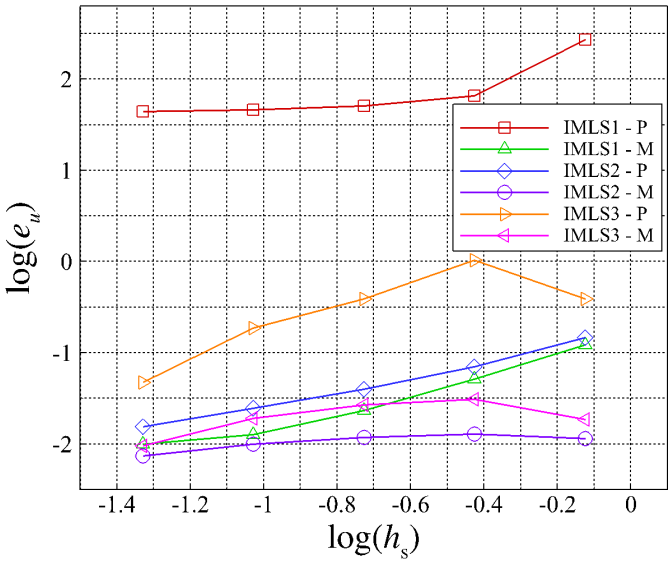

Figure 5.46: Rectangular plate - displacement e_u convergence test

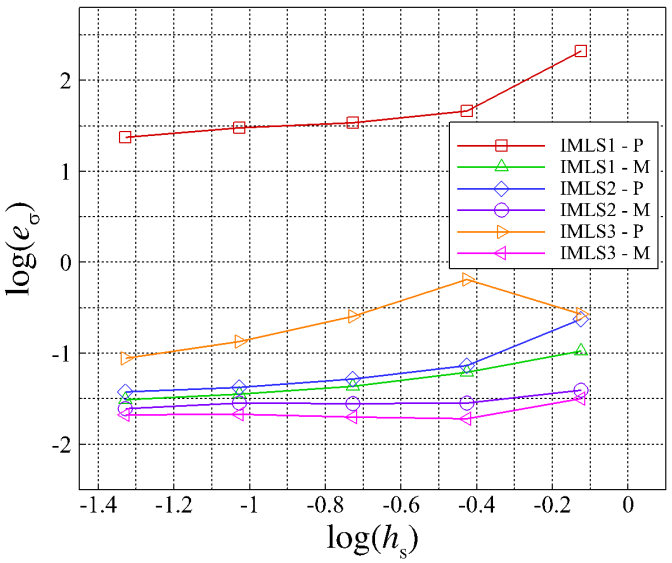

Figure 5.47: Rectangular plate - stress e_σ convergence test

As evident, the meshless interpolation schemes using the first- (IMLS1), the second- (IMLS2) and the third-order (IMLS3) basis are tested. The local approximation domain sizes are taken equal for both fully displacement and mixed meshless approaches in order to objectively compare the accuracy of the methods. Hence, for the interpolation scheme with the first-order basis (IMLS1), the local approximation domain size $r_s = 1.35h_s$ is

applied, for the second-order (IMLS2) $r_s = 2.35h_s$ is utilized and for the third-order (IMLS3) $r_s = 3.5h_s$ is used.

As obvious from the analysis of the convergence rates, the mixed approach is superior to the primal formulation, especially in the case when the lowest order of the interpolation is used, as expected. It can be noted that the mixed approach converges to approximately the same accuracy irrespectively of the MLS basis used. Thereby, it can be concluded that the second- and third-order bases yield practically converged values even when the smallest number of nodes is used. On the other hand, the primal approach with the first-order function (IMLS1-P) does not converge to the referent solution. The mixed approach employing the first-order approximation (IMLS1-M) achieves slightly better accuracy and similar convergence rates as the primal method with the second-order approximation (IMLS2-P). Furthermore, it can be observed that the primal approach with the third-order interpolation function exhibits certain problems attaining accurate solutions if the discretizations with the small number of nodes are used. For further verification of the proposed approach, the distributions of the displacement component u_x, strain components ε_x, ε_y and stress component σ_y along the line $y = -0.75$ are presented in Figures 5.48 - 5.51. Herein, the numerical model with 162 equidistant nodes is used. The distributions obtained by using the primal approach with the first-order interpolation function (IMLS1-P) are expelt from some of the graphs because the results are highly inaccurate and cannot be adequately portrayed.

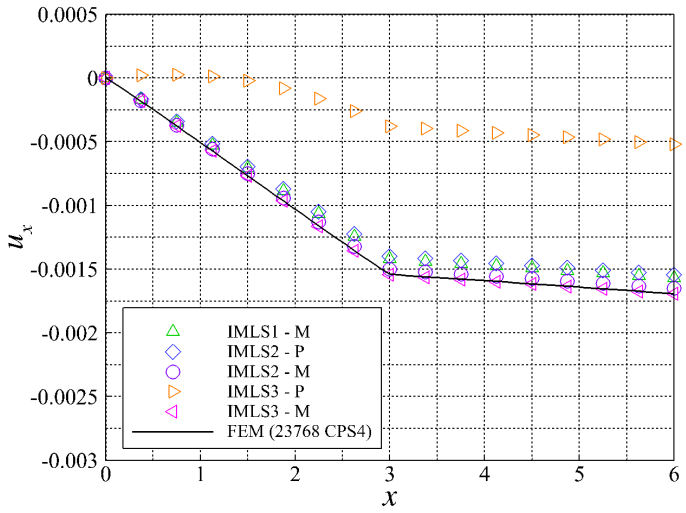

Figure 5.48: Rectangular plate - distribution of displacement u_x for $y = -0.75$

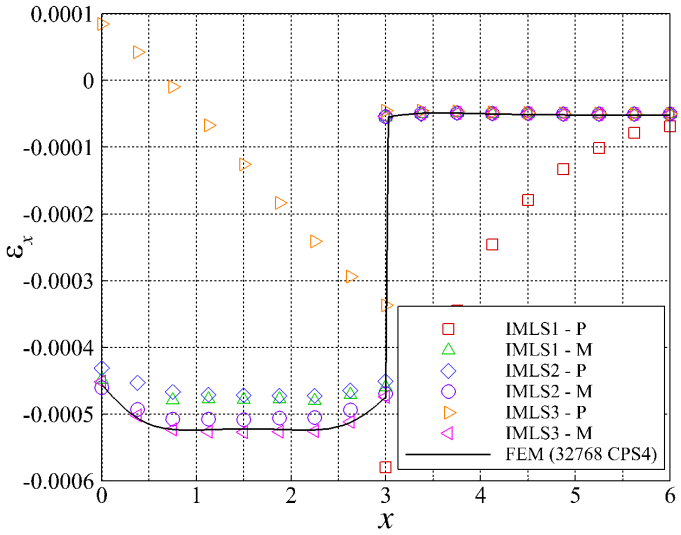

Figure 5.49: Rectangular plate - distribution of strain ε_x for $y = -0.75$

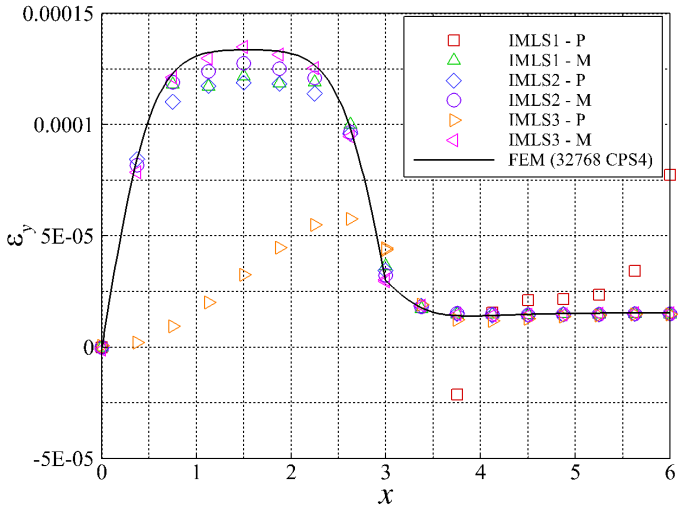

Figure 5.50: Rectangular plate - distribution of strain ε_y for $y = -0.75$

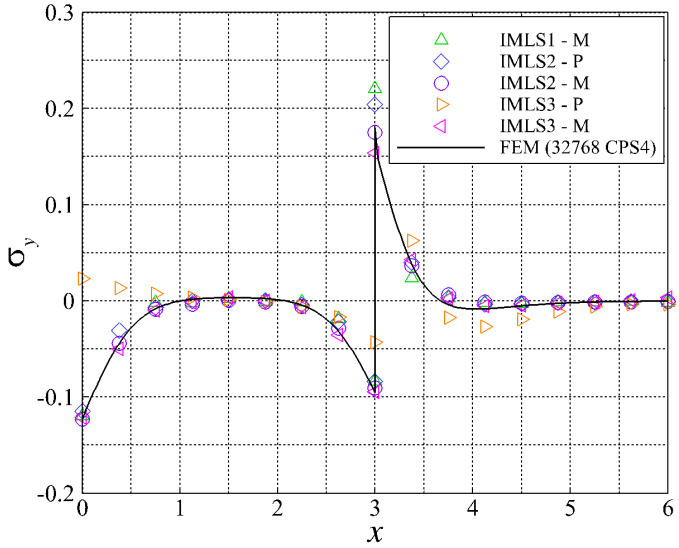

Figure 5.51: Rectangular plate - distribution of stress σ_y for $y = -0.75$

From the presented distributions, it can be deduced that the proposed mixed approach accurately captures the jumps in the strain and stress fields regardless of the choice of the order of the interpolation function, which is not the case for the primal approach. Since the error norms are only calculated using the nodes at $y = -0.75$, to demonstrate the global accuracy of the method, the contour plots of the displacement and strain components obtained by the MLPG2 method and the contour plots of the reference finite element solutions are compared in Figures 5.52 - 5.55.

Figure 5.52: Rectangular plate - contour plot of u_y - reference FEM solution

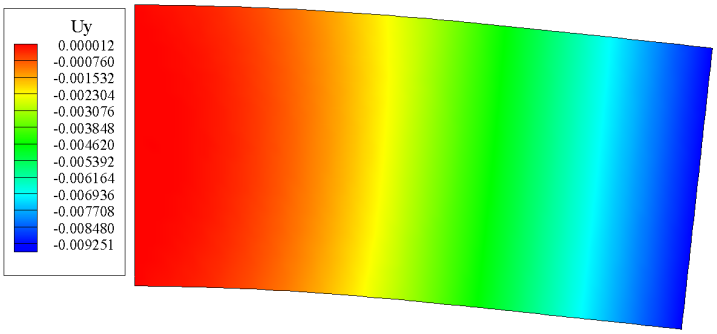

Figure 5.53: Rectangular plate - contour plot of u_y - mixed MLPG2 - 2178 nodes

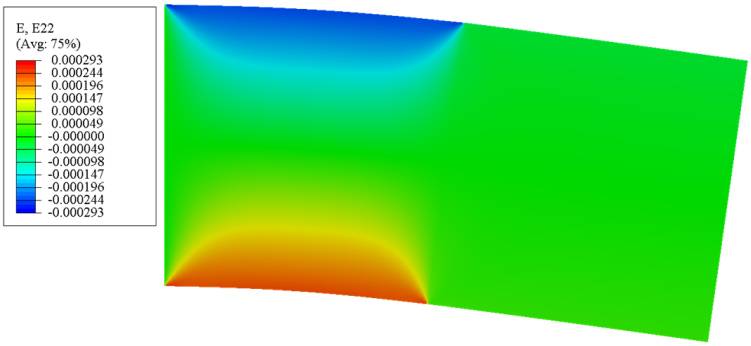

Figure 5.54: Rectangular plate - contour plot of ε_y - reference FEM solution

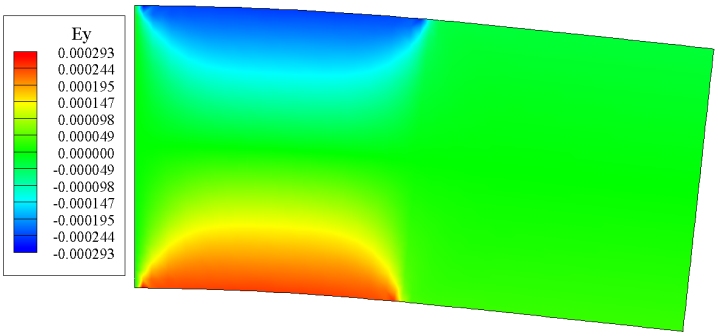

Figure 5.55: Rectangular plate - contour plot of ε_y - mixed MLPG2 - 2178 nodes

In the following, the computational efficiency of the mixed collocation method is assessed. In this study, the total computational time needed for the assembling and solving of the global system of equations and the numerical accuracy of the method is considered and compared to the FEM using two dimensional elements for plane stress analysis. In order to obtain objective results, in this example a homogeneous plate with identical dimensions, loading and constraints as in the previous analysis is considered, and only the discretizations with uniform nodal distributions are employed. The homogeneous plate is taken for the analysis because the analytical solution is known [23] which is used as the referent solution, and the homogeneity has no influence on the computational efficiency

assessment. For the purpose of comparison, the first-order triangular (CPS3) and quadrilateral (CPS4) finite elements from the commercial program package ABAQUS [202] are used, with nodal displacements as degrees of freedom. In the meshless method, the approximations with complete linear (IMLS1) and bilinear basis (IMLS1 BB) are utilized. The FORTRAN code is developed to test the proposed meshless approach. The computational time dependent on the number of degrees of freedom for both the FEM and the mixed MLPG2 method is portrayed in Figure 5.56. Therein, the time is expressed in milliseconds. It is obvious that although there is no numerical integration over the computational domain or the boundaries, the present method is still slower than the comparable FEM formulations for the same number of degrees of freedom, especially in the case of large models. This can be attributed to the non-optimized FORTRAN code used for the meshless simulations. It has been noted that the time needed for solving the equation system steeply increases with the number of degrees of freedom, largely because of the equation solver used, which solves a system of distributed linear equations with a general square matrix, using the LU factorization. Further significant leakage of the computational time can be attributed to the matrix manipulation needed to eliminate the nodal stress variables from the equations system.

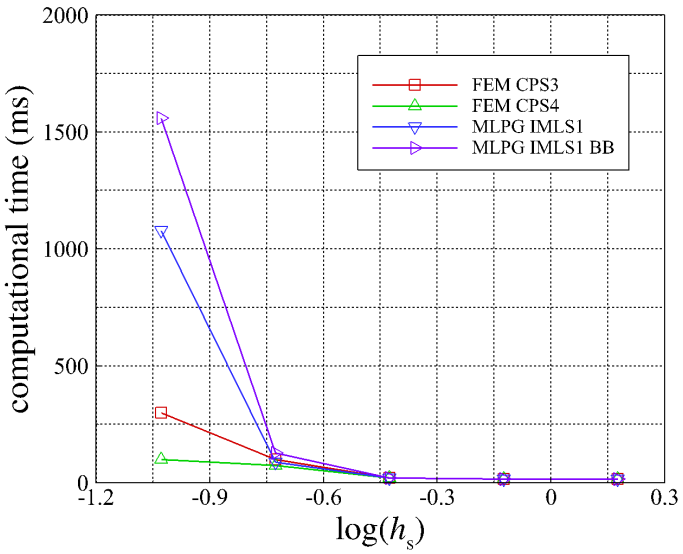

Figure 5.56: Rectangular homogeneous plate - comparison of computational time

The results of convergence tests for the displacement and stress fields are shown in Figures 5.57 and 5.58. All tested formulations achieve similar convergence rates and accuracy for the displacements, while the meshless approach yields considerably more accurate results for the stresses when using the same number of nodes in finer discretizations. This indicates that although in its present form the proposed collocation method is still slower than FEM for the same number of degrees of freedom, it is nevertheless capable of at-

taining the same accuracy as FEM by using models with coarser discretization patterns.

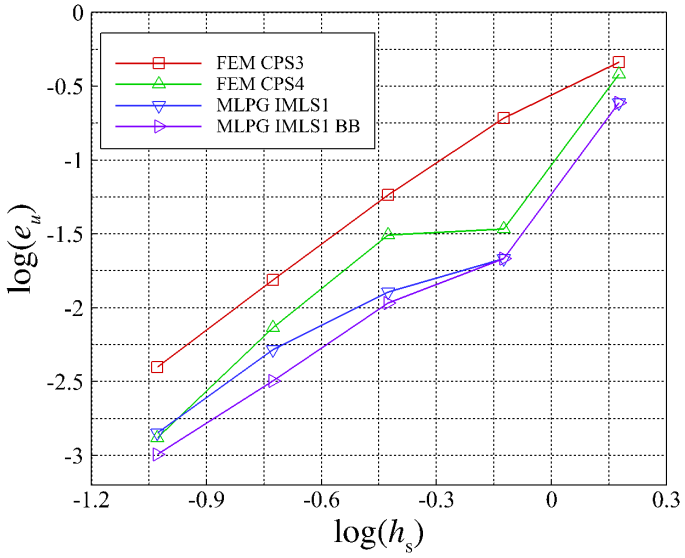

Figure 5.57: Rectangular homogeneous plate - displacement e_u convergence test

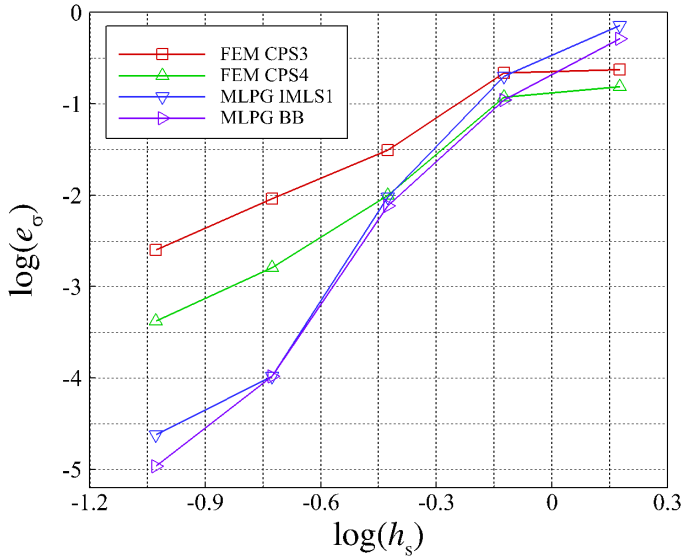

Figure 5.58: Rectangular homogeneous plate - stress e_σ convergence test

5.5.5. Plate with circular inclusion under uniform traction

As the final example, a rectangular square plate of $2L$ x $2L$ with the circular inclusion of radius R, subjected to the unit horizontal traction t^0 is considered, as depicted in Figure 5.59.

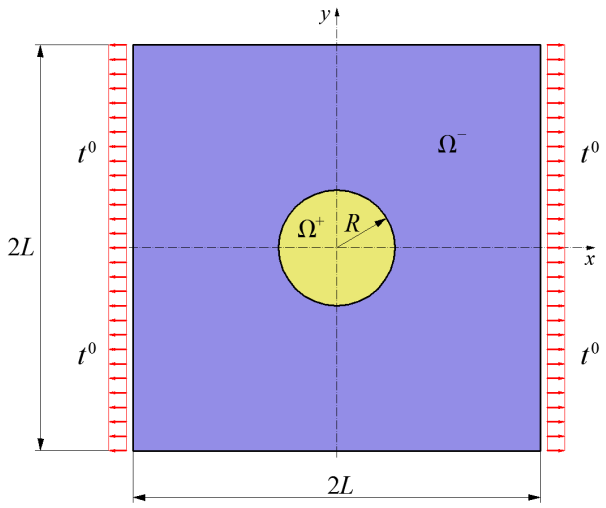

Figure 5.59: Plate with circular inclusion subjected to uniform traction

Due to the symmetry, only one quarter of the plate consisting of the two subdomains Ω^+ and Ω^- is discretized, as shown in Figure 5.60. As obvious, the symmetry boundary conditions are used along the left and bottom edges, while the tractions, $\bar{t}_x^{\mathrm{a}}$ and $\bar{t}_y^{\mathrm{a}}$, taken from the analytical solution [203] are prescribed on all outer edges. The material properties of the plate are $E^- = 1000$, $\nu^- = 0.25$, while the values of $E^+ = 10000$ and $\nu^+ = 0.25$ are chosen for the inclusion.

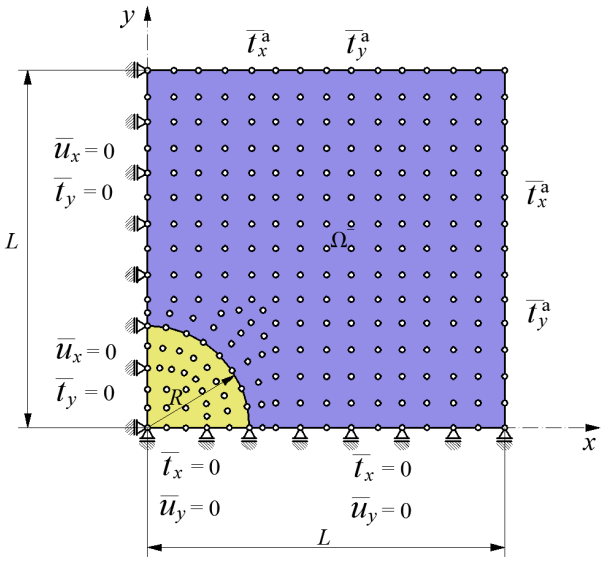

Figure 5.60: Plate with circular inclusion with considered boundary conditions

The computation is performed by using the interpolation functions employing the second- and third-order basis (IMLS2, IMLS3). The accuracy of the numerical solutions are again compared with the analytical solutions [203] by means of the error norms expressed by relations (5.63) and (5.64). In this example, neither approach converges to the analytical solution when the first-order basis (IMLS1) is used, which is the reason

that this basis has not been considered. The convergence rates for the interpolation functions employing the second- and the third order basis are presented in Figures 5.61 and 5.62. Herein, the corresponding local approximation domain sizes are $r_s/h_s = 2.4$ and $r_s/h_s = 3.45$ for the second-order basis and for the third-order basis, respectively, where h_s denotes the average nodal distance. The convergence rates are analyzed using the total number of collocation nodes in the numerical models.

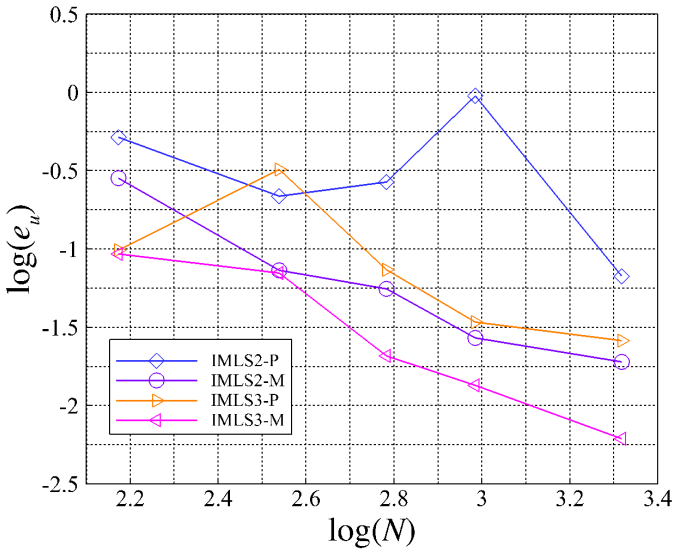

Figure 5.61: Plate with circular inclusion - displacement e_u convergence test

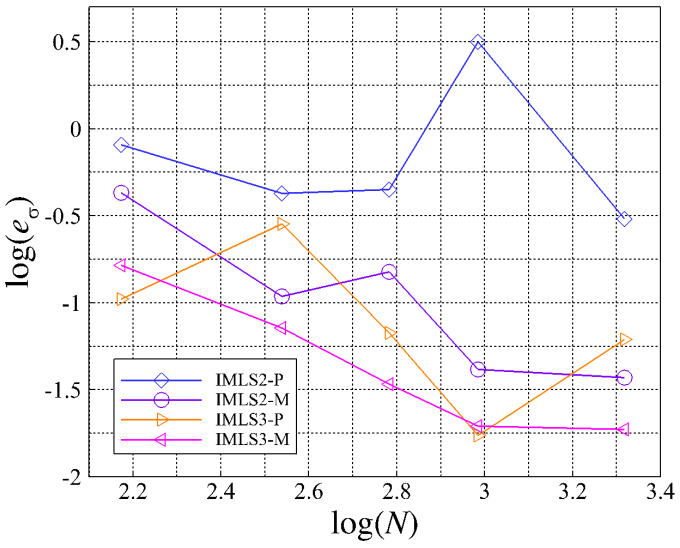

Figure 5.62: Plate with circular inclusion - stress e_σ convergence test

The diagrams portray more stable convergence behavior when the presented mixed approach is employed. In general, the results show that the mixed approach, for the considered interpolation functions, yields globally more accurate results for all discretizations

used, as expected. The discretizations are generated simply by increasing the number of collocation nodes continuously starting with the grid shown in Figure 5.60. In order to check if the influence of the material discontinuity on the structure deformation responses is accurately captured, the distributions of the displacement component u_y, strain components ε_x, ε_y and stress component σ_x are analysed for $x = 0$, and the results are presented in Figures 5.63 - 5.66. These distributions were obtained by the discretization with 606 collocation nodes. Yet again, the distributions obtained by using the second- (IMLS2) and third-order (IMLS3) functions for both approaches are shown.

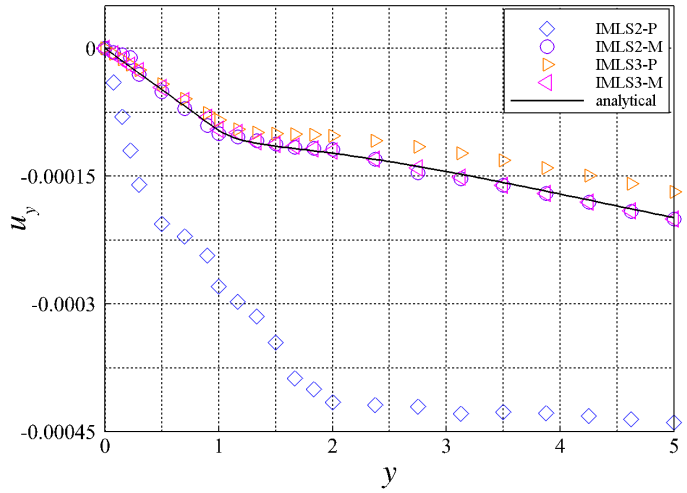

Figure 5.63: Plate with circular inclusion - distribution of displacement u_y for $x = 0$

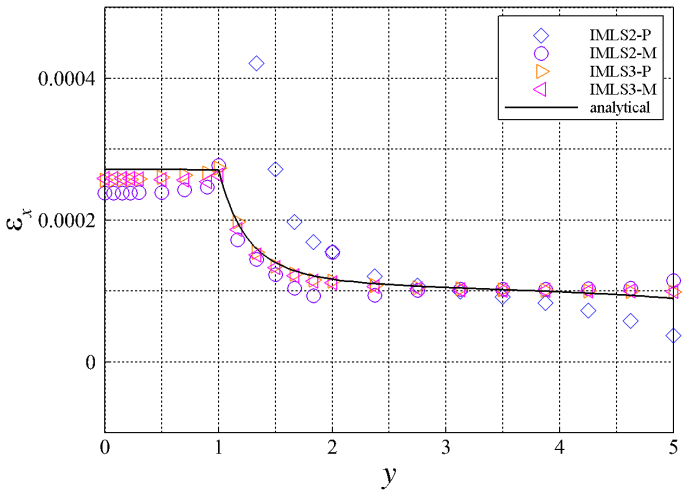

Figure 5.64: Plate with circular inclusion - distribution of strain ε_x for $x = 0$

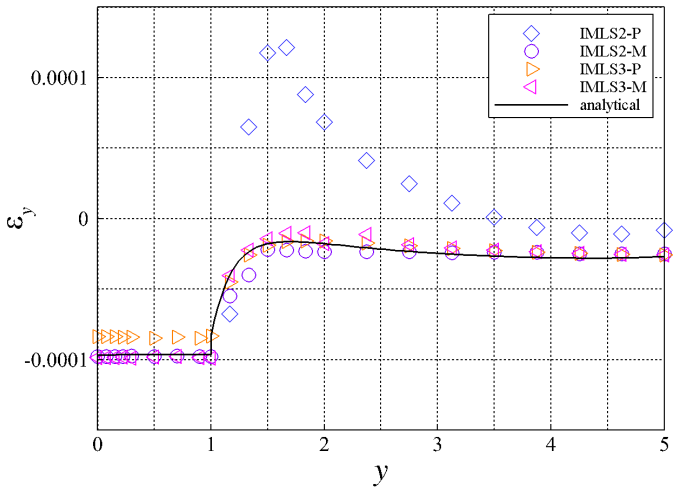

Figure 5.65: Plate with circular inclusion - distribution of strain ε_y for $x = 0$

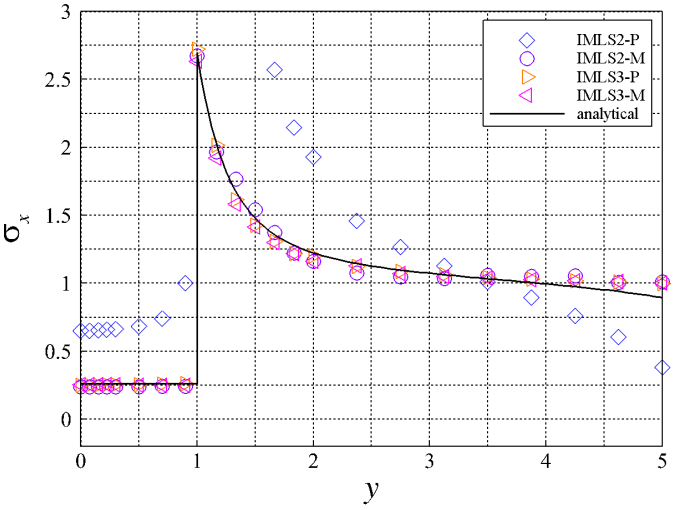

Figure 5.66: Plate with circular inclusion - distribution of stress σ_x for $x = 0$

Again, the mixed approach is more accurate for the same number of nodal discretization points. As obvious, the use of the primal approach in combination with the second-order interpolation functions (IMLS2-P) can result in very large errors in the model. In this example, the numerical efficiency of the proposed collocation formulation is again tested by investigating convergence and computational time, and the results are compared with those obtained by FEM. Here, a more realistic problem is considered, where the geometric boundary between the inclusion and the plate is relatively complex, which requires non-uniform discretization patterns around the interface, as illustrated in Figure 5.60. In addition, large gradients in the strain and stress fields are present in the areas around the interface, as shown in Figures 5.64 - 5.66. The global stress convergence rates are portrayed in Figure 5.67. Herein, the results obtained by the first-order triangular (CPS3), the first-order quadrilateral (CPS4), the second-order triangular (CPS6) and the

quadrilateral (CPS8) elements from ABAQUS [202] are compared with those computed by the proposed mixed MLPG2 utilizing the second- and third-order IMLS functions (IMLS2 and IMLS3, respectively). The available analytical solution from [203] is used as the referent result. The discretized L_2 norm expressed by (5.64) is used as the error indicator computed at all nodes of the numerical models in this test.

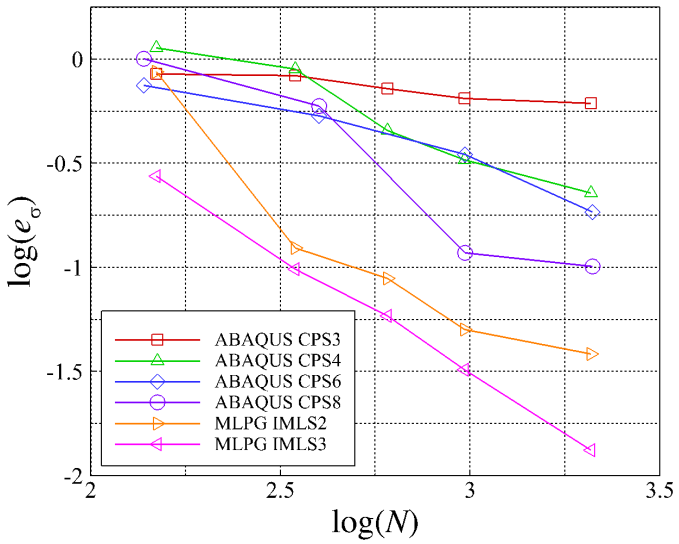

Figure 5.67: Plate with circular inclusion - comparison of numerical stress accuracy

From 5.67, it can be seen that the meshless approach is superior to the above mentioned finite element formulations with respect to the convergence rates and the numerical accuracy. As in the first example concerning rectangular plate, the proposed collocation method can achieve a comparable global accuracy as FEM by using considerably smaller number of discretization nodes. The computational time and the size of the discretized models with respect to the number of nodes needed for a required level of accuracy are presented in Table 5.1 for IMLS2, CPS6 and CPS8 models. The results for the discretization by the first-order elements are not listed in the table because the accuracies required for this test could not be obtained with such models, regardless of the mesh topologies. The computational time for the meshless method is smaller than for FEM, especially for the model with fewer nodes, indicating that the presented approach could be a potentially interesting alternative to FEM in solving similar problems. It is important to emphasize that a further careful optimization of the developed meshless code is necessary in order to make a more trustworthy assessment about the numerical efficiency of the present approach. The contour plots of the analytical solutions for the entire structure are compared to the obtained mixed meshless solutions using the second-order (IMLS2) functions in Figures 5.68 - 5.71, where the strain component ε_x and the stress component σ_x are depicted. Herein, the meshless discretization with 965 nodes is utilized. The accuracy of

Table 5.1: Plate with circular inclusion - comparison of computational costs

e_σ	IMLS2	CPS6	CPS8
0.12401	95 ms / 346 nodes	300 ms / 2875 nodes	200 ms / 966 nodes
0.08847	256 ms / 606 nodes	400 ms / 4112 nodes	300 ms / 2656 nodes

the meshless formulation is again proved.

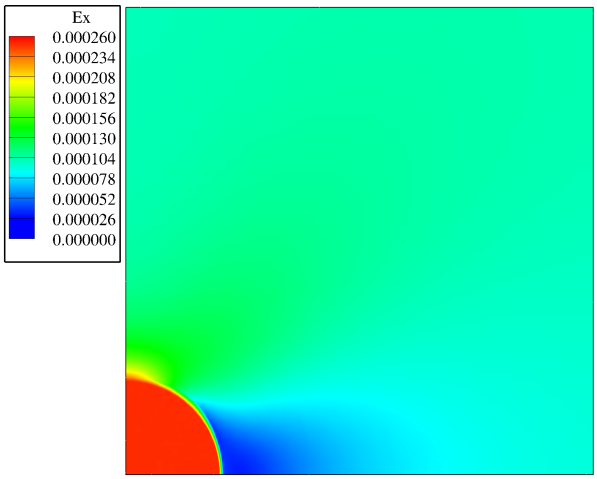

Figure 5.68: Plate with circular inclusion - contour plot of ε_x - analytical solution

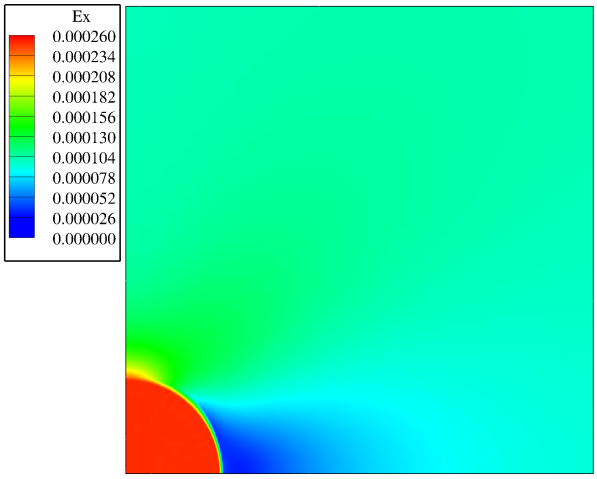

Figure 5.69: Plate with circular inclusion - contour plot of ε_x - mixed MLPG2 - 965 nodes

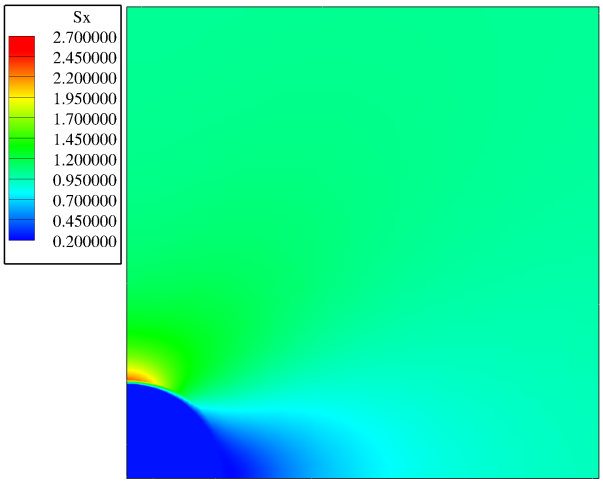

Figure 5.70: Plate with circular inclusion - contour plot of σ_x - analytical solution)

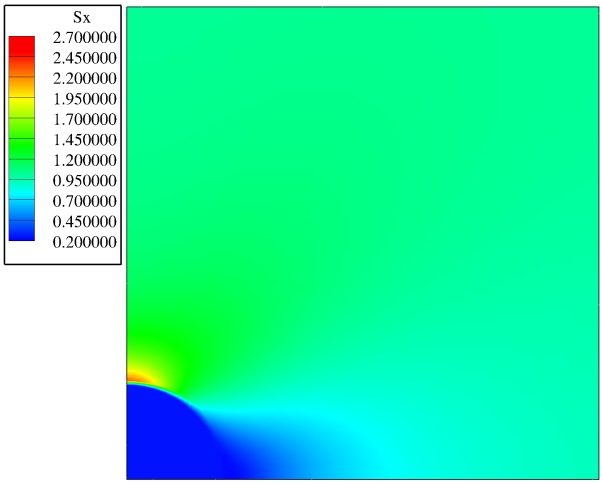

Figure 5.71: Plate with circular inclusion - contour plot of σ_x - mixed MLPG2 - 965 nodes)

6 Meshless modeling of heterogeneous materials using gradient elasticity

In order to more accurately model the deformation of the entire heterogeneous structure, influencing the discontinuity that is present at the interface of different materials in linear elasticity, gradient elasticity theory is considered. Thus, in this chapter staggered gradient elasticity formulations for the modeling of homogeneous, as well as heterogeneous structures are studied. The staggered procedures based on the Aifantis theory have been chosen. Due to the two-step nature of the algorithms, the gradient elasticity problem is solved using two different sets of second-order differential equations where the solution of the first one is used as an input for solving the second set of equations. Herein, various operator-split procedures can be distinguished, as presented in Chapter 2. Hence, for solving the boundary value problem of the heterogeneous materials using the linear gradient elasticity, two different operator-split mixed collocation methods are considered. Both methods are based on the local MLPG concept and use the IMLS functions for approximating unknown field variables. Thus, in this chapter, the newly developed mixed collocation methods are presented and applied for the modeling of deformation, the description of size effects and the removal of singularities (discontinuities). Firstly, the governing equations and the boundary conditions in the displacement-based u-RA and the strain-based ε-RA approach for the heterogeneous material are briefly discussed. Afterward, the discretization of the classical and the gradient boundary value problem, associated with the staggered solution scheme, of heterogeneous material is explained. In addition, the proposed mixed collocation methods are presented in detail. Herein, the discretized forms of the u-RA and ε-RA governing equations and boundary conditions are presented. Since only the collocation methods are considered, the methods do not possess any numerical integration procedures. Hence, the system of discretized equations is easily obtained. Depending on the chosen staggered procedure, different unknown field variables are approximated. In the mixed u-RA approach, for the unknown field variables two components of displacements and four components of gradients of displacements are utilized, while in the mixed ε-RA three components of strains and six components of gradients of

strains are used. As in classical elasticity, all field variables are approximated using the same meshless functions. Due to the interpolatory property of the applied approximations, the essential boundary conditions in both staggered procedures are enforced as simply as in FEM. For impositions of the classical and gradient natural boundary conditions, the direct collocation method is applied. At the interface nodes in the heterogeneous structure, the continuity of the essential boundary conditions and the reciprocity of natural boundary conditions, depending on the utilized staggered procedure, are enforced. The final system of discretized equations of the u-RA procedure has got nodal displacements as unknowns, while the system of the ε-RA procedure has nodal strains as unknowns. In closing of the chapter, several numerical examples are presented. Herein, the deformation modeling of homogeneous and heterogeneous bars is utilized for the verification of the mixed staggered algorithms. For the mentioned one-dimensional problems the obtained numerical results are compared with the obtainable analytical solutions. The numerical example of the homogeneous plate is used to test the modeling of size effects, while the removal of discontinuities is tested on a simple example of a heterogeneous plate.

6.1. Governing equations and boundary conditions in the staggered procedures

In order to present the derivation of the discretized system of equations for strain gradient staggered procedures, a 2-D heterogeneous material Ω ($\Omega = \Omega^+ \cup \Omega^-$) surrounded by the global outer boundary Γ ($\Gamma = \Gamma^+ \cup \Gamma^-$) is divided into two homogeneous subdomains. Since in the staggered procedures two different boundary value problems are solved one after another, the global boundary Γ can be denoted as c or g to distinguish whether the classical or gradient boundary value problem is being solved. Hence, the typical heterogeneous structure analyzed is portrayed in Figure 6.1.

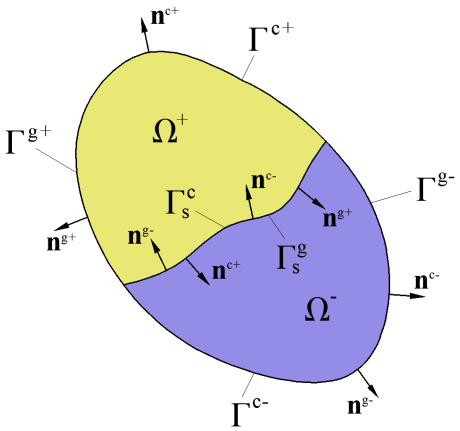

Figure 6.1: Heterogeneous structure for strain gradient staggered procedures

Same analogy applies to all the other boundaries, where some kind of boundary condition is prescribed, e.g. the interface boundary Γ_s is in the classical boundary value problem denoted as Γ_s^c, while in the gradient one it is denoted Γ_s^g. As presented in Chapter 2., the field equations solved in the staggered procedures are different depending at which point the original fourth-order Aifantis gradient elasticity equation is split. Thus, in this section the equations and the corresponding boundary conditions will be presented separately for each of the utilized procedures and for each of the homogeneous materials composing the discretized heterogeneous structure depicted on Figure 6.2.

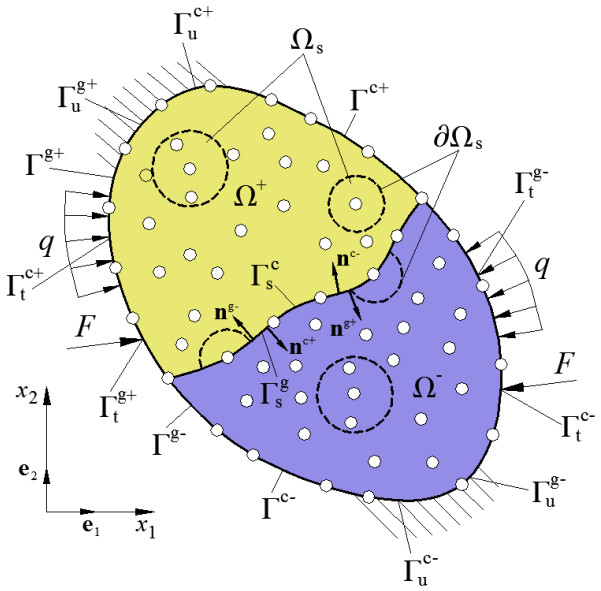

Figure 6.2: Boundary conditions in strain gradient staggered procedures

- ***u*-RA staggered procedure**

  The equations (2.32) and (2.33) are the two sets of second-order partial differential equations that are utilized to describe the deformation of the heterogeneous material defined in Figure 6.2 using the u-RA staggered procedure. These equations are here written for each homogeneous material separately. Thus, the first equations representing the corresponding equivalent to the classical elasticity are equal to

$$\frac{1}{2}C^+_{ijkl}(u^{c+}_{k,jl} + u^{c+}_{l,jk}) + b^+_i = 0, \quad \text{within } \Omega^+, \tag{6.1}$$

$$\frac{1}{2}C^-_{ijkl}(u^{c-}_{k,jl} + u^{c-}_{l,jk}) + b^-_i = 0, \quad \text{within } \Omega^-, \tag{6.2}$$

  while the second equations of the non-local gradient problem described by the non-homogeneous Helmholtz equations are defined as

$$u^{g+}_i - l^2 u^{g+}_{i,mm} = u^{c+}_i, \quad \text{within } \Omega^+, \tag{6.3}$$

$$u^{g-}_i - l^2 u^{g-}_{i,mm} = u^{c-}_i, \quad \text{within } \Omega^-. \tag{6.4}$$

As evident, firstly the classical boundary value problem is solved, whose solution is then used as the input on the right hand side of the gradient equations. In this displacement-based operator procedure, on the outer boundaries of the heterogeneous structure appropriate classical and gradient boundary condition need to be satisfied. Hence, the classical boundary conditions include classical displacements and tractions

$$u_i^{\mathrm{c}+} = \bar{u}_i^{\mathrm{c}+}, \quad \text{on } \Gamma_{\mathrm{u}}^{\mathrm{c}+}, \tag{6.5}$$

$$u_i^{\mathrm{c}-} = \bar{u}_i^{\mathrm{c}-}, \quad \text{on } \Gamma_{\mathrm{u}}^{\mathrm{c}-}, \tag{6.6}$$

$$t_i^{\mathrm{c}+} = \sigma_{ij}^{\mathrm{c}+} n_j^{\mathrm{c}+} = \bar{t}_i^{\mathrm{c}+}, \quad \text{on } \Gamma_{\mathrm{t}}^{\mathrm{c}+}, \tag{6.7}$$

$$t_i^{\mathrm{c}-} = \sigma_{ij}^{\mathrm{c}-} n_j^{\mathrm{c}-} = \bar{t}_i^{\mathrm{c}-}, \quad \text{on } \Gamma_{\mathrm{t}}^{\mathrm{c}-}, \tag{6.8}$$

while the gradient boundary conditions include the gradient displacements and the second-order normal derivatives of gradient displacements [154]

$$u_i^{\mathrm{g}+} = \bar{u}_i^{\mathrm{g}+}, \quad \text{on } \Gamma_{\mathrm{u}}^{\mathrm{g}+}, \tag{6.9}$$

$$u_i^{\mathrm{g}-} = \bar{u}_i^{\mathrm{g}-}, \quad \text{on } \Gamma_{\mathrm{u}}^{\mathrm{g}-}, \tag{6.10}$$

$$R_i^{\mathrm{g}+} = n_j^{\mathrm{g}+} n_k^{\mathrm{g}+} \kappa_{ijk}^{\mathrm{g}+} = \frac{\partial^2 u_i^{\mathrm{g}+}}{\partial n^{\mathrm{g}+2}} = \bar{R}_i^{\mathrm{g}+}, \quad \text{on } \Gamma_{\mathrm{t}}^{\mathrm{g}+}, \tag{6.11}$$

$$R_i^{\mathrm{g}-} = n_j^{\mathrm{g}-} n_k^{\mathrm{g}-} \kappa_{ijk}^{\mathrm{g}-} = \frac{\partial^2 u_i^{\mathrm{g}-}}{\partial n^{\mathrm{g}-2}} = \bar{R}_i^{\mathrm{g}-}, \quad \text{on } \Gamma_{\mathrm{t}}^{\mathrm{g}-}. \tag{6.12}$$

In the equations (6.11) and (6.12), $\kappa_{ijk}^{\mathrm{g}+}$ and $\kappa_{ijk}^{\mathrm{g}-}$ denote the third-order tensors of second derivatives of gradient displacements. Furthermore, to acquire the solution for the entire structure, the interface conditions on the interface boundaries of the classical problem $\Gamma_{\mathrm{s}}^{\mathrm{c}}$ and the gradient problem $\Gamma_{\mathrm{s}}^{\mathrm{g}}$ need to be enforced. According to [156], if the classical elasticity problem is solved, these boundary conditions are the continuity of classical displacement and the reciprocity of classical tractions

$$u_i^{\mathrm{c}+} - u_i^{\mathrm{c}-} = 0, \quad \text{on } \Gamma_{\mathrm{s}}^{\mathrm{c}}, \tag{6.13}$$

$$\sigma_{ij}^{\mathrm{c}+} n_j^{\mathrm{c}+} + \sigma_{ij}^{\mathrm{c}-} n_j^{\mathrm{c}-} = 0, \quad \text{on } \Gamma_{\mathrm{s}}^{\mathrm{c}}, \tag{6.14}$$

and if the gradient problem is considered, the interface boundary conditions include the continuity of gradient displacement and the reciprocity of the first-order normal derivatives of gradient displacement T_i^{g} [156]

$$u_i^{\mathrm{g}+} - u_i^{\mathrm{g}-} = 0, \quad \text{on } \Gamma_{\mathrm{s}}^{\mathrm{g}}, \tag{6.15}$$

$$\frac{\partial u_i^{\mathrm{g}+}}{\partial n^{\mathrm{g}+}} + \frac{\partial u_i^{\mathrm{g}-}}{\partial n^{\mathrm{g}-}} = 0, \quad \text{on } \Gamma_{\mathrm{s}}^{\mathrm{g}}. \tag{6.16}$$

- **ε-RA staggered procedure**

  In this staggered procedure, the deformation modeling of the heterogeneous structure portrayed in Figure 6.2 is achieved by using equations (2.38) and (2.39) and again applying them to each homogeneous material independently. Hence, the first equations of classical elasticity are here written as

$$C^{+}_{ijkl}\varepsilon^{\mathrm{c}+}_{kl,j} + b^{+}_{i} = 0, \quad \text{within } \Omega^{+}, \tag{6.17}$$

$$C^{-}_{ijkl}\varepsilon^{\mathrm{c}-}_{kl,j} + b^{-}_{i} = 0, \quad \text{within } \Omega^{-}. \tag{6.18}$$

  If the above equations are compared to the classical equations from the u-RA procedure given by (6.1) and (6.2), it is easily observed that these equations are the same. The only difference between the mentioned equations is whether the kinematic relations (2.2) are included. The second set of the differential equations for the gradient problem for the ε-procedure is equal to

$$\varepsilon^{\mathrm{g}+}_{ij} - l^2\varepsilon^{\mathrm{g}+}_{ij,mm} = \varepsilon^{\mathrm{c}+}_{ij}, \quad \text{within } \Omega^{+}, \tag{6.19}$$

$$\varepsilon^{\mathrm{g}-}_{ij} - l^2\varepsilon^{\mathrm{g}-}_{ij,mm} = \varepsilon^{\mathrm{c}-}_{ij}, \quad \text{within } \Omega^{-}. \tag{6.20}$$

  Here again, in the first step the classical equations are solved, and the obtained classical strain field is utilized as a source term in the second set of the gradient equations. From the analysis of the staggered procedures in Chapter 2., it can be observed that the classical boundary conditions in these two procedures are identical. Thus, the classical boundary conditions of the ε-RA procedure are equal to (6.5) - (6.8). Since a different operator split procedure is utilized, the gradient boundary conditions are different from the ones presented for the u-RA procedure. Hence, the gradient boundary conditions in this procedure are the gradient strains and the first-order normal derivatives of gradient strains

$$\varepsilon^{\mathrm{g}+}_{ij} = \bar{\varepsilon}^{\mathrm{g}+}_{ij}, \quad \text{on } \Gamma^{\mathrm{g}+}_{\mathrm{u}}, \tag{6.21}$$

$$\varepsilon^{\mathrm{g}-}_{ij} = \bar{\varepsilon}^{\mathrm{g}-}_{ij}, \quad \text{on } \Gamma^{\mathrm{g}-}_{\mathrm{u}}, \tag{6.22}$$

$$R^{\mathrm{g}+}_{ij} = n^{\mathrm{g}+}_{k}\psi^{\mathrm{g}+}_{ijk} = \frac{\partial\varepsilon^{\mathrm{g}+}_{ij}}{\partial n^{\mathrm{g}+}} = \bar{R}^{\mathrm{g}+}_{ij}, \quad \text{on } \Gamma^{\mathrm{g}+}_{\mathrm{t}}, \tag{6.23}$$

$$R^{\mathrm{g}-}_{ij} = n^{\mathrm{g}-}_{k}\psi^{\mathrm{g}-}_{ijk} = \frac{\partial\varepsilon^{\mathrm{g}-}_{ij}}{\partial n^{\mathrm{g}-}} = \bar{R}^{\mathrm{g}-}_{ij}, \quad \text{on } \Gamma^{\mathrm{g}-}_{\mathrm{t}}. \tag{6.24}$$

  In the equations (6.23) and (6.24), $\psi^{\mathrm{g}+}_{ijk}$ and $\psi^{\mathrm{g}-}_{ijk}$ denote the third-order tensors of first derivatives of gradient strains. Yet again, to obtain the solution for the whole heterogeneous material, appropriate boundary conditions at the interface need to be considered. For the classical elasticity problem, the interface boundary conditions

are the same as in the u-RA procedure and are defined by equations (6.13) and (6.14). The interface conditions of the gradient problem in this procedure are the continuity of the gradient strains and reciprocity of the first-order normal derivatives of gradient strains [156]

$$\varepsilon_{ij}^{\mathrm{g}+} - \varepsilon_{ij}^{\mathrm{g}-} = 0, \quad \text{on } \Gamma_{\mathrm{s}}^{\mathrm{g}}, \tag{6.25}$$

$$\frac{\partial \varepsilon_{ij}^{\mathrm{g}+}}{\partial n^{\mathrm{g}+}} + \frac{\partial \varepsilon_{ij}^{\mathrm{g}-}}{\partial n^{\mathrm{g}-}} = 0, \quad \text{on } \Gamma_{\mathrm{s}}^{\mathrm{g}}. \tag{6.26}$$

6.2. Discretization of the structure using staggered procedures

In the same manner as in linear elasticity the discretization of the domain Ω is done by two sets of nodes that can be written as $S^+ = \{\mathbf{x}_I, I = 1, 2, ..., N : \mathbf{x}_I \subseteq \Omega^+ \cup \Gamma^+ \cup \Gamma_{\mathrm{s}}\}$ and $S^- = \{\mathbf{x}_M, M = 1, 2, ..., P : \mathbf{x}_M \subseteq \Omega^- \cup \Gamma^- \cup \Gamma_{\mathrm{s}}\}$, where N and P again denotes the total number of nodes in each homogeneous subdomain. Herein, the same sets and position of the nodes are used for the discretization of both the classical and the gradient boundary value problem. This is suitable due to the use of the staggered solution strategy. In addition, for the discretization of the interfaces $\Gamma_{\mathrm{s}}^{\mathrm{c}}$ and $\Gamma_{\mathrm{s}}^{\mathrm{c}}$ in each separate problem, the overlapping node concept is used. For each considered discretization node the MLPG concept [71] is applied, wherein the local trial domains Ω_{s} are defined around each node $\mathbf{x} \in S^+ \cup S^-$ in order to compute the connectivity between nodes. It should be noted that this is done here only once, since the same sizes of the approximation domains are utilized in both the classical and the gradient boundary value problem. For the nodes positioned on the interface boundaries, the local approximation domains are truncated in such a manner that the discretization nodes from one homogeneous material influence only the nodes belonging to that material. The more detailed collocation procedure of obtaining only the strong form of governing equations has already been shown once before in Chapter 5. for the case of elasto-static equilibrium equations. Therefore, for simplicity reasons it is skipped here due to the analogous nature. In addition, the same MLPG collocation procedure is also applied for the discretization of all the boundary conditions presented in previous section.

Within this research, two different collocation methods are considered for the modeling of gradient elasticity. The methods utilize the presented u-RA and ε-RA staggered solution schemes. Within the solution strategy, both the classical and the gradient problem are discretized using a mixed meshless approach [71]. In both the u-RA and ε-RA, strategy the classical boundary value problem is solved in exactly the same manner since the governing equations and the corresponding boundary conditions are identical. Thus,

in both approaches, the displacement and strain components are chosen as the unknown field variables. Also, for all of the variables, the identical approximation functions are employed, and the approximations are carried out within the homogeneous materials Ω^+ and Ω^-, on the outer boundaries and on the interface boundary in a separate manner. Hence, for the homogeneous material Ω^+, and the boundaries Γ_{u}^+, Γ_{t}^+ and Γ_{s}^+, it can be written

$$u_i^{\mathrm{c}+(h)}(\mathbf{x}) = \sum_{J=1}^{N_{\Omega_{\mathrm{s}}}} \phi_J^+(\mathbf{x})(\hat{u}_i^{\mathrm{c}+})_J, \tag{6.27}$$

$$\varepsilon_{ij}^{\mathrm{c}+(h)}(\mathbf{x}) = \sum_{J=1}^{N_{\Omega_{\mathrm{s}}}} \phi_J^+(\mathbf{x})(\hat{\varepsilon}_{ij}^{\mathrm{c}+})_J, \tag{6.28}$$

where ϕ_J represents the nodal value of two-dimensional shape function for node J, while $(\hat{u}_i^{\mathrm{c}+})_J$ and $(\hat{\varepsilon}_{ij}^{\mathrm{c}+})_J$ denote the nodal values of classical displacement and classical strain components.

The approximations used for the gradient problem are dependent on the utilized staggered procedure. If the gradient problem is solved using the u-RA procedure, for the unknown field variables, gradient displacements and derivatives of gradient displacements are chosen. Thus, for the nodes within the material Ω^+, and the nodes positioned on the interfaces $\Gamma_{\mathrm{u}}^{\mathrm{g}+}$ and $\Gamma_{\mathrm{s}}^{\mathrm{g}+}$, following approximations are written

$$u_i^{\mathrm{g}+(h)}(\mathbf{x}) = \sum_{J=1}^{N_{\Omega_{\mathrm{s}}}} \phi_J^+(\mathbf{x})(\hat{u}_i^{\mathrm{g}+})_J, \tag{6.29}$$

$$(\nabla u_i^{\mathrm{g}+})^{(h)}(\mathbf{x}) = \sum_{J=1}^{N_{\Omega_{\mathrm{s}}}} \phi_J^+(\mathbf{x})(\hat{u}_{\mathrm{G}i}^{\mathrm{g}+})_J, \tag{6.30}$$

where $(\hat{u}_i^{\mathrm{g}+})_J$ represents the nodal values of gradient displacement components and $(\hat{u}_{\mathrm{G}i}^{\mathrm{g}+})_J$ denotes the nodal values of derivatives of gradient displacement components. In addition, along with the above approximations in the u-RA procedure, for the nodes on $\Gamma_{\mathrm{t}}^{\mathrm{g}+}$, also the approximation of second-order displacement derivatives is utilized in the procedure for the gradient natural boundary conditions

$$\Big(\nabla(\nabla u_i^{\mathrm{g}+})\Big)^{(h)}(\mathbf{x}) = \sum_{J=1}^{N_{\Omega_{\mathrm{s}}}} \phi_J^+(\mathbf{x})(\hat{u}_{\mathrm{SG}i}^{\mathrm{g}+})_J, \tag{6.31}$$

where $(\hat{u}_{\mathrm{SG}i}^{\mathrm{g}+})_J$ denotes the nodal values of second derivatives of gradient displacement components. Lastly, if the ε-RA staggered solution procedure is utilized for the unknown field variables, the gradient strains and derivatives of gradient strains are considered. Thus, for the nodes within the material Ω^+, and the nodes positioned on the interfaces $\Gamma_{\mathrm{u}}^{\mathrm{g}+}$, $\Gamma_{\mathrm{t}}^{\mathrm{g}+}$ and $\Gamma_{\mathrm{s}}^{\mathrm{g}+}$, the approximations are

$$\varepsilon_{ij}^{\mathrm{g}+(h)}(\mathbf{x}) = \sum_{J=1}^{N_{\Omega_{\mathrm{s}}}} \phi_J^+(\mathbf{x}_I)(\hat{\varepsilon}_{ij}^{\mathrm{g}+})_J, \tag{6.32}$$

$$(\nabla\varepsilon_{ij}^{\mathrm{g}+})^{(h)}(\mathbf{x}) = \sum_{J=1}^{N_{\Omega_\mathrm{s}}} \phi_J^+(\mathbf{x})(\hat{\varepsilon}_{\mathrm{G}ij}^{\mathrm{g}+})_J. \tag{6.33}$$

Herein, $(\hat{\varepsilon}_{ij}^{\mathrm{g}+})_J$ describes the nodal values of gradient strains and $(\hat{\varepsilon}_{\mathrm{G}ij}^{\mathrm{g}+})_J$ denotes the values of derivatives of gradient strains. All unknown field variable components are analogously approximated over the material domain Ω^-. In addition, it should be stressed that the same nodes are always used for the approximations in classical and gradient problem fields.

6.3. Mixed collocation methods based on staggered procedures

Since the proposed mixed collocation methods have two solution processes, the classical and the gradient boundary value problem, the discretized equations for each of them is here presented individually. Furthermore, the discretized equations for both the u-RA and the ε-RA procedures are presented. Herein, the discretized equations of the classical problem are presented only once since the same approach is applied in both the u-RA and the ε-RA mixed collocation method. Again, as in the previous chapter, different types of nodes are distinguished in the computing. Hence, in both the classical and gradient problem, at the nodes inside the domains Ω^+ and Ω^-, the governing equations of the classical or gradient problem are used, respectively. At the nodes belonging to the outer boundaries $\Gamma^{\mathrm{c}+}$ and $\Gamma^{\mathrm{c}-}$, or $\Gamma^{\mathrm{g}+}$ and $\Gamma^{\mathrm{g}+}$, the corresponding essential and natural boundary conditions are imposed. In addition, on the boundaries, $\Gamma_\mathrm{s}^\mathrm{c}$ and $\Gamma_\mathrm{s}^\mathrm{g}$, the appropriate interface conditions are used. Hence, in this section all discretized equations are derived, presented and discussed.

6.3.1. Discretized equilibrium equations of the classical problem

In order to derive the equilibrium equations in the matrix form equations (6.17) and (6.18) are firstly discretized using the strain approximations defined by (6.28), thus obtaining

$$\sum_{J=1}^{N_{\Omega_\mathrm{s}}} \mathbf{D}_\mathrm{K}^{+\mathrm{T}}\mathbf{D}^+\phi_J^+\hat{\boldsymbol{\varepsilon}}_J^{\mathrm{c}+} + \mathbf{b}_I^+ = \mathbf{0}, \tag{6.34}$$

$$\sum_{J=1}^{N_{\Omega_\mathrm{s}}} \mathbf{D}_\mathrm{K}^{-\mathrm{T}}\mathbf{D}^-\phi_J^-\hat{\boldsymbol{\varepsilon}}_J^{\mathrm{c}-} + \mathbf{b}_M^- = \mathbf{0}, \tag{6.35}$$

where $\mathbf{D}_\mathrm{K}^+$ and $\mathbf{D}_\mathrm{K}^-$ denote kinematic differential operators defined by (5.19) and (5.20), while $\mathbf{D}^+$ and $\mathbf{D}^-$ are elasticity matrices for each homogeneous material. From the analysis

of equations (6.34) and (6.35), it can be concluded again that the total number of equations is lower than the total number of strain unknowns $N_{\varepsilon\text{un}} = 3(N+P)$. Thus, to achieve the closed system of equations, some additional equations are needed. Herein, these equations, similar to the mixed method discussed in the previous chapter, represent the enforced compatibility (2.4) at each node between the approximated strains $\varepsilon_{ij}^{+(h)}(\mathbf{x}_J) \approx \hat{\boldsymbol{\varepsilon}}_J^+, \mathbf{x}_J \in S^+$ and $\varepsilon_{ij}^{-(h)}(\mathbf{x}_J) \approx \hat{\boldsymbol{\varepsilon}}_J^-, \mathbf{x}_J \in S^-$ and the nodal values of displacements $\hat{\mathbf{u}}_L^+; L = 1, 2, ..., N_{\Omega_\text{s}}$ and $\hat{\mathbf{u}}_L^-; L = 1, 2, ..., N_{\Omega_\text{s}}$, respectively. Hence, the following equations can be derived for the heterogeneous structure

$$\boldsymbol{\varepsilon}^{\text{c}+} = \mathbf{D}_\text{K}^+ \mathbf{u}^{\text{c}+}, \tag{6.36}$$

$$\boldsymbol{\varepsilon}^{\text{c}-} = \mathbf{D}_\text{K}^- \mathbf{u}^{\text{c}-}. \tag{6.37}$$

The above equations have to be written at every node, and after discretization using displacement approximation (6.27), we obtain

$$\hat{\boldsymbol{\varepsilon}}_J^{\text{c}+} = \sum_{L=1}^{N_{\Omega_\text{s}}} \mathbf{D}_\text{K}^+ \phi_L^+(\mathbf{x}_J) \hat{\mathbf{u}}_L^{\text{c}+} = \sum_{L=1}^{N_{\Omega_\text{s}}} \mathbf{B}_{JL}^+ \hat{\mathbf{u}}_L^{\text{c}+}, \tag{6.38}$$

$$\hat{\boldsymbol{\varepsilon}}_J^{\text{c}-} = \sum_{L=1}^{N_{\Omega_\text{s}}} \mathbf{D}_\text{K}^- \phi_L^-(\mathbf{x}_J) \hat{\mathbf{u}}_L^{\text{c}-} = \sum_{L=1}^{N_{\Omega_\text{s}}} \mathbf{B}_{JL}^- \hat{\mathbf{u}}_L^{\text{c}-}, \tag{6.39}$$

where matrices $\mathbf{B}_{JL}^+$ and $\mathbf{B}_{JL}^-$ are computed according to relations (5.25) and (5.26). Now, by substituting (6.38) and (6.39) into equations (6.34) and (6.35), the final solvable system with only nodal displacements as unknowns follows. Thus, the final system of equations can be written as

$$\sum_{J=1}^{N_{\Omega_\text{s}}} \mathbf{K}_{IJ}^{\text{c}+} \hat{\mathbf{u}}_J^{\text{c}+} = \mathbf{R}_I^{\text{c}+}, \quad I = 1, 2, ..., N, \tag{6.40}$$

$$\sum_{J=1}^{N_{\Omega_\text{s}}} \mathbf{K}_{MJ}^{\text{c}-} \hat{\mathbf{u}}_J^{\text{c}-} = \mathbf{R}_M^{\text{c}-}, \quad M = 1, 2, ..., P. \tag{6.41}$$

Herein, the nodal stiffness matrices $\mathbf{K}_{IJ}^{\text{c}+}$ and $\mathbf{K}_{MJ}^{\text{c}-}$ are slightly different than in the mixed method presented in the previous chapter and are defined as

$$\mathbf{K}_{IJ}^{\text{c}+} = \sum_{L=1}^{N_{\Omega_\text{s}}} \mathbf{D}_\text{K}^{+\text{T}} \mathbf{D}^+ \phi_J^+ \mathbf{B}_{JL}^+, \tag{6.42}$$

$$\mathbf{K}_{MJ}^{\text{c}-} = \sum_{L=1}^{N_{\Omega_\text{s}}} \mathbf{D}_\text{K}^{-\text{T}} \mathbf{D}^- \phi_J^- \mathbf{B}_{JL}^-, \tag{6.43}$$

while the nodal force vectors $\mathbf{R}_I^+$ and $\mathbf{R}_M^-$ remain the same and are defined by (5.31) and (5.32). As evident, by utilizing this mixed collocation strategy again only the first-order spatial derivatives of the shape functions need to be computed to assemble the nodal stiffness matrices $\mathbf{K}_{IJ}^{\text{c}+}$ and $\mathbf{K}_{MJ}^{\text{c}-}$. Furthermore, the solutions of the classical system of

equations are the classical nodal displacements $\hat{\mathbf{u}}_J^{\mathrm{c}+}$ and $\hat{\mathbf{u}}_J^{\mathrm{c}-}$ which are used as the input for the gradient problem of the u-RA procedure. However, if the ε-RA procedure is utilized, the classical nodal displacements are transformed to classical nodal strains $\hat{\boldsymbol{\varepsilon}}_J^{\mathrm{c}+}$ and $\hat{\boldsymbol{\varepsilon}}_J^{\mathrm{c}-}$ using kinematic relations (6.36) and (6.37).

6.3.2. Discretized boundary conditions of the classical problem

For the nodes positioned on the boundaries $\Gamma_{\mathrm{u}}^{\mathrm{c}+}$ and $\Gamma_{\mathrm{u}}^{\mathrm{c}-}$, the displacement boundary conditions (6.5) and (6.6) are enforced straightforwardly, as in FEM. Hence, the discretized classical essential boundary conditions are equal to

$$\bar{\mathbf{u}}_I^{\mathrm{c}+} = \sum_{J=1}^{N_{\Omega_{\mathrm{s}}}} \phi_J^+(\mathbf{x}_I)\hat{\mathbf{u}}_J^{\mathrm{c}+}, \tag{6.44}$$

$$\bar{\mathbf{u}}_M^{\mathrm{c}-} = \sum_{J=1}^{N_{\Omega_{\mathrm{s}}}} \phi_J^-(\mathbf{x}_M)\hat{\mathbf{u}}_J^{\mathrm{c}-}. \tag{6.45}$$

The discretized equations (6.44) and (6.45) are substituted into the rows of the global stiffness matrix belonging to the node positioned on the classic global displacement boundary. The traction boundary conditions (6.7) and (6.8) for the nodes positioned on the boundaries $\Gamma_{\mathrm{t}}^{\mathrm{c}+}$ and $\Gamma_{\mathrm{t}}^{\mathrm{c}-}$ are also introduced in the global system of equations instead of the equilibrium equations for the given node using the direct collocation approach. Therein, by utilizing the strain approximation (6.28) and the kinematic compatibility conditions (6.36) and (6.37), the classical traction boundary conditions are

$$\mathbf{t}_I^{\mathrm{c}+} = \mathbf{N}_I^{\mathrm{c}+}\mathbf{D}^+ \sum_{J=1}^{N_{\Omega_{\mathrm{s}}}} \mathbf{S}_{IJ}^+ \sum_{L=1}^{N_{\Omega_{\mathrm{s}}}} \mathbf{B}_{JL}^+ \hat{\mathbf{u}}_L^{\mathrm{c}+}, \tag{6.46}$$

$$\mathbf{t}_M^{\mathrm{c}-} = \mathbf{N}_M^{\mathrm{c}-}\mathbf{D}^- \sum_{J=1}^{N_{\Omega_{\mathrm{s}}}} \mathbf{S}_{MJ}^- \sum_{L=1}^{N_{\Omega_{\mathrm{s}}}} \mathbf{B}_{JL}^- \hat{\mathbf{u}}_L^{\mathrm{c}-}, \tag{6.47}$$

where $\mathbf{S}_{IJ}^+$ and $\mathbf{S}_{MJ}^-$ denote the diagonal matrices, (5.55) and (5.56), consisting of shape function values which can again be neglected due to the interpolatory character of the approximation. Hence, the discretized traction equations are written in a simpler form as

$$\bar{\mathbf{t}}_I^{\mathrm{c}+} = \mathbf{N}_I^{\mathrm{c}+}\mathbf{D}^+ \sum_{L=1}^{N_{\Omega_{\mathrm{s}}}} \mathbf{B}_{IL}^+ \hat{\mathbf{u}}_L^{\mathrm{c}+}, \tag{6.48}$$

$$\mathbf{t}_M^{\mathrm{c}-} = \mathbf{N}_M^{\mathrm{c}-}\mathbf{D}^- \sum_{L=1}^{N_{\Omega_{\mathrm{s}}}} \mathbf{B}_{ML}^- \hat{\mathbf{u}}_L^{\mathrm{c}-}. \tag{6.49}$$

Herein, matrices $\mathbf{N}_I^{\mathrm{c}+}$ and $\mathbf{N}_M^{\mathrm{c}-}$ are matrices of unit vector normals associated with the classical problem and computed by (5.39) and (5.40). In the above discretized equations

there is no summation over indices I and M. Finally, for the nodes on the interface boundary $\Gamma_{\mathrm{s}}^{\mathrm{c}}$, the classical interface boundary conditions (6.13) and (6.14) need to be enforced. This is done by employing the expressions (6.44), (6.45) and (6.48), (6.49), which leads to

$$\sum_{L=1}^{N_{\Omega_{\mathrm{s}}}} \phi_L^+(\mathbf{x}_I)\hat{\mathbf{u}}_L^{\mathrm{c}+} = \sum_{L=1}^{N_{\Omega_{\mathrm{s}}}} \phi_L^-(\mathbf{x}_M)\hat{\mathbf{u}}_L^{\mathrm{c}-}, \tag{6.50}$$

$$\mathbf{N}_I^{\mathrm{c}+}\mathbf{D}^+ \sum_{L=1}^{N_{\Omega_{\mathrm{s}}}} \mathbf{B}_{IL}^+ \hat{\mathbf{u}}_L^{\mathrm{c}+} = -\mathbf{N}_M^{\mathrm{c}-}\mathbf{D}^- \sum_{L=1}^{N_{\Omega_{\mathrm{s}}}} \mathbf{B}_{ML}^- \hat{\mathbf{u}}_L^{\mathrm{c}-}. \tag{6.51}$$

These equations are again inserted into the global stiffness matrix in the rows corresponding to the current node positioned on $\Gamma_{\mathrm{s}}^{\mathrm{c}}$. In the above equations, nodes I and M on the interface boundary $\Gamma_{\mathrm{s}}^{\mathrm{c}}$ have the same coordinates since the overlapping node concept is utilized. Furthermore, in the equations (6.50) and (6.91) there is no summation over indices I and M.

6.3.3. Discretized governing equations of the u-RA gradient problem

The governing equations (6.3) and (6.4) are firstly written in their matrix form at the discretization nodes inside the domains Ω^+ and Ω^-

$$\mathbf{u}_I^{\mathrm{g}+} - l^2\left[\boldsymbol{\nabla}^{\mathrm{u}+\mathrm{T}} \cdot \left(\boldsymbol{\nabla}^{\mathrm{u}+}\mathbf{u}_I^{\mathrm{g}+}\right)\right] = \mathbf{u}_I^{\mathrm{c}+}, \tag{6.52}$$

$$\mathbf{u}_M^{\mathrm{g}-} - l^2\left[\boldsymbol{\nabla}^{\mathrm{u}-\mathrm{T}} \cdot \left(\boldsymbol{\nabla}^{\mathrm{u}-}\mathbf{u}_M^{\mathrm{g}-}\right)\right] = \mathbf{u}_M^{\mathrm{c}-}, \tag{6.53}$$

where $\boldsymbol{\nabla}^{\mathrm{u}2} = \boldsymbol{\nabla}^{\mathrm{u}\mathrm{T}} \cdot (\boldsymbol{\nabla}^{\mathrm{u}})$ denotes the Laplacian operator associated with the u-RA procedure written in the matrix form. Hence, the operators $\boldsymbol{\nabla}^{\mathrm{u}+}$ and $\boldsymbol{\nabla}^{\mathrm{u}-}$ are equal to

$$\boldsymbol{\nabla}^{\mathrm{u}+} = \begin{bmatrix} \dfrac{\partial(\ )^+}{\partial x_1}(\mathbf{x}_I) & 0 \\ 0 & \dfrac{\partial(\ )^+}{\partial x_1}(\mathbf{x}_I) \\ \dfrac{\partial(\ )^+}{\partial x_2}(\mathbf{x}_I) & 0 \\ 0 & \dfrac{\partial(\ )^+}{\partial x_2}(\mathbf{x}_I) \end{bmatrix}, \tag{6.54}$$

$$\boldsymbol{\nabla}^{\mathrm{u}-} = \begin{bmatrix} \dfrac{\partial(\ )^-}{\partial x_1}(\mathbf{x}_M) & 0 \\ 0 & \dfrac{\partial(\ )^-}{\partial x_1}(\mathbf{x}_M) \\ \dfrac{\partial(\ )^-}{\partial x_2}(\mathbf{x}_M) & 0 \\ 0 & \dfrac{\partial(\ )^-}{\partial x_2}(\mathbf{x}_M) \end{bmatrix}. \tag{6.55}$$

The governing equations (6.52) and (6.53) are now simultaneously discretized by the approximations (6.29) and (6.30) resulting in

$$\sum_{J=1}^{N_{\Omega_\mathrm{s}}} \phi_J^+ \hat{\mathbf{u}}_J^{\mathrm{g}+} - l^2 \Big[\boldsymbol{\nabla}^{\mathrm{u}+\mathrm{T}} \cdot \Big(\sum_{K=1}^{N_{\Omega_\mathrm{s}}} \phi_K^+ \hat{\mathbf{u}}_{\mathrm{G}K}^{\mathrm{g}+} \Big) \Big] = \mathbf{u}_I^{\mathrm{c}+}, \tag{6.56}$$

$$\sum_{J=1}^{N_{\Omega_\mathrm{s}}} \phi_J^- \hat{\mathbf{u}}_J^{\mathrm{g}-} - l^2 \Big[\boldsymbol{\nabla}^{\mathrm{u}+\mathrm{T}} \cdot \Big(\sum_{K=1}^{N_{\Omega_\mathrm{s}}} \phi_K^- \hat{\mathbf{u}}_{\mathrm{G}K}^{\mathrm{g}-} \Big) \Big] = \mathbf{u}_M^{\mathrm{c}-}, \tag{6.57}$$

where l represents the Aifantis microstructural parameter. In the above equations, $\hat{\mathbf{u}}_{\mathrm{G}}^{\mathrm{g}+}$ and $\hat{\mathbf{u}}_{\mathrm{G}}^{\mathrm{g}-}$ denote the vectors of unknown derivatives of gradient displacements defined by

$$\big[\hat{\mathbf{u}}_{\mathrm{G}}^{\mathrm{g}+}\big]^{\mathrm{T}} = \Big[\frac{\partial \hat{u}_1^{\mathrm{g}+}}{\partial x_1} \quad \frac{\partial \hat{u}_2^{\mathrm{g}+}}{\partial x_1} \quad \frac{\partial \hat{u}_1^{\mathrm{g}+}}{\partial x_2} \quad \frac{\partial \hat{u}_2^{\mathrm{g}+}}{\partial x_2} \Big], \tag{6.58}$$

$$\big[\hat{\mathbf{u}}_{\mathrm{G}}^{\mathrm{g}-}\big]^{\mathrm{T}} = \Big[\frac{\partial \hat{u}_1^{\mathrm{g}-}}{\partial x_1} \quad \frac{\partial \hat{u}_2^{\mathrm{g}-}}{\partial x_1} \quad \frac{\partial \hat{u}_1^{\mathrm{g}-}}{\partial x_2} \quad \frac{\partial \hat{u}_2^{\mathrm{g}-}}{\partial x_2} \Big]. \tag{6.59}$$

As obvious, the equations (6.56) and (6.57) represent an unsolvable system of equations since the global number of unknowns is larger than the number of equations. Thus, the system of equations is here closed simply be enforcing the compatibility at each node between the approximated nodal derivatives of displacements $\hat{\mathbf{u}}_{\mathrm{G}}^{\mathrm{g}+(h)}(\mathbf{x}_K) \approx \hat{\mathbf{u}}_{\mathrm{G}K}^{\mathrm{g}+}, \mathbf{x}_K \in S^+$ and $\hat{\mathbf{u}}_{\mathrm{G}}^{\mathrm{g}-(h)}(\mathbf{x}_K) \approx \hat{\mathbf{u}}_{\mathrm{G}K}^{\mathrm{g}-}, \mathbf{x}_K \in S^-$ and the nodal displacements $\hat{\mathbf{u}}_J^+; J = 1, 2, ..., N_{\Omega_\mathrm{s}}$ and $\hat{\mathbf{u}}_J^-; J = 1, 2, ..., N_{\Omega_\mathrm{s}}$, respectively. The following compatibility equations can be written for the structure

$$\mathbf{u}_{\mathrm{G}}^{\mathrm{g}+} = \mathbf{D}_{\mathrm{K}}^{\mathrm{u}+} \mathbf{u}^{\mathrm{g}+}, \tag{6.60}$$

$$\mathbf{u}_{\mathrm{G}}^{\mathrm{g}-} = \mathbf{D}_{\mathrm{K}}^{\mathrm{u}-} \mathbf{u}^{\mathrm{g}-}, \tag{6.61}$$

where $\mathbf{D}_{\mathrm{K}}^{\mathrm{u}+}$ and $\mathbf{D}_{\mathrm{K}}^{\mathrm{u}-}$ denote the 2-D kinematic differential operators comprised of first-order derivatives with respect to the Cartesian coordinates. Equations (6.60) and (6.61) are now again written at every node and discretized by (6.29) obtaining

$$\hat{\mathbf{u}}_{\mathrm{G}K}^{\mathrm{g}+} = \sum_{J=1}^{N_{\Omega_\mathrm{s}}} \mathbf{D}_{\mathrm{K}}^{\mathrm{u}+} \phi_J^+(\mathbf{x}_K) \hat{\mathbf{u}}_J^{\mathrm{g}+} = \sum_{J=1}^{N_{\Omega_\mathrm{s}}} \mathbf{G}_{KJ}^+ \hat{\mathbf{u}}_J^{\mathrm{g}+} \tag{6.62}$$

$$\hat{\mathbf{u}}^{\mathrm{g}-}_{\mathrm{G}K} = \sum_{J=1}^{N_{\Omega_\mathrm{s}}} \mathbf{D}^{\mathrm{u}-}_{\mathrm{K}} \phi^{+}_{J}(\mathbf{x}_K) \hat{\mathbf{u}}^{\mathrm{g}-}_{J} = \sum_{J=1}^{N_{\Omega_\mathrm{s}}} \mathbf{G}^{-}_{KJ} \hat{\mathbf{u}}^{\mathrm{g}-}_{J}, \tag{6.63}$$

where compatibility matrices $\mathbf{G}^{+}_{KJ}$ and $\mathbf{G}^{-}_{KJ}$ are equal to

$$\mathbf{G}^{+}_{KJ} = \begin{bmatrix} \dfrac{\partial \phi^{+}_{J}}{\partial x_1}(\mathbf{x}_K) & 0 \\ 0 & \dfrac{\partial \phi^{+}_{J}}{\partial x_1}(\mathbf{x}_K) \\ \dfrac{\partial \phi^{+}_{J}}{\partial x_2}(\mathbf{x}_K) & 0 \\ 0 & \dfrac{\partial \phi^{+}_{J}}{\partial x_2}(\mathbf{x}_K) \end{bmatrix}, \tag{6.64}$$

$$\mathbf{G}^{-}_{KJ} = \begin{bmatrix} \dfrac{\partial \phi^{-}_{J}}{\partial x_1}(\mathbf{x}_K) & 0 \\ 0 & \dfrac{\partial \phi^{-}_{J}}{\partial x_1}(\mathbf{x}_K) \\ \dfrac{\partial \phi^{-}_{J}}{\partial x_2}(\mathbf{x}_K) & 0 \\ 0 & \dfrac{\partial \phi^{-}_{J}}{\partial x_2}(\mathbf{x}_K) \end{bmatrix}. \tag{6.65}$$

If the discretized equations (6.62) and (6.63) are now inserted into (6.52) and (6.53), a solvable system of equations is attained with only the nodal gradient displacement components as unknowns. Therefore, the final discretized system of equations can be written for each node as

$$\mathbf{K}^{\mathrm{g}+}_{IJ} \hat{\mathbf{u}}^{\mathrm{g}+}_{J} = \mathbf{F}^{\mathrm{g}+}_{I}, \quad I = 1, 2, ..., N, \tag{6.66}$$

$$\mathbf{K}^{\mathrm{g}-}_{MJ} \hat{\mathbf{u}}^{\mathrm{g}-}_{J} = \mathbf{F}^{\mathrm{g}-}_{M}, \quad M = 1, 2, ..., P, \tag{6.67}$$

where the gradient nodal coefficient matrices $\mathbf{K}^{\mathrm{g}+}_{IJ}$ and $\mathbf{K}^{\mathrm{g}-}_{MJ}$ are equal to

$$\mathbf{K}^{\mathrm{g}+}_{IJ} = \sum_{J=1}^{N_{\Omega_\mathrm{s}}} \mathbf{S}^{\mathrm{u}+}_{IJ} - l^2 \Big[\sum_{K=1}^{N_{\Omega_\mathrm{s}}} \mathbf{G}^{\mathrm{g}+\,\mathrm{T}}_{IK} \sum_{J=1}^{N_{\Omega_\mathrm{s}}} \mathbf{G}^{\mathrm{g}+}_{KJ} \Big], \tag{6.68}$$

$$\mathbf{K}^{\mathrm{g}-}_{MJ} = \sum_{J=1}^{N_{\Omega_\mathrm{s}}} \mathbf{S}^{\mathrm{u}-}_{MJ} - l^2 \Big[\sum_{K=1}^{N_{\Omega_\mathrm{s}}} \mathbf{G}^{\mathrm{g}-}_{MK}{}^{\mathrm{T}} \sum_{J=1}^{N_{\Omega_\mathrm{s}}} \mathbf{G}^{\mathrm{g}-}_{KJ} \Big]. \tag{6.69}$$

Herein, the matrices $\mathbf{S}^{\mathrm{u}+}_{IJ}$ and $\mathbf{S}^{\mathrm{u}-}_{MJ}$ are the diagonal matrices comprised of shape function values defined by

$$\mathbf{S}^{\mathrm{u}+}_{IJ} = \begin{bmatrix} \phi^{+}_{J}(\mathbf{x}_I) & 0 \\ 0 & \phi^{+}_{J}(\mathbf{x}_I) \end{bmatrix}, \tag{6.70}$$

$$\mathbf{S}_{MJ}^{\mathrm{u}-} = \begin{bmatrix} \phi_J^-(\mathbf{x}_M) & 0 \\ 0 & \phi_J^-(\mathbf{x}_M) \end{bmatrix}. \tag{6.71}$$

The gradient nodal force vectors $\mathbf{F}_I^{\mathrm{g}+}$ and $\mathbf{F}_M^{\mathrm{g}-}$ in (6.66) and (6.67) are composed of known values of classical displacements

$$\mathbf{F}_I^{\mathrm{g}+} = -\mathbf{u}_I^{\mathrm{c}+}, \tag{6.72}$$

$$\mathbf{F}_M^{\mathrm{g}-} = -\mathbf{u}_M^{\mathrm{c}-}. \tag{6.73}$$

As obvious, by utilizing the u-RA staggered procedure and the presented mixed meshless strategy, the coefficient matrices $\mathbf{K}_{IJ}^{\mathrm{g}+}$ and $\mathbf{K}_{MJ}^{\mathrm{g}+}$ are assembled using only first-order derivatives of shape functions. Hence, the algorithms based on this approach should be fast and efficient in obtaining accurate results.

6.3.4. Discretized boundary conditions of the u-RA gradient problem

The higher-order essential boundary conditions in this approach consist of enforcing the gradient displacements at the nodes on the boundaries Γ_{u}^+ and Γ_{u}^-. Again, due to the interpolatory properties of the shape functions, these boundary conditions are enforced directly at the nodes as

$$\bar{\mathbf{u}}_I^{\mathrm{g}+} = \sum_{J=1}^{N_{\Omega_{\mathrm{s}}}} \phi_J^+(\mathbf{x}_I)\hat{\mathbf{u}}_J^{\mathrm{g}+}, \tag{6.74}$$

$$\bar{\mathbf{u}}_M^{\mathrm{g}-} = \sum_{J=1}^{N_{\Omega_{\mathrm{s}}}} \phi_J^-(\mathbf{x}_M)\hat{\mathbf{u}}_J^{\mathrm{g}-}. \tag{6.75}$$

The higher-order natural boundary conditions (6.11) and (6.12) on the boundaries $\Gamma_{\mathrm{t}}^{\mathrm{g}+}$ and $\Gamma_{\mathrm{t}}^{\mathrm{g}+}$ are imposed using the direct collocation approach, where firstly the approximation of the second derivatives of displacements (6.31) is utilized leading to

$$\bar{\mathbf{R}}_I^{\mathrm{g}+} = \mathbf{N}_I^{\mathrm{SG}+} \sum_{F=1}^{N_{\Omega_{\mathrm{s}}}} \mathbf{S}_{IF}^{u2+}(\hat{\mathbf{u}}_{\mathrm{SG}}^{\mathrm{g}+})_F, \tag{6.76}$$

$$\bar{\mathbf{R}}_M^{\mathrm{g}-} = \mathbf{N}_M^{\mathrm{SG}-} \sum_{F=1}^{N_{\Omega_{\mathrm{s}}}} \mathbf{S}_{MF}^{u2-}(\hat{\mathbf{u}}_{\mathrm{SG}}^{\mathrm{g}-})_F, \tag{6.77}$$

where $\hat{\mathbf{u}}_{\mathrm{SG}}^{\mathrm{g}+}$ and $\hat{\mathbf{u}}_{\mathrm{SG}}^{\mathrm{g}-}$ denote the vectors of the second-order derivatives of gradient displacements,

$$\left[\hat{\mathbf{u}}_{\mathrm{SG}}^{\mathrm{g}+}\right]^{\mathrm{T}} = \left[\frac{\partial^2 \hat{u}_1^{\mathrm{g}+}}{\partial x_1^2} \quad \frac{\partial^2 \hat{u}_1^{\mathrm{g}+}}{\partial x_2^2} \quad 2\frac{\partial^2 \hat{u}_1^{\mathrm{g}+}}{\partial x_1 \partial x_2} \quad \frac{\partial^2 \hat{u}_2^{\mathrm{g}+}}{\partial x_1^2} \quad \frac{\partial^2 \hat{u}_2^{\mathrm{g}+}}{\partial x_2^2} \quad 2\frac{\partial^2 \hat{u}_2^{\mathrm{g}+}}{\partial x_1 \partial x_2} \right], \tag{6.78}$$

$$\left[\hat{\mathbf{u}}_{\mathrm{SG}}^{\mathrm{g}-}\right]^{\mathrm{T}} = \left[\frac{\partial^2 \hat{u}_1^{\mathrm{g}-}}{\partial x_1^2} \quad \frac{\partial^2 \hat{u}_1^{\mathrm{g}-}}{\partial x_2^2} \quad 2\frac{\partial^2 \hat{u}_1^{\mathrm{g}-}}{\partial x_1 \partial x_2} \quad \frac{\partial^2 \hat{u}_2^{\mathrm{g}-}}{\partial x_1^2} \quad \frac{\partial^2 \hat{u}_2^{\mathrm{g}-}}{\partial x_2^2} \quad 2\frac{\partial^2 \hat{u}_2^{\mathrm{g}-}}{\partial x_1 \partial x_2} \right], \tag{6.79}$$

while the matrices $\mathbf{S}_{IF}^{\mathrm{u2}+}$ and $\mathbf{S}_{MF}^{\mathrm{u2}-}$ are diagonal 6 by 6 matrices, comprised of shape function values, written analogous to (6.70) and (6.71). Furthermore, $\mathbf{N}_{I}^{\mathrm{SG}+}$ and $\mathbf{N}_{M}^{\mathrm{SG}-}$ are the matrices composed of unit normal vectors associated with the second-order derivatives of gradient displacements equal to

$$\mathbf{N}_{I}^{\mathrm{SG}+} = \begin{bmatrix} n_1^{\mathrm{g}+}(\mathbf{x}_I)^2 & n_2^{\mathrm{g}+}(\mathbf{x}_I)^2 & n_1^{\mathrm{g}+}(\mathbf{x}_I)n_2^{\mathrm{g}+}(\mathbf{x}_I) & 0 & 0 & 0 \\ 0 & 0 & 0 & n_1^{\mathrm{g}+}(\mathbf{x}_I)^2 & n_2^{\mathrm{g}+}(\mathbf{x}_I)^2 & n_1^{\mathrm{g}+}(\mathbf{x}_I)n_2^{\mathrm{g}+}(\mathbf{x}_I) \end{bmatrix}, \tag{6.80}$$

$$\mathbf{N}_{M}^{\mathrm{SG}-} = \begin{bmatrix} n_1^{\mathrm{g}-}(\mathbf{x}_M)^2 & n_2^{\mathrm{g}-}(\mathbf{x}_M)^2 & n_1^{\mathrm{g}-}(\mathbf{x}_M)n_2^{\mathrm{g}-}(\mathbf{x}_M) & 0 & 0 & 0 \\ 0 & 0 & 0 & n_1^{\mathrm{g}-}(\mathbf{x}_M)^2 & n_2^{\mathrm{g}-}(\mathbf{x}_M)^2 & n_1^{\mathrm{g}-}(\mathbf{x}_M)n_2^{\mathrm{g}-}(\mathbf{x}_M) \end{bmatrix}. \tag{6.81}$$

Here, in order to derive the discretized equation of the natural boundary conditions dependent on the nodal values of the gradient displacements, firstly the compatibility between the second-order and the first-order derivatives of displacements needs to be applied. Hence, for the heterogeneous structure this compatibility is equal to

$$\mathbf{u}_{\mathrm{SG}}^{\mathrm{g}+} = \mathbf{D}_{\mathrm{K}}^{\mathrm{u2}+}\mathbf{u}_{\mathrm{G}}^{\mathrm{g}+}, \tag{6.82}$$

$$\mathbf{u}_{\mathrm{SG}}^{\mathrm{g}-} = \mathbf{D}_{\mathrm{K}}^{\mathrm{u2}-}\mathbf{u}_{\mathrm{G}}^{\mathrm{g}-}, \tag{6.83}$$

where $\mathbf{D}_{\mathrm{K}}^{\mathrm{u2}+}$ and $\mathbf{D}_{\mathrm{K}}^{\mathrm{u2}-}$ are the 2-D differential operators connecting second- and first-order derivatives of gradient displacements. Firstly, the equations (6.82) and (6.83) are now introduced into (6.76) and (6.77). Secondly, the compatibility between the first-order gradients and the gradient displacements defined by (6.60) and (6.61), along with the displacement approximation (6.29), are utilized. This procedure leads to the following discretized expressions for the gradient natural boundary conditions

$$\bar{\mathbf{R}}_{I}^{\mathrm{g}+} = \mathbf{N}_{I}^{\mathrm{SG}+}\sum_{F=1}^{N_{\Omega_{\mathrm{s}}}}\mathbf{S}_{IF}^{\mathrm{u2}+}\sum_{K=1}^{N_{\Omega_{\mathrm{s}}}}\mathbf{H}_{FK}^{+}\sum_{J=1}^{N_{\Omega_{\mathrm{s}}}}\mathbf{G}_{KJ}^{+}\hat{\mathbf{u}}_{J}^{\mathrm{g}+}, \tag{6.84}$$

$$\bar{\mathbf{R}}_{M}^{\mathrm{g}-} = \mathbf{N}_{M}^{\mathrm{SG}-}\sum_{F=1}^{N_{\Omega_{\mathrm{s}}}}\mathbf{S}_{MF}^{\mathrm{u2}-}\sum_{K=1}^{N_{\Omega_{\mathrm{s}}}}\mathbf{H}_{FK}^{-}\sum_{J=1}^{N_{\Omega_{\mathrm{s}}}}\mathbf{G}_{KJ}^{-}\hat{\mathbf{u}}_{J}^{\mathrm{g}-}. \tag{6.85}$$

In the above equations, for the simplicity of computation, the diagonal matrices $\mathbf{S}_{IF}^{\mathrm{u2}+}$ and $\mathbf{S}_{MF}^{\mathrm{u2}-}$ are again omitted due to the interpolatory property of the shape functions. The final discretized equations for the natural boundary conditions are then equal to

$$\bar{\mathbf{R}}_{I}^{\mathrm{g}+} = \mathbf{N}_{I}^{\mathrm{SG}+}\sum_{K=1}^{N_{\Omega_{\mathrm{s}}}}\mathbf{H}_{IK}^{+}\sum_{J=1}^{N_{\Omega_{\mathrm{s}}}}\mathbf{G}_{KJ}^{+}\hat{\mathbf{u}}_{J}^{\mathrm{g}+}, \tag{6.86}$$

$$\bar{\mathbf{R}}_{M}^{\mathrm{g}-} = \mathbf{N}_{M}^{\mathrm{SG}-}\sum_{K=1}^{N_{\Omega_{\mathrm{s}}}}\mathbf{H}_{MK}^{-}\sum_{J=1}^{N_{\Omega_{\mathrm{s}}}}\mathbf{G}_{KJ}^{-}\hat{\mathbf{u}}_{J}^{\mathrm{g}-}. \tag{6.87}$$

Yet again, in the above equations there is no summation over indices I and M. In (6.86) and (6.87) the matrices $\mathbf{H}^{+}_{IK}$ and $\mathbf{H}^{-}_{MK}$ that connect the second- and first- derivatives of displacements are computed by

$$\mathbf{H}^{+}_{IK} = \begin{bmatrix} \dfrac{\partial \phi^{+}_{K}}{\partial x_1}(\mathbf{x}_I) & 0 & 0 & 0 \\ 0 & 0 & \dfrac{\partial \phi^{+}_{K}}{\partial x_2}(\mathbf{x}_I) & 0 \\ \dfrac{\partial \phi^{+}_{K}}{\partial x_2}(\mathbf{x}_I) & 0 & 0 & 0 \\ 0 & \dfrac{\partial \phi^{+}_{K}}{\partial x_1}(\mathbf{x}_I) & 0 & 0 \\ 0 & 0 & 0 & \dfrac{\partial \phi^{+}_{K}}{\partial x_2}(\mathbf{x}_I) \\ 0 & \dfrac{\partial \phi^{+}_{K}}{\partial x_2}(\mathbf{x}_I) & 0 & 0 \end{bmatrix}, \tag{6.88}$$

$$\mathbf{H}^{-}_{MK} = \begin{bmatrix} \dfrac{\partial \phi^{-}_{K}}{\partial x_1}(\mathbf{x}_M) & 0 & 0 & 0 \\ 0 & 0 & \dfrac{\partial \phi^{-}_{K}}{\partial x_2}(\mathbf{x}_M) & 0 \\ \dfrac{\partial \phi^{-}_{K}}{\partial x_2}(\mathbf{x}_M) & 0 & 0 & 0 \\ 0 & \dfrac{\partial \phi^{-}_{K}}{\partial x_1}(\mathbf{x}_M) & 0 & 0 \\ 0 & 0 & 0 & \dfrac{\partial \phi^{-}_{K}}{\partial x_2}(\mathbf{x}_M) \\ 0 & \dfrac{\partial \phi^{-}_{K}}{\partial x_2}(\mathbf{x}_M) & 0 & 0 \end{bmatrix}, \tag{6.89}$$

while the matrices $\mathbf{G}^{+}_{KJ}$ and $\mathbf{G}^{-}_{KJ}$ are defined in (6.64) and (6.65). These equations are now inserted into the global coefficient matrix in the rows corresponding to the node positioned on $\Gamma^{\mathrm{g}+}_{\mathrm{t}}$ and $\Gamma^{\mathrm{g}-}_{\mathrm{t}}$, respectively. For the nodes on the boundary $\Gamma^{\mathrm{g}}_{\mathrm{s}}$, the interface conditions (6.15) and (6.16) are discretized by using approximations (6.29) and (6.30), while also utilizing the discretized compatibility conditions, (6.60) and (6.61), in the reciprocity of the gradient natural boundary conditions. Hence, the final form of the discretized interface conditions for this procedure states

$$\sum_{J=1}^{N_{\Omega_{\mathrm{s}}}} \phi^{+}_{J}(\mathbf{x}_I)\hat{\mathbf{u}}^{\mathrm{g}+}_{J} = \sum_{J=1}^{N_{\Omega_{\mathrm{s}}}} \phi^{-}_{J}(\mathbf{x}_M)\hat{\mathbf{u}}^{\mathrm{g}-}_{J}, \tag{6.90}$$

$$\mathbf{N}^{\mathrm{Gu}+}_{I} \sum_{J=1}^{N_{\Omega_{\mathrm{s}}}} \mathbf{G}^{+}_{IJ}\hat{\mathbf{u}}^{\mathrm{g}+}_{J} = -\mathbf{N}^{\mathrm{Gu}-}_{M} \sum_{J=1}^{N_{\Omega_{\mathrm{s}}}} \mathbf{G}^{-}_{MJ}\hat{\mathbf{u}}^{\mathrm{g}-}_{J}, \tag{6.91}$$

where $\mathbf{N}_I^{\mathrm{Gu}+}$ and $\mathbf{N}_M^{\mathrm{Gu}-}$ denote the matrices composed of unit normal vectors associated to the derivatives of gradient displacements defined by

$$\mathbf{N}_I^{\mathrm{Gu}+} = \begin{bmatrix} n_1^{\mathrm{g}+}(\mathbf{x}_I) & 0 & n_2^{\mathrm{g}+}(\mathbf{x}_I) & 0 \\ 0 & n_1^{\mathrm{g}+}(\mathbf{x}_I) & 0 & n_2^{\mathrm{g}+}(\mathbf{x}_I) \end{bmatrix}, \tag{6.92}$$

$$\mathbf{N}_M^{\mathrm{Gu}-} = \begin{bmatrix} n_1^{\mathrm{g}-}(\mathbf{x}_M) & 0 & n_2^{\mathrm{g}-}(\mathbf{x}_M) & 0 \\ 0 & n_1^{\mathrm{g}-}(\mathbf{x}_M) & 0 & n_2^{\mathrm{g}-}(\mathbf{x}_M) \end{bmatrix}. \tag{6.93}$$

These equations are substituted into the global coefficient matrix in the rows corresponding to the current node positioned on $\Gamma_{\mathrm{s}}^{\mathrm{g}}$. Here yet again, nodes I and M on the interface boundary $\Gamma_{\mathrm{s}}^{\mathrm{g}}$ have the same coordinates since the overlapping node concept is utilized. Furthermore, in the equations (6.90) and (6.91) there is no summation over indices I and M.

6.3.5. Discretized governing equations of the ε-RA gradient problem

The derivation of the discretized governing equations is quite similar to the previously presented procedure for the u-RA approach. Firstly, the governing equations (6.19) and (6.20) are written in the matrix form at the collocation nodes laying inside the homogeneous materials represented by domains Ω^+ and Ω^-

$$\boldsymbol{\varepsilon}_I^{\mathrm{g}+} - l^2\left[\boldsymbol{\nabla}^{\varepsilon+\mathrm{T}} \cdot \left(\boldsymbol{\nabla}^{\varepsilon+}\boldsymbol{\varepsilon}_I^{\mathrm{g}+}\right)\right] = \boldsymbol{\varepsilon}_I^{\mathrm{c}+}, \tag{6.94}$$

$$\boldsymbol{\varepsilon}_M^{\mathrm{g}-} - l^2\left[\boldsymbol{\nabla}^{\varepsilon-\mathrm{T}} \cdot \left(\boldsymbol{\nabla}^{\varepsilon-}\boldsymbol{\varepsilon}_M^{\mathrm{g}-}\right)\right] = \boldsymbol{\varepsilon}_M^{\mathrm{c}-}. \tag{6.95}$$

where $\boldsymbol{\nabla}^{\varepsilon 2} = \boldsymbol{\nabla}^{\varepsilon\mathrm{T}} \cdot (\boldsymbol{\nabla}^{\varepsilon})$ denotes the Laplacian operator written in the matrix form associated with the ε-RA approach. Thus, the comprising operators $\boldsymbol{\nabla}^{\varepsilon+}$ and $\boldsymbol{\nabla}^{\varepsilon-}$ are defined as

$$\boldsymbol{\nabla}^{\varepsilon+} = \begin{bmatrix} \dfrac{\partial(\ )^+}{\partial x_1}(\mathbf{x}_I) & 0 & 0 \\ 0 & \dfrac{\partial(\ )^+}{\partial x_1}(\mathbf{x}_I) & 0 \\ 0 & 0 & \dfrac{\partial(\ )^+}{\partial x_1}(\mathbf{x}_I) \\ \dfrac{\partial(\ )^+}{\partial x_2}(\mathbf{x}_I) & 0 & 0 \\ 0 & \dfrac{\partial(\ )^+}{\partial x_2}(\mathbf{x}_I) & 0 \\ 0 & 0 & \dfrac{\partial(\ )^+}{\partial x_2}(\mathbf{x}_I) \end{bmatrix}, \tag{6.96}$$

$$\boldsymbol{\nabla}^{\varepsilon-} = \begin{bmatrix} \dfrac{\partial(\ )^-}{\partial x_1}(\mathbf{x}_M) & 0 & 0 \\ 0 & \dfrac{\partial(\ )^-}{\partial x_1}(\mathbf{x}_M) & 0 \\ 0 & 0 & \dfrac{\partial(\ )^-}{\partial x_1}(\mathbf{x}_M) \\ \dfrac{\partial(\ )^-}{\partial x_2}(\mathbf{x}_M) & 0 & 0 \\ 0 & \dfrac{\partial(\ )^-}{\partial x_2}(\mathbf{x}_M) & 0 \\ 0 & 0 & \dfrac{\partial(\ )^-}{\partial x_2}(\mathbf{x}_M) \end{bmatrix}. \tag{6.97}$$

The equations (6.94) and (6.95) are now discretized using the relations (6.32) and (6.33) which leads to

$$\sum_{J=1}^{N_{\Omega_\mathrm{s}}} \phi_J^+ \hat{\boldsymbol{\varepsilon}}_J^{\mathrm{g}+} - l^2 \Big[\boldsymbol{\nabla}^{\varepsilon+\mathrm{T}} \cdot \Big(\sum_{K=1}^{N_{\Omega_\mathrm{s}}} \phi_K^+ \hat{\boldsymbol{\varepsilon}}_{\mathrm{G}K}^{\mathrm{g}+} \Big) \Big] = \boldsymbol{\varepsilon}_I^{\mathrm{c}+}, \tag{6.98}$$

$$\sum_{J=1}^{N_{\Omega_\mathrm{s}}} \phi_J^- \hat{\boldsymbol{\varepsilon}}_J^{\mathrm{g}-} - l^2 \Big[\boldsymbol{\nabla}^{\varepsilon-\mathrm{T}} \cdot \Big(\sum_{K=1}^{N_{\Omega_\mathrm{s}}} \phi_K^- \hat{\boldsymbol{\varepsilon}}_{\mathrm{G}K}^{\mathrm{g}-} \Big) \Big] = \boldsymbol{\varepsilon}_M^{\mathrm{c}-}, \tag{6.99}$$

where $\hat{\boldsymbol{\varepsilon}}_{\mathrm{G}}^{\mathrm{g}+}$ and $\hat{\boldsymbol{\varepsilon}}_{\mathrm{G}}^{\mathrm{g}-}$ denote the vectors of unknown derivatives of gradient strains defined by

$$\big[\hat{\boldsymbol{\varepsilon}}_{\mathrm{G}}^{\mathrm{g}+}\big]^{\mathrm{T}} = \Big[\frac{\partial \hat{\varepsilon}_{11}^{\mathrm{g}+}}{\partial x_1} \quad \frac{\partial \hat{\varepsilon}_{22}^{\mathrm{g}+}}{\partial x_1} \quad \frac{\partial \hat{\varepsilon}_{12}^{\mathrm{g}+}}{\partial x_1} \quad \frac{\partial \hat{\varepsilon}_{11}^{\mathrm{g}+}}{\partial x_2} \quad \frac{\partial \hat{\varepsilon}_{22}^{\mathrm{g}+}}{\partial x_2} \quad \frac{\partial \hat{\varepsilon}_{12}^{\mathrm{g}+}}{\partial x_2} \Big], \tag{6.100}$$

$$\big[\hat{\boldsymbol{\varepsilon}}_{\mathrm{G}}^{\mathrm{g}-}\big]^{\mathrm{T}} = \Big[\frac{\partial \hat{\varepsilon}_{11}^{\mathrm{g}-}}{\partial x_1} \quad \frac{\partial \hat{\varepsilon}_{22}^{\mathrm{g}-}}{\partial x_1} \quad \frac{\partial \hat{\varepsilon}_{12}^{\mathrm{g}-}}{\partial x_1} \quad \frac{\partial \hat{\varepsilon}_{11}^{\mathrm{g}-}}{\partial x_2} \quad \frac{\partial \hat{\varepsilon}_{22}^{\mathrm{g}-}}{\partial x_2} \quad \frac{\partial \hat{\varepsilon}_{12}^{\mathrm{g}-}}{\partial x_2} \Big]. \tag{6.101}$$

Herein, from the analysis of equations (6.98) and (6.99), it can be seen that an unsolvable system of equations is obtained where the nodal unknowns include nodal strains and the derivatives of nodal strains. The number of global unknowns is larger than the total number of equations. Hence, additional equations are again needed in order to close the system of equations. Here, this is done by imposing the compatibility at each node between the nodal derivatives of strains $\hat{\boldsymbol{\varepsilon}}_{\mathrm{G}}^{\mathrm{g}+(h)}(\mathbf{x}_K) \approx \hat{\boldsymbol{\varepsilon}}_{\mathrm{G}K}^{\mathrm{g}+}, \mathbf{x}_K \in S^+$ and $\hat{\boldsymbol{\varepsilon}}_{\mathrm{G}}^{\mathrm{g}-(h)}(\mathbf{x}_K) \approx \hat{\boldsymbol{\varepsilon}}_{\mathrm{G}K}^{\mathrm{g}-}, \mathbf{x}_K \in S^-$ and the nodal strains $\hat{\boldsymbol{\varepsilon}}_J^+; J = 1, 2, ..., N_{\Omega_\mathrm{s}}$ and $\hat{\boldsymbol{\varepsilon}}_J^-; J = 1, 2, ..., N_{\Omega_\mathrm{s}}$, respectively. Hence, the compatibility equations for the heterogeneous structure using this procedure state

$$\boldsymbol{\varepsilon}_{\mathrm{G}}^{\mathrm{g}+} = \mathbf{D}_{\mathrm{K}}^{\varepsilon+} \boldsymbol{\varepsilon}^{\mathrm{g}+}, \tag{6.102}$$

$$\boldsymbol{\varepsilon}_{\mathrm{G}}^{\mathrm{g}-} = \mathbf{D}_{\mathrm{K}}^{\varepsilon-} \boldsymbol{\varepsilon}^{\mathrm{g}-}. \tag{6.103}$$

The compatibility equations are now utilized at every nodes and discretized using (6.32) leading to

$$\hat{\boldsymbol{\varepsilon}}_{\mathrm{G}K}^{\mathrm{g}+} = \sum_{J=1}^{N_{\Omega_\mathrm{s}}} \mathbf{D}_{\mathrm{K}}^{\varepsilon+} \phi_J^+(\mathbf{x}_K) \hat{\boldsymbol{\varepsilon}}_J^{\mathrm{g}+} = \sum_{J=1}^{N_{\Omega_\mathrm{s}}} \mathbf{V}_{KJ}^+ \hat{\boldsymbol{\varepsilon}}_J^{\mathrm{g}+} \tag{6.104}$$

$$\hat{\boldsymbol{\varepsilon}}^{\mathrm{g}-}_{\mathrm{G}K} = \sum_{J=1}^{N_{\Omega_\mathrm{s}}} \mathbf{D}^{\varepsilon-}_{\mathrm{K}} \phi^{+}_{J}(\mathbf{x}_K) \hat{\boldsymbol{\varepsilon}}^{\mathrm{g}-}_{J} = \sum_{J=1}^{N_{\Omega_\mathrm{s}}} \mathbf{V}^{-}_{KJ} \hat{\boldsymbol{\varepsilon}}^{\mathrm{g}-}_{J}. \tag{6.105}$$

In the equations (6.104) and (6.105) the compatibility matrices are computed as

$$\mathbf{V}^{+}_{KJ} = \begin{bmatrix} \dfrac{\partial \phi^{+}_{J}}{\partial x_1}(\mathbf{x}_K) & 0 & \\ 0 & \dfrac{\partial \phi^{+}_{J}}{\partial x_1}(\mathbf{x}_K) & 0 \\ 0 & 0 & \dfrac{\partial \phi^{+}_{J}}{\partial x_1}(\mathbf{x}_K) \\ \dfrac{\partial \phi^{+}_{J}}{\partial x_2}(\mathbf{x}_K) & 0 & 0 \\ 0 & \dfrac{\partial \phi^{+}_{J}}{\partial x_2}(\mathbf{x}_K) & 0 \\ 0 & 0 & \dfrac{\partial \phi^{+}_{J}}{\partial x_2}(\mathbf{x}_K) \end{bmatrix}, \tag{6.106}$$

$$\mathbf{V}^{-}_{KJ} = \begin{bmatrix} \dfrac{\partial \phi^{-}_{J}}{\partial x_1}(\mathbf{x}_K) & 0 & \\ 0 & \dfrac{\partial \phi^{-}_{J}}{\partial x_1}(\mathbf{x}_K) & 0 \\ 0 & 0 & \dfrac{\partial \phi^{-}_{J}}{\partial x_1}(\mathbf{x}_K) \\ \dfrac{\partial \phi^{-}_{J}}{\partial x_2}(\mathbf{x}_K) & 0 & 0 \\ 0 & \dfrac{\partial \phi^{-}_{J}}{\partial x_2}(\mathbf{x}_K) & 0 \\ 0 & 0 & \dfrac{\partial \phi^{-}_{J}}{\partial x_2}(\mathbf{x}_K) \end{bmatrix}. \tag{6.107}$$

The nodal compatibility relations (6.104) and (6.105) are now introduced into equations (6.98) and (6.99). In this manner the solvable system of equations is attained with nodal strains as the only unknown variables. Thus, the final discretized equations are equal to

$$\mathbf{K}^{\mathrm{g}+}_{IJ} \hat{\boldsymbol{\varepsilon}}^{\mathrm{g}+}_{J} = \mathbf{F}^{\mathrm{g}+}_{I}, \quad I = 1, 2, ..., N, \tag{6.108}$$

$$\mathbf{K}^{\mathrm{g}-}_{MJ} \hat{\boldsymbol{\varepsilon}}^{\mathrm{g}-}_{J} = \mathbf{F}^{\mathrm{g}-}_{M}, \quad M = 1, 2, ..., P, \tag{6.109}$$

where the gradient nodal coefficient matrices $\mathbf{K}^{\mathrm{g}+}_{IJ}$ and $\mathbf{K}^{\mathrm{g}-}_{MJ}$ can be presented as

$$\mathbf{K}^{\mathrm{g}+}_{IJ} = \sum_{J=1}^{N_{\Omega_\mathrm{s}}} \mathbf{S}^{\varepsilon+}_{IJ} - l^2 \Big[\sum_{K=1}^{N_{\Omega_\mathrm{s}}} {\mathbf{V}^{\mathrm{g}+}_{IK}}^{\mathrm{T}} \sum_{J=1}^{N_{\Omega_\mathrm{s}}} \mathbf{V}^{\mathrm{g}+}_{KJ} \Big], \tag{6.110}$$

$$\mathbf{K}^{\mathrm{g}-}_{MJ} = \sum_{J=1}^{N_{\Omega_\mathrm{s}}} \mathbf{S}^{\varepsilon-}_{MJ} - l^2 \Big[\sum_{K=1}^{N_{\Omega_\mathrm{s}}} {\mathbf{V}^{\mathrm{g}-}_{MK}}^{\mathrm{T}} \sum_{J=1}^{N_{\Omega_\mathrm{s}}} \mathbf{V}^{\mathrm{g}-}_{KJ} \Big]. \tag{6.111}$$

In the above equations, the matrices $\mathbf{S}_{IJ}^{\varepsilon+}$ and $\mathbf{S}_{MJ}^{\varepsilon-}$ are diagonal and equal to

$$\mathbf{S}_{IJ}^{\varepsilon+} = \begin{bmatrix} \phi_J^+(\mathbf{x}_I) & 0 & 0 \\ 0 & \phi_J^+(\mathbf{x}_I) & 0 \\ 0 & 0 & \phi_J^+(\mathbf{x}_I) \end{bmatrix}, \tag{6.112}$$

$$\mathbf{S}_{MJ}^{\varepsilon-} = \begin{bmatrix} \phi_J^-(\mathbf{x}_M) & 0 & 0 \\ 0 & \phi_J^-(\mathbf{x}_M) & 0 \\ 0 & 0 & \phi_J^-(\mathbf{x}_M) \end{bmatrix}. \tag{6.113}$$

Herein, the gradient nodal force vectors $\mathbf{F}_I^{\mathrm{g}+}$ and $\mathbf{F}_M^{\mathrm{g}-}$ in equations (6.108) and (6.109) consist of known values of the nodal classical strains

$$\mathbf{F}_I^{\mathrm{g}+} = -\boldsymbol{\varepsilon}_I^{\mathrm{c}+}, \tag{6.114}$$

$$\mathbf{F}_M^{\mathrm{g}-} = -\boldsymbol{\varepsilon}_M^{\mathrm{c}-}. \tag{6.115}$$

From the analysis of nodal coefficient matrices $\mathbf{K}_{IJ}^{\mathrm{g}+}$ and $\mathbf{K}_{MJ}^{\mathrm{g}+}$ obtained by the presented mixed ε-RA procedure it is seen here again that only the first-order derivatives of shape functions have to be calculated in the assembling process. This lowers the needed computational time and effort, since no higher-order derivatives are evaluated.

6.3.6. Discretized boundary conditions of the ε-RA gradient problem

As presented before, the boundary conditions considered in the ε-RA procedure are different from the ones presented earlier in the u-RA procedure. In this procedure, the essential boundary conditions are the nodal values of gradient strains that need to be imposed on $\Gamma_{\mathrm{u}}^{\mathrm{g}+}$ and $\Gamma_{\mathrm{u}}^{\mathrm{g}-}$. Herein, this is again done in a straightforward manner due to the interpolatory properties of the shape functions. Thus, it can be written

$$\bar{\boldsymbol{\varepsilon}}_I^{\mathrm{g}+} = \sum_{J=1}^{N_{\Omega_{\mathrm{s}}}} \phi_J^+(\mathbf{x}_I)\hat{\boldsymbol{\varepsilon}}_J^{\mathrm{g}+}, \tag{6.116}$$

$$\bar{\boldsymbol{\varepsilon}}_M^{\mathrm{g}-} = \sum_{J=1}^{N_{\Omega_{\mathrm{s}}}} \phi_J^-(\mathbf{x}_M)\hat{\boldsymbol{\varepsilon}}_J^{\mathrm{g}-}. \tag{6.117}$$

The gradient natural boundary conditions in this procedure are defined by (6.23) and (6.24) and are enforced on the boundaries $\Gamma_{\mathrm{t}}^{\mathrm{g}+}$ and $\Gamma_{\mathrm{t}}^{\mathrm{g}+}$ using a mixed approach. Firstly, the approximation of derivatives of gradient strains (6.33) is utilized leading to

$$\bar{\mathbf{R}}_I^{\mathrm{g}+} = \mathbf{N}_I^{\mathrm{G}\varepsilon+} \sum_{K=1}^{N_{\Omega_{\mathrm{s}}}} \mathbf{S}_{IK}^{+} \hat{\boldsymbol{\varepsilon}}_{\mathrm{G}K}^{\mathrm{g}+}, \tag{6.118}$$

$$\bar{\mathbf{R}}_M^{\mathrm{g}-} = \mathbf{N}_M^{\mathrm{G}\varepsilon-} \sum_{K=1}^{N_{\Omega_\mathrm{s}}} \mathbf{S}_{MK}^{-} \hat{\boldsymbol{\varepsilon}}_{\mathrm{G}K}^{\mathrm{g}-}, \tag{6.119}$$

where $\hat{\boldsymbol{\varepsilon}}_{\mathrm{G}}^{\mathrm{g}+}$ and $\hat{\boldsymbol{\varepsilon}}_{\mathrm{G}}^{\mathrm{g}-}$ denote the vectors of unknown derivatives of gradient strains defined by (6.100) and (6.101) at K^{th} node influencing the approximations. In addition, matrices $\mathbf{N}_I^{\mathrm{G}\varepsilon+}$ and $\mathbf{N}_M^{\mathrm{G}\varepsilon-}$ are composed of the unit normal vectors associated with derivatives of gradient strains and are computed as

$$\mathbf{N}_I^{\mathrm{G}\varepsilon+} = \begin{bmatrix} n_1^{\mathrm{g}+}(\mathbf{x}_I) & 0 & 0 & n_2^{\mathrm{g}+}(\mathbf{x}_I) & 0 & 0 \\ 0 & n_1^{\mathrm{g}+}(\mathbf{x}_I) & 0 & 0 & n_2^{\mathrm{g}+}(\mathbf{x}_I) & 0 \\ 0 & 0 & n_1^{\mathrm{g}+}(\mathbf{x}_I) & 0 & 0 & n_2^{\mathrm{g}+}(\mathbf{x}_I) \end{bmatrix}, \tag{6.120}$$

$$\mathbf{N}_M^{\mathrm{G}\varepsilon-} = \begin{bmatrix} n_1^{\mathrm{g}-}(\mathbf{x}_M) & 0 & 0 & n_2^{\mathrm{g}-}(\mathbf{x}_M) & 0 & 0 \\ 0 & n_1^{\mathrm{g}-}(\mathbf{x}_M) & 0 & 0 & n_2^{\mathrm{g}-}(\mathbf{x}_M) & 0 \\ 0 & 0 & n_1^{\mathrm{g}-}(\mathbf{x}_M) & 0 & 0 & n_2^{\mathrm{g}-}(\mathbf{x}_M) \end{bmatrix}. \tag{6.121}$$

To obtain the discretized equations for the gradient natural boundary conditions with nodal gradient strains as the only unknowns, the compatibility conditions (6.104) and (6.105) are introduced into (6.118) and (6.119). Thus, the following equations can be written

$$\bar{\mathbf{R}}_I^{\mathrm{g}+} = \mathbf{N}_I^{\mathrm{G}\varepsilon+} \sum_{K=1}^{N_{\Omega_\mathrm{s}}} \mathbf{S}_{IK}^{\varepsilon 2+} \sum_{J=1}^{N_{\Omega_\mathrm{s}}} \mathbf{V}_{KJ}^{+} \hat{\boldsymbol{\varepsilon}}_J^{\mathrm{g}+}, \tag{6.122}$$

$$\bar{\mathbf{R}}_M^{\mathrm{g}-} = \mathbf{N}_M^{\mathrm{G}\varepsilon-} \sum_{K=1}^{N_{\Omega_\mathrm{s}}} \mathbf{S}_{MK}^{\varepsilon 2-} \sum_{J=1}^{N_{\Omega_\mathrm{s}}} \mathbf{V}_{KJ}^{-} \hat{\boldsymbol{\varepsilon}}_J^{\mathrm{g}-}. \tag{6.123}$$

For more simple computation, the 6 by 6 diagonal matrices $\mathbf{S}_{IK}^{\varepsilon 2+}$ and $\mathbf{S}_{MK}^{\varepsilon 2-}$, calculated analogous to relations (6.112) and (6.113), composed of shape function values, can again be omitted so the final expressions are

$$\bar{\mathbf{R}}_I^{\mathrm{g}+} = \mathbf{N}_I^{\mathrm{G}\varepsilon+} \sum_{J=1}^{N_{\Omega_\mathrm{s}}} \mathbf{V}_{IJ}^{+} \hat{\boldsymbol{\varepsilon}}_J^{\mathrm{g}+}, \tag{6.124}$$

$$\bar{\mathbf{R}}_M^{\mathrm{g}-} = \mathbf{N}_M^{\mathrm{G}\varepsilon-} \sum_{J=1}^{N_{\Omega_\mathrm{s}}} \mathbf{V}_{MJ}^{-} \hat{\boldsymbol{\varepsilon}}_J^{\mathrm{g}-}. \tag{6.125}$$

In the equations (6.124) and (6.125) there is no summation over indices I and M. The equations (6.124) and (6.125) are now introduced into the global coefficient matrix in the rows corresponding to the current node on boundaries $\Gamma_{\mathrm{t}}^{\mathrm{g}+}$ and $\Gamma_{\mathrm{t}}^{\mathrm{g}-}$, respectively. At the nodes positioned on the interface boundary $\Gamma_{\mathrm{s}}^{\mathrm{g}}$, the conditions according to (6.25) and (6.26) are discretized, by applying the approximations (6.32) and (6.33). In the reciprocity of the gradient natural boundary conditions the compatibility conditions (6.104)

and (6.105) are used. Thereafter, the final forms of the discretized interface boundary conditions for this procedure are

$$\sum_{J=1}^{N_{\Omega_\mathrm{s}}} \phi_J^+(\mathbf{x}_I)\hat{\boldsymbol{\varepsilon}}_J^{\mathrm{g}+} = \sum_{J=1}^{N_{\Omega_\mathrm{s}}} \phi_J^-(\mathbf{x}_M)\boldsymbol{\varepsilon}_J^{\mathrm{g}-}, \tag{6.126}$$

$$\mathbf{N}_I^{\mathrm{G}\varepsilon+} \sum_{J=1}^{N_{\Omega_\mathrm{s}}} \mathbf{V}_{IJ}^+ \hat{\boldsymbol{\varepsilon}}_J^{\mathrm{g}+} = -\mathbf{N}_M^{\mathrm{G}\varepsilon-} \sum_{J=1}^{N_{\Omega_\mathrm{s}}} \mathbf{V}_{MJ}^- \hat{\boldsymbol{\varepsilon}}_J^{\mathrm{g}-}. \tag{6.127}$$

Yet again, it should be noted that in the above equations there is no summation over indices I and M.

6.4. Numerical examples - gradient linear elasticity

The presented mixed staggered u-RA and ε-RA procedures are tested using several numerical examples. Since the derivation of analytical solutions for the strain gradient elasticity problems is complex in nature, it is only possible for a limited number of cases. Hence, here one-dimensional problems, dealing with homogeneous and heterogeneous bars, are used in order to verify the accuracy and efficiency of the proposed methods. Therein, both presented approaches are used. In the case of the heterogeneous bar, the ability of the methods to remove discontinuities from the strain field is also tested. Two-dimensional problems utilizing plates are used to model the size effects in the case of the homogeneous plate and the removal of discontinuities in the case of the heterogeneous plate. For the two-dimensional examples, only the u-RA procedure is used. Furthermore, for all numerical computations presented in this section only mixed collocation methods with the IMLS approximation are utilized.

6.4.1. Homogeneous bar subjected to force

For the first numerical example, a homogeneous bar subjected to force depicted in Figure 6.3 is chosen. The bar has a unit cross section, $A = 1$, and is of unit length, $L = 1$. The material properties of the bar are given with Young's modulus $E = 1$.

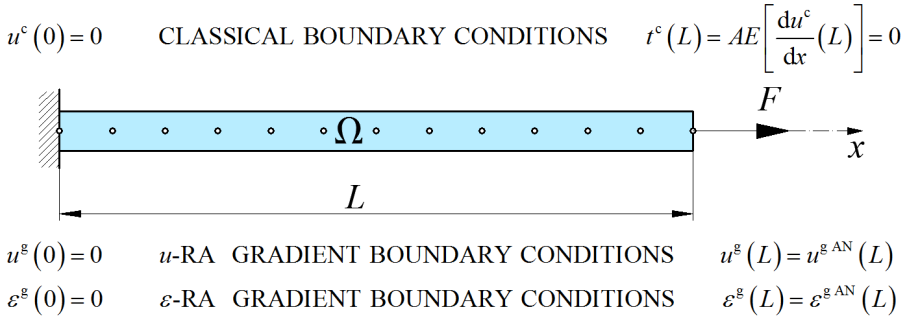

Figure 6.3: Homogeneous bar with boundary conditions

The left side of the bar is clamped, while on the right side the unit force $F = 1$ is applied. For this example, both the u-RA and the ε-RA procedure are considered. The boundary conditions for both of the applied operator-split methods are also shown on Figure 6.3. Therein, the gradient boundary conditions prescribed at the right end are denoted as $u^{g\,AN}$ and $\varepsilon^{g\,AN}$. Both sets of boundary conditions are taken from the analytical solution [204] obtained by solving the fourth-order Aifantis differential equation. Since the analytical solution of the problem is available, in order to determine the suitable size of a approximation domain, the parametric studies for the presented problem are performed. The influence of the approximation domain size (r_s/h_s) is investigated for both approaches. The uniform grid of nodes is used for the discretization, with the average nodal distance h_s. For the purpose of parametric studies, two different discretizations using 20 and 40 nodes are considered. Furthermore, the parametric analysis is done for the ratio of the Aifantis parameter to the length of the bar equal to $l/L = 0.2$ and for the first-order approximation functions. The results of the studies are portrayed in Figures 6.4 and 6.5. Herein, for the u-RA, the parametric study of displacement accuracy employing (5.63) is presented, while for the ε-RA the parametric study of strain accuracy has been done employing a L_2-norm analogous to (5.64).

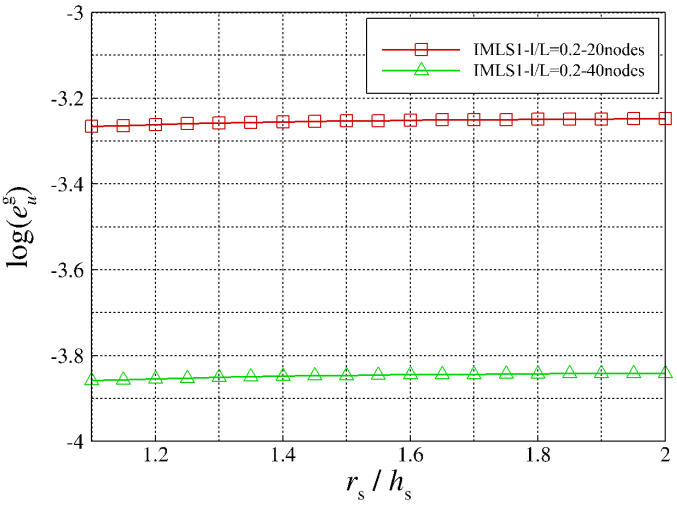

Figure 6.4: Homogeneous bar - u-RA parametric study - IMLS1 functions

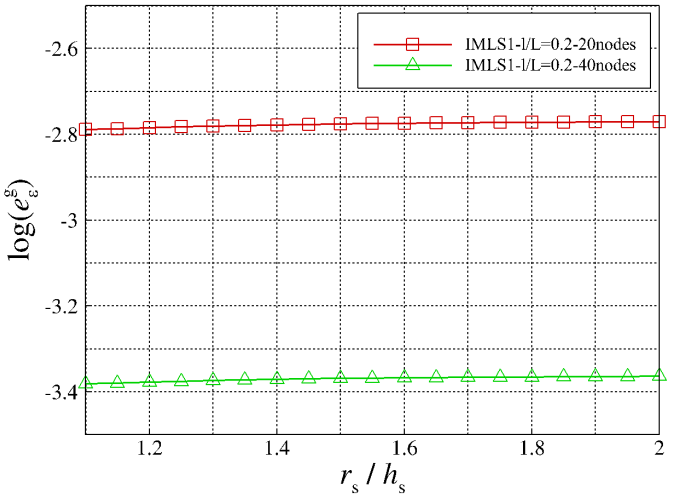

Figure 6.5: Homogeneous bar - ε-RA parametric study - IMLS1 functions

From the results it can be concluded that, for this example, the size of the approximation domain does not influence the accuracy of the solution. It can be also observed that both methods possess high numerical accuracy even if a low number of discretization nodes is used. For further verification of this statement, the global accuracy of the methods is analyzed using the convergence tests, which are depicted in Figures 6.6 and 6.7. For the analysis, the first-, second- and third-order approximation functions with the local approximation domain sizes $r_s/h_s = 1.2$ for IMLS1, $r_s/h_s = 2.25$ for IMLS2 and $r_s/h_s = 3.2$ for IMLS3 are used, respectively.

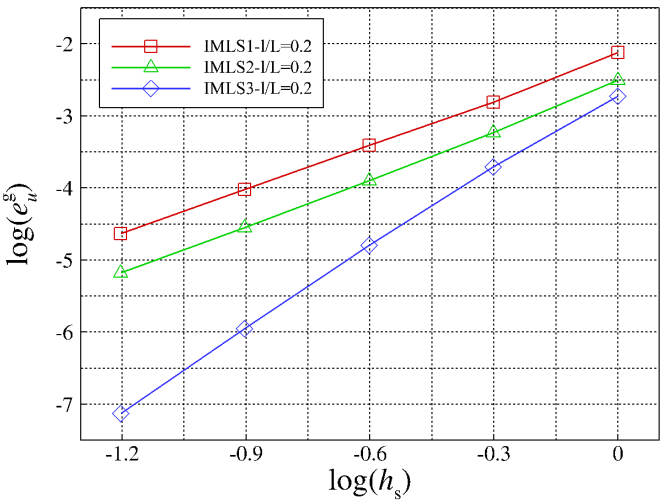

Figure 6.6: Homogeneous bar - u-RA displacements convergence study

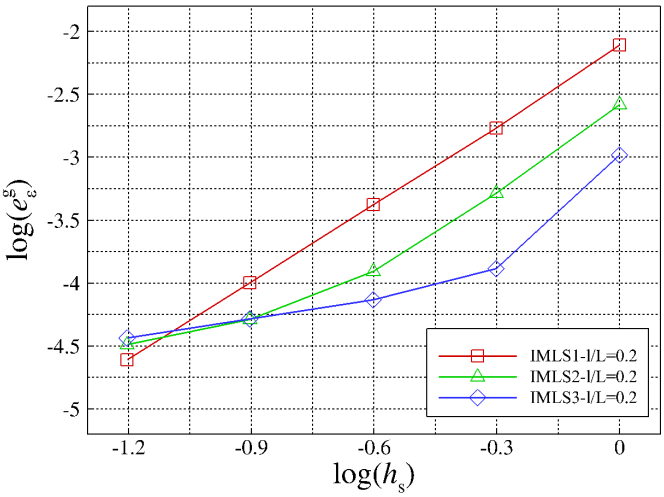

Figure 6.7: Homogeneous bar - ε-RA strain convergence study

From the above studies, it is easily seen that both mixed staggered methods converge to the accurate solutions regardless of the order of the used IMLS function. As evident, the application of higher-order functions results in globally more accurate solutions for the same number of nodes. It can be stated that the methods are suitable for modeling material deformation using the Aifantis theory of gradient elasticity. To demonstrate this claim in detail, the obtained distributions of gradient displacement u_x^{g} and gradient strain $\varepsilon_x^{\mathrm{g}}$ along the length of the bar are shown in Figures 6.8 and 6.9. The distributions are presented for various values of microstructural parameter l in order to test the higher-order gradient behaviour of the structure, i.e. the influence of the underlying microstructure on the deformation of the entire structure (size effect). Since the obtained distributions are virtually the same for both the u-RA and the ε-RA approach, they are drawn only once. It should also be noted that in the ε-RA procedure the displacements are calculated in a

post-processing step by employing kinematic relations. For the purpose of presenting the distributions, the discretization consisting of 20 nodes is utilized.

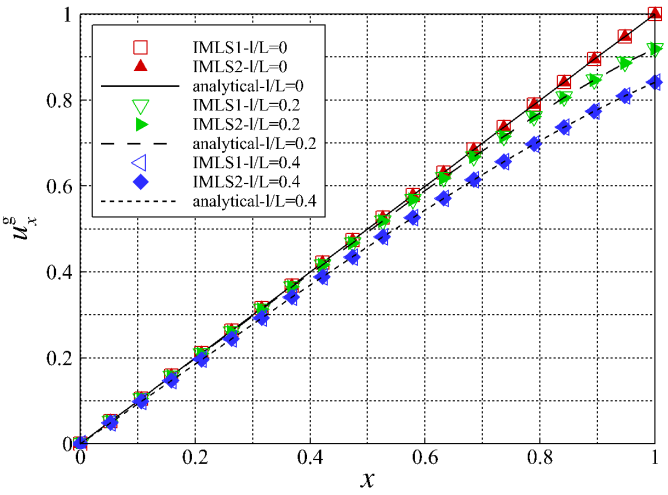

Figure 6.8: Homogeneous bar - distribution of displacement u_x^{g}

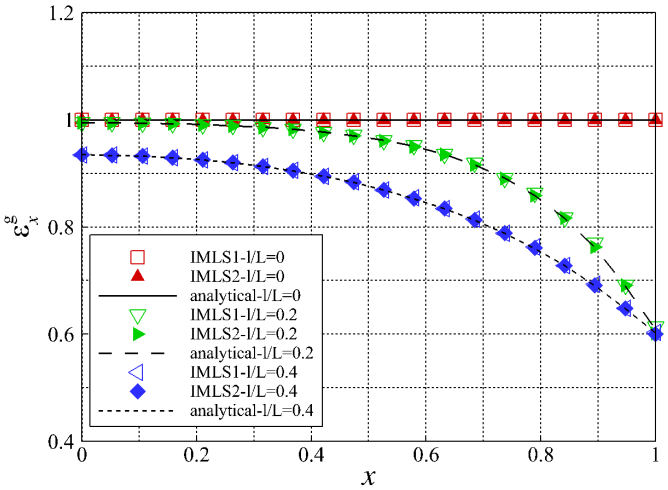

Figure 6.9: Homogeneous bar - distribution of strain $\varepsilon_x^{\mathrm{g}}$

As obvious from Figures 6.8 and 6.9, the methods accurately capture the material deformation for arbitrarily chosen value of the Aifantis parameter. Also, the use of a low-order meshless approximation suffices in achieving accurate solution for this example. It should also be noted that the classical solution of the considered problem is obtained when $l = 0$. Furthermore, it is necessary to stress that by increasing the value of the microstructural parameter, the values of displacement and strain begin to decrease.

6.4.2. Heterogeneous bar with essential boundary conditions

In the next example, a heterogeneous bar with displacements prescribed at both ends is analyzed. The geometry of the bar is presented in Figure 6.10. The bar is composed of two different homogeneous materials with unit cross section area ($A^+ = A^- = 1$) and with lengths $L = 10$. The material property of the left part of the bar is equal to $E^+ = 5$, while the property of the right is $E^- = 1$. Furthermore, in the analysis of deformation equal values of the Aifantis microstructural parameter l have been utilized for both homogeneous materials.

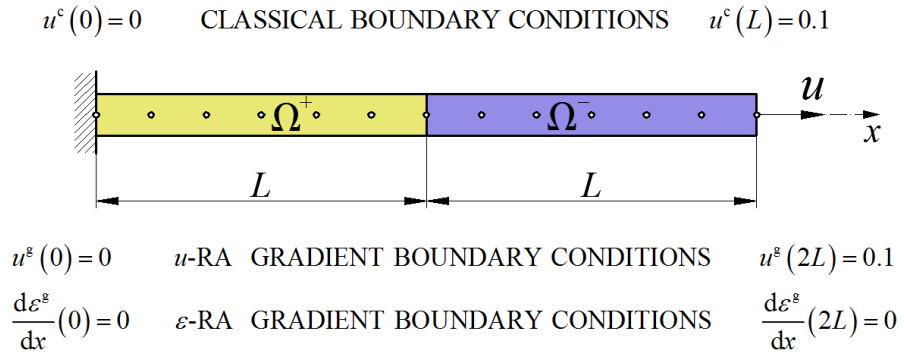

Figure 6.10: Heterogeneous bar with boundary conditions

Here, both presented staggered procedures are again tested. Since the analytical solution [156] of this problem can be derived, the boundary conditions in both procedures can be taken such as that they yield the same deformation behaviour. The utilized boundary conditions are presented in Figure 6.10. Firstly the influence of the approximation domain size on the accuracy of the solution for both procedures is tested. For that purpose, uniform grids are utilized, comprising of 20, 40 and 80 nodes. Furthermore, the influence of the microstructure on the deformation behaviour of the heterogeneous bar is modeled by utilizing the ratio $l/L = 0.2$. Only the first-order IMLS functions are again used to test the influence of the size of the approximation domain (r_s/h_s). As in the previous example, the accuracy of the u-RA procedure is tested using L_2 displacement error norm, while the accuracy of the ε-RA is computed using the L_2 strain error norm. Parametric studies have been performed and the results presented in Figures 6.11 and 6.12.

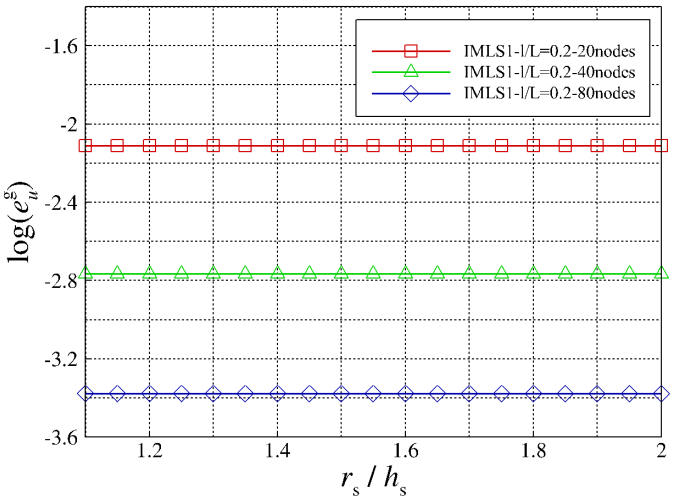

Figure 6.11: Heterogeneous bar - u-RA parametric study - IMLS1 functions

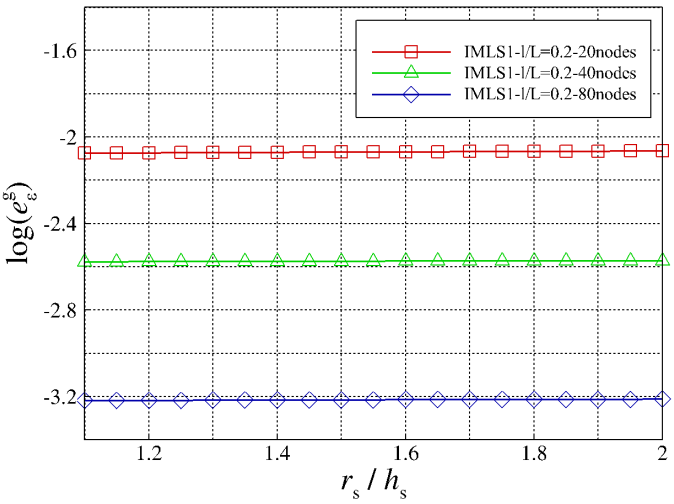

Figure 6.12: Heterogeneous bar - ε-RA parametric study - IMLS1 functions

As obvious, the approximation domain size for the considered discretizations does not have any influence on the accuracy of the meshless solution. From the analysis of the results portrayed in Figures 6.11 and 6.12, it is easily observed that both the u-RA and the ε-RA procedure are able to accurately describe the deformation of the heterogeneous bar even if only the first-order approximation is applied. Also, accurate results are achieved even for a low number of nodes. Furthermore, in order to demonstrate the global accuracy of the mixed collocation staggered methods, the convergence tests are carried out. The convergence rates obtained using the the first-, second- and third-order IMLS approximations are portrayed in Figures 6.13 and 6.14. For the scheme with the first-order basis (IMLS1), the local approximation domain size $r_s/h_s = 1.15$ is utilized, for the scheme using the second-order basis (IMLS2) $r_s/h_s = 2.2$ is applied and for the scheme employing the third-order basis (IMLS3) $r_s/h_s = 3.2$ is used.

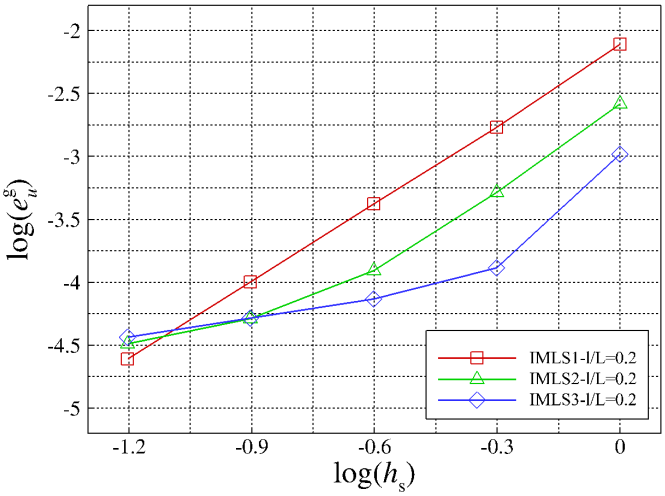

Figure 6.13: Heterogeneous bar - u-RA displacements convergence study

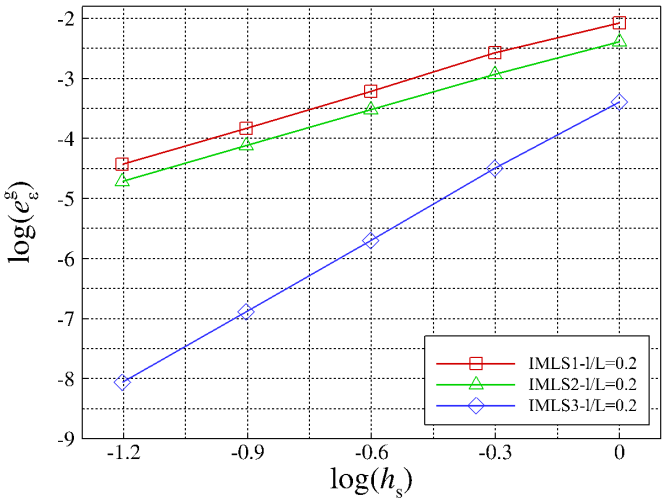

Figure 6.14: Heterogeneous bar - ε-RA strain convergence study

From the portrayed convergence tests, it can be again concluded that the proposed methods yield accurate solutions regardless of the utilized order of the approximation. Also, again as expected, the application of higher-order IMLS functions results in more accurate solutions for the same discretization and a higher convergence rate. The convergence rates suggest that the mixed staggered methods are able to appropriately model the deformation of heterogeneous structures with gradient elasticity. To further analyze and observe the material behaviour at the interface or near the interface of the homogeneous materials, the obtained distributions of gradient displacement u_x^g and gradient strain ε_x^g are plotted in Figures 6.15 and 6.16. The distributions are again presented for various values of the Aifantis parameter l in order to inspect the ability of the methods to remove discontinuities in the strain field. These discontinuities are always present when heterogeneous boundary value problem is solved using only linear elasticity theory. Both the

mixed u-RA and the mixed ε-RA procedure give exactly the same distributions. Here, yet again the displacement field in the ε-RA is determined in the post-processing step. The obtained distributions are computed using the discretization of 20 equidistant nodes.

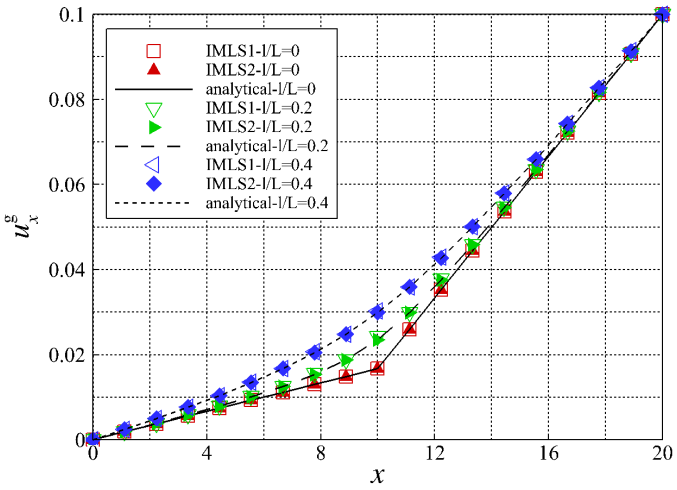

Figure 6.15: Heterogeneous bar - distribution of displacement u_x^{g}

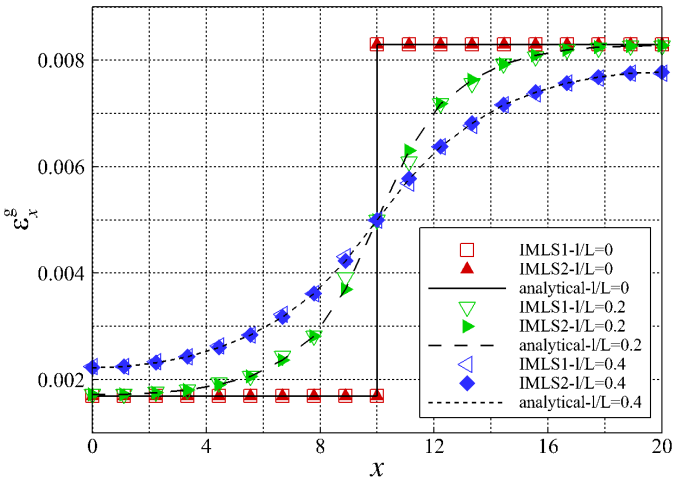

Figure 6.16: Heterogeneous bar - distribution of strain $\varepsilon_x^{\mathrm{g}}$

Finally, it can be concluded that the methods accurately describe the deformation responses of a heterogeneous material for any choice of the microstructural parameter l. Accurate displacement and strain distributions are observed for both orders of approximation functions. For the case when $l = 0$, the classical linear elasticity solution is achieved, as expected. However, it should be noted that in that case instead of the proposed reciprocity of the first-order of the normal derivatives at the interface in the u-RA procedure, the reciprocity of second-order normal derivatives has to be utilized in order to observe the derivative jump at the material interface. As evident from the distribution of the gradient strain $\varepsilon_x^{\mathrm{g}}$ depicted in Figure 6.16, for any value of the microstructural parameter

larger than zero ($l > 0$), the derivative jump is removed and the smoothing effect at and around the interface of the homogeneous materials is observed.

6.4.3. Homogeneous plate under uniform traction load

A simple two-dimensional example of a homogeneous plate is chosen in order to test the ability of the proposed mixed u-RA formulation to describe size effects. In other words, the effects when the mechanical response of a material depends on the dimensions of the corresponding microstructure. The homogeneous plate is subjected to the uniform traction load at the right edge, while fixed on the left side. The geometry of the homogeneous plate with all the utilized boundary conditions is portrayed in Figure 6.17.

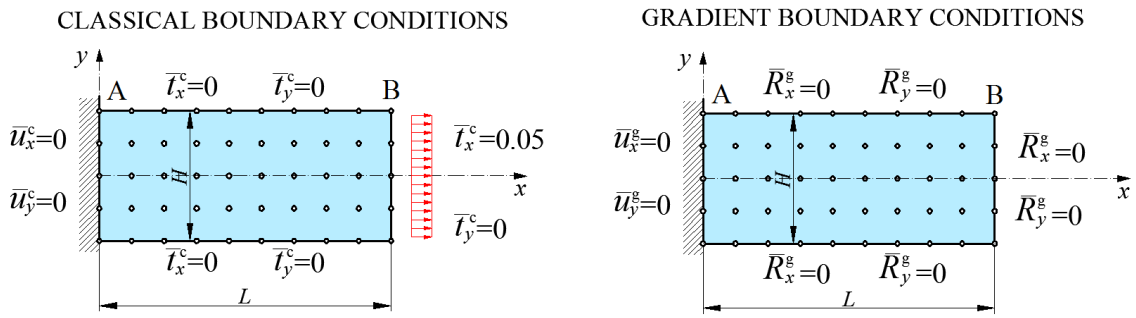

Figure 6.17: Homogeneous plate with boundary conditions

The length of the plate is $L = 6$, while the height is $H = 3$. The material properties of the plate are chosen as $E = 1$ and $\nu = 0.25$. The numerical discretization employing 481 structured grid of nodes is considered. Before the numerical tests two auxiliary definitions of strain ratio and stiffness ratio are defined. The strain ratio is tested at the upper left point A ($x = 0$, $y = 1.5$) of the plate. It is defined as

$$\text{strain ratio} = \frac{(\varepsilon_{\text{eq}}^{\text{c}})_{\text{A}}}{(\varepsilon_{\text{eq}}^{\text{g}})_{\text{A}}}, \tag{6.128}$$

where the classical and gradient equivalent strains are computed as

$$\varepsilon_{\text{eq}} = \sqrt{\frac{2}{3}\varepsilon_{ij}^{\text{dev}}\varepsilon_{ij}^{\text{dev}}}. \tag{6.129}$$

In the equation (6.130), the $\varepsilon_{ij}^{\text{dev}}$ denotes the strain deviator tensor

$$\boldsymbol{\varepsilon}^{\text{dev}} = \boldsymbol{\varepsilon} - \frac{1}{3}\text{tr}(\boldsymbol{\varepsilon})\mathbf{I}. \tag{6.130}$$

The stiffness ratio is tested at point B ($x = 6$, $y = 1.5$) of the plate and is computed as

$$\text{stiffness ratio} = \frac{\frac{\bar{t}_x^{\text{c}}}{(u_{\text{eq}}^{\text{c}})_{\text{B}}}}{\frac{\bar{t}_x^{\text{c}}}{(u_{\text{eq}}^{\text{g}})_{\text{B}}}}, \tag{6.131}$$

where u_{eq} denotes the equivalent displacements

$$u_{\text{eq}} = \sqrt{u_x^2 + u_y^2}. \tag{6.132}$$

Now, the computations of the strain ratio (6.128) and the stiffness ratio (6.131) for different values of the microstructural parameter l are carried out. The computations are done using the first- and the second-order IMLS functions. Herein, the sizes of the approximation domains $r_{\text{s}}/h_{\text{s}} = 1.4$ and $r_{\text{s}}/h_{\text{s}} = 2.3$ are utilized, respectively. The logarithm of strain ratio and stiffness ratio are plotted as functions of the logarithm of the normalized plate height (H/l) in Figures 6.18 and 6.19.

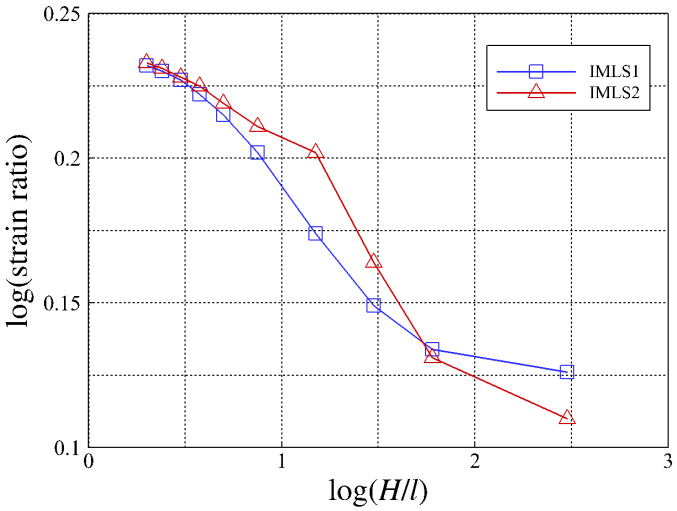

Figure 6.18: Homogeneous plate - size effect for strain ratio

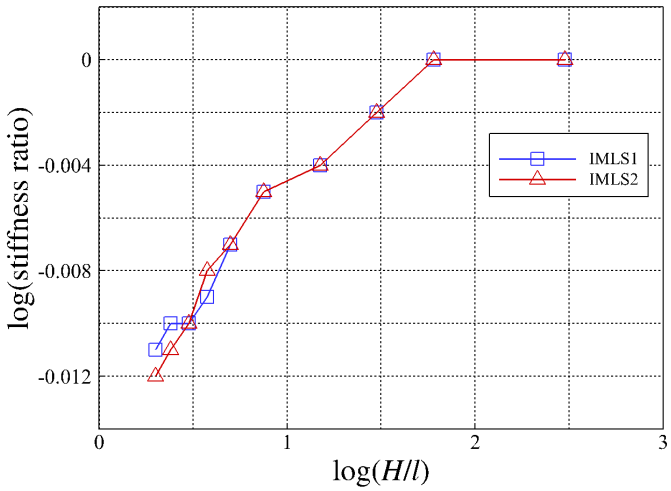

Figure 6.19: Homogeneous plate - size effect for stiffness ratio

As evident from the graphs, for increasing values of l the strain ratio increases and the stiffness ratio decreases. Hence, the higher-order term introduced in the constitutive

gradient elasticity equation smooths the strain field and the maximum strain is lowered, which increases the strain ratio. On the other hand, the maximum displacement is also lowered for greater values of l that decreases the stiffness ratio. It can be concluded that the proposed mixed u-RA staggered collocation method can be used to model size effects.

6.4.4. Heterogeneous plate under uniform displacement

As the last example, a heterogeneous plate is utilized in order to test the ability of the mixed u-RA procedure to remove discontinuities from the strain field. The material properties of the left part of the plate are taken as $E^+ = 1000$ and $\nu^+ = 0.25$, while the material data of the right side are $E^- = 10000$ and $\nu^- = 0.3$. The geometry of each homogeneous subdomain is defined by the length $L = 3$ and the height $H = 3$. The left edge of the heterogeneous plate is clamped, while the unit displacement is imposed on the right edge. The geometry of the plate and all other boundary conditions of the problem are depicted in Figure 6.20.

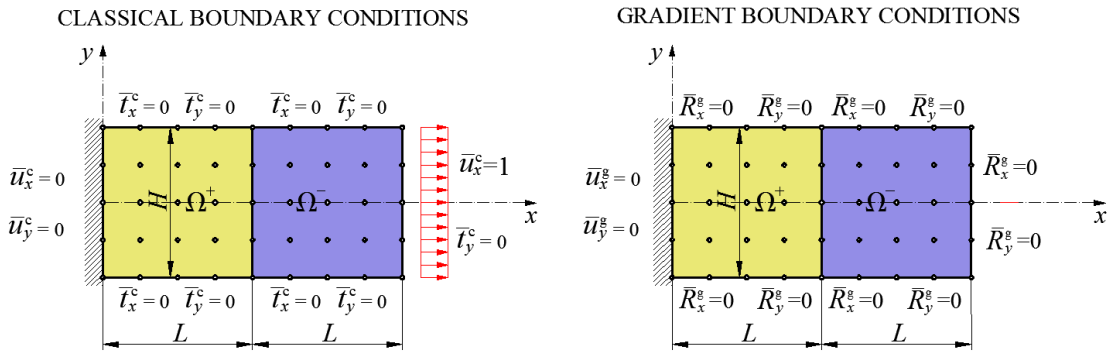

Figure 6.20: Heterogeneous plate with boundary conditions

For verification of the mixed u-RA approach, the distributions of the strain components ε_x^g and ε_{xy}^g along the line $y = 0.9$ are portrayed in Figures 6.21 - 6.22 for different values of the microstructural parameter l. The plate is discretized by uniform nodal distributions in both x and y directions using 242 nodes. The second-order IMLS functions are utilized for the solution of the problem with the size of the approximation domain $r_s = 2.4h_s$.

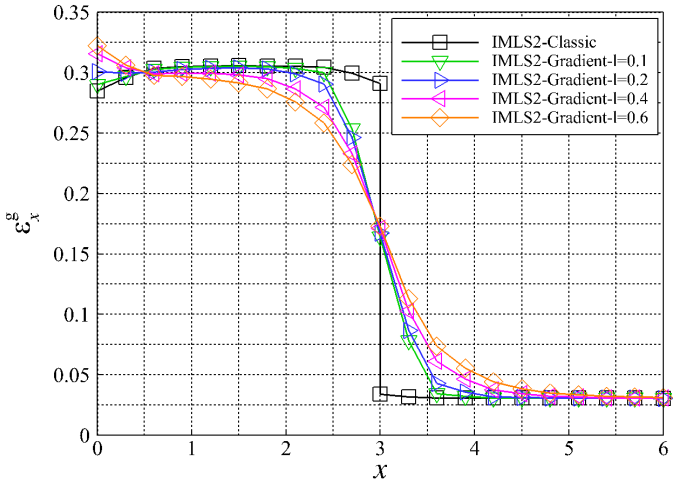

Figure 6.21: Heterogeneous plate - distribution of strain $\varepsilon_x^{\mathrm{g}}$ for $y = 0.9$

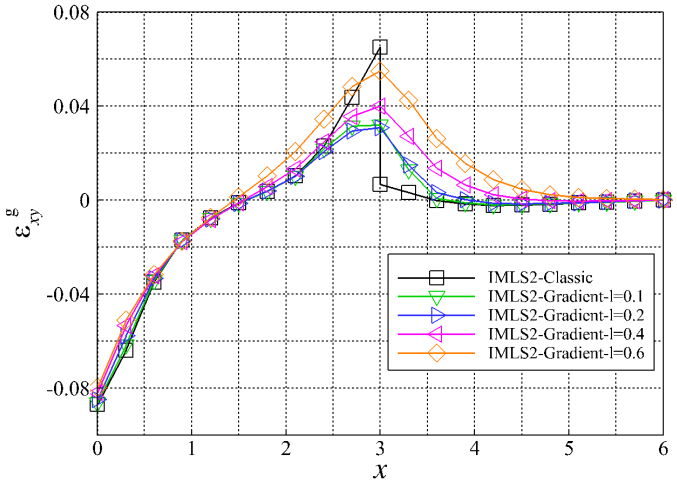

Figure 6.22: Heterogeneous plate - distribution of strain $\varepsilon_{xy}^{\mathrm{g}}$ for $y = 0.9$

As evident from the distributions of the strain components, the use of the microstructural parameter larger than zero causes the change in the strain field at and around the interface of the homogeneous materials. Thus, no discontinuity is observed when the Aifantis gradient elasticity is utilized. It can be concluded that the proposed method is suitable for smoothing the discontinuities in the strain field. This can also be demonstrated at the global level by depicting the contour plots for the entire heterogeneous structure. Hence, in Figures 6.23 and 6.24 the contour plots of the strain components $\varepsilon_y^{\mathrm{c}}$ and $\varepsilon_y^{\mathrm{g}}$ are portrayed. The smoothing effects on the material boundary are easily visible.

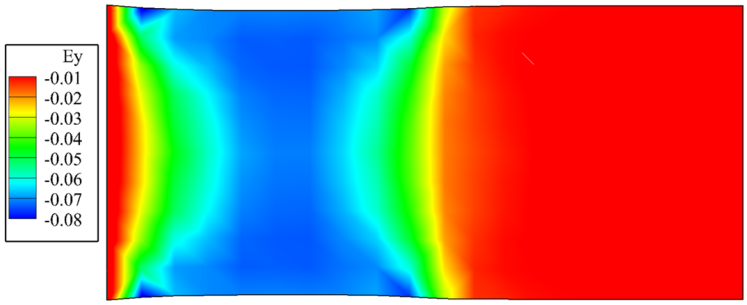

Figure 6.23: Heterogeneous plate - distribution of strain $\varepsilon_y^{\mathrm{c}}$

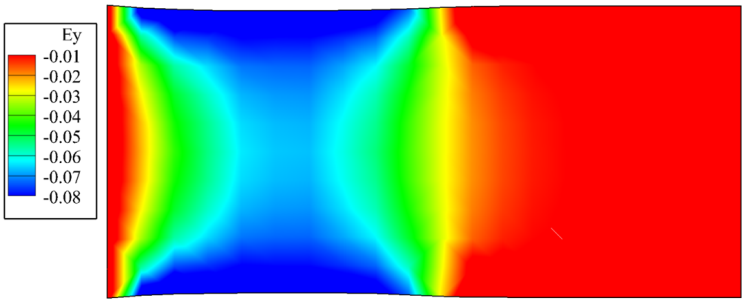

Figure 6.24: Heterogeneous plate - distribution of strain $\varepsilon_y^{\mathrm{g}}$ for $l = 0.2$

7 Conclusions and future investigations

The mixed collocation methods based on the Meshless Local Petrov-Galerkin (MLPG) concept have been proposed and applied for the modeling of deformation responses of heterogeneous structures. The developed methods are based on the theories of classical and gradient linear elasticity. Hence, the conclusions are also given separately for each of used formulation theories.

Firstly, the mixed collocation method for modeling of classical linear elastic deformation response of heterogeneous materials is proposed. Herein, the equilibrium equations are discretized at collocation nodes, so there is no need for numerical integration and the final system of equations is obtained in a faster and computationally more efficient manner in comparison to the existing meshless methods. The method of the overlapping nodes is used for the discretization of the interface boundary between homogeneous areas with different material characteristics. In these nodes, the displacement continuity and traction reciprocity conditions are enforced. In the mixed method, the approximation of the stress and displacement components using the same meshless functions is utilized. For the approximation the interpolatory Moving Least Squares (MLS) functions and Radial Point Interpolation Method (RPIM) functions are used. Due to the interpolatory property of the meshless shape functions, the essential boundary conditions are enforced straightforwardly at the nodes positioned on the boundaries with the prescribed displacement boundary conditions. A solvable system of equations is obtained by applying additional compatibility relations between the approximated fields at the collocation nodes. As a result, in the proposed mixed method only the first-order derivatives of meshless shape functions have to be computed, which contributes to numerical efficiency.

From the available literature, it can be seen that in this Thesis the mixed meshless method is applied for the first time for the modeling of heterogeneous materials. Within the thesis, the accuracy of the presented mixed approach is compared to the standard fully displacement (primal) collocation approach, where only the displacement field is approximated. From the analysis of convergence rates, it can be deduced that the fully

displacement approach practically does not converge if the first-order functions are applied. On the other hand, the presented mixed approach with the first-order functions can achieve high accuracy and convergence rates comparable to those obtained by the primal method with the second-order functions, at least in the case of the uniform discretization of the structure. The primal approach seems to exhibit oscillatory convergence behaviour even when higher-order approximations are utilized, while the mixed approach reproduces very accurate solutions for all of the considered examples. Hence, it can be stated that the proposed mixed approach is more robust than the primal approach. In addition, if the equal size of the support domain is considered, it achieves better global accuracy than the primal approach. One of the reason for the mixed method superiority over the primal approach is the lower-order of derivatives appearing in the governing equations. Furthermore, the presented mixed approach accurately captures the jumps in the strain and stress fields at material interfaces. In addition, the numerical efficiency of the proposed method for classical linear elasticity is estimated in comparison to FEM with respect to accuracy, convergence rates and computational time. For the purpose of comparison with FEM, the triangular and quadrilateral finite elements from the commercial software package ABAQUS are utilized. The present method yields convergence rates which are larger or comparable to those obtained by FEM, while it is at the same time more accurate for the same number of degrees of freedom. On the other hand, the FEM method is still faster for equal number of degrees of freedom. Nevertheless, as the collocation method needs less nodes to achieve the same level of global accuracy as FEM, the computational time required for solving an engineering problem might be smaller or comparable to that of FEM. It is known that the efficiency of meshless methods may depend on the chosen values of various numerical parameters. Hence, a detailed testing of the influence of relevant parameters on the accuracy of the considered methods is conducted. Thereby, the support domain size and the values of RBF shape parameters are investigated. In this way, the values of the parameters that ensure good accuracy of the methods are chosen. The stability of the methods is tested only with regard to the choice of the numerical meshless approximation parameters. Thus, the research of the stability of the mixed methods regarding the selection of approximation functions for the unknown field values was not conducted in the scope of this Thesis. Nevertheless, a new mixed meshless collocation method for the deformation modeling of heterogeneous materials based on classical linear elastic formulation of the boundary value problem is developed. This mixed method achieves greater accuracy and numerical efficiency in describing deformation processes of heterogeneous materials, in comparison to the existing numerical meshless methods and FEM.

Secondly, two different mixed collocation methods based on the gradient elasticity

theory have been proposed. So far, in the previous scientific investigations, the meshless collocation methods have not yet been considered for the modeling of materials described by higher-order theories. Herein, the operator-split procedures are considered. Hence, the problem is solved in a staggered manner using the Aifantis strain gradient theory with only one unknown microstructural parameter. Therein, firstly the boundary value problem of classical elasticity is solved, whose solution is then used as the input for the corresponding gradient boundary value problem. For description of both problems identical spatial discretizations, with the same positions of nodes, are utilized. Given that only collocation methods are used, there is no need for numerical integration, which increases the numerical efficiency. In the classical problem, the same functions are used to approximate the strain and displacement components in both mixed methods. As in the classical linear elastic case the solution for the entire heterogeneous structure is determined by enforcing appropriate essential and natural boundary conditions along the interfaces of the homogeneous subdomains. Herein, all independent variables are approximated in such a manner that each homogeneous subdomain is treated as a separate problem and the equations are satisfied directly at the nodes. The application of the staggered solution scheme and the mixed meshless approach result in a accurate and stable numerical formulations where only first-order derivatives of shape functions need to be calculated. This low-order of needed derivatives also decreases the computational time of the methods.

The gradient theory is used here in order to more accurately capture the material behaviour near the interface between regions with different material properties and to remove jumps in the strain fields that can be observed when a classical theory of linear elasticity is used. Furthermore, the methods are also utilized for the modeling of physical phaenomena in which the microstructure has a significant impact on the deformation of a considered solid body. The methods are firstly verified on one-dimensional examples, where the ability of the methods to describe the realistic deformation behaviour around the interface of two different homogeneous materials is tested. It has been shown that with the use of appropriate boundary conditions the methods are able to reproduce the classical solution of the problem for the zero value of the Aifantis internal length parameter. In two-dimensional examples, the methods are used to describe the influence of the size of the solid body on the deformation behaviour (the size effect). In comparison to the available solutions from the literature, it can be concluded that the proposed methods show significant potential for solving similar problems. It should be noted that the proposed gradient numerical methods can remove discontinuities in the strain field and smooth the fields around the interface boundary between different materials. This enables more natural description of transitions in the physical field distributions between various homogeneous material regions inside heterogeneous structures. Hence, two new efficient

mixed meshless collocation formulations based on a gradient deformation theory, which do not require numerical integration, are developed.

In further research, the focus will be aimed to extending the proposed mixed meshless methods based on staggered gradient elasticity, to solve the original fourth-order differential equation arising from Aifantis gradient theory. Due to the high-order derivatives that need to be calculated in the problem the well-known solution stability problems of collocation methods will come into effect. In order to alleviate the stability issues the weak-strong meshless formulation will also be considered. On the other hand, the proposed mixed methods could be also employed in the research field of fracture mechanics to try to describe the process of damage evolution through a heterogeneous material.

Životopis

Boris Jalušić rođen je 11. kolovoza 1984. u Čakovcu. Osnovnu školu pohađao je također u Čakovcu, gdje je 1999. godine upisao gimnaziju matematičko-prirodoslovnog usmjerenja. Nakon završene gimnazije, upisuje studij strojarstva na Fakultetu strojarstva i brodogradnje u Zagrebu, gdje je diplomirao 2009. godine na smjeru Inženjersko modeliranje i računalne simulacije. Od 2010. godine zaposlen je kao asistent na Zavodu za tehničku mehaniku na Fakultetu strojarstva i brodogradnje u Zagrebu, gdje pohađa poslijediplomski studij, smjer Teorija konstrukcija. Kao istraživač sudjelovao je na tri znanstvena projekta. Pritom, se stručno usavršava sudjelovanjem na mnogim inozemnim radionicama i stručnim skupovima. Također, tijekom istraživanja boravio je tri mjeseca na Sveučilištu Leibniz u Hannoveru, Njemačka, 2016. godine. Uz istraživački rad, aktivno je sudjelovao u nastavi iz više kolegija dodiplomskog i diplomskog studija. Član je Hrvatskog društva za mehaniku. Autor je 12 znanstvenih radova, od kojih je jedan objavljen u SCIE znanstvenom časopisu, a jedan prihvaćen za objavljivanje u CC znanstvenom časopisu. Aktivno u govoru i pismu koristi engleski jezik, a pasivno poznaje njemački jezik.

Biography

Boris Jalušić was born on August 11, 1984 in Čakovec, Croatia. He attended primary school in the place of birth, where in 1999 he also enrolled in grammar school oriented on mathematical and natural sciences. Afterward, he enrolled at graduate study at the Faculty of Mechanical Engineering and Naval Architecture. In 2009 he graduated at the Faculty with most of the studies completed on Engineering modeling and computer simulations. Since 2010, he has been employed as a research assistant at the Institute of Applied Mechanics at the Faculty of Mechanical Engineering and Naval Architecture, where he is enrolled in the postgraduate studies in Theory of Structures and Design. He has been working as a research assistant on three scientic projects. In doing so, he is improving his professional knowledge by attending many international workshops and scientific conferences. Also, during the research period in 2016 he conducted his work as a guest researcher for the duration of three months at the Leibniz University in Hanover, Germany. In addition, he has been involved in the teaching activities in a number of courses from the graduate study. He is a member of the Croatian Society of Mechanics. He is the author of 12 scientific publications, from which one in published in a SCIE scientific journal, and one is accepted for publication in a CC scientific journal. He has a very good knowledge of English language and basic knowledge of German language.

Bibliography

[1] C. Miehe; A. Koch. Computational micro-to-macro transitions of discretized microstructures undergoing small strains. *Archive of Applied Mechanics*, 72(4):300–317, 2002.

[2] V. G. Kouznetsova. *Computational homogenization for the multi-scale analysis of multi-phase materials*. PhD thesis, Technische Universiteit Eindhoven, 2002.

[3] L. Kaczmarczyk; C. J. Pearce; N. Bićanić. Scale transition and enforcement of RVE boundary conditions in second-order computational homogenization. *International Journal for Numerical Methods in Engineering*, 74(3):506–522, 2008.

[4] A. Romkes; J. T. Oden; K. Vemaganti. Multi-scale goal-oriented adaptive modeling of random heterogeneous materials. *Mechanics of Materials*, 38(8-10):859872, 2006.

[5] M. Jiang; I. Jasiuk; M. Ostoja-Starzewski. Apparent elastic and elastoplastic behavior of periodic composites. *International Journal of Solids and Structures*, 39(1):199–212, 2002.

[6] J. P. Gardner. *Micromechanical modeling of composite materials in finite element analysis using an embedded cell approach*. PhD thesis, Massachusetts Institute of Technology, 1994.

[7] V. G. Kouznetsova; M. G. D. Geers; W. A. M. Brekelmans. Multi-scale second-order computational homogenization of multi-phase materials: a nested finite element solution strategy. *Computer Methods in Applied Mechanics and Engineering*, 193(48-51):5525–5550, 2004.

[8] I. Temizer; P. Wriggers. Homogenization in finite thermoelasticity. *Journal of the Mechanics and Physics of Solids*, 59(2):344–372, 2011.

[9] H. J. Kim; C. C. Swan. Voxel-based meshing and unit-cell analysis of textile composites. *International Journal for Numerical Methods in Engineering*, 56(7):977–1006, 2003.

[10] H. J. Kim; C. C. Swan. Algorithms for automated meshing and unit cell analysis of periodic composites with hierarchical tri-quadratic tetrahedral elements. *International Journal for Numerical Methods in Engineering*, 58(11):1683–1711, 2003.

[11] R. A. Toupin. Elastic materials with couple-stresses. *Archive for Rational Mechanics and Analysis*, 11(1):385–414, 1962.

[12] R. D. Mindlin. Micro-structure in linear elasticity. *Archive for Rational Mechanics and Analysis*, 16(1):51–78, 1964.

[13] H. Askes; E. C. Aifantis. Gradient elasticity in statics and dynamics: An overview of formulations, length scale identification procedures, finite element implementations and new results. *International Journal of Solids and Structures*, 48(13):1962–1990, 2011.

[14] A. C. Eringen. On differential equations of nonlocal elasticity and solutions of screw dislocation and surface waves. *Journal of Applied Physics*, 54(9):4703–4710, 1983.

[15] E. C. Aifantis. On the role of gradients in the localization of deformation and fracture. *International Journal of Engineering Science*, 30(10):1279–1299, 1992.

[16] G. Engel; K. Garikipati; T. J. R. Hughes; M. G. Larson; L. Mazzei; R. L. Taylor. Continuous/discontinuous finite element approximations of fourth-order elliptic problems in structural and continuum mechanics with applications to thin beams and plates, and strain gradient elasticity. *Computer Methods in Applied Mechanics and Engineering*, 191(34):3669–3750, 2002.

[17] P. E. Fischer. *C^1 Continuous Methods in Computational Gradient Elasticity*. PhD thesis, Universität Erlangen-Nürnberg, 2011.

[18] E. Amanatidou; N. Aravas. Mixed finite element formulations of strain-gradient elasticity problems. *Computer Methods in Applied Mechanics and Engineering*, 191(15-16):1723–1751, 2002.

[19] T. D. Dang; B. V. Sankar. Meshless Local Petrov-Galerkin Formulation for Problems in Composite Micromechanics. *AIAA Journal*, 45(4):912–921, 2007.

[20] I. Ahmadi; M. M. Aghdam. A Truly Generalized Plane Strain Meshless Method for Combined Normal and Shear Loading of Fibrous Composites. *Engineering Analysis with Boundary Elements*, 35(3):395–403, 2011.

[21] S. N. Atluri; S. Shen. *The Meshless Local Petrov-Galerkin (MLPG) Method*. Tech Science Press, USA, 2002.

[22] G. R. Liu. *Mesh Free Methods: Moving Beyond the Finite Element Method*. CRC Press, Boca Raton, USA, 2003.

[23] G. R. Liu; Y. T. Gu. *An Introduction to Meshfree Methods and Their Programming*. Springer, Dordrecht, Netherlands, 2005.

[24] Y. Chen; J. Lee; A. Eskandarian. *Meshless Methods in Solid Mechanics*. Springer, New York, USA, 2006.

[25] W. Chen; Z.-J. Fu; C. S. Chen. *Recent Advances in Radial Basis Function Collocation Methods*. Springer Berlin Heidelberg, 2014.

[26] Z. Tang; S. Shen; S. N. Atluri. Analysis of materials with strain-gradient effects: A Meshless Local Petrov-Galerkin (MLPG) approach, with nodal displacements only. *CMES - Computer Modeling in Engineering & Sciences*, 4(1):177–196, 2003.

[27] S. N. Atluri; S. P. Shen. The Meshless Local Petrov-Galerkin (MLPG) Method - A Simple & Less-costly Alternative to the Finite Element and Boundary Element Methods. *CMES - Computer Modeling in Engineering & Sciences*, 3(1):11–51, 2002.

[28] S. N. Atluri; T. Zhu. A new Meshless Local Petrov-Galerkin (MLPG) approach in computational mechanics. *Computational Mechanics*, 22(2):117–127, 1998.

[29] S. N. Atluri; J. Y. Cho; H.-G. Kim. Analysis of thin beams, using the meshless local Petrov-Galerkin method, with generalized moving least squares interpolations. *Computational Mechanics*, 24(5):334–347, 1999.

[30] S. N. Atluri; S. Shen. The basis of meshless domain discretization: the meshless local Petrov-Galerkin (MLPG) method. *Advances in Computational Mathematics*, 23(1):73–93, 2005.

[31] N. R. Aluru. A point collocation method based on reproducing kernel approximations. *International Journal for Numerical Methods in Engineering*, 47(6):1083–1121, 2000.

[32] X. Liu; K. Tai. Point interpolation collocation method for the solution of partial differential equations. *Engineering Analysis with Boundary Elements*, 30(7):598–609, 2006.

[33] T. Jarak; J. Hoster; B. Jalušić; J. Sorić. Numerical Analysis of 2-D Linear Elastic Problems by MLPG Method. In Z. Virag; H. Kozmar.; I. Smojver, editor, *Book of Abstracts of the 7th International Congress of Croatian Society of Mechanics*, pages 153–154, Zadar, Croatia, 22-25 May 2012.

[34] B. Jalušić; T. Jarak; J. Sorić. On the enforcement of Neumann boundary conditions in the mixed MLPG collocation method for 2-D linear elastic problems. In S. N. Atluri; I. Vušanović; B. Šarler, editor, *Book of Abstracts of ICCES MM 2012: ICCES Special symposium on Meshless & Other Novel Computational Methods*, page 16, Budva, Montenegro, 2-6 September 2012.

[35] S. N. Atluri; Z. D. Han; A. M. Rajendran. A New Implementation of the Meshless Finite Volume Method, Through the MLPG "Mixed" Approach. *CMES - Computer Modeling in Engineering & Sciences*, 6(6):491–513, 2004.

[36] Z. Han; S. N. Atluri. A Truly-Meshless Galerkin Method Through the MLPG "Mixed" Approach. *Journal of Marine Science and Technology*, 19(4):444–452, 2011.

[37] S. Long; S. N. Atluri. A Meshless Local Petrov-Galerkin Method for Solving the Bending Problem of a Thin Plate. *CMES - Computer Modeling in Engineering & Sciences*, 3(1):53–63, 2002.

[38] T. Jarak; J. Sorić; J. Hoster. Analysis of Shell Deformation Responses by the Meshless Local Petrov-Galerkin (MLPG) Approach. *CMES - Computer Modeling in Engineering & Sciences*, 18(3):235–246, 2007.

[39] H. Askes; E. C. Aifantis. Numerical modeling of size effects with gradient elasticity - Formulation, meshless discretization and examples. *International Journal of Fracture*, 117(4):347–358, 2002.

[40] C. W. Liu; E. Taciroglu. Enriched reproducing kernel particle method for piezoelectric structures with arbitrary interfaces. *International Journal for Numerical Methods in Engineering*, 67(11):1565–1586, 2006.

[41] D. Wang; Y. Sun; L. Li. A Discontinuous Galerkin Meshfree Modeling of Material Interface. *CMES - Computer Modeling in Engineering & Sciences*, 45(1):57–82, 2009.

[42] L. W. Cordes; B. Moran. Treatment of Material Discontinuity in the Element-Free Galerkin Method. *Computer Methods in Applied Mechanics and Engineering*, 139(96):75–89, 1996.

[43] R. C. Batra; M. Porfiri; D. Spinello. Treatment of Material Discontinuity in Two Meshless Local Petrov-Galerkin (MLPG) Formulations of Axisymmetric Transient Heat Conduction. *International Journal for Numerical Methods in Engineering*, 61(14):2461–2479, 2004.

[44] A. Carpinteri; G. Ferro; G. Ventura. An augmented lagrangian approach to material discontinuities in meshless methods. *Computational Mechanics*, 37(3):207–220, 2006.

[45] J. Sorić. *Metoda konačnih elemenata*. Golden Marketing, Zagreb, 2004.

[46] T. Belytschko; Y. Y. Lu; L. Gu; M. Tabbara. Element-free galerkin methods for static and dynamic fracture. *International Journal of Solids and Structures*, 32(17-18):2547–2570, 1995.

[47] S. N. Atluri. *The Meshless Method (MLPG) for Domain & BIE Discretization*. Tech Science Press, Forsyth, USA, 2004.

[48] Y. C. Cai; H. H. Zhu. Direct Imposition of Essential Boundary Conditions and Treatment of Material Discontinuities in the EFG Method. *Computational Mechanics*, 34(4):330–338, 2004.

[49] S. Masuda; H. Noguchi. Analysis of Structure with Material Interface by Meshfree Method. *CMES - Computer Modeling in Engineering & Sciences*, 11(3):131–143, 2006.

[50] Q. Li; S. Shen; Z. D. Han; S. N. Atluri. Application of Meshless Local Petrov-Galerkin (MLPG) to Problems with Singularities and Material Discontinuities in 3-D Elasticity. *CMES - Computer Modeling in Engineering & Sciences*, 4(5):571–585, 2003.

[51] K. Šalkauskas. Moving least squares interpolation with thin-plate splines and radial basis functions. *Computers & Mathematics with Applications*, 24(12):177–185, 1992.

[52] Y. Krongauz; T. Belytschko. EFG Approximation with Discontinuous Derivatives. *International Journal for Numerical Methods in Engineering*, 41(7):1215–1233, 1998.

[53] D. W. Kim; Y. C. Yoon; W. K. Liu; T. Belytschko. Extrinsic meshfree approximation using asymptotic expansion for interfacial discontinuity of derivative. *Journal of Computational Physics*, 221(1):370–394, 2007.

[54] D. W. Kim; Y. Kim. Point collocation methods using the fast moving least-square reproducing kernel approximation. *International Journal for Numerical Methods in Engineering*, 56(10):1445–1464, 2003.

[55] D. W. Kim; W. K. Liu; Y. C. Yoon; T. Belytschko, S. H. Lee. Meshless point collocation method with intrinsic enrichment for interface problems. *Computational Mechanics*, 40(6):1037–1052, 2007.

[56] J.-S. Chen; L. Wang; H.-Y. Hu; S.-W. Chi. Subdomain radial basis collocation method for heterogeneous media. *International Journal for Numerical Methods in Engineering*, 80(2):163–190, 2009.

[57] T. D. Dang; B. V. Sankar. Meshless Local Petrov-Galerkin Micromechanical Analysis of Periodic Composites Including Shear Loadings. *CMES - Computer Modeling in Engineering & Sciences*, 26(3):169–187, 2008.

[58] I. Ahmadi; N. Sheikhy; M. M. Aghdam; S. S. Nourazar. A New Local Meshless Method for Steady-State Heat Conduction in Heterogeneous Materials. *Engineering Analysis with Boundary Elements*, 34(12):1105–1112, 2010.

[59] N. A. Fleck; J. W. Hutchinson. Strain Gradient Plasticity. *Advances in Applied Mechanics*, 33:295–361, 1997.

[60] J. Pamin; H. Askes; R. de Borst. Two gradient plasticity theories discretized with the element-free Galerkin method. *Computer Methods in Applied Mechanics and Engineering*, 192(20-21):2377–2403, 2003.

[61] S. Banihani; S. De. Method of finite spheres solution of micron-scale plasticity based on a strain gradient formulation. *Computers & Structures*, 86(23-24):2109–2122, 2008.

[62] Y. Yang; A. Misra. Higher-Order Stress-Strain Theory for Damage Modeling Implemented in an Element-free Galerkin Formulation. *CMES - Computer Modeling in Engineering & Sciences*, 64(1):1–36, 2010.

[63] C. Sansour; S. Skatulla. A strain gradient generalized continuum approach for modelling elastic scale effects. *Computer Methods in Applied Mechanics and Engineering*, 198(15-16):1401–1412, 2009.

[64] Y. Sun; K. M. Liew. The buckling of single-walled carbon nanotubes upon bending: The higher order gradient continuum and mesh-free method. *Computer Methods in Applied Mechanics and Engineering*, 197(33-40):3001–3013, 2008.

[65] J. Lv; H. W. Zhang; D. S. Yang. Multiscale method for mechanical analysis of heterogeneous materials with polygonal microstructures. *Mechanics of Materials*, 56:38–52, 2013.

[66] V. Kouznetsova; M. G. D. Geers; W. A. M. Brekelmans. Multi-scale constitutive modelling of heterogeneous materials with a gradient-enhanced computational homogenization scheme. *International Journal for Numerical Methods in Engineering*, 54(8):1235–1260, 2002.

[67] J. Reddy. *An Introduction to the Finite Element Method*. McGraw-Hill Education, 2005.

[68] R. Trobec; G. Kosec; M. Šterk; B. Šarler. Comparison of local weak and strong form meshless methods for 2-D diffusion equation. *Engineering Analysis with Boundary Elements*, 36(3):310–321, 2012.

[69] H. Li; S. S. Mulay. *Meshless Methods and Their Numerical Properties*. CRC Press, Boca Raton, USA, 2013.

[70] A. J. M. Ferreira; E. J. Kansa; G. E. Fasshauer; V. M. A. Leitao. *Progress on Meshless Methods*. Springer Science + Business Media B. V., 2009.

[71] S. N. Atluri; H. T. Liu; Z. D. Han. Meshless Local Petrov-Galerkin (MLPG) Mixed Collocation Method for Elasticity Problems. *CMES - Computer Modeling in Engineering & Sciences*, 14(3):141–152, 2006.

[72] O. C. Zienkiewicz; R. L. Taylor; J. Z. Zhu. *The Finite Element Method: Its Basis and Fundamentals*. Elsevier, 2013.

[73] H. K. Versteeg; W. Malalasekera. *An Introduction to Computational Fluid Dynamics : The Finite Volume Method*. Longman Scientific & Technical, 1995.

[74] S. Li; W. K. Liu. Meshfree and particle methods and their applications. *Applied Mechanics Review*, 55(1):1–34, 2002.

[75] T. Belytschko; Y. Krongauz; D. Organ; M. Fleming; P. Krysl. Meshless methods: An overview and recent developments. *Computer Methods in Applied Mechanics and Engineering*, 139(1-4):3–47, 1996.

[76] B. Jalušić; J. Sorić; T. Jarak. Mixed Meshless Local Petrov Galerkin (MLPG) Collocation Method for Modeling of Heterogeneous Materials. In E. Oñate; X. Oliver; A. Huerta, editor, *Proceedings of the 11th World Congress on Computational Mechanics (WCCM XI)*, Barcelona, Spain, 20-25 July 2014.

[77] S. Li; W. K. Liu. Moving least-square reproducing kernel method Part II: Fourier analysis. *Computer Methods in Applied Mechanics and Engineering*, 139(1-4):159–193, 1996.

[78] W. Han; X. Meng. Some Studies of the Reproducing Kernel Particle Method. In M. Griebel; M. A. Schweitzer, editor, *Meshfree Methods for Partial Differential Equations*, volume 26 of *Lecture Notes in Computational Science and Engineering*, pages 193–210. Springer Berlin Heidelberg, 2003.

[79] T.-P. Fries; H.-G. Matthies. *Classification and Overview of Meshfree Methods*. Technical University Braunschweig, Brunswick, Germany, 2004.

[80] V. P. Nguyen; T. Rabczuk ; S. Bordas; M. Duflot. Meshless methods: A review and computer implementation aspects. *Mathematics and Computers in Simulation*, 79(3):763–813, 2008.

[81] N. Perrone; R. Kao. A general finite difference method for arbitrary meshes. *Computers & Structures*, 5(1):45–57, 1975.

[82] R. Mathon; R. L. Johnston. The approximate solution of elliptic boundary-value problems by fundamental solutions. *SIAM Journal on Numerical Analysis*, 14(4):638–650, 1977.

[83] L. B. Lucy. A numerical approach to the testing of the fission hypothesis. *Astronomical Journal*, 82(12):1013–1024, 1977.

[84] B. Nayroles; G. Touzot; P. Villon. Generalizing the finite element method: Diffuse approximation and diffuse elements. *Computational Mechanics*, 10(5):307–318, 1992.

[85] T. Belytschko; Y. Y. Lu; L. Gu. Element-free Galerkin methods. *International Journal for Numerical Methods in Engineering*, 37(2):229–256, 1994.

[86] W. K. Liu; S. Jun; Y. F. Zhang. Reproducing kernel particle methods. *International Journal for Numerical Methods in Fluids*, 20(8-9):1081–1106, 1995.

[87] E. Oñate; S. Idelsohn; O. C. Zienkiewicz; R. L. Taylor; C. Sacco. A stabilized finite point method for analysis of fluid mechanics problems. *Computer Methods in Applied Mechanics and Engineering*, 139(1-4):315–346, 1996.

[88] C. A. Duarte; J. T. Oden. H-p clouds - h-p meshless method. *Numerical Methods for Partial Differential Equations*, 12(6):673–705, 1996.

[89] J. M. Melenk; I. Babuška. The partition of unity finite element method: Basic theory and applications. *Computer Methods in Applied Mechanics and Engineering*, 139(1-4):289–314, 1996.

[90] N. Sukumar; B. Moran; T. Belytschko. The natural element method in solid mechanics. *International Journal for Numerical Methods in Engineering*, 43(5):839–887, 1998.

[91] G. R. Liu; Y. T. Gu. A point interpolation method. In *Proceedings of the 4th Asia-Pacific Conference on Computational Mechanics*, pages 1009–1014, Singapore, 1999.

[92] T. Zhu; J. Zhang; S. N. Atluri. A meshless numerical method based on the local boundary integral equation (LBIE) to solve linear and non-linear boundary value problems. *Engineering Analysis with Boundary Elements*, 23(5-6):375–389, 1999.

[93] T. Strouboulis; I. Babuška; K. Copps. The design and analysis of the Generalized Finite Element Method. *Computer Methods in Applied Mechanics and Engineering*, 181(1-3):43–69, 2000.

[94] S. N. Atluri; T.-L. Zhu. The meshless local Petrov-Galerkin (MLPG) approach for solving problems in elasto-statics. *Computational Mechanics*, 25(2):169–179, 2000.

[95] S.-H. Park; S.-K. Youn. The least-squares meshfree method. *International Journal for Numerical Methods in Engineering*, 52(9):997–1012, 2001.

[96] S. R. Idelsohn; E. Oñate; N. Calvo; F. D. Pin. Meshless Finite Element Ideas. In H.A. Mang; F.G. Rammerstorfer; J. Eberhardsteiner, editor, *Proceedings of the Fifth World Congress on Computational Mechanics (WCCM V)*, Vienna, Austria, 2002.

[97] Y. L. Wu; G. R. Liu. A meshfree formulation of local radial point interpolation method (LRPIM) for incompressible flow simulation. *Computational Mechanics*, 30(5-6):355–365, 2003.

[98] W. K. Liu; W. Han; H. Lu; S. Li; J. Cao. Reproducing kernel element method. Part I: Theoretical formulation. *Computer Methods in Applied Mechanics and Engineering*, 193(12-14):933–951, 2004.

[99] B. Šarler; J. Perko; C.-S. Chen. Radial basis function collocation method solution of natural convection in porous media. *International Journal of Numerical Methods for Heat & Fluid Flow*, 14(2):187–212, 2004.

[100] H.-Y. Hu; Z.-C. Li; A. H.-D. Cheng. Radial basis collocation methods for elliptic boundary value problems. *Computers & Mathematics with Applications*, 50(1-2):289–320, 2005.

[101] H. Arzani; M. H. Afshar. Solving Poisson´s equation by the discrete least square meshless method. *WIT Transactions on Modelling and Simulation*, 42:23–31, 2006.

[102] G. R. Liu; G. Y. Zhang. Edge-based smoothed point interpolation methods. *International Journal of Computational Methods*, 5(4):621–646, 2008.

[103] S. V. Guvernyuk; G. Ya. Dynnikova. Modeling the flow past an oscillating airfoil by the method of viscous vortex domains. *Fluid Dynamics*, 42(1):1–11, 2007.

[104] B. Li; F. Habbal; M. Ortiz. Optimal transportation meshfree approximation schemes for fluid and plastic flows. *International Journal for Numerical Methods in Engineering*, 83(12):1541–1579, 2010.

[105] E. H. Ooi; V. Popov. An efficient implementation of the radial basis integral equation method. *Engineering Analysis with Boundary Elements*, 36(5):716–726, 2012.

[106] T. Most; C. Bucher. A Moving Least Squares weighting function for the Element-free Galerkin Method which almost fulfills essential boundary conditions. *Structural Engineering and Mechanics*, 21(3):315–332, 2005.

[107] X. Liu; G. R. Liu; K. Tai; K. Y. Lam. Radial point interpolation collocation method (RPICM) for partial differential equations. *Computers & Mathematics with Applications*, 50(8-9):1425–1442, 2005.

[108] H.-F. Chan; C.-M. Fan. The Local Radial Basis Function Collocation Method for Solving Two-Dimensional Inverse Cauchy Problems. *Numerical Heat Transfer, Part B: Fundamentals: An International Journal of Computation and Methodology*, 63(4):284–303, 2013.

[109] G. R. Liu; Y. T. Gu. A meshfree method: meshfree weak-strong (MWS) form method for 2-D solids. *Computational Mechanics*, 33(1):2–14, 2003.

[110] G. R. Liu; Y. L. Wu; H. Ding. Meshfree weak-strong (MWS) form method and its application to incompressible flow problems. *International Journal for Numerical Methods in Fluids*, 46(10):1025–1047, 2004.

[111] Q. Li; J. Sorić; T. Jarak; S. N. Atluri. A locking-free meshless local Petrov-Galerkin formulation for thick and thin plates. *Journal of Computational Physics*, 208(1):116–133, 2005.

[112] K. M. Liew; X. Zhao; A. J. M. Ferreira. A review of meshless methods for laminated and functionally graded plates and shells. *Composite Structures*, 93(8):2031–2041, 2011.

[113] E. C. Aifantis. Strain gradient interpretation of size effects. *International Journal of Fracture*, 95:299–314, 1999.

[114] H. Qiang; W. Gao. Meshless local discontinuous Petrov-Galerkin method with application to blasting problems. *Transactions of Tianjin University*, 14(5):376–383, 2008.

[115] G. R. Liu; G. Y. Zhang. *Smoothed Point Interpolation Methods: G Space Theory and Weakened Weakform*. World Scientific Publishing, Singapore, 2013.

[116] D. Wang; J.-S. Chen; L. Sun. Homogenization of magnetostrictive particle-filled elastomers using an interface-enriched reproducing kernel particle method. *Finite Elements in Analysis and Design*, 39(8):765–782, 2003.

[117] H. Lu; D. W. Kim; W. K. Liu. Treatment of discontinuity in the reproducing kernel element method. *International Journal for Numerical Methods in Engineering*, 63(2):241–255, 2005.

[118] H. Zhang; J. Wu; D. Wang. Free vibration analysis of cracked thin plates by quasi-convex coupled isogeometric-meshfree method. *Frontiers of Structural and Civil Engineering*, 9(4):405–419, 2015.

[119] H. Zhang; D. Wang. An isogeometric enriched quasi-convex meshfree formulation with application to material interface modeling. *Engineering Analysis with Boundary Elements*, 60:37–50, 2015.

[120] X. Zhang; P. Zhang. Heterogeneous Heat Conduction Problems by an Improved Element-Free Galerkin Method. *Numerical Heat Transfer, Part B: Fundamentals: An International Journal of Computation and Methodology*, 65(4):359–375, 2014.

[121] T. Jarak; J. Sorić. Analysis of rectangular square plates by the mixed meshless local Petrov-Galerkin (MLPG) approach. *CMES - Computer Modeling in Engineering & Sciences*, 38(3):231–261, 2008.

[122] T. Most. A natural neighbour-based moving least squares approach for the Element-free Galerkin method. *International Journal for Numerical Methods in Engineering*, 71(2):224–252, 2007.

[123] G. R. Liu; G. Y. Zhang; Y. T. Gu; Y. Y. Wang. A meshfree radial point interpolation method (RPIM) for three-dimensional solids. *Computational Mechanics*, 36(6):421–430, 2005.

[124] C. Q. Ru; E. C. Aifantis. A simple approach to solve boundary-value problems in gradient elasticity. *Acta Mechanica*, 101(1-4):59–68, 1993.

[125] J. Sorić; T. Jarak. Mixed meshless formulation for the analysis of shell-like structures. *CMES - Computer Modeling in Engineering & Sciences*, 199(17-20):1153–1164, 2010.

[126] L. Shu; S. N. Atluri. Topology-optimization of structures based on the MLPG mixed collocation method. *CMES - Computer Modeling in Engineering & Sciences*, 26(1):61–74, 2008.

[127] T. Zhang; Y. He; L. Dong; S. Li; A. Alotaibi; S. N. Atluri. Meshless Local Petrov-Galerkin Mixed Collocation Method for Solving Cauchy Inverse Problems of Steady-State Heat Transfer. *CMES - Computer Modeling in Engineering & Sciences*, 97(6):509–533, 2014.

[128] I. Alfirević. *Tenzorski račun I - Tenzorska mehanika*. Golden Marketing - Tehnička knjiga, 2006.

[129] G. A. Holzapfel. *Nonlinear solid mechanics*. John Wiley & Sons, Ltd., 2000.

[130] W. Voigt. Theoretische Studien über die Elasticitätsverhltnisse der Krystalle. I. Ableitung der Grundgleichungen aus der Annahme mit Polarität begabter Moleküle. *Abhandlungen der Mathematischen Classe der Königliche Gesellschaft der Wissenschaften zu Göttingen*, 34:3–52, 1887.

[131] W. Voigt. Theoretische Studien über die Elasticitätsverhältnisse der Krystalle. II. Untersuchung des elastischen Verhaltens eines Cylinders aus krystallinscher Substanz, auf dessen Mantelfläche keine Kräfte wirken, wenn die in seinem Innern wirkenden Spannungen längs der Cylinderaxe constant sind. *Abhandlungen der Math-*

ematischen Classe der Königlichen Gesellschaft der Wissenschaften zu Göttingen, 34:53–79, 1887.

[132] E. Cosserat; F. Cosserat. *Théorie des corps déformables*. Hermann Archives, 1909.

[133] E. Aero; E. Kuvshinskii. Fundamental equations of the theory of elastic media with rotationally interacting particles. *Soviet Physics - Solid State 2*, pages 1272–1281, 1961.

[134] V. Pal'mov. Fundamental equations of the theory of asymmetric elasticity. *Journal of Applied Mathematics and Mechanics*, 28:496–505, 1964.

[135] I. Kunin. Theory of elasticity with spatial dispersion. One-dimensional complex structure. *Journal of Applied Mathematics and Mechanics*, 30:1025–1034, 1966.

[136] R. Toupin. Theories of elasticity with couple-stresses. *Archive for Rational Mechanics and Analysis*, 17:85–112, 1964.

[137] R. D. Mindlin. Second gradient of strain and surface-tension in linear elasticity. *International Journal of Solids and Structures*, 1:417–438, 1965.

[138] E. Kröner. On the physical reality of torque stresses in continuum mechanics. *International Journal of Engineering Science*, 1:261–278, 1963.

[139] N. Triantafyllidis; E. C. Aifantis. A gradient approach to localization of deformation. I. Hyperelastic materials. *Journal of Elasticity*, 16(3):225–237, 1986.

[140] E. C. Aifantis. The physics of plastic deformation. *International Journal of Plasticity*, 3(3):211–247, 1987.

[141] L. Tenek, E. C. Aifantis. A two-dimensional finite element implementation of a special form of gradient elasticity. *CMES - Computer Modeling in Engineering & Sciences*, 3(6):731–741, 2002.

[142] H. Askes; I. Gitman. Non-singular stresses in gradient elasticity at bi-material interface with transverse crack. *International Journal of Fracture*, 156(2):217–222, 2009.

[143] J. Y. Shu; W. E. King; N. A. Fleck. Finite elements for materials with strain gradient effects. *International Journal for Numerical Methods in Engineering*, 44(3):373–391, 1999.

[144] A. Zervos. Finite elements for elasticity with microstructure and gradient elasticity. *International Journal for Numerical Methods in Engineering*, 73(4):564–595, 2008.

[145] B. Altan; E. C. Aifantis. On some aspects in the special theory of gradient elasticity. *Journal of the Mechanical Behavior of Materials*, 8(3):231–282, 1997.

[146] D. J. Unger; E. C. Aifantis. The asymptotic solution of gradient elasticity for mode III. *International Journal of Fracture*, 71(2):27–32, 1995.

[147] M. Y. Gutkin; E. C. Aifantis. Dislocations and disclinations in the gradient theory of elasticity. *Physics of the Solid State*, 42(12):1980–2988, 1999.

[148] H. Askes; E. C. Askes. Gradient Elasticity Theories in Statics and Dynamics - A Unification of Approaches. *International Journal of Fracture*, 139(2):297–304, 2006.

[149] E. C. Aifantis. Gradient Effects at Macro, Micro, and Nano Scales. *Journal of the Mechanical Behavior of Materials*, 5(3):355–375, 1994.

[150] I. M. Gitman; H. Askes, E. C. Aifantis. The Representative Volume Size in Static and Dynamic Micro-Macro Transitions. *International Journal of Fracture*, 135(1):3–9, 2005.

[151] H. Askes; A. S. J. Suiker; L. J. Sluys. A classification of higher-order strain-gradient models - linear analysis. *Archive of Applied Mechanics*, 72(2):171–188, 2002.

[152] D. J. Unger; E. C. Aifantis. Strain gradient elasticity theory for antiplane shear cracks. Part I: Oscillatory displacements. *Theoretical and Applied Fracture Mechanics*, 34(3):243–252, 2000.

[153] T. Lesičar. *Multiscale Modeling of Heterogeneous Materials Using Second-Order Homogenization*. PhD thesis, Faculty of Mechanical Engineering and Naval Architecture, 2015.

[154] C. Polizzotto. Gradient elasticity and nonstandard boundary conditions. *International Journal of Solids and Structures*, 40(26):7399–7423, 2003.

[155] H. Askes; A. V. Metrikine. Higher-order continua derived from discrete media: continualisation aspects and boundary conditions. *International Journal of Solids and Structures*, 42(1):187–202, 2005.

[156] H. Askes; I. Morata; E. C. Aifantis. Finite element analysis with staggered gradient elasticity. *Computers & Structures*, 86(11-12):12661279, 2008.

[157] D. J. Unger; E. C. Aifantis. Strain gradient elasticity theory for antiplane shear cracks. Part II: Monotonic displacements. *Theoretical and Applied Fracture Mechanics*, 34(3):253265, 2000.

[158] B. Jalušić; J. Sorić; T. Jarak. Modeling of Deformation Responses Using Meshless Local Petrov-Galerkin (MLPG) Approach Based on Strain Gradient Elasticity. In ECCOMAS 2016 Congress Organizing Committee, editor, *Proceedings of European Congress on Computational Methods in Applied Sciences and Engineering (ECCOMAS 2016)*, Crete, Greece, 5-10 July 2016.

[159] M. Y. Gutkin. Nanoscopics of Dislocations and Disclinations in Gradient Elasticity. *Reviews on Advanced Materials Science*, 1(1):27–60, 2000.

[160] J. Fish; T. Belytschko. *A First Course in Finite Elements*. John Wiley & Sons, Ltd., 2007.

[161] S. Li; S. N. Atluri. The MLPG Mixed Collocation Method for Material Orientation and Topology Optimization of Anisotropic Solids and Structures. *CMES - Computer Modeling in Engineering & Sciences*, 30(1):37–56, 2008.

[162] S. N. Atluri; J. Sladek; V. Sladek; T. Zhu. The local boundary integral equation (LBIE) and it's meshless implementation for linear elasticity. *Computational Mechanics*, 25(2):180–198, 2000.

[163] P. Breitkopf; A. Rassineux; J.-M. Savignat; P. Villon. Integration constraint in diffuse element method. *Computer Methods in Applied Mechanics and Engineering*, 193(12-14):1203–1220, 2004.

[164] H. Wendland. *Scattered Data Approximation*. Cambridge University Press, 2005.

[165] Q. Du; M. Gunzburger; L. Ju. Meshfree, probabilistic determination of point sets and support regions for meshless computing. *Computer Methods in Applied Mechanics and Engineering*, 191(13-14):1349–1366, 2002.

[166] J. Belinha. *Meshless Methods in Biomechanics - Bone Tissue Remodelling Analysis*. Springer, 2014.

[167] N. Sukumar; R. W. Wright. Overview and construction of meshfree basis functions: from moving least squares to entropy approximants. *International Journal for Numerical Methods in Engineering*, 70(2):181–205, 2007.

[168] G. E. Fasshauer. *Meshfree Approximation Methods using MATLAB*. World Scientific Publishing, 2007.

[169] P. Lancaster; K. Salkauskas. *Curve and surface fitting: An introduction*. Academic Press Ltd., London, 1986.

[170] W. K. Liu; S. Li; T. Belytschko. Moving Least Square Reproducing Kernel Methods (I) Methodology and Convergence. *Computer Methods in Applied Mechanics and Engineering*, 143(1-2):113–154, 1997.

[171] S. Skatulla. *Computational aspects of generalized continua based on moving least square approximations*. PhD thesis, The University of Adelaide, 2006.

[172] T. Belytschko; M. Fleming. Smoothing, enrichment and contact in the Element-free Galerkin method. *Computers & Structures*, 71(2):173–195, 1999.

[173] P. Krysl; T. Belytschko. ESFLIB: A Library to Compute the Element Free Galerkin Shape Functions. *Computer Methods in Applied Mechanics and Engineering*, 190(15-17):2181–2205, 2001.

[174] D. Levin. The Approximation Power of Moving Least-Squares. *Mathematics of Computation*, 67(224):1517–1531, 1998.

[175] J. J. Monaghan. An introduction to SPH. *Computer Physics Communications*, 48(1):89–96, 1988.

[176] M. Macri; S. De; M. S. Shepard. Hierarchical tree-based discretization for the method of finite spheres. *Computers and Structures*, 81(8-11):798–803, 2003.

[177] W. Han; X. Meng. Error analysis of the reproducing kernel particle method. *Computer Methods in Applied Mechanics and Engineering*, 190(46-47):6157–6181, 2001.

[178] J. Hoster. *Bezmrežna numerička metoda za analizu ploča*. PhD thesis, Fakultet strojarstva i brodogradnje, 2011.

[179] J. G. Wang; G. R. Liu. A point interpolation meshless method based on radial basis functions. *International Journal for Numerical Methods in Engineering*, 54(11):1623–1648, 2002.

[180] J. G. Wang; G. R. Liu; P. Lin. Numerical analysis of Biot's consolidation process by radial point interpolation method. *International Journal of Solids and Structures*, 39(6):1557–1573, 2002.

[181] J. G. Wang; G. R. Liu. On the optimal shape parameters of radial basis functions used for 2-D meshless methods. *Computer Methods in Applied Mechanics and Engineering*, 191(23-24):2611–2630, 2002.

[182] C. Piret. *Analytical and Numerical Advances in Radial Basis Functions*. PhD thesis, Faculty of the Graduate School, University of Colorado, 2007.

[183] R. L. Hardy. Theory and applications of the multiquadric-biharmonic method 20 years of discovery 19681988. *Computers & Mathematics with Applications*, 19(8-9):163–208, 1990.

[184] E. J. Kansa. Multiquadrics - A scattered data approximation scheme with applications to computational fluid-dynamics - I. surface approximations and partial derivative estimates. *Computers & Mathematics with Applications*, 19(8-9):127–145, 1990.

[185] C. J. Coleman. On the use of radial basis functions in the solution of elliptic boundary value problems. *Computational Mechanics*, 17(6):418–422, 1996.

[186] M. Sharan. Application of the multiquadric method for numerical solution of elliptic partial differential equations. *Applied Mathematics and Computation*, 84(2-3):275–302, 1997.

[187] M. A. T. Figueiredo. On Gaussian Radial Basis Function Approximations: Interpretation, Extensions, and Learning Strategies. In *Proceedings of the 15th International Conference on Pattern Recognition*, Barcelona, Spain, 3-7 January 2000.

[188] S. A. Sarra. Integrated multiquadric radial basis function approximation methods. *Computers & Mathematics with Applications*, 51(8):1283–1296, 2006.

[189] G. Roussos; B. J. C. Baxter. Rapid evaluation of radial basis functions. *Journal of Computational and Applied Mathematics*, 180(1):51–70, 2005.

[190] B. Jalušić; J. Sorić; T. Jarak. On the Optimization of Shape Parameters in the Local Radial Point Interpolation Collocation Method for Modeling of Heterogeneous Materials. In I. Kožar; N. Bićanić; G. Jelenić; M. Ćanađija, editor, *Proceedings of the 8th International Congress of Croatian Society of Mechanics*, Opatija, Croatia, 29 September - 2 October 2015.

[191] C. Franke; R. Schaback. Solving partial differential equations by collocation using radial basis functions. *Applied Mathematics and Computation*, 93(1):73–82, 1998.

[192] G. R. Liu; Y. T. Gu. Boundary meshfree methods based on the boundary point interpolation methods. *Engineering Analysis with Boundary Elements*, 28(5):475–487, 2004.

[193] M. A. Goldberg; C. S. Chen; H. Bowman. Some recent results and proposals for the use of radial basis functions in the BEM. *Engineering Analysis with Boundary Elements*, 23(4):285–296, 1999.

[194] X. H. Wu; S. P. Shen; W. Q. Tao. Meshless local Petrov-Galerkin collocation method for two-dimensional heat conduction problems. *CMES - Computer Modeling in Engineering & Sciences*, 22(1):65–76, 2007.

[195] T. Most; C. Bucher. New concepts for moving least squares: An interpolating non-singular weighting function and weighted nodal least squares. *Engineering Analysis with Boundary Elements*, 32(6):461–470, 2008.

[196] X. Liu; G. R. Liu; K. Tai; K. Y. Lam. Radial point interpolation collocation method (RPICM) for the solution of nonlinear poisson problems. *Computational Mechanics*, 36(4):298–306, 2005.

[197] G. R. Liu; J. Zhang; H. Li; K. Y. Lam; B. B. T. Kee. Radial point interpolation based finite difference method for mechanics problems. *International Journal for Numerical Methods in Engineering*, 68(7):728–754, 2006.

[198] S. Li; S. N. Atluri. Topology-optimization of Structures Based on the MLPG Mixed Collocation Method. *CMES - Computer Modeling in Engineering & Sciences*, 26(1):61–74, 2008.

[199] J. Sorić; J. Hoster; T. Jarak; B. Jalušić. Mixed Meshless Plate Analysis Using B-Spline Interpolation. *Transaction of FAMENA*, 39(1):1–14, 2015.

[200] S.-A. Papanicolopulos; A. Zervos; I. Vardoulakis. A three-dimensional C^1 finite element for gradient elasticity. *International Journal for Numerical Methods in Engineering*, 77(10):1396–1415, 2009.

[201] G. R. Liu; Z. Wang; G. Y. Zhang; Z. Zong; S. Wang. An Edge-Based Smoothed Point Interpolation Method for Material Discontinuity. *Mechanics of Advanced Materials and Structures*, 19(1-3):3–17, 2012.

[202] ABAQUS. *Standard*. Dassault Systemes, Providence, Rhode Island, USA, 2014.

[203] M. Kachanov; B. Shafiro; I. Tsukrov. *Handbook of Elasticity Solutions*. Springer Science + Business Media, 2003.

[204] S. Papargyri-Beskou; D. Beskos. Static Analysis of Gradient Elastic Bars, Beams, Plates and Shells. *The Open Mechanics Journal*, 4(65-73), 2010.